Quantum Gas Microscopy of Bosonic Correlations in the Continuum

by

Jinggang Xiang

Submitted to the Department of Physics
in partial fulfillment of the requirements for the degree of

DOCTOR OF PHILOSOPHY IN PHYSICS

at the

MASSACHUSETTS INSTITUTE OF TECHNOLOGY

May 2025

Authored by: Jinggang Xiang
Department of Physics
April 4, 2025

Certified by: Wolfgang Ketterle
John D. MacArthur Professor of Physics, Thesis Supervisor

Accepted by: Lindley Winslow
Professor of Physics
Associate Department Head

Quantum Gas Microscopy of Bosonic Correlations in the Continuum

by

Jinggang Xiang

Submitted to the Department of Physics
on April 4, 2025, in partial fulfillment of the
requirements for the degree of
Doctor of Philosophy in Physics

Abstract

This thesis details the complete upgrade and renovation of an existing experimental platform into a high-resolution quantum gas microscope for ultracold ^{87}Rb atoms. Quantum gas microscopes enable site-resolved imaging, providing unprecedented access to quantum statistical effects and many-body phenomena. While such instruments are often employed to study physics in optical lattices, we have innovatively adapted our apparatus to investigate bulk system behavior.

A major part of this project involved upgrading the scientific apparatus and retrofitting the previous system. We introduced new optical components, including a high-NA objective, and improved the vacuum system for better optical access. Extensive lab renovations, from upgrading the optical table to reorganizing the laser and imaging setups, were carried out to enhance mechanical and thermal stability.

Rigorous optical benchmarking confirmed that the objective achieves diffraction-limited imaging, which is critical for resolving single atoms. This capability allowed us to detect density fluctuations at the scale of the thermal de Broglie wavelength in a quasi-two-dimensional gas of ^{87}Rb atoms. In an experiment resembling Hanbury Brown and Twiss interferometry, we measured a 30% enhancement in the second-order correlation function *in situ*, demonstrating strong bosonic bunching. This outcome underscores the microscope's precision and the importance of high-resolution imaging in capturing subtle quantum statistical effects.

The successful realization of this apparatus demonstrates the utility of quantum gas microscopes in probing bulk systems. With this new platform in place, future studies can explore critical phenomena, many-body correlations, matter-wave emission, and quantum simulations with cold atoms.

Thesis Supervisor: Wolfgang Ketterle
Title: John D. MacArthur Professor of Physics

Acknowledgments

My time at MIT has been a long journey. During those years, many important people were involved. I would like to use the acknowledgment section to document their influences on me properly.

First, I would like to thank my advisor, Prof. Wolfgang Ketterle.

Wolfgang has influenced my academic path even before I started my PhD at MIT. When I was in my last year of undergraduate, his 8.421 lectures on YouTube were a great learning source for a student new to atomic physics. I always find myself going back to those videos and rediscovering a new perspective. I have been learning and mimicking Wolfgang's approaches to science and experiments ever since, and I hope I get at least some of it. His passion for teaching and explaining things in plain language also shaped my taste for science and motivated me to get better at understanding and presenting.

Wolfgang's endless energy has been a great source. No matter how busy he is, Wolfgang always find time for his students. His energy is radiating and contagious.

Wolfgang also strikes me as one of the most optimistic people in my life. Maybe this trait is one of the necessary conditions for success. I remember there were countless times in our weekly meetings, when we were frustrated about things that did not work, he always lifted us by helping us think deeply about the reasons and brainstorm alternatives. He believed in me before I did. I feel very fortunate to have his unwavering support throughout my years at MIT, as I only learned in the last few years of my PhD that I should never take that support for granted.

Next, I would like to thank my friend and labmate, Enid Cruz-Colón. Being one year younger than me, Enid has overlapped for the longest time during my PhD at MIT. Without her, my PhD project would be simply impossible. We went through the whole renovation process of the BEC4 together, adding modern equipment to this 20-year-old "ship of Theseus". We went through all the ups and downs of the experiment, and I feel extremely fortunate to have worked together with Enid during those times. I am so happy to see you grow into the leadership role.

My friendship with Enid extends beyond lab work. I enjoyed every bit of our random conversations about cats, food, Mandarin, religion, politics, sports, and life in general. She has been a very caring and supportive friend to me. Witnessing Enid exploring her life bravely and passionately around Boston has been a pleasure, as it also greatly inspires me. Enid was one of the main forces making sure I stayed social and sane. Kudos for convincing me to climb again, some fun was had for sure.

Dr. Julius de Hond has been an important person in my PhD. Julius joined MIT at the same time as I did. He was a postdoc at BEC4. It took us no time to realize how efficient Julius functions. His ability to learn things fast and implement things quickly and nicely amazed me. I want to write down most the most-Julius moments here. It should make a good story.

During his last year at MIT, we were planning to prepare a birthday gift for Julius. We decided to make a candle using a beer can as the container for wax. The beer can was special as it was a local brewing brand, and that specific beer was called "Julius", although Julius himself was never a beer person. We melted the wax and poured it into the can with a wick centered. The next day, the wax had solidified, and we noticed that the surface of the wax was not flat around the wick: it had sunk at the center around the wick. The surface was lower in the center and higher on the rim, forming some kind of curvature. We did not think too deeply, as we thought there might have been some imperfection in the curing process.

However, the moment we presented this gift to Julius, he recognized that the phenomenon is related to "solidification pipes". Then he recommended a paper to us and explained why the surface would display that curvature.

Being a sharp theorist and a handy experimentalist, Julius is very humble and modest. Other than physics, his passion for nature has been a great inspiration for me. Those surprising visits of the American robins and their babies in front of the BEC4 office made the spring of 2022 special.

I also want to thank Dr. Woo Chang Chung. Woo Chang was the senior PhD student before me. His meticulous style of research has shaped my style in a good way. I remember me lacking confidence of running the machine by myself. Woo Chang

would encourage me by saying running the machine is as simple as driving a car, only later I discovered that he did not know how to drive at that time. Woo Chang also laid out the foundational design and planning works of the BEC4 microscope. Thank you for teaching me all the tricks in the lab and thank you for being very supportive and responsive during my job search.

There are more BEC4 members to be thanked. Candice Chua, the younger generation of BEC4. It was fortunate for us to have Candice on BEC4. She joined BEC4 from a slightly different trajectory. She embraced all the challenges and brought joy and connection to the team. I was so happy for Candice winning the best poster award at QuARC. Dr. Will Miner, the latest addition to the BEC4 team as our new postdoc. Will brought his passion and intensity from JILA to MIT since day one. He took initiative immediately when he joined our group although at that time we were not doing science, we were frustrated by the clogged Zeeman slower. Will calmed us down and helped us debug the machine. Without him, we were certainly not able to finish the paper in time. I am excited about the future direction of BEC4 as I know the it "will" be in good hands.

Jacob Fricke was a Master's student in BEC4. Although he stayed for only one year, he left a strong influence on the lab, including building one of the crucial components of the microscope. His infectious energy made our time working together enjoyable and memorable.

There are other people from CUA I want to express my thanks to. Eunice Lee and Hanzhen Lin from BEC5 have been great colleagues and friends to me and the whole BEC4 lab. Eunice and Hanzhen always went the extra mile for others, whether it was discussing physics, lending equipment, proofreading manuscripts, or helping us debug. Hanzhen is the electronics guru of the Ketterle group. We always turned to him for experimental questions. He was also responsible for organizing the Friday lunch meeting every week, which is a big service to the Ketterle group. I would also like to thank Yu-Kun Lu and Guoqing Wang. I always enjoyed discussing physics with them, as I would learn new things from those conversations every time.

I feel very fortunate to have Alexander Yu Chuang as my cohort. Alex and I

formed a study group to prepare for the oral exams together with Yu-Kun, and we took many classes together. Outside academia, Alex has kept me sane and active by inviting me almost every weekend to some sports activities, including basketball, biking, disc golf, and pickleball. I am happy and excited that our friendship and those weekend sports can continue on the West Coast after my graduation.

From sharing equipment to collaboration, CUA has been a wonderful community for AMO physicists. I would like to thank the following members of CUA for their support and camaraderie: Jesse Amato-Grill, Paul Niklas Jepsen, Ivana Dimitrova, Hyungmok Son, Juliana Park, Matthew Peters, Beili Hu, Alyssa Rudelis, Li Du, Michael Cantara, Jiahao Lyu, Yiming Zhang, Huan Bui, Eric Wolf, Ruixiao Yao, Yicheng Bao, and Muqing Xu.

I would also like to thank my roommate Jixiang. Jixiang is a super handy experimentalist, both in his condensed matter experiments and in maintaining our apartment. I greatly enjoyed our conversations about many-body physics and probability theory. Your presence has made my stay in Cambridge a wonderful experience.

I would like to thank my friends Charleen and Jingnan. Thank you for inviting me to the fantastic climbing trip at Arcadia. Those bird watching excursions, especially those owl-encounters, will be remembered fondly.

I would like to thank my mother and father. Without you, I would not be able to come to the US let alone finish my PhD. You always support me and care about the well-being of me. I felt guilty that the visa had kept us separated for way too long. Too long that I missed important parts of your life. I am happy that we will see other soon. I miss you.

I would like to thank two cats of mine: Lila and Disco. They were both FIP survivors, which is something I felt very fortunate and proud of. The resilience they show in their life has always been a pure inspiration to me. They served as great emotional support during the later part of PhD, and I hope I have provided similar benefits to them.

Last but not least, I would like to thank Tianyun Hua, my best friend, my partner in crime, and my love for life. Those adventures with you have always been my

happiest times. I learned so much from you on how to be a better person and a better partner. You are always there for me, and knowing that fills me with determination. I am excited we can grow together and excited about our next chapters.

Contents

1 Introduction **21**

1.1 Quantum simulation 21

1.1.1 Optical lattice 22

1.2 Quantum gas microscopy 23

1.2.1 Discretized vs continuous 24

1.2.2 Physics in the continuum 24

1.3 Thesis outline 26

2 Spin Mott **29**

2.1 Mott insulator 29

2.2 Spin-1 Hamiltonian 30

2.2.1 Quench dynamics 31

2.2.2 Ground state: spin Mott 31

2.3 Limitation of bulk detection 33

3 Design and Calibration of the Microscope **35**

3.1 Optical resolution 35

3.1.1 Airy disk 36

3.1.2 Criteria 37

3.2 Microscope design 39

3.2.1 Objective specifications 39

3.2.2 Viewport window 40

3.3 Measurement of the viewport surface profile 42

3.3.1 Phase-shifting interferometer . . . 42
3.3.2 Zernike polynomials . . . 46
3.3.3 Measured surface profile . . . 49
3.4 Aberration and correction . . . 50
3.4.1 Astigmatism . . . 50
3.4.2 Coma . . . 56
3.5 Benchmark result . . . 59
3.5.1 Strehl Ratio . . . 59
3.5.2 Measured point-spread-function . . . 61

4 The BEC4 Machine 63
4.1 Main chamber . . . 63
4.1.1 MOT loading and magnetic trap . . . 64
4.1.2 Transfer beam: tODT . . . 65
4.1.3 Beam displacer . . . 65
4.1.4 Anti-ODT . . . 68
4.2 New science chamber . . . 69
4.2.1 Overview of the vacuum system . . . 69
4.2.2 Baking to ultra-high vacuum . . . 70
4.2.3 HR coating crazing after baking . . . 73
4.2.4 Laser setup . . . 76
4.2.5 Magnetic field control . . . 78
4.2.6 Floating table . . . 81

5 Quantum Gas Microscopy 85
5.1 Introduction . . . 85
5.2 Trapping and cooling . . . 86
5.2.1 Optical traps . . . 86
5.3 Laser cooling under the microscope . . . 90
5.3.1 Considerations for cooling . . . 90
5.3.2 Polarization gradient cooling . . . 92

5.4 Alignment procedure . . . 98
5.4.1 Coarse alignment . . . 98
5.4.2 Fine alignment . . . 99
5.5 Fluorescence imaging . . . 102
5.5.1 Optical setup . . . 102
5.6 Reconstruction algorithm . . . 103
5.6.1 Deconvolution . . . 107
5.6.2 Identify single isolated atoms . . . 110
5.6.3 Calibration . . . 113
5.6.4 Threshold . . . 117

6 Correlations in the Bosonic Fields 121
6.1 Hanbury Brown and Twiss experiment . . . 121
6.1.1 A tale of two interferometers . . . 121
6.1.2 A semi-classical explanation . . . 123
6.1.3 From photons to atoms . . . 130

7 Microscopic Study of the Correlation 137
7.1 Experimental setup . . . 137
7.1.1 Parameter regime . . . 138
7.1.2 Sequence . . . 140
7.2 Thermometry . . . 141
7.3 Data Analysis . . . 143
7.3.1 Spatial and thermal dependence . . . 145
7.3.2 Thermal vs BEC . . . 146
7.3.3 Systematic errors . . . 149
7.4 Quantum point spread fucntion . . . 152
7.4.1 Quench dynamics . . . 152
7.4.2 Model the blurring . . . 154
7.5 Other corrections . . . 156
7.5.1 Quasi two-dimensionality . . . 156

7.5.2 Finite system size corrections 157

8 Conclusion and Outlook **163**

8.1 Conclusion 163

8.1.1 Building 163

8.1.2 Scientific project 164

8.2 Outlook 165

8.2.1 Hardware 165

8.2.2 More on *in situ* correlation 165

8.2.3 Matter-wave emission 165

A Preparation of the Spin-Mott State: A Spinful Mott Insulator of Repulsively Bound Pairs **169**

List of Figures

1-1 Two approaches to probe physics in the continuum: absorption imaging vs. fluorescence imaging with a quantum gas microscope. 25

2-1 Transient enhancement and reduction of the spin alignment by coherent spin dynamics. 32

2-2 Preparation of the spin-Mott state for various pairing energies D. . . 33

3-1 Comparison of different criteria for resolution limit. 38

3-2 Optical setup for surface profiler. 44

3-3 Visualization of the first 21 Zernike polynomials. 47

3-4 Measured and reconstructed surface profile of the viewport window. . 49

3-5 Zernike coefficients derived from the viewport surface profile. 51

3-6 Astigmatism aberration in the viewport surface profile. 52

3-7 Zemax simulation illustrating how tilting the eyepiece at a small angle can compensate for the astigmatic aberration introduced by the deformed viewport. 54

3-8 Point-spread function measurements with objective rotation. 57

3-9 Illustrations on an effective tilt of the objective before refurbishing. . 58

3-10 Measured point spread function using the SNOM fiber tip. 62

4-1 Overview of the optical setup for the transport beam tODT. 66

4-2 Detailed illustration of using a plate window to displace a point source. 67

4-3 Repeated measurements of the tODT position stability across runs before temperature stabilization. 68

4-4 Photos of the new vacuum system assembly. 70
4-5 Baking temperature and vacuum pressure monitored over several days. 71
4-6 Photo of the crazed in-vacuum high-reflective coating after baking. . . 73
4-7 Cross-section view of the final viewport configuration after HR coating crazing due to baking. 76
4-8 Photos of the magnetic coils around the science chamber. 79
4-9 Photos of the in-vacuum RF antenna in the new science chamber. . . 80
4-10 Schematics of the floating table and raw fluorescence images taken before the machine table is floated. 82

5-1 Schematic illustrating the main laser beams involved in quantum gas microscopy. 87
5-2 Comparison of the cross-sectional profiles of the light sheet beams. . . 89
5-3 Optical beam path for the fifth molasses beams propagating through the objective. 94
5-4 Lifetime of total atom loss in deep pinning lattices under optimal polarization-gradient cooling, measured via absorption imaging. . . . 97
5-5 Using the spherical aberration as an indicator to find the right focal plane. 101
5-6 Illustration of the imaging system layout of the microscope. 102
5-7 Simulated fluorescence images with variable numerical apertures. . . . 105
5-8 Modulation transfer function of a diffraction-limited imaging system with a numerical aperture (NA) 0.8. 106
5-9 Raw fluorescence image and its deconvolutions using various regularization filters. 109
5-10 Determining the optimal threshold for binarizing the image post-deconvolution. 111
5-11 Using hit-or-miss transform to identify single and isolated atoms. . . 112
5-12 Illustration for calibrating the pinning lattice angles and magnification. 114
5-13 Finding the angles of the underlying lattice. 115
5-14 Illustration for calibrating the underlying pinning lattice origin. . . . 116

5-15 From raw a fluorescence image to a reconstructed lattice site occupation. 118
5-16 Two consecutive exposures separated by 1.5 seconds. 119

6-1 Two types of stellar interferometers. 122
6-2 Illustration of light emitted by a large number of uncorrelated emitters. 125
6-3 Interference pattern generated by N random emitters. 129
6-4 Interference pattern from N random sources measured in the near and far fields. 131
6-5 Illustration of the phase space distribution for measuring bosonic bunching *in situ* vs far field 134
6-6 *In situ* and far-field speckle patterns. 136

7-1 Second-order correlation function for an ensemble of thermal rubidium atoms at various temperatures. 139
7-2 Experimental setup. 140
7-3 Temperature determination. 142
7-4 Experimental overview. 144
7-5 Spatial and thermal dependence of the second-order correlation function. 147
7-6 Second-order correlation function evaluated in the thermal gas vs. in the BEC. 148
7-7 Correction for spatial inhomogeneity. 151
7-8 Illustration of how pinning lattices are used to sample the density distribution of an ultracold gas in a continuum, along with their limitations. 153
7-9 Fundamental resolution limit for one-point and two-point detections. 154
7-10 Illustration demonstrating how the finite trap frequency along the z-direction reduces the contrast of the second-order correlation function. 157
7-11 $g^{(2)}$ corrections with finite atom number. 160

8-1 Simulation of matter-wave emission under the microscope. 167

List of Tables

3.1 Technical specifications of the BEC4 ^{87}Rb microscope objective. . . . 39

3.2 Typical Zernike polynomials and associated optical aberrations. . . . 48

4.1 Final baking temperatures for key vacuum components. 72

4.2 Bias field of side bias coils. 80

Chapter 1

Introduction

This thesis presents the research progress in building a quantum gas microscope for ultracold ^{87}Rb. The work naturally divides into two parts: the development of the microscope to achieve quantum gas microscopy, and the microscopic study of bosonic correlations.

The quantum gas microscope project was initially motivated by the goal of expanding the capabilities of quantum simulation in optical lattices, particularly for exploring quantum magnetism. Along the way, we discovered that this system can also be used to probe physics in the continuum. In this chapter, I begin by reviewing the concept of quantum simulation, followed by a brief discussion of quantum gas microscopy. Then, I will motivate the use of quantum gas microscopes for studying physics in the continuum. The chapter concludes with an outline of the thesis.

1.1 Quantum simulation

The concept of quantum simulation traces its roots back to a visionary idea proposed by Richard Feynman in the early 1980s [1]. He recognized that simulating quantum systems using classical computers quickly becomes intractable as the system size grows, due to the exponential scaling of the Hilbert space. Feynman suggested that the most natural way to study quantum systems is by using another controllable quantum system that itself obeys similar laws to those of the system of interest.

This idea of analog computation of quantum systems is regarded today as quantum simulation [2].

Since the experimental realization of Bose-Einstein condensation [3–5] and degenerate Fermi gases [6–8], ultracold atoms have emerged as an ideal platform for quantum simulation [9]. With the development of optical lattices, the concept of using neutral atoms to mimic the Hamiltonian for electrons in solid crystals has significantly advanced the exploration of quantum phase transitions [10, 11], quantum magnetism [12,13], topological matter [14,15], and non-equilibrium dynamics [16,17].

1.1.1 Optical lattice

Optical lattices are a key component of neutral atom quantum simulators. They create a periodic potential for atoms, allowing them to tunnel between lattice sites and interact with one another. This setup is analogous to the crystal lattice experienced by electrons in real materials. In this section, I briefly review the underlying theory, which will be useful in later chapters.

An optical lattice is a periodic potential formed by interfering laser beams and can be understood as a special case of an optical dipole trap. Optical dipole traps confine neutral atoms via the AC Stark shift induced by an off-resonant laser. The oscillating electric field polarizes the atom, leading to an energy shift proportional to the local intensity. For red-detuned light ($\omega_L < \omega_0$), the AC Stark shift is negative, and atoms are attracted to regions of maximum intensity. For blue-detuned light ($\omega_L > \omega_0$), the shift is positive, and atoms are drawn to regions of minimum intensity. Since the trapping light can be far-detuned, spontaneous scattering is suppressed, making the potential effectively conservative. The trap depth $U(r)$ depends on atomic properties and scales linearly with the light intensity [18].

$$U(r) = \frac{3\pi c^2}{2\omega_0^3} \frac{\Gamma}{\Delta} I(r), \tag{1.1}$$

where c is the speed of light, Γ is the natural decay rate of the atomic transition, and $\Delta = \omega_L - \omega_0$ is the detuning of the laser frequency ω_L from the atomic resonance ω_0.

$I(r)$ is the spatial profile of the intensity, which is standing waves for optical lattices.

Optical lattices are commonly characterized in terms of the recoil energy E_r, which is the kinetic energy an atom gains when it absorbs or emits a single lattice photon. Mathematically, $E_\mathrm{r} = \frac{\hbar^2 k^2}{2m}$, where k is the wave number of the lattice light and m is the atomic mass. This energy scale sets a convenient benchmark for comparing the depth of the periodic potential formed by interfering laser beams.

1.2 Quantum gas microscopy

One of the most notable quantum simulations with atoms in optical lattices is the observation of the superfluid to Mott insulator phase transition [10]. Since then, there has been great interest in cold atom systems in optical lattices. In the seminal paper [10], researchers identified different quantum phases by taking absorption images to observe the momentum distribution of the atomic cloud after releasing it from the optical lattice. Although effective for probing momentum space, absorption imaging ultimately lacks spatial resolution. In pursuit of better spatial resolution, quantum gas microscopes were invented around 2009 [19, 20].

First, let me clarify the term "quantum gas microscope": it refers to an optical microscope designed for imaging quantum gases. Compared to conventional imaging methods such as absorption imaging, the defining feature of quantum gas microscopes is their capability to detect single atoms with high fidelity and high spatial resolution. The paradigm of quantum gas microscopy involves fluorescence imaging of atoms held in an optical lattice. The optical lattice plays a central role, distinguishing this technique from other *in situ* readouts of neutral atoms, such as optical tweezer arrays [21–23]. It also sets the resolution scale of the imaging system to be on the order of the optical wavelength, as optical lattices are typically generated by interference patterns. Typically, through laser cooling in a deep optical lattice, atoms can scatter photons without changing their spatial location for several seconds. The objective lens is designed to collect photons scattered at large angles, enabling spatial resolution on the order of the lattice spacing, that is, hundreds of nanometers. Depending on

the atomic species and lattice geometry, a software-based reconstruction algorithm is often required to sharpen the fluorescence images and ultimately convert a two-dimensional camera image into a matrix representing lattice site occupations.

Since 2009, many cold atom experiments have implemented quantum gas microscopes for different atomic species, including rubidium [19, 20, 24, 25], lithium [26–30], potassium [31, 32], cesium [33, 34], strontium [35], ytterbium [36], erbium [37], and even cold molecules [38].

1.2.1 Discretized vs continuous

As mentioned earlier, the development of quantum gas microscopes should be seen in the broader context of quantum simulation. These microscopes were originally conceived to expand the capabilities of neutral atom quantum simulators. In condensed matter physics, high-resolution *in situ* probes like scanning tunneling microscopy are standard tools. Likewise, neutral atom platforms benefit greatly from a powerful microscope capable of resolving individual lattice sites. A central focus in the quantum simulation community has been the study of Hubbard models. Quantum gas microscopes have enabled direct observation of phenomena such as magnetic ordering [39–41], transport [42, 43], and doping [44, 45].

The BEC4 group had been conducting research on quantum simulation using the Bose-Hubbard model, with a particular focus on exploring quantum magnetism in a spin-1 Hamiltonian. Our primary detection method was absorption imaging, which only reveals the global properties of the system. Eventually, we reached the limitations of this bulk detection technique, which motivated us to upgrade to a quantum gas microscope in hopes of gaining access to more microscopic, site-resolved information.

1.2.2 Physics in the continuum

However, during the development of the microscope, we realized an alternative path. Rather than using the quantum gas microscope solely to study many-body phenomena on a lattice, we could instead use it to probe physics in the continuum as illustrated in

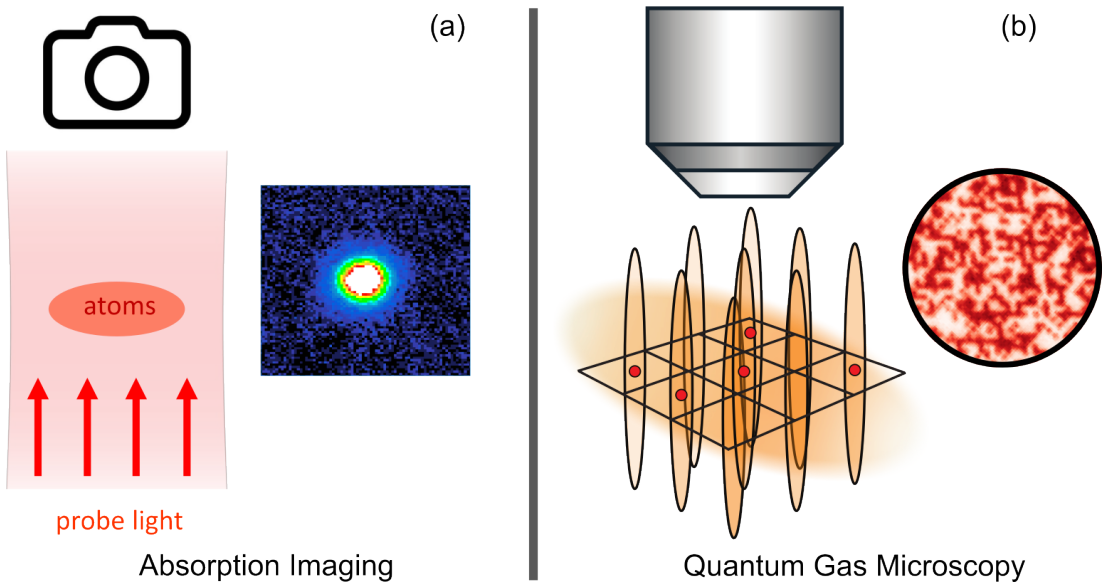

Figure 1-1: **Two approaches to probing physics in the continuum: absorption imaging vs. fluorescence imaging with a quantum gas microscope.** (a) Conventional absorption imaging. A resonant probe beam is shone onto the atomic cloud, which casts a shadow that is imaged onto a camera. Due to limited optical resolution and the line-of-sight integral, absorption images typically reveal only global properties of the cloud, such as the total atom number and the temperature. A representative absorption image is shown. (b) Fluorescence imaging with a high-resolution microscope. Atoms are pinned in place by deep optical lattices, and the photons they scatter are collected by a high-numerical-aperture objective. A representative fluorescence image is shown, which reveals microscopic information such as the location of each individual atom.

Fig. 1-1. By rapidly ramping up deep optical lattices after state preparation, we freeze the atomic motion and effectively take a snapshot of the many-body wavefunction in real space. This approach opened up a compelling and previously underexplored direction, with several related works emerging around the same time [46–49].

The high spatial resolution of the quantum gas microscope reveals significantly more information than earlier detection techniques. In particular, we use it to probe *in situ* bosonic density-density correlations. Due to limitations in detector resolution, such correlations have historically been studied in the far field. Earlier *in situ* experiments investigated enhanced density fluctuations at length scales much larger than the thermal de Broglie wavelength [50], temporal correlations [51], or fluctuations inferred indirectly via Fourier analysis of phase-contrast images [52]. In contrast, our work presents the first direct *in situ* observation of density fluctuations at the scale of the thermal de Broglie wavelength in an ultracold gas of bosons.

1.3 Thesis outline

- Chapter 1 serves as an introduction to the thesis, which centers on the construction of a quantum gas microscope and the scientific discoveries it enabled. In this chapter, quantum gas microscopy is introduced within the broader context of quantum simulation using cold atoms in optical lattices. The chapter concludes with a brief overview of the scientific project: the *in situ* observation of bosonic density-density correlations, highlighting the novelty of applying quantum gas microscopy to study physics in the continuum.

- Chapter 2 briefly reviews a scientific project conducted prior to the microscope upgrade, namely the quantum simulation of a one-dimensional spin-1 Hamiltonian. In this work, we successfully prepared the ground state of the spin-1 Hamiltonian under a specific condition and investigated its lifetime. Although this project is not directly connected to the quantum gas microscope, it is documented here for completeness.

- Chapter 3 introduces the custom-made high-NA microscope objective, the main character of the play. It outlines the key design considerations behind its development and details several optical calibration benchmarks conducted to verify performance, including a white-light interferometer measurement of the surface profile and a point spread function analysis.

- Chapter 4 describes the BEC4 apparatus. During my PhD, the quantum gas microscope upgrade required a major rebuild of the science chamber. This chapter documents the existing components of the machine (the main chamber) and details the hardware upgrades made to the new science chamber to ensure compatibility with the microscope.

- Chapter 5 focuses on achieving successful quantum gas microscopy. It explains the optical setup around the new science chamber and the optimizations for laser cooling and trapping, detailing the alignment procedure of the microscope within the experiment. Lastly, it discusses the deconvolution and reconstruction algorithm, the final component in the quantum gas microscope workflow.

- Chapter 6 focuses on developing an intuitive understanding of bosonic correlations, which is the central topic of study. By using the analogy of an optical speckle, we draw connections to the seminal Hanbury Brown and Twiss (HBT) experiments. While placing our experiment within the reference frame of HBT, we also highlight the novelty of our work: probing the correlations *in situ* instead of in the far field.

- Chapter 7 details a key experiment enabled by the quantum gas microscope: the *in situ* measurement of bosonic correlations. Rather than using optical lattices to study discretized many-body Hamiltonians, we employ pinning lattices to freeze the motion of a two-dimensional continuous sample and probe its *in situ* density correlations. In this experiment, we report the first direct *in situ* observation of density fluctuations on the scale of the thermal de Broglie wavelength in an ultracold gas of bosons.

- Chapter 8 concludes the thesis and offers a scientific outlook on several future directions enabled by the quantum gas microscope.

Chapter 2

Spin Mott

BEC4 has been exploring the use of bosons in optical lattices for quantum simulation for over a decade. During the first half of my PhD at MIT, I focused on completing projects related to the quantum simulation of one-dimensional spin-1 Hamiltonians. Although this work is not directly related to the main topic of the thesis—quantum gas microscopy—it is important to document the efforts in quantum simulation using lattice systems with bulk detection. If the rest of the thesis forms the mainland, then this chapter is more like an enclave.

These endeavors resulted in two scientific publications [53, 54], one of which has been discussed in detail in a prior PhD thesis [55], while the other has not been covered in any thesis and is included as Appendix A. In this chapter, I will briefly summarize the results presented in the latter publication [54]. At the end of the section, I will use this project to motivate the development of the quantum gas microscope.

2.1 Mott insulator

Many quantum simulators are based on Hubbard models. An important phase of the Hubbard model, whether bosonic or fermionic, is the Mott insulator. Due to strong on-site interactions, atoms tend to localize. With the appropriate number of atoms (i.e., the correct chemical potential), it is possible to prepare a state where exactly one atom occupies each lattice site. This state is an interaction-induced insulator, as

any charge excitation or transport requires a finite amount of energy.

Mott insulator states of ultracold atoms in optical lattices have played a central role in ultracold atoms research [2, 56]. Because they are a well-isolated low-entropy state protected by an energy gap, such states have been considered as qubits [57], as a starting point for adiabatic state preparation [58, 59], and for studies of many-body physics [9], in particular quantum magnetism [60]. They were used in seminal work on Heisenberg spin Hamiltonians [12, 13, 61] and as a platform to study Rydberg crystals [62] and magnetic polarons [63].

2.2 Spin-1 Hamiltonian

Our system comprises two different hyperfine states of ^{87}Rb in a (spin-dependent) optical lattice. In one dimension, and assuming equal tunneling for both components, the system can be described by the two-component Bose-Hubbard Hamiltonian [64]:

$$\begin{aligned} H = & -t \sum_i \left(a_i^\dagger a_{i+1} + b_i^\dagger b_{i+1} + \text{H.c.} \right) \\ & + \frac{U}{2} \sum_i \sum_{k \in \{a,b\}} n_i^k \left(n_i^k - 1 \right) + U_{AB} \sum_i n_i^a n_i^b. \end{aligned} \tag{2.1}$$

Here n_i^k is the number operator acting on component k on site i, t is the nearest-neighbor tunneling parameter; U and U_{AB} are the intra- and interspecies on-site interactions, respectively, where we have assumed $U = U_{AA,BB}$.

In the Mott insulator regime, the optical lattices are sufficiently deep such that the on-site interaction suppresses first-order tunneling, and exchange processes are only possible via second-order tunneling. For two atoms per site with two internal states, the Bose–Hubbard Hamiltonian is approximated by an effective spin Hamiltonian

$$H = -J \sum_{\langle ij \rangle} \mathbf{S}_i \cdot \mathbf{S}_j + D \sum_i (S_i^z)^2 - B \sum_i S_i^z, \tag{2.2}$$

where $\mathbf{S}_i$ are spin-1 operators, $\langle ij \rangle$ are pairs of nearest-neighboring sites, J is the exchange constant, D is the uniaxial single-ion anisotropy constant, and B is a fictitious magnetic bias field.

Our previous work has focused on understanding the spin-1 model as described in Eqn. 2.2. Spin-1 models are qualitatively different from spin-1/2 models. When the spin degree of freedom is added to a Mott insulator, it opens up a richer phase diagram [64]. We have been the first group to explore them with ultracold atoms. For this Hamiltonian, we have studied both quench dynamics and ground state properties.

2.2.1 Quench dynamics

Because preparing spinful ground states can be challenging, many experiments probed spin dynamics through quenches, where an initial spin-polarized state is suddenly rotated into a spin superposition. This has enabled the study of the transport of bound states [65] and spin waves in isotropic [66] and anisotropic [67, 68] $S = 1/2$ Heisenberg models. We have also studied the relaxation of rotated spin states in $S = 1$ Heisenberg models [53].

We realized this spin Hamiltonian using a rubidium Mott insulator with two atoms per site in two internal states, $|a\rangle$ and $|b\rangle$. Although the contact interactions between atoms in the same hyperfine state, U_{aa}, U_{bb}, and in different hyperfine states, U_{ab}, differ by only a few percent, this small difference gives rise to an on-site interaction anisotropy $D = U_{aa,bb} - U_{ab} \sim 10\,\mathrm{Hz}$, which is comparable to the exchange coupling J. As shown in Fig. 2-1, by tuning J via the lattice depth, we were able to pass through the resonance point where $J \approx D$, and observed new features in the dynamics and thermalization of the system after preparing an out-of-equilibrium state in one-dimensional spin chains.

2.2.2 Ground state: spin Mott

For a spinful Mott insulator with two particles per site, if the on-site interaction energy U_{AB} between opposite spins is considerably lower than that between identical

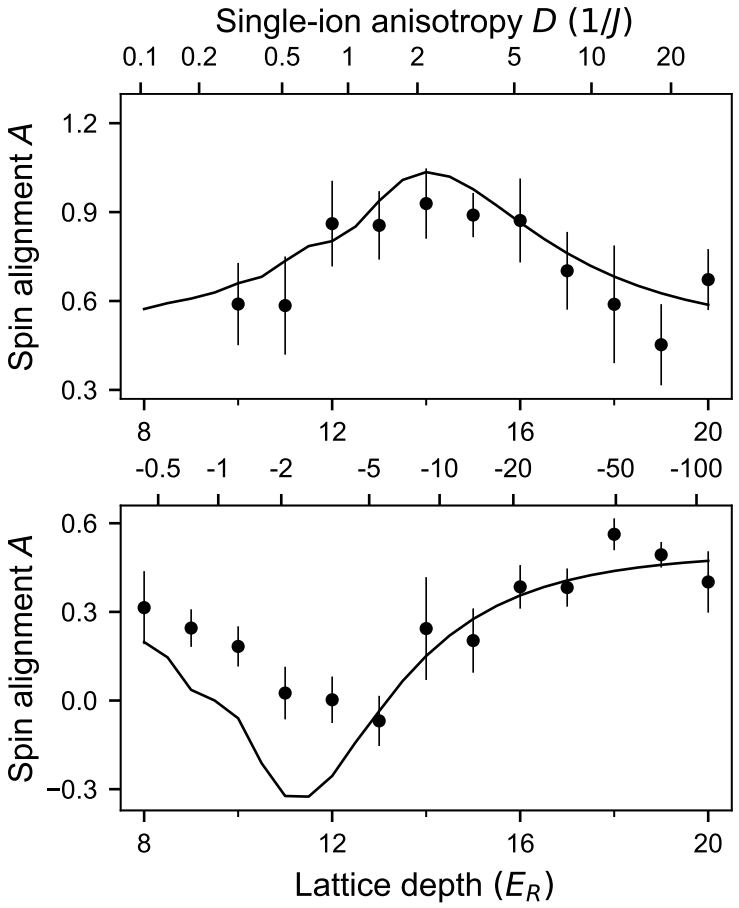

Figure 2-1: **Transient enhancement and reduction of the spin alignment by coherent spin dynamics.** The change in spin alignment A is strongest when $|D/J| \sim 2$. Measurements were done for both positive (top) and negative (bottom) values of D/J. The top axis in both figures indicates the D/J ratio. Solid lines are the results of MPS-TEBD calculations.

spins (U), there is an effective pairing energy $D = U - U_{AB}$ favoring the formation of repulsively bound pairs of opposing spins. The ground state of the $N = 2$ Mott insulator, then, is a Mott insulator of spin-paired doublons with an excitation gap D. This implies that a spinful $N = 2$ Mott insulator has a region in its phase diagram where the excitation gap is of scale D or U, which typically corresponds to 50 nK for rubidium.

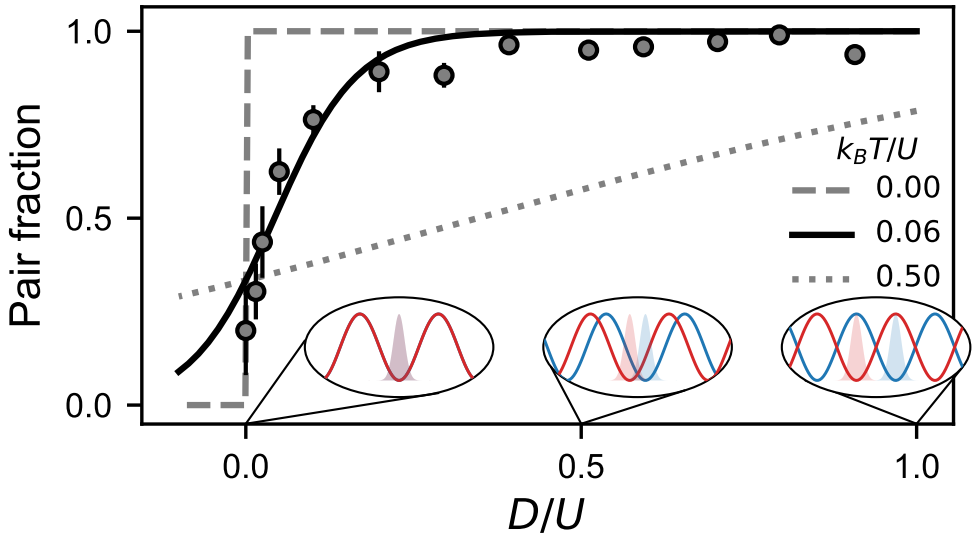

Figure 2-2: **Preparation of the spin-Mott state for various pairing energies D.** The decrease of the spin pairing fraction for small D is explained by a finite temperature.

As shown in Fig. 2-2, we can prepare the spin Mott state with high fidelity as indicated by the high pair fraction when the pairing energy D is comparable to the interaction energy between identical spins U.

2.3 Limitation of bulk detection

We can successfully prepare the spin Mott state, which is the ground state of the Hamiltonian (Eqn. 2.2) when the pairing energy D is dominant. While the spin-Mott insulator is a product state, it can be used as a starting point for adiabatically preparing correlated spin states such as the xy ferromagnet [58, 64], which is the ground state when the exchange term J is dominating.

Similar schemes have been proposed for fermions, where the (gapped) band insulator can be used to adiabatically prepare an antiferromagnet [59]. In that case the initial product state is stabilized by the bandgap, whereas in our case it is stabilized by the pairing energy D. This difference in energy scales also makes our system suitable for studying spin-charge separation [69].

Adiabatic state preparation requires that the gaps between many-body states are traversed sufficiently slowly; in a Landau–Zener model of avoided crossings, the maximum rate is set by the coupling between states [70–72]. In a deep lattice this scales with second-order tunneling as $\propto 4t^2/U$ [58,73]. Furthermore, coupling between different many-body states scales inversely with the number of sites in a chain. For our present system the superexchange scale is maximally 10 Hz at a longitudinal lattice depth of 12 E_r.

Preliminary results showed that we were not able to reach adiabaticity in a bulk lattice. This is possibly due to competing heating processes, or because our system of spin chains is inhomogeneous, with some chains having holes and with a wide distribution of chain lengths. All these shortcomings can be avoided with quantum microscope with which we can prepare different chain lengths using a digital micromirror device (DMD). Post-selection can reject chains with holes. In a chain with finite length N, the energy gap scales with 1/N, so we will start out with small chains for which adiabaticity is protected by a larger gap.

The idea of applying adiabatic state preparation to a spin-1 Hamiltonian in a microscopic setting has been successfully implemented by researchers at USTC recently. Using a quantum gas microscope, along with self-developed techniques such as staggered-immersion cooling [74], they observed the elusive counterflow superfluidity (CSF) in a two-component Mott insulator [75]. Their success is a compelling demonstration of how a quantum gas microscope can reveal physics that is extremely challenging to access using only bulk detection methods.

Chapter 3

Design and Calibration of the Microscope

The effort to resolve increasingly smaller features has been a central pursuit in science and technology. Whether in imaging or fabrication, the ability to distinguish or create fine details is crucial for progress. However, the resolution of an optical system is fundamentally constrained by the wavelength of light, even in a perfect imaging system without aberrations. This limit arises from the wave nature of light, which prevents an optical system from capturing or generating arbitrarily small features through conventional means.

3.1 Optical resolution

A useful way to understand why conventional optics struggle with small features is to view a lens as a low-pass spatial filter. Fine details in an object correspond to large spatial frequency components, represented by wavevectors k_x and k_y. If these values exceed a certain threshold, the corresponding wavevector in the z-direction, k_z, becomes imaginary, meaning these details do not propagate and are effectively filtered out. As discussed by Pendry [76], techniques such as near-field imaging and metamaterials seek to recover these lost high-frequency components, allowing optical systems to surpass conventional resolution limits.

Define the smallest separation d between two point sources an imaging system can resolve to be the optical resolution limit. Due to the wave nature of photons, the optical resolution of a microscope is on the order of:

$$d = k\frac{\lambda}{\mathrm{NA}} = k\frac{\lambda}{\mathrm{n}\sin\theta}. \tag{3.1}$$

The resolution limit is proportional to the wavelength λ used for imaging. For ^{87}Rb, λ is 780 nm. Atoms with a shorter resonant wavelength will have the advantage in the resolution. Here, k is a constant prefactor on the order of unity. As will be shown later, different criteria yield slightly different values of k.

The resolution limit is inversely proportional to the numerical aperture (NA) of the system. The NA is the product of the index of refraction and the sine value of the half-opening angle of the light allowed by the entrance pupil. To improve NA, one can design lenses that can collect larger divergence of the rays at the cost of bigger lenses and more sophisticated aberration compensation. However, the sine value has an upper bound of 1. Another way one can increase the index of the refraction n. This is often referred to as "solid immersion". For example, solid immersion techniques are widely used in biology and lithography. For quantum gas microscopes, similar ideas are implemented in the rubidium microscope at Harvard, the lithium microscope at Harvard, and the potassium microscope at MIT. The drawback of this design is that usually it requires in-vacuum optics which can be hard to align. It also requires that the atoms be located much closer to the viewport window to minimize spherical aberration, which result in limited optical access.

3.1.1 Airy disk

The focused spot of a homogeneously illuminated ideal lens is equivalent to the Fraunhofer diffraction pattern of a homogeneously illuminated circular aperture. The resulting intensity pattern is known as the "Airy disk", which can be analytically expressed as:

$$I(\theta) = I_0 \left[\frac{2J_1(ka \sin\theta)}{ka \sin\theta} \right]^2 = I_0 \left[\frac{2J_1(x)}{x} \right]^2 . \tag{3.2}$$

Here, $I(\theta)$ represents the intensity at an angular position θ relative to the optical axis, while I_0 is the peak intensity at the center of the diffraction pattern. The term $J_1(x)$ denotes the first-order Bessel function of the first kind. The parameter $k = \frac{2\pi}{\lambda}$ is the wave number, where λ is the wavelength of the incident light. The aperture is assumed to be a circular opening of radius a, leading to the dimensionless parameter $x = ka \sin\theta$.

The function in Eq. (3.2) describes the diffraction-limited intensity distribution, featuring a bright central maximum (the Airy disk) surrounded by a series of concentric rings of decreasing intensity. The first dark ring occurs at $x \approx 3.83$, which corresponds to the first zero of $J_1(x)$.

3.1.2 Criteria

Several criteria have been proposed to define the resolution limit of an optical system. As shown in Fig. 3-1, these different criteria highlight various aspects of optical resolution, depending on the application and imaging conditions.

The Rayleigh criterion states that two point sources can be resolved when the peak intensity of the Airy disk from one source coincides with the first intensity minimum of the Airy disk from the other source. The separation of the two point sources at the Rayleigh criterion is $0.61\lambda/\text{NA}$.

The Abbe criterion gives the minimum separation of the two point sources to be $0.5\lambda/\text{NA}$. This is exactly the period of the interference pattern formed at the focal plane of an ideal lens when illuminated by two collimated beams at the angular limit of the numerical aperture (NA). As a result, the Abbe limit is commonly referenced in discussions of Fourier optics, for example, in lithography.

Sparrow's limit is the separation between two point sources at which the combined point spread function (PSF) exhibits no dip in intensity at the midpoint, in-

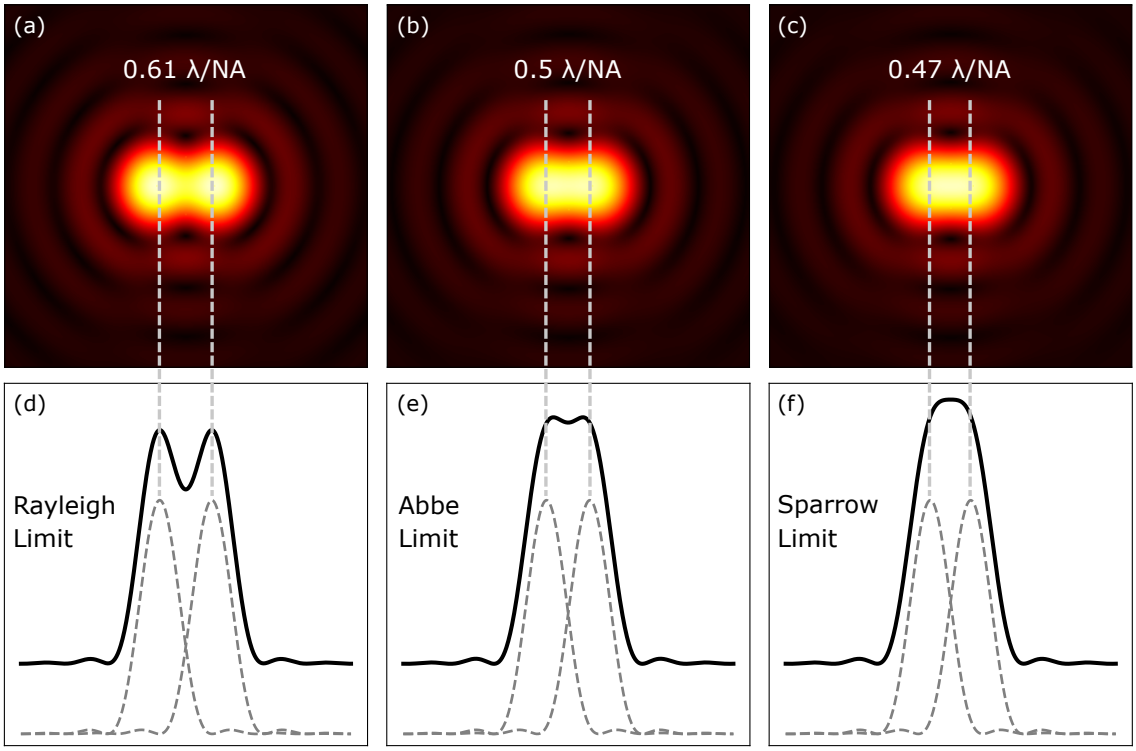

Figure 3-1: **Comparison of different criteria for resolution limit.** (a,b,c) Simulating the diffraction-limited image of two ideal point emitters by placing two Airy disks next to each other. Those density plots are adjusted to enhance the visibility of the diffraction rings by setting a gamma correction with the power-law exponent being 0.5. Three images are corresponding to Rayleigh, Abbe, and Sparrow limits. (d,e,f) The center cuts of the two-dimensional density plots. Solid black lines show the combined intensity of two Airy disks. Gray dashed lines indicate the individual Airy disks for each point emitter.

stead forming a flat intensity plateau between the peaks. Mathematically it means the second-order derivation is zero at the midpoint. This limit represents a smaller separation compared to the Rayleigh criterion and is expressed as $0.47\lambda/\mathrm{NA}$.

3.2 Microscope design

3.2.1 Objective specifications

For the ^{87}Rb microscope objective, here are the design specifications:

Table 3.1: Technical specifications of the BEC4 ^{87}Rb microscope objective.

Manufacturer	Special Optics
Numerical Aperture (NA)	0.8
Design Wavelengths	780 nm, 671 nm, 626 nm, 532 nm
Effective Focal Length	30 mm
Working Distance	6.5 mm in vacuum + 5 mm in fused silica viewport

Using the Rayleigh criterion assuming NA = 0.8, the optical resolution limit for the BEC4 microscope objective is $0.61 \times \frac{780\ \mathrm{nm}}{0.8} \approx 595$ nm, which is slightly larger than the lattice spacing 532 nm intended to use to localize the atoms. People in the field sometimes define a dimensionless factor β as the ratio between the optical resolution limit and the pinning lattice spacing [33].

Obviously, it is advantageous to have a β value less than 1. In that case, two atoms residing in nearest neighbor lattice sites can be resolved directly in optical imaging without further processing. Note that it is quite common for rubidium microscopes to have a β value slightly larger than 1 due to the relatively long near-infrared imaging wavelength. However, it is worth noting that with the development of sophisticated deconvolution and reconstruction algorithm, one can retrieve the underlying lattice occupation information of the microscope images with high fidelity even for a β value as large as 2.2 [33].

3.2.2 Viewport window

The vacuum viewport window is the first optical element in the imaging system. Since highly divergent rays pass through this element, its optical quality is critical for achieving diffraction-limited performance. Any imperfections in the viewport, such as variations in thickness or surface flatness, can introduce aberrations that degrade image quality.

The objective is designed to work with an ideal 5 mm-thick fused silica viewport. Fused silica is chosen for its favorable optical and mechanical properties. It has a refractive index of $n = 1.45$ and is well-suited for high-power laser applications compared to other materials like N-BK7. Additionally, its low thermal expansion coefficient (0.55×10^{-6} K^{-1}) ensures minimal distortion due to temperature fluctuations.

Two key factors of the viewport significantly impact the final imaging quality: thickness and flatness. The required specifications for the viewport depend on the numerical aperture (NA) of the objective. A higher NA demands stricter tolerances on surface flatness to maintain wavefront integrity and minimize aberrations. Conversely, if the effective NA is reduced—by limiting the collection angle of rays—the flatness requirement becomes less stringent.

Thickness

The objective is designed to work with a fused silica viewport window with a nominal thickness of 5 mm. However, in practice, the absolute thickness of the viewport may vary slightly from this designed value.

Fortunately, the objective's design is resilient to small deviations in viewport thickness, provided that the atom-to-viewport distance is adjusted accordingly and the image is refocused by modifying the distance between the eyepiece and the camera.

Zemax simulations indicate that assuming a plano-convex lens with a focal length of 2 meters as the eyepiece (e.g., LA1258 from Thorlabs), the system can compensate for viewport thickness variations as follows:

- For the ideal 5.00 mm viewport thickness, the camera must be positioned 2020.1 mm from the eyepiece, while the atoms should be 6.500 mm from the viewport.

- If the viewport thickness decreases to 4.85 mm, the atom-to-viewport distance must be adjusted to 6.531 mm, and the camera must be moved to 2417.3 mm from the eyepiece.

- If the viewport thickness increases to 5.15 mm, the atom-to-viewport distance must be set to 6.469 mm, and the camera should be positioned 1731.2 mm from the eyepiece.

In conclusion, within a reasonable viewport thickness variation range of ± 150 μm, diffraction-limited optical performance can be fully recovered by optimizing the atom position and refocusing the image. However, while the optical performance remains intact, the magnification will change under these conditions. This change is simply a scaling of the final image and can be understood as a result of the viewport acting like a weak lens. Varying its thickness slightly modifies its focusing power, ultimately altering the effective focal length of the entire objective assembly.

An interesting observation from Zemax simulations is that if an air gap exists between the objective and the viewport, full optical performance can still be recovered by moving the atoms closer to the viewport. This suggests the existence of an approximate "conservation rule": the total air thickness from the atom position to the first lens element of the objective remains nearly constant for maintaining diffraction-limited performance. In other words, if the atoms are shifted closer to the viewport by x mm, the objective can be moved away from the viewport by approximately x mm to compensate and restore optical performance.

This finding could be useful when working with glass cells and mounting the objective on a translation stage, as it provides a practical method to maintain high imaging quality despite small adjustments in the optical setup. However, it is unclear whether this principle generalizes to other high-NA objective designs, which may require case-by-case investigation.

Flatness

As mentioned earlier, fused silica has a relatively low thermal expansion coefficient (CTE) of 0.55×10^{-6} K^{-1}, compared to stainless steel, which has a significantly higher CTE of 16×10^{-6} K^{-1}. To maintain a good vacuum seal, the viewport window must be tightly bonded to the stainless steel chamber. This is typically achieved through a process called brazing, where two materials are joined at high temperatures.

Our viewport is manufactured by UKAEA (United Kingdom Atomic Energy Authority), which employs an in-house technique to mitigate stress buildup during the brazing process. Their design incorporates a ring structure that holds the viewport, made from a material with a CTE intermediate between fused silica and stainless steel. This design choice helps reduce the thermal stress caused by differential expansion.

Despite efforts to bridge the CTE mismatch using a third alloy, the brazing process remains difficult to control precisely. As a result, the viewport window often develops a deformation resembling a "potato chip" shape, indicating a break in rotational symmetry due to built-in tension.

For the UKAEA vacuum viewport assembly, the resulting deformation is typically on the order of a few wavelengths (λ). A more quantitative measurement of this deformation is detailed in the following sections.

3.3 Measurement of the viewport surface profile

To assess the impact of viewport deformation on optical performance, it is essential to quantitatively measure the surface profile of the viewport. We built a white-light surface profiler for this purpose, which is based on a phase-shifting interferometer.

3.3.1 Phase-shifting interferometer

Fig. 3-2 shows the whole optical setup for the interferometer. It can be separated into two parts. The first part shown in Fig.3-2(a) is the delay line to compensate for the optical path length difference when dealing with low-coherence light source.

It also makes it more convenient for mounting testing viewports and easier to probe different surfaces.

The second part shown in Fig. 3-2(b) is the main interferometer. It is a Twyman-Green interferometer which is a variant of the Michelson interferometer. One key feature is the use of a beam expander to enlarge the area that the interferograms probe. A shear interferometer is used to carefully align the beam expander. The beam diameter after beam expansion is 20 mm, which is larger than the area that the fluorescent light of the atoms will pass through. In this interferometer, one arm is a reference optical flat ($\lambda/10$) and the other arm is the target viewport of interest. Sicne the viewport has an anti-reflection coating for the center wavelength of the probing light, the optical flat is also coated similarly to match the weak reflection intensity.

Although technically the wavefront information is already encoded in a single-shot of the interferogram. To improve the signal-to-noise ratio of the surface profile reconstruction, especially for the interferogram with low fringe visibility in this case, Phase-shifting interferometry is implemented. It is also insensitive to the homogeneity of the illumination. Phase-shifting interferometry, or PSI, is a method that records a series of interferograms where the phase of one of the two interfering beams is changed by a known amount and direction between images [77].

Light source

The spectrum of the light source can be found in Colin Kennedy's PhD thesis [78]. To summarize, it is a superluminescent diode (SLD) laser source with a center wavelength being 840 nm and a FWHM of the spectrum of 30 nm, which corresponds to a coherence length of 24 μm. This partially coherent laser source helps to avoid superfluous interference patterns generated by all kinds of surfaces in the beam path. Particularly the two parallel surfaces of the viewport will both generate interferograms with similar intensity and hence very hard to separated with a high-coherence light source.

The two arms will only generate an interferogram when the difference between the optical paths of the two arms is within the optical coherence length of the SLD

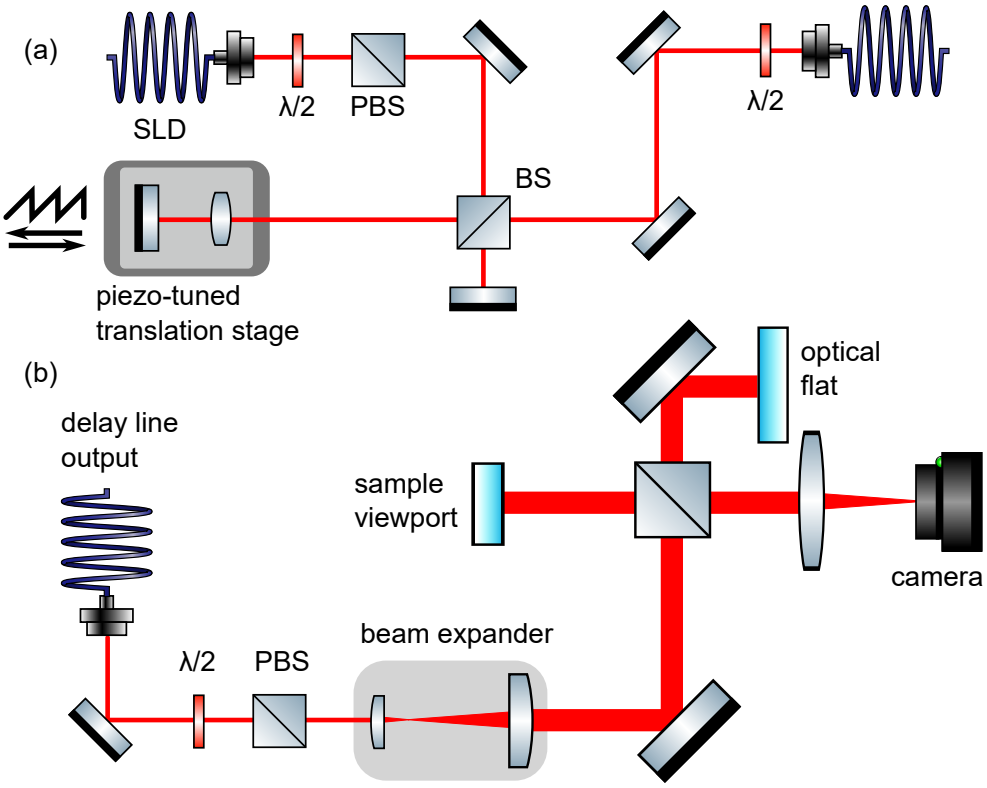

Figure 3-2: **Optical setup for surface profiler.** (a) A delay-line setup to compensate the optical path length difference occurred in the test setup. Since light with low coherence length is used in the interferometer and vacuum viewport is not easy to mount with optical mounts, a delay-line can free the need to exactly match the optical path length in the setup. One arm the position of the reflecting mirror can be fine controlled by a pizeo adjustable translation stage. The retro-reflecting mirror is also mounted in a cat's eye style to minimize the alignment deviation when arm length is changed. Two beams with optical path length differences are both coupled into a fiber and send to the main interferometer. (b) A Twyman-Green interferometer to measure the surface profile of vacuum viewports.

laser. To fine tune the optical path length difference of each arm, a delay-line setup is implemented as shown in Fig. 3-2(a).

Reconstruct surface profile

In a Twyman-Green interferometer, rays hitting different parts of the surface will experience different optical paths. When interfered with the other arm where rays are reflecting off an optical flat, they will develop an optical path difference (OPD). Assuming the surface profile deviation from a flat surface is small such that divergence/convergence of the wavefront is negligible, the surface profile $h(x, y)$ is directly mapped to the optical wavefront $\phi(x, y)$:

$$\phi(x, y) = 2\pi \frac{\text{OPD}}{\lambda} = \frac{4\pi h(x, y)}{\lambda} \tag{3.3}$$

There is a factor of 2 coming from the rays are retro-reflecting off the test surface. The obtained interferogram $I(x, y)$ can be expressed as:

$$I(x, y) = I_{\text{dc}}(x, y) + I_{\text{ac}}(x, y) \cos\left[\phi(x, y) + \phi_0\right] \tag{3.4}$$

$I_{\text{dc}}(x, y)$ is the DC offset of the interferogram due to the intensity imbalance between two arms. $I_{\text{ac}}(x, y)$ is the amplitude of the intensity oscillation for a single pixel as the overall phase is being shifted. ϕ_0 is a global phase of the interferogram which is being scanned by the piezo translation stage. It can be set to 0 for the initial position without lose of generality.

To retrieve the information of the phase map $\phi(x, y)$, at least three measurements are required. For example, three phases of 0°, 90° and 180° will produce the following interferograms:

$$\begin{aligned}
\phi_0 = 0^\circ, \quad I_1(x,y) = &\quad I_{\mathrm{dc}}(x,y) + I_{\mathrm{ac}}(x,y)\cos\left[\phi(x,y)\right] \\
\phi_0 = 90^\circ, \quad I_2(x,y) = &\quad I_{\mathrm{dc}}(x,y) - I_{\mathrm{ac}}(x,y)\sin\left[\phi(x,y)\right] \\
\phi_0 = 180^\circ, \quad I_3(x,y) = &\quad I_{\mathrm{dc}}(x,y) - I_{\mathrm{ac}}(x,y)\cos\left[\phi(x,y)\right]
\end{aligned}$$

From these three measurements, the phase map can be calculated as:

$$\phi(x,y) = \arctan\left(\frac{I_1 + I_3 - 2I_2}{I_1 - I_3}\right) \tag{3.5}$$

Since the value of arctan function is within $\left(-\frac{\pi}{2}, \frac{\pi}{2}\right)$, the obtain $\phi(x,y)$ would have discontinued jumps due to phase wrapping. The test viewports is assumed to be smooth, i.e., only have low-frequency deformation hence the surface profile $h(x,y)$ should be continuous. To address this discrepancy, the phase map $\phi(x,y)$ needs to be unwrapped to ensure that the phase differences between neighbor pixels are within π.

3.3.2 Zernike polynomials

To quantitatively analyze the surface profile, we use the Zernike polynomials $Z_n^m(\rho,\theta)$. In the notation, n and m are integers with $n \geq |m| \geq 0$, θ is the azimuthal angle, and $\rho \in [0,1]$ is the radial distance. Zernike polynomials are a set of basis functions that satisfy the orthogonality property on the continuous unit disk. Zernike polynomials are often used to quantify surface or wavefront aberrations, as they form a complete set of basis functions. The first 21 terms of the Zernike polynomials are visualized in pyramid format in Fig. 3-3. From up to bottom, the radial index n increases. From left to right, the azimuthal index m increases. The higher orders have more high-frequency oscillations compared to the lower orders.

There are many conventions (maybe too many) regarding the definitions and indexing of the Zernike polynomials. In the thesis, I adopt the fringe indexing scheme commonly used in interferogram analysis, lens design, and commercial optical simu-

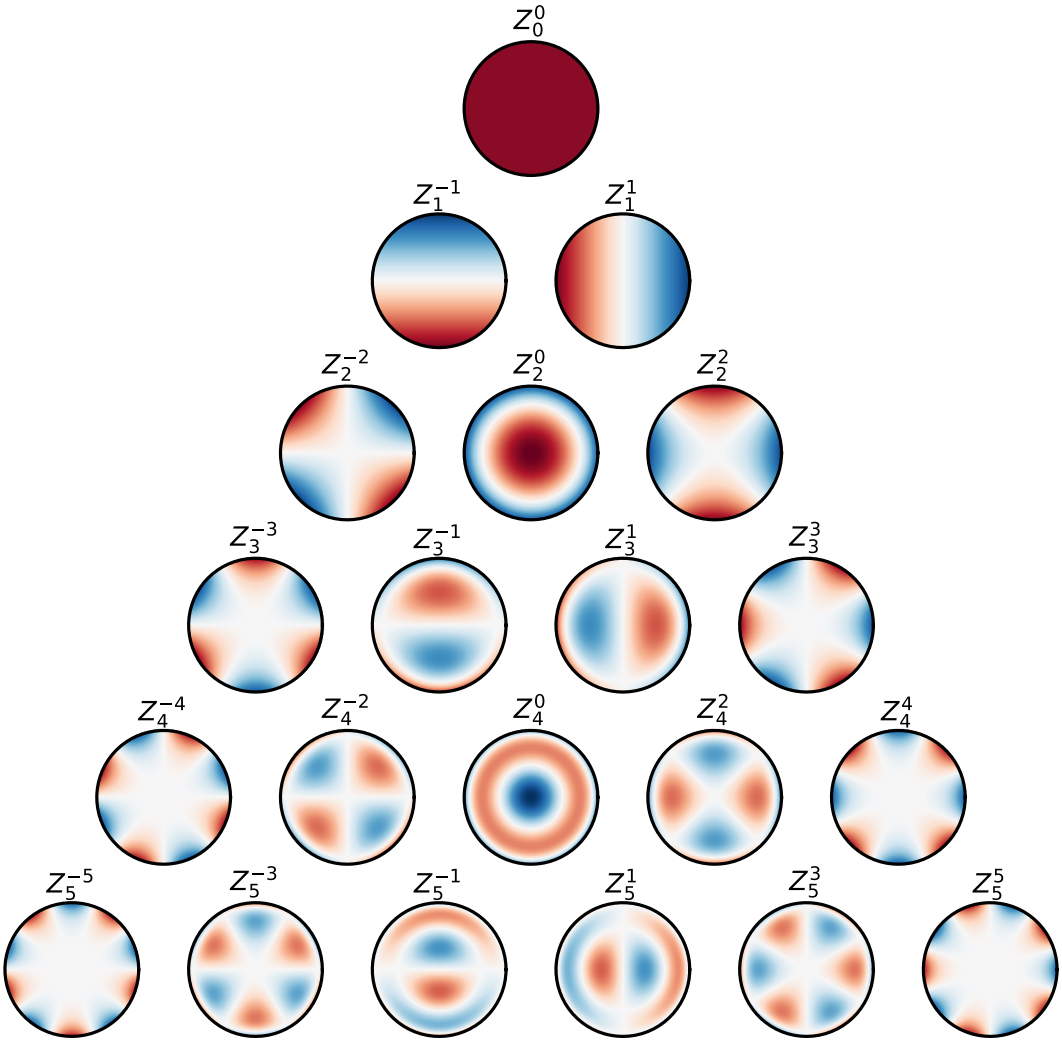

Figure 3-3: Visualization of the first 21 Zernike polynomials ordered by the radial function index n vertically and the azimuthal index m horizontally. There are more oscillations within the unit disk as the order index n and m increase.

lating software such as Zemax [79]. Under this convention, Zernike polynomials can be written as:

$$Z_n^m(\rho,\theta) = \begin{cases} R_n^m(\rho)\cos(m\theta) & \text{if } m \geq 0, \\ R_n^{|m|}(\rho)\sin(|m|\theta) & \text{if } m < 0, \end{cases} \tag{3.6}$$

the radial polynomials $R_m^n(\rho)$ are defined as:

$$R_n^m(\rho) = \sum_{k=0}^{\frac{n-|m|}{2}} (-1)^k \frac{(n-k)!}{k!\left(\frac{n+|m|}{2}-k\right)!\left(\frac{n-|m|}{2}-k\right)!}\rho^{n-2k} \tag{3.7}$$

when $n-m$ is even, and $R_n^m(\rho)$ when $n-m$ is odd.

Nine terms of commonly used Zernike polynomials are listed below. Note that they are not normalized and kept to be consistent with the convention Zemax uses.

Table 3.2: Typical Zernike polynomials and associated optical aberrations.

n	m	$Z_n^m(\rho,\theta)$	**Aberration Name**
0	0	1	Piston
1	1	$\rho\cos(\theta)$	Tilt X
1	-1	$\rho\sin(\theta)$	Tilt Y
2	0	$2\rho^2-1$	Defocus
2	2	$\rho^2\cos(2\theta)$	Astigmatism X
2	-2	$\rho^2\sin(2\theta)$	Astigmatism Y
3	1	$(3\rho^3-2\rho)\cos(\theta)$	Coma X
3	-1	$(3\rho^3-2\rho)\sin(\theta)$	Coma Y
4	0	$6\rho^4-6\rho^2+1$	Primary spherical

Those lower-order Zernike polynomials are often used in optical metrology and hence have their own names. For example, the piston term Z_0^0 is a homogeneous DC offset which does not introduce any optical aberrations. Two tilt terms along the X and Y axis (Z_1^1 and Z_1^{-1}) shift the resulting imaging position but add no other optical aberrations. Defocus term, Z_2^0, as its name suggests, can be correct by refocusing the imaging system. As a result, defocusing is usually considered benign. In the later sections, we will discuss the correction for the coma aberration Z_3^1 and Z_3^{-1} introduced by an effective tilt of the objective. We will encounter the spherical aberration Z_4^0 in Chapter 5 when we discuss the alignment and optimization of the objective. For the remaining part of Chapter 3, we will focus on the astigmatism aberration Z_2^2 and

Z_2^{-2} introduced by the viewport window deformation.

3.3.3 Measured surface profile

In Fig. 3-4, the vacuum surface deformation of the UKAEA viewport is shown. Within a circular region of 20 mm in diameter, a peak-to-valley deformation of approximately 3 waves is observed. This value is quite typical, as similar deformations were found when we tested viewports from other manufacturers.

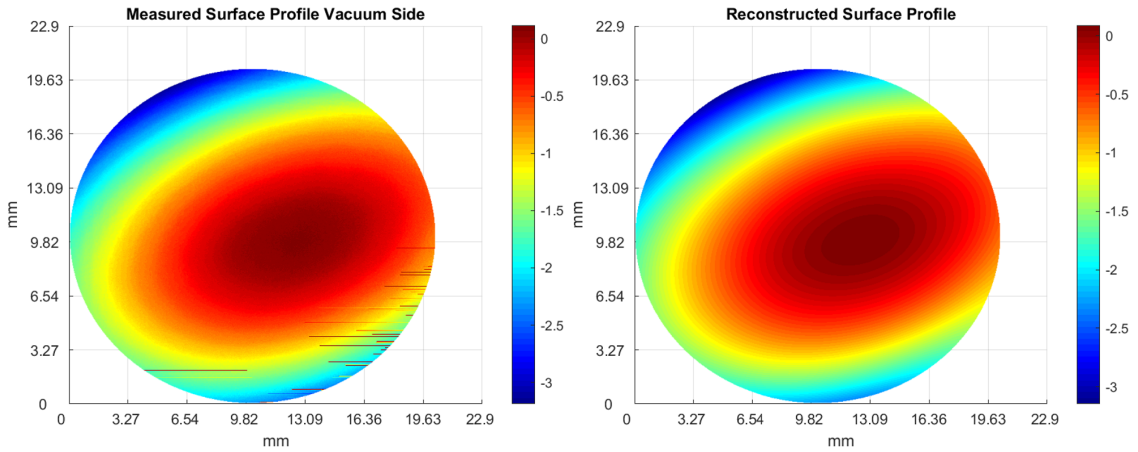

Figure 3-4: **Measured and reconstructed surface profile of the viewport window.** The surface profile is obtained by phase unwrapping of the interferogram. The left panel shows the measured surface profile, while the right panel presents the Zernike decomposition and reconstruction result of the measured profile. The reconstruction is necessary for quantitatively analyzing aberrations, and the fit shows excellent agreement. The color bar represents the deformation in units of wavelength, which in this case is 840 nm.

The deformation appears as an elliptical warp ("potato chip" shape), which is consistent with the brazing technique being uncontrolled and asymmetric. The right panel of Fig. 3-4 shows the reconstructed surface profile after decomposing the measured profile (left panel) into the Zernike basis.

We also measured the air-side deformation of this viewport window by adjusting the delay-line value, and the results exhibit very similar behavior to the vacuum side. Therefore, it is reasonable to assume that the vacuum viewport deforms but remains parallel. For collimated beams, this implies that the viewport introduces almost no

aberration in the transmitted wavefront, as the glass thickness remains uniform at each point. This observation also explains why an objective with a lower numerical aperture (NA) can tolerate more viewport aberration [26].

3.4 Aberration and correction

In Fig. 3-5, the first 36 orders of the Zernike coefficients are shown, obtained by decomposing the measured surface profile into the Zernike basis.

The weight of the coefficients clearly indicates that the major deformation of the viewport is low-frequency, as higher-order terms are negligible (smaller than $\lambda/10$).

Among the dominant terms, Piston and tilts do not contribute to optical aberrations, as they can be arbitrarily introduced by the interferometer. The defocus term is on the order of one wavelength (λ). We confirmed through Zemax simulations that a physical deformation in the shape of defocus primarily contributes to defocus aberration in the transmitted wavefront, which can be easily corrected by refocusing the camera. Therefore, the defocus term can also be neglected.

3.4.1 Astigmatism

The only remaining non-negligible physical deformation of the viewport is astigmatism.

We confirmed with Zemax that this physical deformation leads to astigmatic aberration in the final transmitted wavefront. This wavefront aberration arises because the light has different focusing power in two orthogonal directions. It breaks the rotational symmetry and is more challenging to correct compared to defocus.

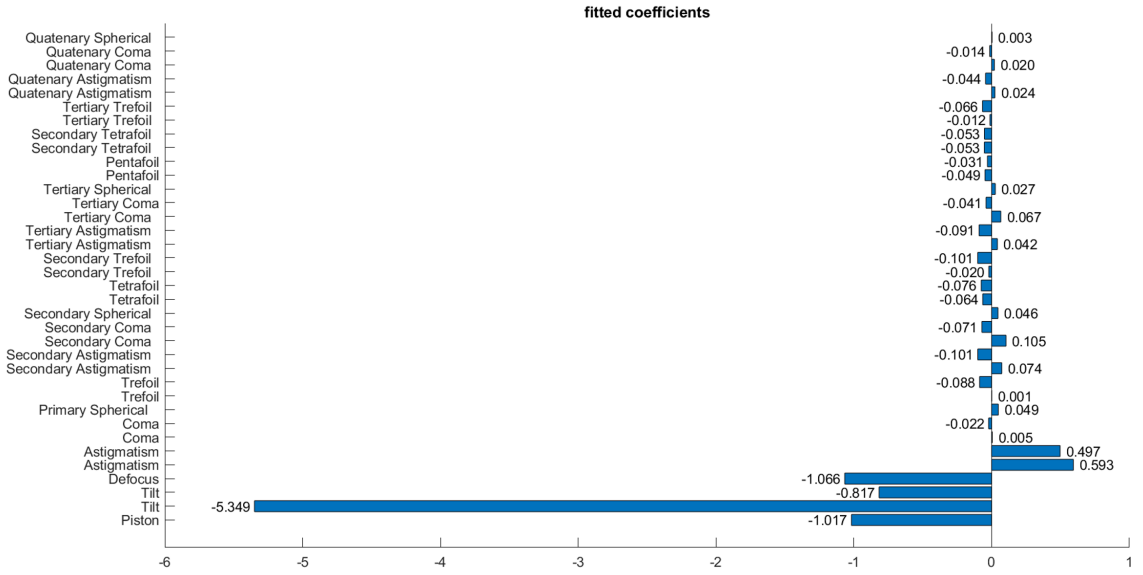

Figure 3-5: **Zernike coefficients derived from the viewport surface profile.** The first 36 orders of the Zernike terms after decomposing the measured surface profile are shown. Notice that the major deformation arises from astigmatism and defocus. The deformation of the window is primarily low-frequency, while the higher-order terms are negligible.

Fig. 3-6 shows the surface deformation contribution from the astigmatism terms only. Within a circular area of 20 mm in diameter, the peak-to-valley deformation of 1.6 waves is attributed to astigmatism. The 20 mm region is chosen to encompass the area sampled by rays at the full 0.8 NA.

Using this measurement result in Zemax, we found a significant degradation in the final imaging performance. The Strehl ratio drops below 0.5 at full NA, which completely defeats the purpose of a large NA if not corrected.

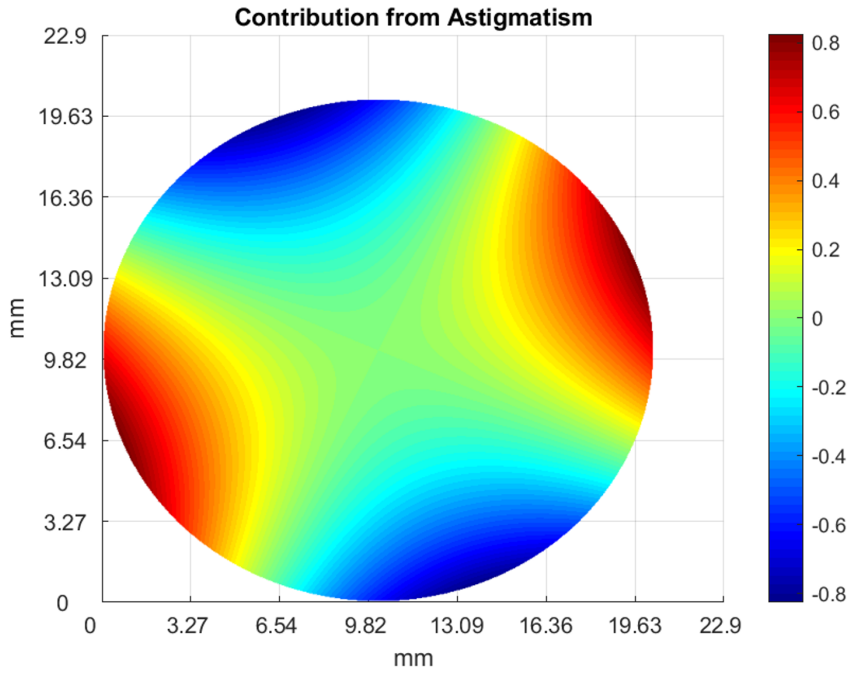

Figure 3-6: **Astigmatism aberration in the viewport surface profile.** Based on the measurement and Zernike decomposition, only the astigmatic deformation significantly affects optical performance. The color bar is in units of waves (840 nm). A peak-to-valley value of 1.6 waves for astigmatism is observed within a circular area of 20 mm in diameter.

Correction

To summarize, viewport deformation is ubiquitous in all vacuum chambers that require conventional metal-to-glass bonding. Naturally, switching to a full-glass cell would completely eliminate this issue. This problem is particularly significant for experiments requiring a high numerical aperture. Similar deformation can be detrimental to a 0.8-NA objective but negligible for a 0.6-NA objective [26]. That could be an argument for in-vacuum solid immersion lenses to lower the NA requirement for the out-of-vacuum objectives [80, 81].

Researchers have explored various methods to address this viewport issue. Before describing our final approach, I will document a few different strategies that have been attempted by other people and us.

First, there are several mechanical methods to mitigate viewport deformation during the manufacturing process. In the original Munich rubidium microscope, Weit-

enberg mentioned that viewport deformation could be slightly adjusted by applying torque to the vacuum bolts during installation [82]. In principle, one could monitor the shape change while tightening the vacuum bolts around the bucket window. However, in our test setup, which mimicked the mechanical design of our vacuum viewport assembly, we found that tightening the bolts did not transfer any noticeable stress to the viewport window.

Along similar lines, researchers from Tsinghua University demonstrated that a T-shaped viewport can effectively reduce deformation [83]. This design features a thinner edge to decouple stress and tension buildup during the bonding process while maintaining a thicker center to meet optical requirements. However, it does not completely eliminate astigmatic deformation and may require selecting from multiple viewport samples. Additionally, their objective has a smaller NA, allowing them to tolerate slightly more deformation than we can.

Several research groups have attempted to mitigate viewport deformation by polishing the deformed windows. Magnetorheological Finishing (MRF) appears to be the most effective polishing solution, as demonstrated by the potassium microscope at MIT, where it provided a clean, flat surface suitable for optical contact bonding [84]. However, at the time when we required this technology, no vendors were available to perform MRF for us.

The USTC rubidium microscope group reported using Ion Beam Figuring (IBF) to polish out the deformation [85]. While IBF initially showed some success in eliminating the deformation, the improvement ultimately degraded after the viewport underwent baking.

Inspired by the successful implementation of a fully-glued vacuum glass cell from the University of Bonn [86], we dedicated significant effort to testing whether gluing the viewport window to the stainless steel assembly would be a viable solution. After extensive evaluation, we identified Epo-Tek H77 as the most suitable epoxy for this purpose. This adhesive cures in 24 hours, and its slow curing process ensures a uniform stress distribution. After baking, the viewport surface deformation exhibited only a defocusing term, with a peak-to-valley deformation on the order of one wavelength.

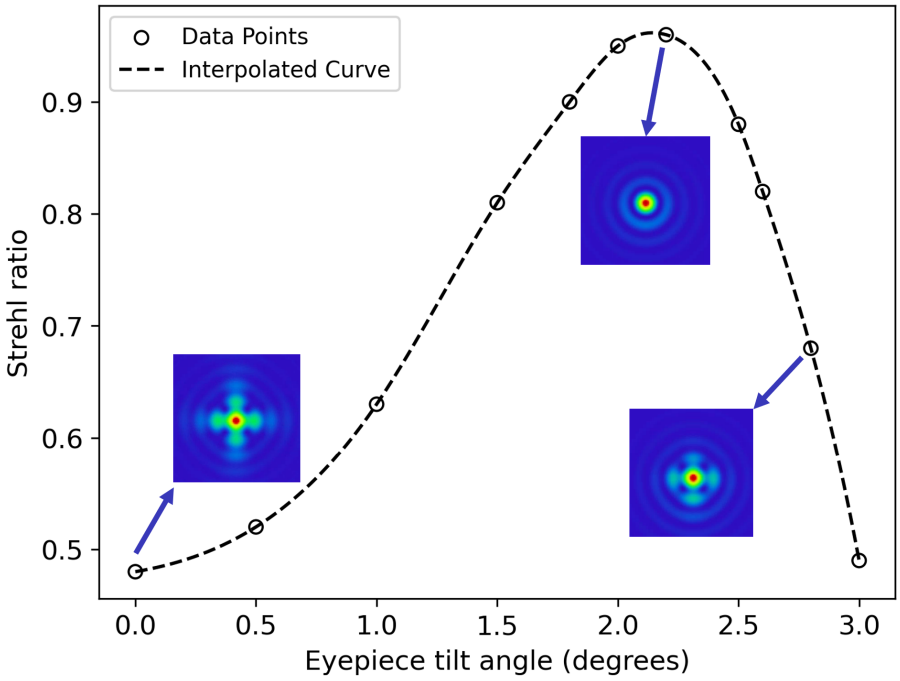

Figure 3-7: **Zemax simulation illustrating how tilting the eyepiece at a small angle can compensate for the astigmatic aberration introduced by the deformed viewport.** In the Zemax simulation, we assume only astigmatic deformation in the viewport, with the deformation magnitude based on surface profiler measurements. As the eyepiece tilt angle is adjusted, the Strehl ratio reaches an optimal value of more than 0.95, indicating that diffraction-limited performance can be restored.

.

The glued viewport initially appeared promising, as it was able to maintain ultra-high vacuum (UHV) at 7×10^{-11} Torr. However, after several weeks in UHV, the pressure gradually increased to above 10^{-10} Torr. Residual gas analysis suggested that the pressure rise could be related to water permeation [87], although the result was not conclusive.

A simple optical solution

In the end, we discovered a simple optical solution that allows the optical system to function effectively despite the deformed vacuum viewport.

Since astigmatism arises from a difference in focusing power along two orthogonal directions, we initially considered using a cylindrical lens pair to correct for it. However, we soon realized that the difference in focusing power was so small that simply

tilting the eyepiece at a slight angle would suffice.

Tilting the eyepiece (in this case, a plano-convex lens with a diameter of 3 inches) breaks the rotational symmetry of the imaging system and can be adjusted to compensate for the asymmetry introduced by the deformation of the viewport window.

We verified the idea first by performing a ray-tracing simulation as shown in Fig 3-7. In the Zemax simulation, we assume that the viewport deformation consists solely of astigmatism, with its magnitude determined from surface profiler measurements. The simulation models how tilting the eyepiece can compensate for the aberration introduced by the deformed viewport.

Initially, when no tilt is applied to the eyepiece, the Strehl ratio (SR) is below 0.5, indicating significant optical degradation. The SR is a metric bounded between 0 and 1 that quantifies how closely a real optical system performs compared to an ideal one; we will return to this concept and explain it in detail in later sections. This result confirms that viewport-induced astigmatism severely impacts imaging performance and would prevent diffraction-limited resolution if left uncorrected.

Tilting the eyepiece introduces astigmatism aberration into the transmitted wavefront due to the asymmetric refraction caused by the off-axis angle. When the eyepiece tilt is correctly matched to the viewport deformation, the two astigmatism contributions cancel out, effectively restoring the wavefront quality. As the eyepiece tilt angle increases, the SR improves, reaching an optimal value of over 0.95 at a specific tilt angle. This suggests that diffraction-limited performance can be recovered through precise alignment. However, if the tilt angle becomes too large, the correction becomes excessive, and new aberrations are introduced, leading to a decrease in the SR.

Beyond optical simulation, this method of correcting astigmatism was experimentally verified through measurements of the point-spread function of the imaging system. The final results will be discussed in later sections.

3.4.2 Coma

We were fully aware of the potential astigmatism aberrations before testing the imaging system. Therefore, we began by pairing the objective with a flat viewport window of the correct thickness. This approach allowed us to decouple the effects of real deformed viewport windows. However, we were surprised to discover another unexpected aberration.

SNOM fiber tip

We used an SNOM fiber tip as a point source. They are micro-tip probes commonly used in scanning near-field microscopy. The SNOM fiber used in our case is the E50-SM600-AL-200 from K-TEK Nanotechnology. Its tip aperture is rated at 200 nm, which is smaller than the diffraction limit set by the Rayleigh criterion (≈ 600 nm).

Point spread function

During the testing of the point spread function of the objective with SNOM fiber tips, initially, we found that we could not achieve a Strehl ratio higher than 0.5 after optimizing the alignment and focusing. In addition to the low Strehl ratio, we also found that the shape of the point-spread-function is not rotationally symmetric. Instead, it has a preferential direction where intensities are concentrated, resembling a comet-tail. We also note that the comet-tail rotates as we rotate the microscope objective. This aberration pattern is very similar to the coma aberration as illustrated in Fig 3-8.

An effective tilt of the objective

Usually, the coma aberration arises when dealing with off-axis objects. Together with the fact that the aberration pattern is correlated with the rotation of the objective. We form a hypothesis that our objective is slightly tilted like the Pisa Tower. Note that this tilt will not be a problem if we choose to mount the objective on a 5-axis stage where the tilting degrees of freedom can be fully controlled. In that sense, it

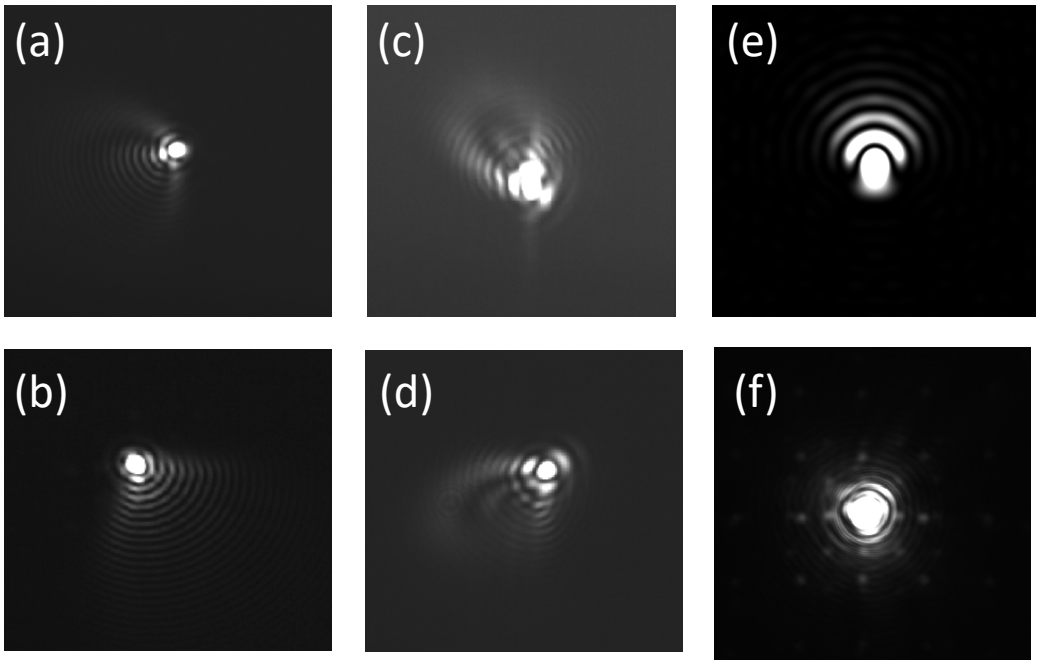

Figure 3-8: **Point-spread function measurements with objective rotation.** (a)-(d) Images of the SNOM fiber tip after optimizing the alignment and focus. Each subfigure corresponds to a 90° rotation of the objective. The resulting comet-tail pattern rotates accordingly, indicating the aberration is related to the objective itself. (e) Simulated point-spread-function assuming a first-order coma aberration with a P-V value of 0.8 λ. (f) Measured point-spread-function after inserting lens tissues with the optimal thickness and re-optimizing alignment and focus. The asymmetric pattern is significantly reduced.

is our design that the objective sits directly on the viewport window, which puts a requirement on the mechanical precision of the objective. The optical axis is determined once the objective is mounted. If the very first surface is not perpendicular to the optical axis, the objective will be tilted as illustrated in Fig. 3-9(b).

To test this theory, we insert a lens tissue to raise the height on the edge where the meniscus lens is in contact with the viewport window. As illustrated in Fig. 3-9(c), we hope this will correct for the tilt effect. The exact location of the lens tissue is chosen to match the orientation of the aberration comet-tail pattern and is backed up by simulation. To our surprise, after inserting the lens tissue and re-optimizing the alignment, we are able to achieve a Strehl ratio higher than 0.75. We found that we needed to insert 3 layers of lens tissue to form a really clean image with a Strehl ratio higher than 0.75. The thickness of the lens tissue is found to be somewhere between

25 μm to 40 μm. So 3 layers is a poor man's spacer for about 75 μm to 120μm. The tilt is introduced over an area with a diameter of 1 inch. So a crude model would be the objective's end surface is not flush against the viewport, instead, it has a tilt angle of $\approx$ 4 mrad, which is on the same order as predicted by Zemax simulation.

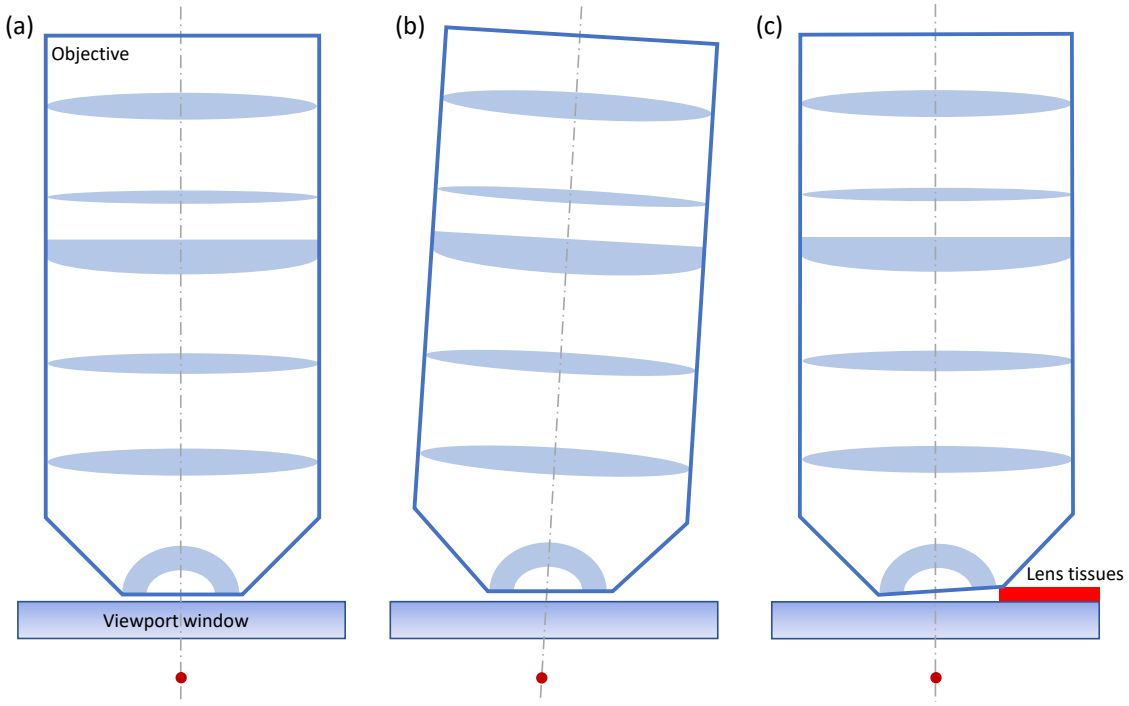

Figure 3-9: **Illustrations on an effective tilt of the objective before refurbishing.** (a) Ideal scenario. The objective is designed to sit on the viewport window. The optical axis is parallel to the norm of the viewport surface. The atom (dark red disk) is aligned to the optical axis. (b) Our hypothesis for the defect objective. The objective has an overall tilt of the housing possibly due to the machining precision of the end surface. (c) Hacky way to correct for the coma aberration. Three layers of lens tissues are inserted at the correct corner to tilt the whole objective optical axis back. Note that the internal lens elements shown are for illustration purposes only and do not represent the actual optical design.

We found that this effective tilt problem persists in all three objectives that we purchased from Special Optics. Private conversation with the group at Tsinghua University confirms that they also observe similar behavior of their Special Optics objectives featuring a similar design, although a small NA of 0.75. In the end, we sent all three objectives back to Special Optics for refurbishing. They confirmed what we had discovered and suggested it could have been due to parts being misaligned

during the shipping process. After the objectives came back from repair, all of them performed up to the specifications without any arbitrary tilting.

Finally, there is one more interesting finding about the coma aberration story. At first glance, people may say the effective tilt can be compensated by moving the atom to the position where the tilted optical axis indicates. However, in that case the highly diverging rays will pass through the viewport window at a small angle. When rays pass through a parallel window plate, the resulting aberration depends on the NA of the rays [88]. For very small NA, the dominant aberration is astigmatism. This is precisely the reason why a tilt eyepiece can be effective in correcting for astigmatism as the rays hitting the eyepiece have zero NA. For large NA in this case, the dominant aberration is coma. In other words, by moving the atom to the new focal point, the coma aberration is not caused by the objective but by the viewport window.

3.5 Benchmark result

I have introduced the concept of the Strehl ratio without explaining it in Fig. 3-7. Here I will explain it in detail.

3.5.1 Strehl Ratio

There are many ways of calibrating the optical performance of a diffraction-limited microscope. One way is to look at the phase information of the wavefront after the objective. For an objective designed for infinity, the output wavefront from a point source should be plane waves. Metrology methods like the Fizeau interferometer with bearing balls as a retroreflector has been used to map the wavefront information [89]. This method does not include the eyepiece which directly study the performance of the objective. Conjugate to the phase information, one can also measure the intensity information of the microscope. For example, measuring the modulation transfer function using a test target (1951 USAF). However, this modulation transfer function measurement depends heavily on how the test pattern is illuminated. And considering the objective will be used for measuring fluorescing atoms in the end,

directly imaging a point source using the microscope will be a much more direct comparison and will be discussed in the details later.

Strehl ratio S is used to quantitatively analyze the performance of the microscope system. The Strehl ratio is a dimensionless measure of the quality of an optical image formed by an imaging system. In essence, it compares the peak intensity of the observed point spread function (PSF) to the peak intensity that would be produced by an ideal, aberration-free optical system. Intuitively, it explains how well the intensity is focused down to a spot. It takes a value from 0 to 1 as the normalized peak intensity cannot exceed the peak intensity of the Airy disk. In principle, the FWHM of the point-spread-function can also be used as a figure of merit. However, we found the Strehl ratio to be much more sensitive than the FWHM measurements when the system is close to be diffraction-limited.

It is worth noting that the Strehl Ratio is only a good measurement when the system is close to be diffraction-limited. In practice, we found that a Strehl Ratio below 0.4 is not so meaningful in terms of guiding the optimization and alignment. Common industry practice considers a lens "diffraction-limited" when the Strehl Ratio is greater than 0.8 [90, 91].

When the system is close to be diffraction-limited, the Strehl ratio can be approximated by this formula [92]:

$$S \approx \exp\left(-\sigma_\phi^2\right) = \exp\left(-4\pi^2\sigma_w^2/\lambda^2\right) \tag{3.8}$$

where σ_ϕ is the root mean square deviation over the aperture of the wavefront phase. σ_ϕ is proportional to the phase error expressed by waves $\sigma_\phi = 2\pi\sigma_w/\lambda$. According to this equation, to achieve a Strehl ratio of 0.8 or higher, the root mean square of the wavefront aberration must be smaller than $\lambda/13$.

3.5.2 Measured point-spread-function

After correcting all aberrations, primarily astigmatism, and coma, we present the best measured point-spread function following careful alignment and optimization, as shown in Fig. 3-10. This measurement was conducted using the UKAEA vacuum viewport.

The alignment process involved several critical adjustments. First, we scanned the position of the SNOM fiber tip in the x-y plane to ensure it was centered in the field of view of the objective. Second, we carefully adjusted the fiber tip's position along the z-axis to place it at the optimal focal plane, minimizing spherical aberration. Lastly, we fine-tuned the eyepiece tilt angle to compensate for astigmatism aberration.

All these steps had to be performed iteratively while continuously monitoring the instantaneous change of the Strehl ratio in real time.

As shown in Fig. 3-10, the radial profile of the point-spread function is plotted. We carefully calibrated the magnification of the system by translating the SNOM fiber and recording how many pixels the image shifted on the camera. Additionally, we performed a Zernike fit to the measured point-spread function. The resulting Strehl ratio reaches 0.82, indicating that our system is diffraction-limited.

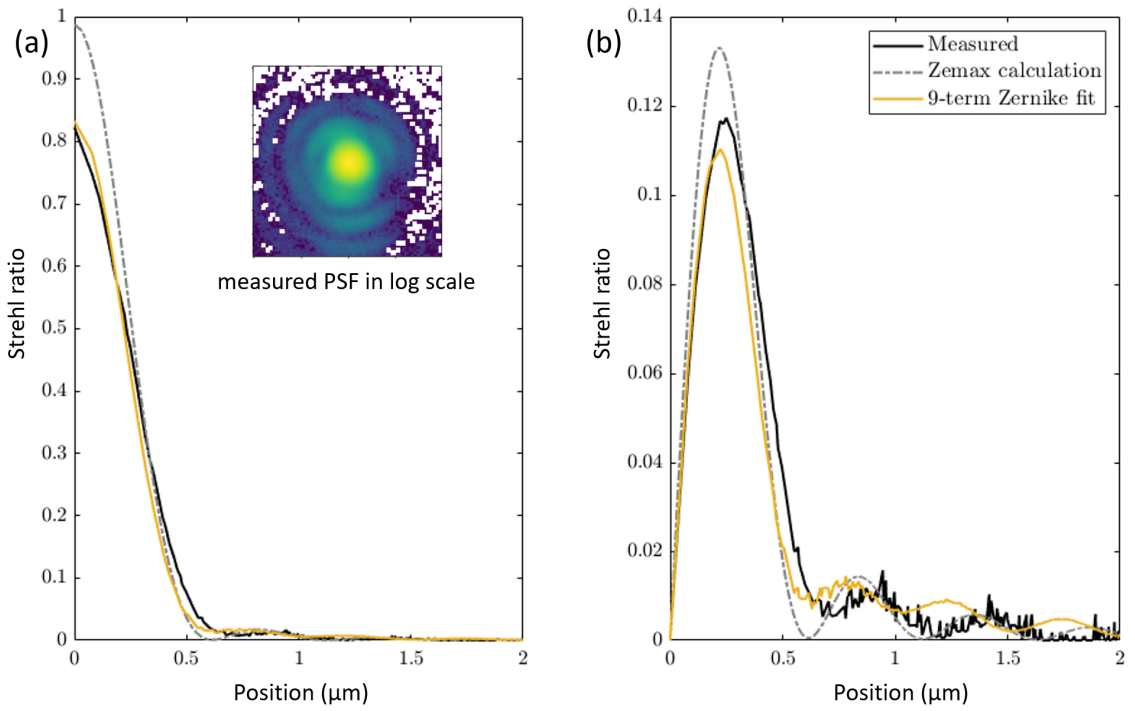

Figure 3-10: **Measured point spread function using the SNOM fiber tip.** (a) The radially averaged intensity distribution of the point-spread function. The gray dashed line represents the ideal Airy disk for an NA of 0.8. The solid black line shows the measured distribution, with a Strehl ratio of 0.82. The yellow solid line corresponds to the fit using the first nine Zernike terms, estimating the residual aberration. The inset presents a logarithmic scale plot of the measured point-spread function, where diffraction rings are visible. The X-axis has been converted to the object plane with a calibrated magnification. (b) The radial power density distribution $|r\mathrm{PSF}(r)|$.

Chapter 4

The BEC4 Machine

The scientific apparatus at BEC4 was built more than 20 years ago [93] and has remained highly productive over the past two decades. However, its bulk detection method, based on absorption imaging, has ultimately limited the depth and range of research that could be explored. More than half of my PhD has been dedicated to upgrading this workhorse into a modern quantum gas microscope. Therefore, the following two chapters will document this process in detail.

In this chapter, I will discuss the design of the BEC4 machine, tracing the journey of atoms from 400 K in the oven section to the fluorescence detection of ultracold atoms at 10 nK. This includes a brief review of the existing setup, with a primary focus on the renovations and upgrades implemented during my PhD.

4.1 Main chamber

The BEC4 machine features a two-chamber design, consisting of a "main chamber" for magneto-optical trap (MOT) loading and evaporation in the magnetic trap, and a "science chamber" for producing Bose-Einstein condensates (BECs) and loading them into optical lattices. The two chambers are separated by approximately 40 cm.

4.1.1 MOT loading and magnetic trap

The two-chamber design can be pretty friendly when it comes to upgrade. During my PhD, we did not have to rebuild the entire apparatus; instead, we replaced the old science chamber without breaking the vacuum of the main chamber. Dividing the experiment into two sections offers the advantage of maintaining a good vacuum. Additionally, a two-chamber system provides increased optical access, facilitating more complex laser configurations for addressing the atoms. However, this design inevitably limits the sequence run time, as the atoms must be physically transported between the two chambers in an adiabatic way. Furthermore, it imposes stringent requirements on the initial atom loading efficiency, as losses occur during translation.

We place a rubidium ampoule in the oven section, which contains approximately 5 grams of rubidium. The oven is heated to 73 °C—a relatively low temperature—to extend its operational lifetime while maintaining sufficient atomic flux. After cooling via the Zeeman slower, the atoms are captured by three pairs of counter-propagating beams in an optical molasses configuration, where they are locally trapped to form a MOT.

After about 12 seconds of MOT loading, the atoms are transferred into a cloverleaf-style Ioffe-Pritchard magnetic trap and further cooled through radio-frequency-induced forced evaporation. Notably, during evaporation, a peak current of 525 A runs through the coils for several seconds to generate the required magnetic fields. Consequently, all magnetic trap coils are constructed using hollow-core magnetic wire with water cooling. To ensure a high cooling-water flux, we employ a booster pump that increases the water pressure to 210 psi. The Zeeman slower coils are also designed with water cooling capability, although their peak operating current is significantly lower, around 30 A.

During operation, we accidentally discovered that part of the Zeeman slower section was clogged, possibly due to its smaller inner diameter compared to the magnetic trap coils (3.5 mm vs. 5 mm). Fortunately, this partial clogging did not degrade the overall performance of the Zeeman slower. The details of the main chamber's con-

struction and operation can be found in previous BEC4 theses [78, 93].

4.1.2 Transfer beam: tODT

After atoms have been trapped in the magnetic trap and cooled close to quantum degeneracy, we adiabatically transfer the atoms from the magnetic trap to an elongated optical dipole trap, which we refer to as "tODT" (t stands for transfer).

The tODT is formed by focusing a collimated beam down with a plano-convex lens that has a focal length of 500 mm as shown in Fig. 4-1. We estimate that the beam waist at the focal point to be about 30 μm. As a result, this trap features a very elongated shape with high radial trap frequencies and a loose axial frequency. The tODT has a total power of about 1 W.

4.1.3 Beam displacer

The two-chamber design of our apparatus and the way we mount the microscope objective impose special requirements on the atom transportation system. We transport the cold atoms from the main chamber, after evaporation in the magnetic trap, to the science chamber using a mechanical translation stage. The atoms are trapped in the tODT beam, which is focused by a lens mounted on the translation stage. As the lens translates, the atoms are carried along a straight path for approximately 40 cm.

There are three key elements that need to be aligned. First, the center of the main chamber, which is defined by the surrounding magnetic coil geometry, as this is where the MOT and magnetic trapping are optimized. Second, the focal plane of the microscope objective. Since we chose to mount the objective by letting it sit directly on the top viewport instead of mounting it to a translation stage, the focal plane is fixed with respect to the science chamber and cannot be adjusted. Lastly, the translation stage axis, which must be parallel to the line connecting the center of the main chamber and the focal spot of the microscope objective.

This presents an overdetermined problem, meaning that perfect alignment cannot be achieved by adjusting only the translation stage. To solve this problem, we

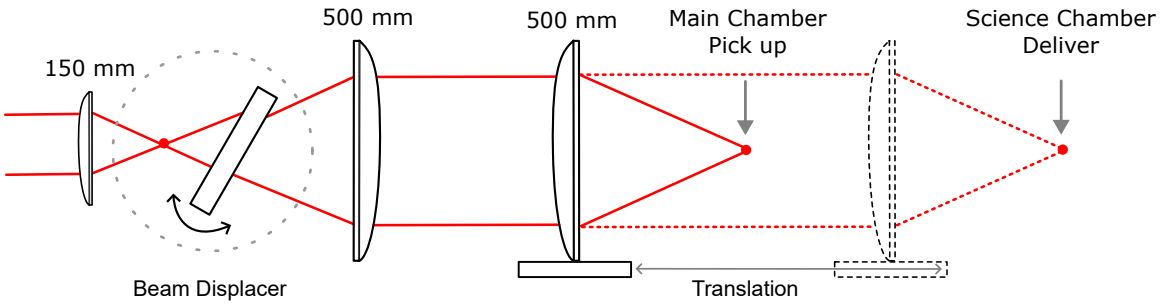

Figure 4-1: **Overview of the optical setup for the transport beam tODT.** The transport beam is formed by 1064 nm laser at a power of 1 W. After some beam shaping, it forms an intermediate image before the beam displacer and gets re-imaged onto the atoms by a one-to-one telescope. The last lens with a focal length of 500 mm is mounted on a mechanical translation stage with air bearing. It translates the atoms from the main chamber to the science chamber separated by about 40 cm in 3 s.

introduced a beam displacer device. It is entirely home-built from off-the-shelf optomechanical components.

The beam displacer provides additional degrees of freedom to address the overdetermined alignment problem. The working principle is illustrated in Fig. 4-2: tilting a parallel window causes the image or virtual image of the focusing rays to shift. This displacement can be quantitatively controlled by adjusting the tilt angle.

As shown in Fig. 4-2, using Snell's law, the displacement Δy of the point-source in the direction that is perpendicular to the beam propagation direction can be estimated to be:

$$\Delta y = d \sin\phi \left(1 - \frac{\cos\phi}{\sqrt{n^2 - \sin^2\phi}}\right) \tag{4.1}$$

Here d denoted the thickness of the window. In our case, a thickness of 12 mm fused silica window is used to balance the displacement range and precision. n is the index of refraction of the window and we already assume the index of refraction of air to be 1 in this expression. ϕ is the tilt angle, defined as the angle between the norm of the parallel window plate and the optical axis. As indicated in Fig. 4-2, when the tilt angle ϕ is changed by gimbal rotation, the lateral position of virtual image S' of the point-source S form by the window plate will also change.

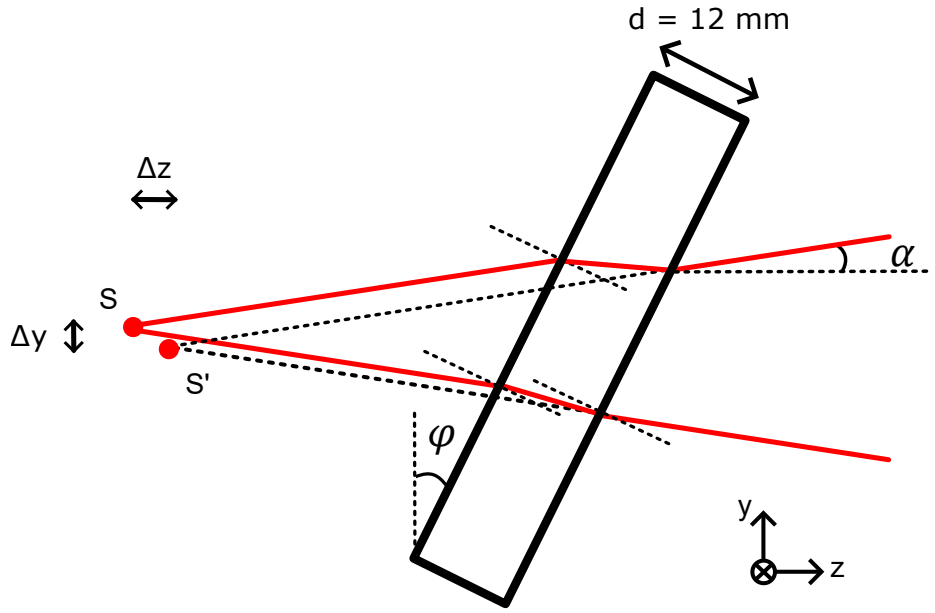

Figure 4-2: **Detailed illustration of using a plate window to displace a point source.** Due to refraction, the tilted window plate maintains the divergence of a point source. The imaging optics after the window plate will see a virtual source S' displaced from the original source location S.

Although technically Eqn. 4.1 is only valid for parallel beam incident, the NA of our beam is small enough to make this equation a good approximation. We use two motorized rotational stages of Newport PR50CC, Newport SMC100 motion controller and a Raspberry PI to build a customized gimbal rotation mount to hold a 12 mm thick fused silica window. The two rotational stages are assembled orthogonally to provide independent beam displacement in both x and y direction. We calibrate the lateral displacement of the virtual souce to be 64.8 μm per degree of rotation. Technical details of the construction and communication with this home-built device can be found in this Master thesis [94].

Note that in Fig. 4-2, the point-source is also displaced in the beam propagation direction, indicated by Δz. This longitudinal displacement of the virtual image can be simply compensated by adjusting the initial and final travel coordinates of the translation stage.

4.1.4 Anti-ODT

The focus of the tODT beam is translated by shifting the position of the final focusing lens on a translation stage over a distance of approximately 40 cm in over 3 seconds. The single-pass transfer efficiency, measured based on atom loss, is approximately 80% [55].

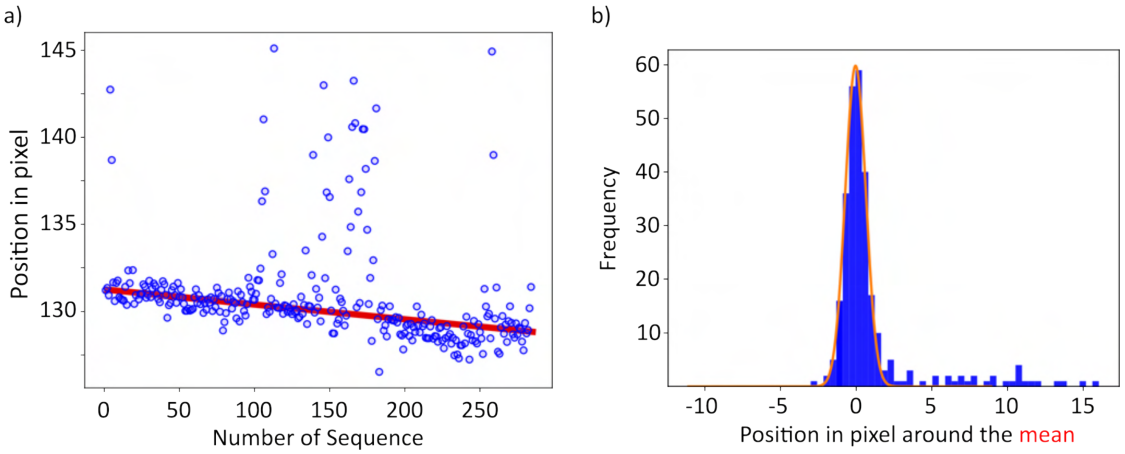

Figure 4-3: **Repeated measurements of the tODT position stability across runs before temperature stabilization.** (a) The tODT beam vertical position imaged after transport to the science chamber. The red solid line represents a linear fit, indicating an overall drift. (b) Histogram of the data in (a), with a standard deviation of 1.9 μm, assuming a Gaussian distribution. Figure adapted from [94].

Since the traveling distance of the tODT beam is relatively large, there will be drift and fluctuations of the final beam delivery position in the science chamber. Fig. 4-3 shows a typical position change when the whole machine is warming up. We image the vertical position of the atoms in the science chamber after its delivery from tODT. The imaging magnification yields 2.88 μm per camera pixel.

There is a clear trend of drift as the machine undergoes thermalization. Additionally, some large fluctuations exceeding 2σ may arise from hysteresis in the mechanical system, as they predominantly appear on one side of the mean value. However, the stability of the delivery position can be significantly improved after the entire room reaches thermal equilibrium.

To further mitigate potential thermal stability issues, we set up an anti-ODT beam in the science chamber. This beam is named "anti-ODT" because it propagates

collinearly with the tODT beam but in the opposite direction. After the tODT beam is delivered to the science chamber, the atoms are adiabatically transferred into the anti-ODT.

Since the optics for this beam are mounted directly near the machine with no mechanical movement involved, its passive stability is significantly better than that of the tODT beam. The anti-ODT is aligned by back-coupling the beam into the fiber that launches the tODT, ensuring good overlap. It has a larger beam waist of 50 μm than the tODT, allowing it to reliably capture atoms despite tODT beam instability.

4.2 New science chamber

The new science chamber and the main chamber are separated by a gate valve, which ensures the independence of the vacuum, especially in emergency situations. In addition to the gate valve, they are physically connected by a short bellow. The bellow provides mechanical flexibility, aiding in the coarse alignment of the heights of the two chambers.

4.2.1 Overview of the vacuum system

The new science chamber is a custom-made, octagon-shaped ultra-high vacuum (UHV) chamber constructed from 316 stainless steel by Kimball Physics. It features two primary 6 in. CF ports on the top and bottom, along with eight 2.75 in. CF ports on the sides. Additionally, it includes a feedthrough for electrical connections to the in-vacuum RF antenna.

Six of the eight side ports serve as viewports for optical access, while the remaining two connect to the main chamber and the chimney housing the titanium sublimation pump. The side viewports are coated by Laseroptik GmbH to reduce reflections, specifically optimized for wavelengths of 532 nm, 780 nm, 1064 nm, and 1596 nm.

As shown in Fig. 4-4, the new vacuum system assembly consists of two major pumps to maintain the UHV: a 70 L/s ion pump, which operates continuously, and a titanium sublimation pump, which is fired once every few years. Large flanges are

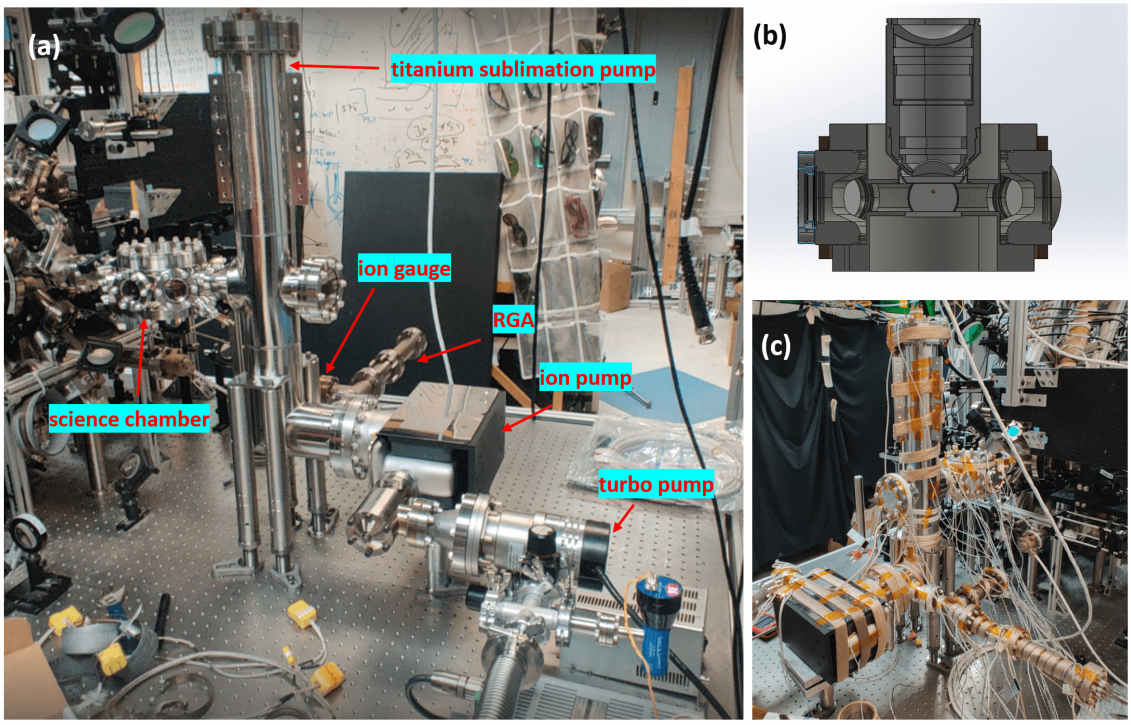

Figure 4-4: **Photos of the new vacuum system assembly.** (a) Photograph of the new vacuum system assembly, with labels indicating key components. (b) Cross-sectional view of the science chamber. (c) Photograph of the new vacuum system assembly wrapped in heat tapes before baking, with multiple thermocouples attached for monitoring. During the baking stage, all the parts are covered in layers of vacuum-compatible aluminum foils to contain heat.

used to ensure high vacuum conductance. The titanium sublimation pump is housed in a chimney to ensure a large surface area while avoiding line-of-sight deposition of titanium on any viewport windows. Additionally, there is a turbo pump port for vacuum baking, which can be valved off and disconnected using an angle valve.

For monitoring, we installed an ion gauge, positioned away from the science chamber to prevent local heat build-up for the hot filament. It provides an estimate of the vacuum conditions in the science chamber. We also have an RGA (residual gas analyzer) available for leak checks.

4.2.2 Baking to ultra-high vacuum

Baking is crucial in ultra-high vacuum (UHV) systems because heating can accelerate the rate at which molecules outgass. This process ensures that trapped water vapor

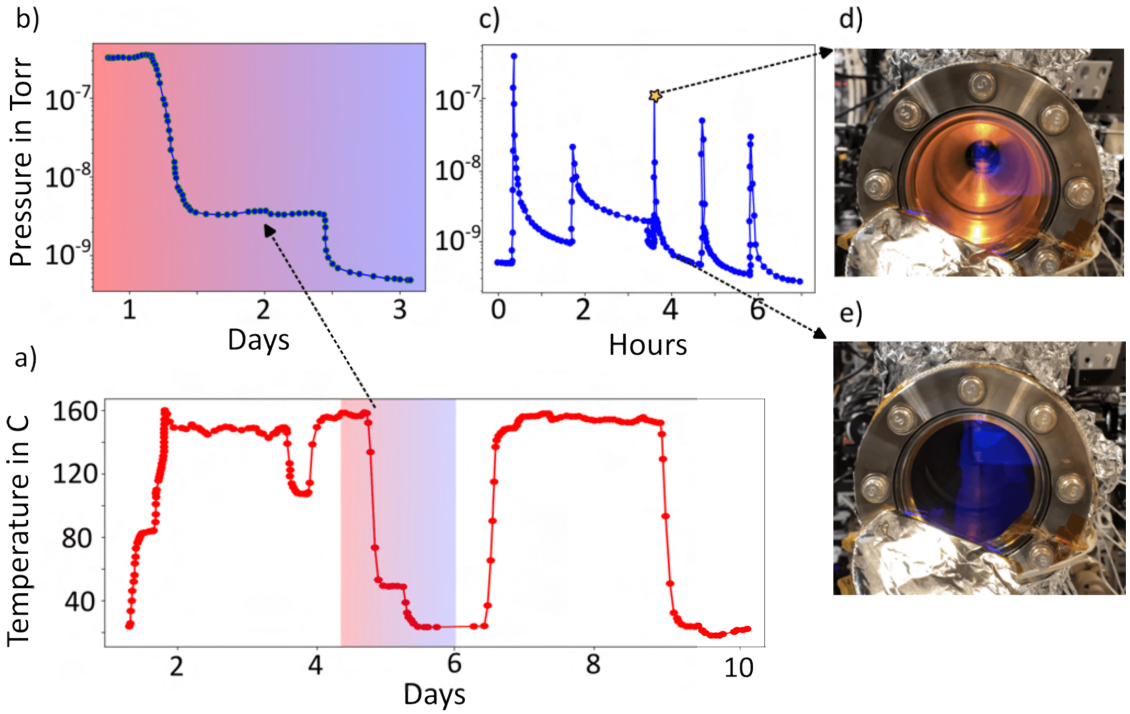

Figure 4-5: **Baking temperature and vacuum pressure monitored over several days.** (a) The plot shows the temperature monitored at the re-entrant bucket viewport over several days. Two baking stages are evident from the temperature variation, with the peak temperature kept below 160 °C. (b) Plot of pressure variation measured by the ion gauge during the initial temperature cooldown. (c) The pressure was measured at low temperatures in the chamber while the titanium sublimation pump was activated repeatedly over several hours. Photographs (d) and (e) show the glowing light from the hot titanium filaments, which become visible when the pressure reaches its peak. As the filaments cool and stop glowing, the pressure stabilizes at a plateau. Figure adapted from [94].

and other impurities are efficiently released and pumped out, resulting in a lower pressure when cooled down to room temperature [95].

Thanks to the two-chamber design, we did not have to bake the entire machine. Instead, we closed the gate valve between the main chamber and the new science chamber, allowing us to bake only the new science chamber assembly.

As shown in Fig. 4-4(c), the new vacuum assembly was wrapped in heat tapes before baking, with multiple thermocouples attached for monitoring. During the baking stage, all components were covered in layers of vacuum-compatible aluminum foil to retain heat.

We performed a two-stage baking process, where each stage consisted of a slow temperature ramp-up, a hold period at the peak temperature, and a controlled temperature ramp-down. We ensured that the temperature changed gradually during the ramp-up and ramp-down phases to minimize thermal stress—specifically, slower than 10 °C per hour. Additionally, we reduced spatial temperature gradients by using multiple heating tapes and variable transformers, allowing for fine-tuned local temperature control with greater flexibility. Throughout the entire baking process, we also logged the vacuum pressure readings from the ion gauge.

In the first stage of baking, we began with only the turbo pump to lower the vacuum pressure to the right range before switching on the ion pump. During this process, we performed degassing on the ion gauge and RGA filaments.

In the second stage of baking, we closed the angle valve to disconnect the turbo pump in order to reach a lower pressure. At this point, we relied solely on the ion pump before firing the titanium sublimation pump.

Each baking stage lasted approximately one week, with a day allocated for ramping up and ramping down at the beginning and end. The system was maintained at the peak equilibrium temperature for several days until the pressure readings stopped decreasing. The final baking temperature varied across different components, as shown in the following table:

Table 4.1: Final baking temperatures for key vacuum components.

Vacuum Component	**Baking Temperature (°C)**
Titanium sublimation pump chimney	220
Ion pump	200
Ion gauge	170
Science chamber	140
Viewports	140
Bellow connecting two chambers	90

At the end of the baking process, after cooling down to room temperature, the ion gauge reading at the science chamber assembly (see Fig. 4-4(a) for the exact probe location) was 8×10^{-11} Torr, while the ion gauge for the main chamber recorded a pressure of 4×10^{-11} Torr.

4.2.3 HR coating crazing after baking

For the top viewport window, we applied a high-reflectivity (HR) coating on the vacuum side. The multilayer coating is HR at 1064 nm, serving as a retro-reflector for the vertical lattice, while an anti-reflection (AR) coating at 780 nm maximizes fluorescence photon collection. The coating was applied by Blue Ridge Optics.

To our surprise, when we uncovered the aluminum foil after baking, we found that the HR coating on the top viewport had completely crazed, as shown in Fig. 4-6.

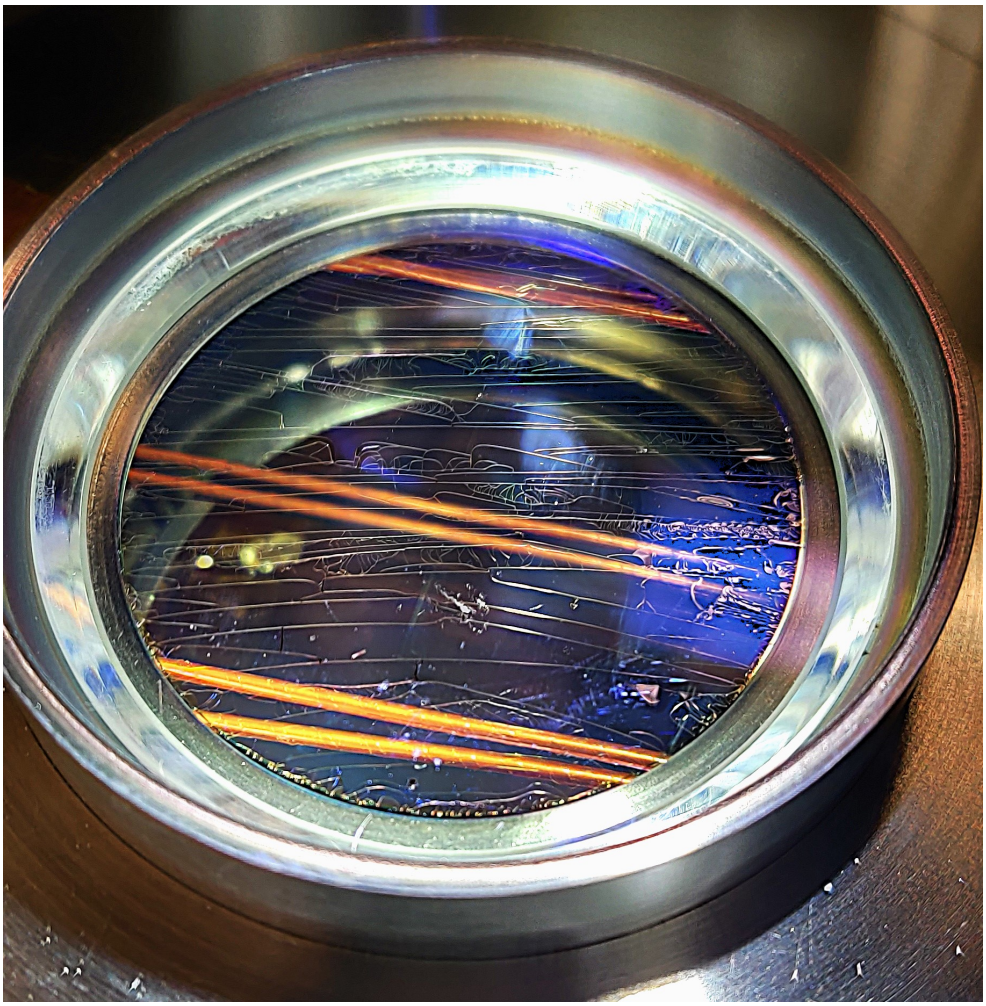

Figure 4-6: **Photo of the crazed in-vacuum high-reflective coating after baking.** The thin, dense white horizontal lines are the crazing of the coating. It is only visible at certain angles of illumination. The viewport still holds ultra-high vacuum yet its optical transmission and reflection performance are completely deteriorated and cannot be used.

This was something we had never encountered before. After conducting a litera-

ture search, we found reports and evidence that other groups had also observed HR coating crazing after baking. Notably, the lithium microscope at Princeton University experienced similar behavior [26]. They reported that their HR coating was "partially damaged" after bakeout.

Around the same time, the Vuletić group at MIT was also upgrading their apparatus. They had HR-coated in-vacuum cavity mirrors that similarly degraded after the baking process. They later conducted a more systematic investigation into this phenomenon, in which they microscopic examined the coating after bakeout [96].

It seems to be related to the thickness of the coating [96]. HR coatings typically consist of many more layers than AR coatings, which explains why all reported incidents involve HR coatings. Apparently, not all in-vacuum HR coatings will craze after bakeout, and we do not fully understand why this happened to our viewport. However, we can offer a few pieces of advice to future readers. Hopefully, you are reading this early enough in your building process:

- Double-check with your coating manufacturer that the HR coating is compatible with high-temperature baking in UHV.
- Avoid sonicating the viewport with strong alcohol solution [26,97]; if necessary, clean it gently with lens tissue.
- Be cautious during bakeout, especially regarding temperature gradients, both temporal and spatial. Avoid thermally stressing the coating because a large tensile stress will likely cause crazing [98].
- Be conservative with the final baking temperature. In our case, we only went up to 140 °C, which is already on the lower side. Consider using an even lower temperature for longer baking duration, such as 120 °C.

4 mm + 1 mm solution

The devastating incident caught us completely off guard. The viewport window crazed so severely that we seriously doubted its ability to transmit light, let alone function as

a reflector. At the time (September of 2022), the lead time for manufacturing a new vacuum viewport assembly was extremely long, on the order of a year. The crazed HR coating was clearly beyond repair and could not be used. Fortunately, we did not allow it to upset us for too long and identified a solution to move forward. A hacky way (maybe) but it worked.

During the testing and calibration phase, we had also measured the surface profile and thickness of the bottom vacuum viewport, which was also designed as a recessed bucket window. The bottom viewport assembly shared a similar design and dimensions to the top assembly, except that the bottom viewport window was 4 mm thick instead of 5 mm. It had a broadband AR coating on both the vacuum and air sides. The 4 mm viewport window exhibited similar deformations to the crazed 5 mm one, and the astigmatism aberration introduced by this deformation could be corrected in the same way as described in Chapter 3. We even measured the point-spread function after adding another flat 1 mm fused silica plate to the 4 mm viewport and achieved a diffraction-limited spot after optimization.

We realized that we could repurpose the bottom viewport assembly as the top assembly. The missing 1 mm thickness could be compensated by placing a 1 mm thick fused silica window on the air side of the viewport. The HR coating could also be restored by applying a coating to the added 1 mm thick compensation window.

It was a coincidence that the original bottom viewport window was designed to be 4 mm thick. The "4 mm plus 1 mm" scheme would not have worked if the bottom viewport had originally been 5 mm thick or more. We also happened to have another backup bucket window on the shelf to serve as the new bottom window. Although the recess dimension was slightly larger than designed (likely because this bucket window assembly was originally a backup for the main chamber), an added zero-length reducer compensated for the extra length.

In the end, we proceeded with the "4 mm plus 1 mm" viewport as the top viewport and a recessed bucket with a similar dimension and broadband AR coating as the bottom viewport. As illustrated in Fig. 4-7, the objective now sits directly on the 1 mm compensating plate. The bottom side of this plate was coated to highly reflect

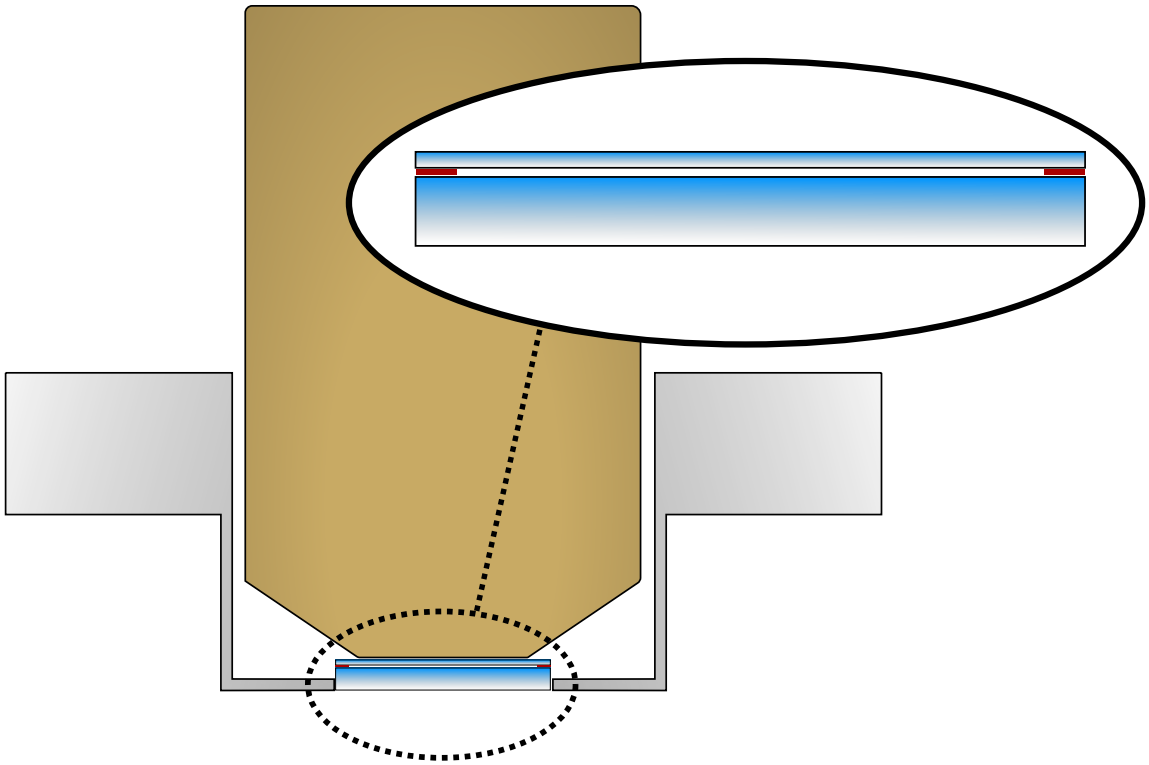

Figure 4-7: **Cross-section view of the final viewport configuration.** We replaced the crazed 5 mm viewport to a 4 mm viewport plus 1 mm fused silica compensation plate. The 4 mm viewport has broadband AR coating on both sides. The 1 mm plate has HR coating for 1064 nm on the bottom surface. To avoid unwanted optical contact between the two viewports, thin spacers are inserted.

1064 nm, while the top side had a broadband AR coating. Spacers with a thickness of approximately 25 μm were inserted between the 1 mm compensation plate and the viewport window to provide well-defined optical interfaces for the dielectric coating to function properly. The three spacers were made from Kapton films and were arranged at 120° intervals to form a three-point contact.

4.2.4 Laser setup

For the BEC4 experiment, two major laser wavelengths are used.

780 nm

The 780 nm lasers are used for laser cooling and trapping. We have two TA systems from TOPTICA.

One is a relatively new TA Pro and, according to its specifications, can output up to 4 W. To extend its operational lifetime, we run it at 75% of its maximum capacity. It is locked to a rubidium cell via polarization rotation spectroscopy [99] and serves multiple purposes, including Zeeman slowing, optical molasses, MOT, imaging, and polarization gradient cooling under the microscope.

The other TA-100 is relatively old, and this early model can only output about 200 mW. It is locked to a different rubidium cell and is used for repumping atoms out of the $F = 1$ manifold during laser cooling and imaging.

1064 nm

The 1064 nm lasers are fiber amplifier systems used for trapping atoms. We have three Nufern fiber amplifiers, all seeded by a 2 W Mephisto laser from Coherent, Inc. The seed laser is split into three branches with frequency offsets to prevent cross-interference.

One of the Nufern amplifiers can output approximately 4 W and is used to provide light for the tODT beam.

The other two Nufern amplifiers can output nearly 40 W each. To extend their operational lifetimes, we run them at 70% of their maximum capacity. One of the high-power Nufern amplifiers supplies power to the horizontal pinning lattices, while the other generates the anti-ODT and a light sheet for fluorescence imaging. The details of these optical traps will be explained in the next chapter.

Other lasers

We have a superluminescent diode laser at 840 nm, capable of outputting up to 30 mW. It is used as a dimple trap to finely control atom number stability [78]. Additionally, we have a Ti:sapphire laser from M Squared, which was previously used for spin-dependent lattices in past projects [54].

4.2.5 Magnetic field control

In addition to all the new optomechanical upgrades, we also redesigned the magnetic field control around the new science chamber.

Gradient coils

Initially, we planned to use a larger magnetic field gradient to spectroscopically address a single layer of atoms in a vertical lattice, allowing us to prepare a two-dimensional sample [24, 25, 82, 85]. So we designed gradient coils with that purpose in mind. In the end, we found that the optical solution (light sheet) was much simpler to implement and more robust compared to the magnetic field gradient method, so we opted for the light sheet. Nevertheless, the gradient coils are still capable of generating large magnetic field gradients.

We planned to have about 10 kHz detuning between vertical lattice layers for the rubidium transition from $|1, -1\rangle$ to $|2, -2\rangle$. Since the lattice spacing of 532 nm, it would required a field gradient of at least 90 G/cm. With the coils mounted outside the vacuum chamber, it requires hundreds of amps of current to generate such a gradient. So we have to use hollow-core magnetic wires to make those coils. We use coils from MWS Wire and non-magnetic epoxy NM25-1 from COTRONICS to wind those coils. The coils are connected to the main water cooling manifold which can push 210 psi of water through. We use EMS 300-500 power supply to drive the gradient coil pair and supply at most 210 A before it is voltage limited. At the full output of 210 A, we are able to generate a magnetic field gradient of 100 G/cm.

Bias coils

We installed bias coils mounted to the side viewports. Each coil assembly, as shown in Fig. 4-8, consists of approximately 116 turns. Epoxy was applied during winding to maintain mechanical integrity. The coils can operate continuously at up to 5 A without significant heating. We use Agilent 6651A and Agilent 6641A power supplies to drive these two pairs of coils. These coils are used to fine-tune the local bias field

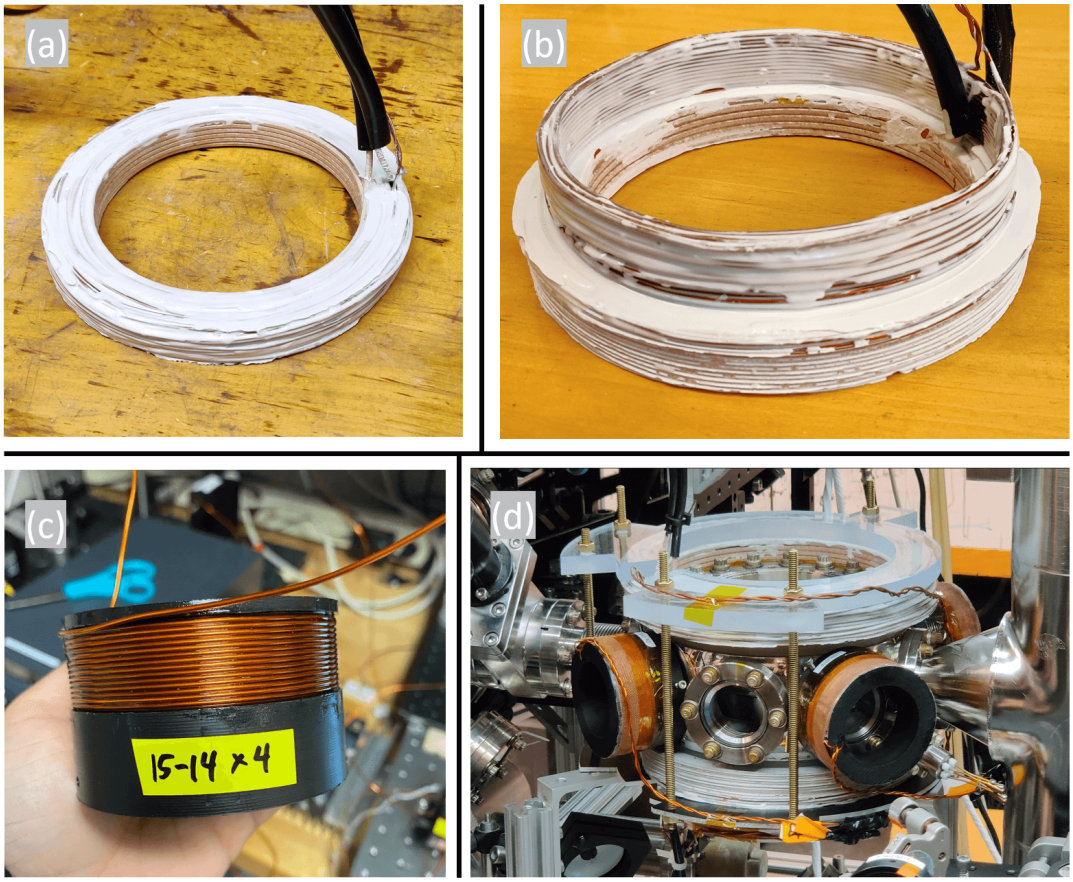

Figure 4-8: **Photos of the magnetic coils around the science chamber.**(a) Top gradient coil (hollow core) and the top vertical bias coil (normal magnetic wires). It is hard to be seen from the picture, but the vertical bias coils wraps around the inner hollow-core coils. (b) Bottom gradient coil (hollow core) and the bottom vertical bias coil (normal magnetic wires). Note the bias coils is attach to the surface of the hollow-core coils. (c) The number of turns alternates as 15-14-15. . . , with a total of 8 layers. The coils are wound against a custom-made mounting bracket designed to fit around the 2.75-inch CF viewports. (d) Side view of the gradient and bias coils installed onto the science chamber.

at the few-Gauss level and to project the magnetic gradient in the horizontal plane.

Here is the calibrated bias field generated by these two pairs of the side bias coils at the middle position:

Table 4.2: Bias field of side bias coils.

Coil Orientation	**Bias Field (G/A)**	**Resistance (Ω)**
doorAC - ovenPC	0.75	0.78
doorPC - ovenAC	0.77	0.86

RF antenna

From previous experiments, we often struggled to achieve a high Rabi frequency when driving RF transitions. Without in-vacuum coils, we had to position the coils as close as possible to the atoms.

Since the new chamber has an electrical feedthrough and sufficient optical clearance, we installed a small and simple RF antenna inside the vacuum chamber this time.

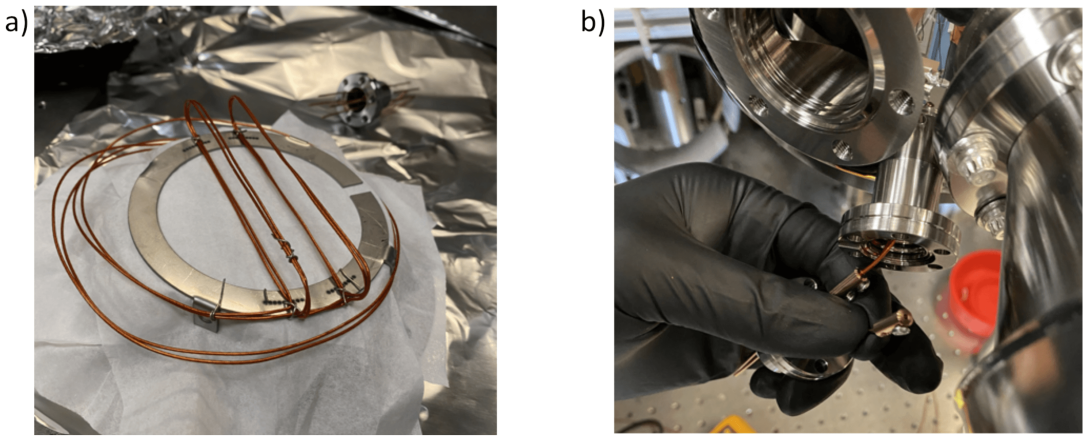

Figure 4-9: **Photos of the in-vacuum RF antenna in the new science chamber.** (a) Picture of the rectangular RF antenna in a Helmholtz configuration, mounted on a sheet stainless steel platform. (b) The electric connection of the in-vacuum antenna is routed via a feedthrough. Figure adapted from [94].

As shown in Fig. 4-9, the in-vacuum RF coil has a single-loop rectangular shape in a Helmholtz configuration. It is mounted against a stainless steel platform. Both the coil and the stainless steel platform are chosen to be UHV-compatible.

4.2.6 Floating table

There are several noteworthy mechanical upgrades in the new machine compared to the old one. For example, we replaced all scattered optical boards with a custom unibody aluminum honeycomb breadboard. This design aims to mitigate vibrations and noise by converting much of the instability into common mode. Another key upgrade is the implementation of a floating optical table.

The BEC4 lab operated without a floating table for more than a decade. One reason for this was the presence of a long Zeeman slower mounted at a 45-degree angle in the vertical plane. This setup required significant vertical space, as the oven section was positioned near the ceiling. Consequently, the optical table supporting the main apparatus had relatively short legs.

For years, we believed that no feasible short floating legs could fit under our optical table. Additionally, we were concerned about the performance of a retrofitted floating table, as we estimated that the center of mass of the apparatus would be quite high.

However, upon obtaining the first few microscope fluorescence images, we immediately noticed significant global blurring from shot to shot as shown in Fig. 4-10 (b) and (c). It indicated that the system was experiencing vibrations or drift during the exposure time, which is on the order of a second. The fact that the blurring did not occur consistently suggested the presence of environmental instability.

Furthermore, we carefully built interferometers to measure the passive stability at various locations on the optical table and found that the shaking was substantial, particularly between the chamber and the table. The shaking consistently worsened as the interferometer arm length increased.

An even simpler method to visualize the vibrations is to place a half-filled beaker on the table and inspect the reflection of a stable point source off the water surface. When the beaker is placed on a non-floating table, the reflection exhibits noticeable jittering, whereas on a floating table, the reflection remains stable. All of those pieces of evidence convinced us that improving the passive mechanical stability was essential before proceeding with further experiments.

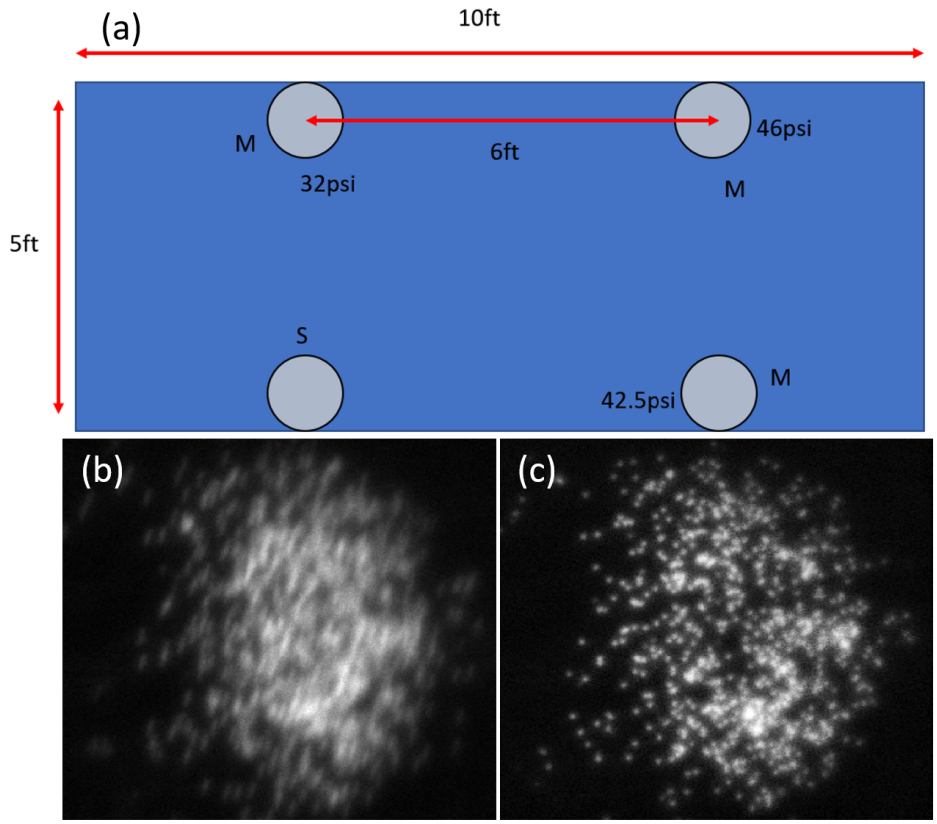

Figure 4-10: **Schematics of the floating table and raw fluorescence images taken before the machine table is floated.** (a) Placement of the floating table legs and the corresponding air pressure. Note that one leg ("S") is intentionally left unregulated to prevent over-regulation. (b) and (c) Fluorescence images taken within a single sequence run before floating the table. The two images were captured approximately one second apart, meaning the underlying atomic distribution should be nearly identical. However, in (b), a noticeable global blurring is present, indicating mechanical instability.

We purchased a set of four Micro-g Modular Free-Standing Posts from TMC. To our knowledge, TMC is the only manufacturer that provides floating table legs as short as 12 inches in height. We replaced the old legs without significantly disturbing the alignment of the machine. The exact placement of the floating legs and the corresponding air pressure is shown in Fig. 4-10(a). The placement was chosen to match the estimated high center of mass of the apparatus.

Fortunately, we did not experience any rocking of the apparatus after floating. This issue can arise due to improper weight distribution or incorrect selection of

the mechanical damping filter, as reported by other groups. After installation and supplying compressed air, the entire experimental table was lifted by 2 cm, remaining within the headroom tolerance. The floating table significantly improved the stability of the fluorescence images, allowing for further optical fine-tuning.

Chapter 5

Quantum Gas Microscopy

5.1 Introduction

The paradigm for imaging in quantum gas microscopes has been fluorescence imaging, where atoms scatter photons while being illuminated by resonant imaging beams. This technique allows individual atoms to be imaged with high fidelity against a clean background. For alkali atoms, the exposure time is typically on the order of a second [25–27, 80–82, 85]. The need for long exposure times arises because each atom must scatter a sufficient number of photons to be clearly distinguished from background noise, all while avoiding excessive recoil heating that could lead to atom loss.

While most quantum gas microscopes rely on long-exposure fluorescence imaging, certain atomic species allow for significantly shorter exposure times. These systems often require specialized engineering to maintain high signal-to-noise ratios. For instance, the erbium microscope at Harvard uses a two-dimensional dynamic accordion lattice to separate atoms before imaging [89]. The ytterbium microscope at Tokyo Institute of Technology employs a specially designed optical lattice with a much deeper trap depth for the excited state, enabling efficient photon cycling [100]. These short-exposure microscopes frequently involve lanthanide elements, which have multiple valence electrons offering additional optical transitions, as well as heavier atomic masses that reduce recoil heating.

The rubidium quantum gas microscope at BEC4 falls into the more conventional category, where long-exposure fluorescence imaging is required. In this chapter, I will discuss the essential components required to achieve quantum gas microscopy. These can be broadly divided into two major categories: hardware and software. The hardware section focuses on the experimental realization of trapping and cooling individual atoms in an optical lattice. The software section details the deconvolution and reconstruction algorithms required for image processing, which play a crucial role in extracting site-resolved atom distributions from raw fluorescence images.

5.2 Trapping and cooling

In Fig. 5-1, the major laser beams for the BEC4 machine and their propagation directions are shown. The 1064 nm beams are used to generate optical lattices and a light sheet for trapping while the 780 nm beams are used to perform sub-Doppler cooling and generate fluorescence photons.

5.2.1 Optical traps

Pinning lattices

In this project, the optical lattices are mainly used as a pinning lattice to freeze the motion of the atoms during fluorescence imaging. As shown in Fig. 5-1, two 1064 nm beams in the horizontal plane are focused onto the atom and retro-reflected back. The two beams have a detuning on the order of 100 MHz to prevent cross-interference. For the retro-reflected beam, we couple it back to the fiber that launched the beam to ensure the optimal interference contrast. We use a pellicle beamsplitter to monitor the power of the retro-reflected beam during alignment. As a result, we form a square lattice with a lattice constant of 532 nm.

To achieve good fidelity under the microscope, the lattice depth is usually on the order of 3000 E_r [25,31,82,85]. For rubidium in an optical lattice formed by 1064 nm laser light, this corresponds to a temperature of 300 μK.

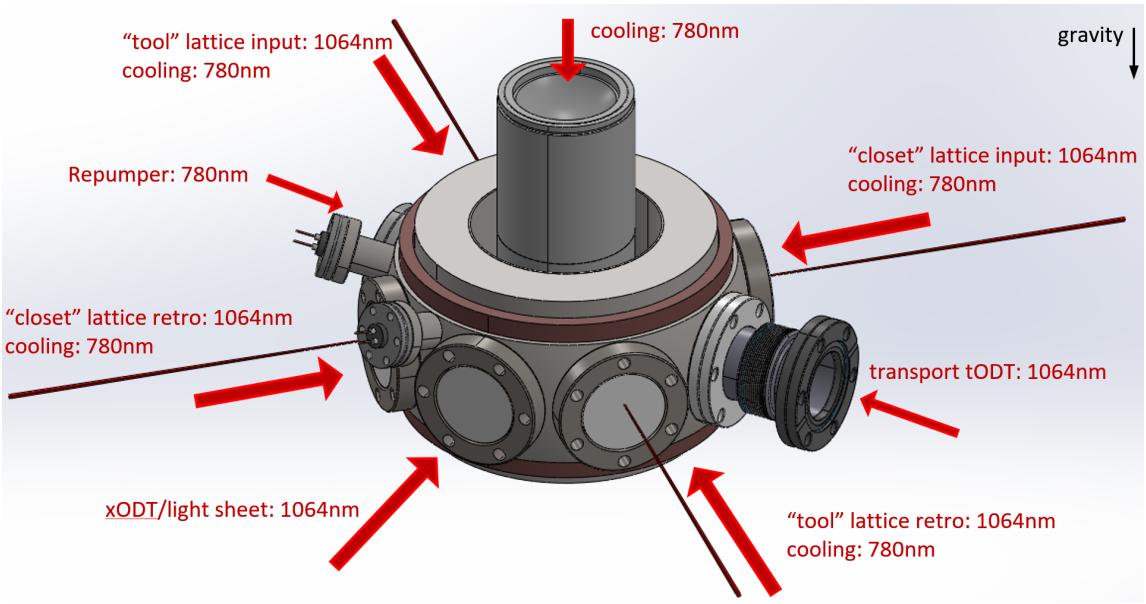

Figure 5-1: **Schematic illustrating the main laser beams involved in quantum gas microscopy.** The laser beams can be divided into two categories: trapping and cooling. All 1064 nm beams are used for trapping, including a transport beam (todt), a two-dimensional optical lattice, and a light sheet. Following the convention of previous BEC4 students, the two orthogonal lattice directions are referred to as "tool" and "closet." All 780 nm beams are used for sub-Doppler cooling, including five main cooling beams and a repumper beam. Note that, in the horizontal plane, the cooling beams share the same path as the lattice beams.

In our experiment, we also build cylindrical telescopes to modify the lattice beam into an elliptical shape at the focal point to enhance the local intensity and therefore, lattice depth. We ended up using a beam shape with 2-to-1 aspect ratio, with beam waists of $(w_{\text{horizotal}},\ w_{\text{vertical}}) = (70\ \mu m,\ 35\ \mu m)$. With this beam shape, we can generate a lattice depth exceeding $3000E_{\text{r}}$ when the input beam is more than 5 W. It can be beneficial to use a larger beam waist if sufficient laser power is available, as it reduces curvature and creates a more homogeneous light field on the atomic cloud.

Light sheet

The quantum gas microscope requires the sample to be two-dimensional due to its limited depth of field. The depth of field scales roughly as λ/NA^2; in our case, it is on the order of 1.2 μm. As mentioned in Chapter 4, some groups choose to use a large magnetic field gradient with a vertical lattice to prepare a two-dimensional sample [24, 25, 82, 85]. We choose an optical solution. To compress the atomic cloud extent below the depth of field, we use an optical dipole trap with a high trap frequency in the vertical direction. A high trap frequency results in a smaller oscillator length and, consequently, a reduced cloud width. However, for field homogeneity (which we will discuss further in later sections), the trap frequency in the horizontal plane needs to be as low as possible. To simultaneously satisfy both requirements, we need a highly asymmetric trap.

To prepare such a two-dimensional sample during imaging, we build a cylindrical telescope to shape the beam into an elliptical profile before it is focused down by an aspheric lens onto the atoms. Due to its extreme aspect ratio, we refer to this beam as a "light sheet."

To achieve the tightest confinement possible for the light sheet, we place the last lens as close to the side viewport window as we can. We use a diffraction-limited aspheric lens (Thorlabs AL75150H) which features an NA of 0.21 and a focal length of 150 mm. Ultimately, the achievable NA is limited by the geometry of our re-entrant top viewport as shown in Fig. 5-2(c).

The optical quality of the final focusing lens affects the beam shape of the light

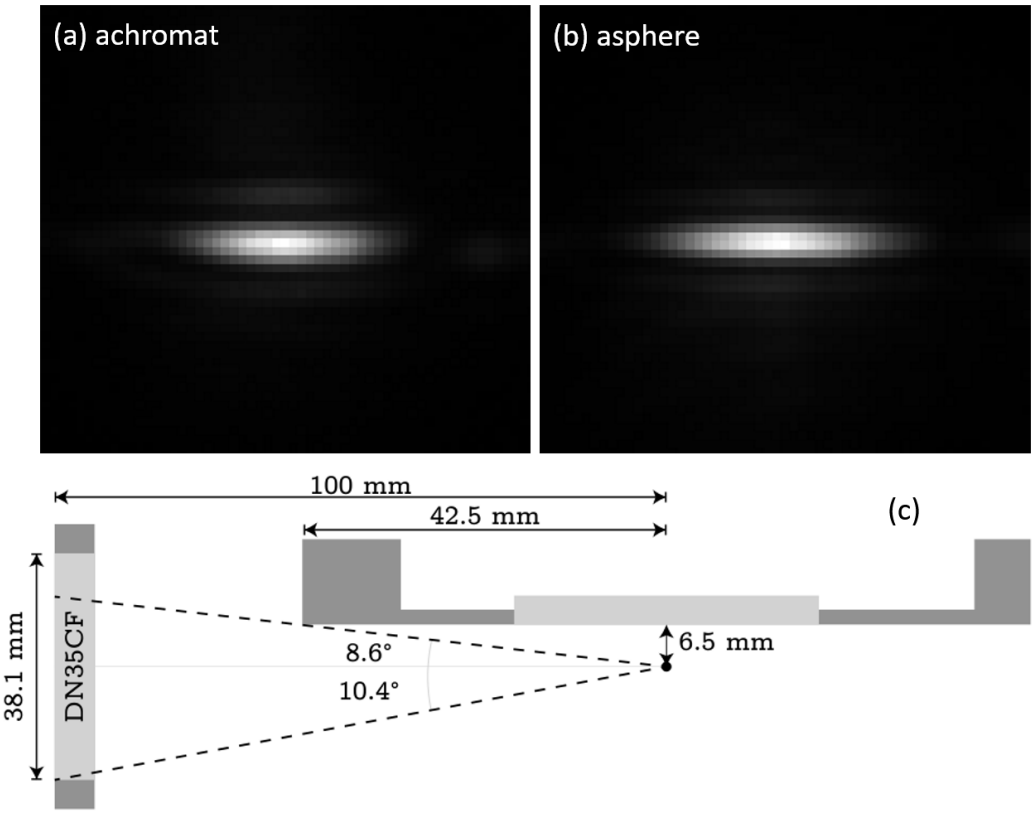

Figure 5-2: **Comparison of the cross-sectional profiles of the light sheet beams.** The light sheet is re-imaged onto a camera with a magnification of 4.7. The optical quality of the last lens that focuses the light sheet onto the atoms can have a noticeable effect. (a) The last lens is an achromat. (b) The last lens is an asphere (Thorlabs AL75150H). (c) Diagram of the optical access from the side, as it is limited by the bucket window and the viewport diameter.

sheet. As shown in Fig. 5-2(a)-(b), the improvement from using an achromat to an aspheric lens is noticeable for an NA of ≈ 0.2. In the end, we are able to build a light sheet with beam waists of $(w_{\text{horizontal}}, w_{\text{vertical}}) = (42\ \mu m, 7.5\ \mu m)$. The Rayleigh range of the light beam is $\approx 170\ \mu m$. The atomic cloud can be trapped by the light sheet alone.

5.3 Laser cooling under the microscope

5.3.1 Considerations for cooling

The microscope "sees" the atoms by collecting fluorescence photons. Laser cooling is a common way to generate fluorescence photons. It also serves the purpose of keeping the temperature of the atomic cloud low such that atoms can be trapped locally by deep optical lattices. These two aspects are highly related, like two sides of one coin. The photons for imaging are generated from the cooling process and cooling ensures a high fidelity of the imaging.

Achieving optimal cooling is crucial for the fidelity and signal-to-noise ratio of the quantum gas microscope. Better cooling leads to a lower equilibrium temperature, which helps to keep atoms trapped for a longer duration. To achieve a reasonable signal-to-noise ratio, each atom must scatter a sufficient number of photons before being lost from its lattice site.

Photon number

Almost all the quantum gas microscope groups use fluorescence imaging, during which atoms are excited by resonant light and spontaneously emit photons. The lower boundary of the resolution limit Δx can be estimated by [101]:

$$(\Delta x)^2 = \frac{\text{rms}_{\text{PSF}}^2 + \Delta_{\text{px}}^2/12}{N_{\text{ph}}} + \frac{8\pi \text{rms}_{\text{PSF}}^4 \sigma_b^2}{N_{\text{ph}}^2 \Delta_{\text{px}}^2} \tag{5.1}$$

where rms_{PSF} is the rms width of a Gaussian point spread function, Δ_{px} corresponds to the size of a camera pixel in the object plane, N_{ph} is the average number of detected

photons per atom, and σ_b is the rms background noise. It is obvious that the more photons collected, the better the resolution in determining the position of the emitting atom.

Photon collection efficiency

Photon collection efficiency due to the geometric limitation of the objective is: $\Omega/4\pi = (1-\sqrt{1-\mathrm{NA}^2})/2 = 20\%$, where the numerical aperture (NA) is set to be 0.8. Taking into account other factors of photon loss, such as coating losses, and the non-unity quantum efficiency of the detector, it can be assumed that the overall collection efficiency is between $5\% \sim 10\%$.

Meanwhile, it is also important to maintain power efficiency, meaning that the cooling light should have as little power as possible, because it can reflect off the inside walls of the vacuum chamber and thus creating a significant stray light background.

As a rule of thumb, in quantum gas microscope experiments, ∼1000 photons collected from one atom with an exposure time of $\sim$ 1s is good enough to produce clean images with high fidelity [102], indicating a decent scattering rate will be $\sim$ 20 kHz.

Heating during the imaging

While the spontaneously emitted photons give rise to the imaging signal, they can also become detrimental to the imaging fidelity through recoil heating.

In free space the increase of kinetic energy due to recoil of an atom initially at rest is $E_{\mathrm{rec}} = \frac{\hbar^2 k^2}{2m}$. If the spontaneous emission happens inside a tight trap the probability to change into an excited vibrational state is $\approx \eta^2$, but when this happens, its energy increases by $\hbar\omega = E_{\mathrm{rec}}/\eta^2$, so that on average the energy increase is again E_{rec}. Here η is the Lamb-Dicke parameter which is commonly used to parametrise the confinement strength in harmonic traps:

$$\eta = \sqrt{\frac{\hbar k^2}{2m\omega_{\mathrm{trap}}}}, \tag{5.2}$$

One way to improve the situation is to increase the depth of the optical lattice. Typically one needs a lattice of several hundreds to thousands of E_{rec} depth. Assuming the momentum accumulation due to recoil is diffusive, it will take $N = \frac{9\lambda^2}{4a^2} \times V_0$ scattering events for the atom to gain enough kinetic energy to escape the lattice site, where a is the lattice spacing and V_0 is the lattice depth in the unit of recoil energy.

At first glance, N can reach to ≈ 5000 if the pinning lattice is $\approx 1000E_{\text{rec}}$ deep for rubidium atoms. However, before the atom escapes from the lattice site, it can populate the higher bands and thus tunnel to the neighboring sites at a much faster rate. This implies that atoms must stay in the bottom few bands in order for the tunneling to be negligible, which can bring the effective number of scattered photons down by an order of magnitude [80].

There are also other heating mechanisms such as the lattice noise and the anti-trapping nature of the excited state. Therefore, at experimentally achievable lattice depths, in most cases one must cool the atoms while simultaneously scattering photons.

5.3.2 Polarization gradient cooling

Different atomic species require different cooling schemes to reach ultracold temperatures.

For atoms such as lithium, sodium and potassium, Raman sideband cooling in an optical lattice or tightly confining trap is commonly used [26, 27, 31, 46]. When the trap's oscillation frequencies exceed the two-photon transition linewidth, motional sidebands become resolvable, enabling the selective removal of vibrational quanta — similar to ion trap sideband cooling. This method is advantageous because it is not constrained by the small hyperfine structure of these atoms.

In contrast, polarization-gradient cooling is particularly effective for species like rubidium. This technique relies on well-resolved hyperfine structure in the excited state, which allows for efficient cooling using available laser wavelengths, making polarization-gradient cooling a natural and effective choice for our quantum gas microscope.

In a two-level system, Doppler cooling arises when a laser is tuned below the atomic transition frequency. When the Zeeman levels of the ground state atom are considered, temperatures much lower than the Doppler limit can be achieved. One famous realization is the laser cooling with two counter-propagating beams with orthogonal linear polarizations. It works for both free and bound atoms [103]. The local polarization of the light field changes along the direction of light propagation, so these types of sub-Doppler cooling schemes are named polarization gradient cooling.

$\sigma^+ - \sigma^-$ configuration

A more well-known example of polarization gradient cooling is the $lin \perp lin$ configuration. Two counter-propagating beams with orthogonal linear polarization create a spatial polarization modulation. This configuration is well explained in many textbooks and is often referred to as "Sisyphus cooling" [104].

In our experiment. we use the $\sigma^+ - \sigma^-$ configuration for our polarization gradient cooling where two beams with orthogonal circular polarizations propagate along opposite directions towards the atoms.

The resulting polarization field is a pure rotation of linear polarization. In this "corkscrew" polarization case, for a $J = 1$ to $J' = 2$ optical transition, an atom at rest is optically pumped into a distribution of ground states having alignment (different populations for states with different $|m|$) along the polarization axis but no orientation (asymmetry of positive and negative m-level population). When the atom moves parallel to the laser-propagation axis at a finite velocity, an orientation develops along this axis due to the non-adiabaticity for the atomic state to follow the optical pumping. The population asymmetry is such that the most populated state is the one that absorbs light most strongly from the circularly polarized wave opposing its motion. The asymmetry in the absorption accounts for the damping force in this cooling scheme [105].

Five beams

Polarization gradient cooling is clear to model in one dimension, but as it becomes three-dimensional, the beams running in different axes can interfere with each other and create a complicated polarization pattern. Nevertheless, the cooling still works quite effectively despite of the convoluted 3D polarization pattern.

One challenge in polarization gradient cooling under the microscope is the limited optical access. As shown in Fig. 5-1, we implement five-beam scheme to cool the atomic cloud in all three directions.

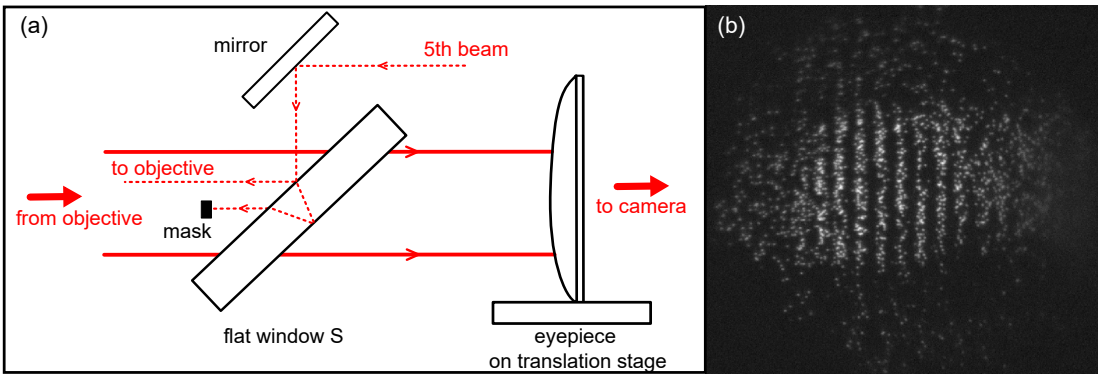

Figure 5-3: **Optical beam path for the fifth molasses beams propagating through the objective.** (a) The solid red lines indicate the beam path for imaging, while the dashed red lines represent the path of the fifth molasses beam (vertical) directed toward the objective. Window S is a 3-inch interference flat with anti-reflection coatings on both sides, optimized for 780 nm. Consequently, more than 99% of the 780 nm light transmits through the window, ensuring that it does not affect the imaging photon collection efficiency. However, a small fraction of the fifth beam, also at 780 nm, can still be weakly reflected. This faint reflection is focused near the atoms by the objective, generating enough intensity for cooling in the vertical direction. It is crucial to mask off the superfluous spot created by reflections from the back surface to mitigate unwanted interferences. (b) The fluorescence image when the extra reflection spot is left unblocked.

Cooling in the horizontal plane is relatively straightforward, we use counter-propagating beams with opposite circular polarizations in two orthogonal directions. However, in the vertical direction, since we cannot launch a beam toward the microscope as it cannot be separated from the fluorescence photons, we send a beam through the microscope. This is similar to some rubidium microscopes that have used [25, 82, 85]. Some other rubidium microscopes have mentioned that they were

able to use only four beams to cool the cloud in all three directions by creating a significant angle and projection in the vertical direction [106]. Fig. 5-3 shows the optical setup for the 5th beam. We use an interference flat coated for anti-reflection on 780 nm to couple in the cooling light. The flatness guarantees that no noticeable transmission wavefront aberration is introduced for the imaging beam. Although the reflection of the anti-reflection coating is fairly weak, the 5th beam get focused by the objective to significantly increase its beam intensity at the atom position.

One thing to note is that there will be a surplus reflection of the back side of the flat window. This beam has the similar intensity as the main one reflecting off the front surface. Together these two beam will get focused by the objective onto the atom and will interfere to generate a long-period lattice. This intensity modulation of the cooling beam result in a temperature modulation in the final cooling temperature and will cause a loss of atoms as shown in the fluorescence image in Fig. 5-3 (b). It can be avoided by placing a small mask to block the extra reflection fully and prevent interference from happening.

Since the added mask is close to the center of the imaging beam path, it only blocks a tiny fraction of the frequency information close to the DC component. So it will not introduce a noticeable degradation to the final image resolution.

Power and detuning

The power and size of the beam ultimately determine the intensity of the cooling light. Along with the detunings, they set the scattering rate:

$$\Gamma_{\mathrm{sc}} = \frac{\Gamma}{2} \cdot \frac{s_{\mathrm{tot}}}{1 + s_{\mathrm{tot}} + \left(\frac{2\Delta}{\Gamma}\right)^2}, \tag{5.3}$$

where Γ is the natural decay rate of the transition, s_{tot} is the total saturation parameter, which depends on the intensities of all the beams used for cooling, and Δ is the detuning from resonance.

The total five beams are derived from the MOT cooling light in the main chamber and have $\sim$ 100 Hz frequency offsets in each direction to prevent unwanted mutual

interference across different orthogonal directions. Overall, they have a global red detuning Δ on the order of tens of MHz with respect to the transition. Note that the global red detuning Δ includes the differential AC stark shift from the optical lattices and light sheet. At $\sim 3000\ E_\mathrm{r}$ in each trap direction, this differential AC stark shift is on the order of tens of MHz. To have an optimal cooling performance in the final experiment, both the power and detuning of each beam are scanned as we monitor the molasses lifetime of the atoms cooled in the deep pinning lattice.

Bias field

The polarization gradient cooling is able to achieve sub-Doppler temperature.

Whether it is the Sisyphus scheme (lin $\perp$ lin) or the $\sigma^+ - \sigma^-$ configuration in our system, it relies on the degeneracy of the ground levels of the atoms. At finite bias field, the Larmor precession frequency of the atom can be of the same order of magnitude as the optical pumping rate, leading to competition between the two processes. As a result, Larmor precession interferes with optical pumping and disrupts polarization gradient cooling [105].

Therefore, careful control of the bias field at the atom position is crucial for achieving optimal cooling performance. We use three independent bias coils around the science chamber to control the bias field in the x, y, and z directions. Each pair of bias coils is capable of generating a field of a few Gauss. The optimal bias field is found to be in the tens of mG range rather than at zero field.

We use a Glan-Taylor polarizer to clean the input beam polarization of the 1064 nm light, minimizing any vector AC Stark shift that may arise from residual circularity in the optical lattice. However, it does not significantly affect the optimal bias field at which the lifetime is the longest. We do not fully understand why the bias field that yields the best molasses lifetime is not at zero field.

Lifetime

All cooling parameters are optimized while monitoring the lifetime of total atom loss in deep pinning lattices. The atomic sample, either a Bose-Einstein condensate

(BEC) or a thermal gas, is first prepared. The pinning lattices and light sheet are then quenched to full power, followed by the activation of the polarization-gradient cooling beam and repump light. The cloud is held under these conditions for a set duration before the cooling and trapping beams are suddenly switched off. Absorption imaging is immediately performed from a side viewport.

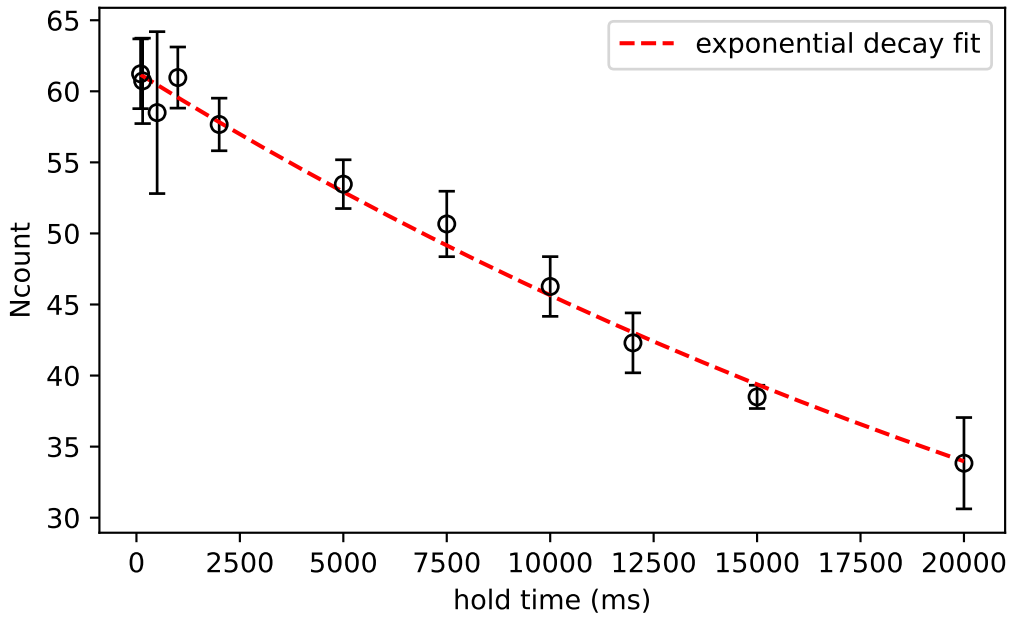

Figure 5-4: **Lifetime of total atom loss in deep pinning lattices under optimal polarization-gradient cooling, measured via absorption imaging.** We measure the total atom number decay as a function of the hold time while the atoms are confined in a combination of deep lattices and a light sheet. During this hold time, both the polarization gradient cooling and the repump light remain on. The black circles (with error bars indicating the standard deviation from three repeated runs) represent the measured data. The red dashed line is an exponential decay fit, yielding a lifetime of 34 seconds.

From the absorption imaging, we can extract a quantity proportional to the total atom number. As shown in Fig. 5-4, the number of atoms remaining after molasses cooling in the deep pinning lattice decays exponentially with the hold time. An exponential fit yields a lifetime of 34 seconds, which is comparable to the vacuum-limited lifetime.

Note that optimizing the cooling parameters by monitoring the global atom number decay may not be the best approach for quantum gas microscope operation.

Ultimately, we aim to optimize the fidelity of a few hundred atoms, which is too few to be visible in an absorption image. Nevertheless, this serves as a good starting point and is very close to the optimal cooling parameters for fluorescence imaging.

5.4 Alignment procedure

In this section, I will discuss the alignment procedures of the microscope. First, I want to highlight the difficulty of the alignment process, which is twofold.

One challenge arises from the two-chamber design, as mentioned in Chapter 4. The delivery position of the tODT beam must be within the small field of view (about 100 μm $\times$ 100 μm) for the atoms to be imaged through the objective.

The second challenge is the lack of degrees of freedom for tuning the position and alignment of the objective. Typically, mounting the objective on a stage with translation and tilt control allows for precise alignment with the atoms. However, in our case, we prioritized stability over tunability by placing the objective directly on top of the viewport window. As a result, we have no freedom to move the objective to align with the atoms. Instead, we must move the atoms to the focal plane and optical axis of the objective, which is challenging because it requires coordinating the realignment of all involved laser beams. This makes the alignment procedure significantly more time-consuming, as optimizing one parameter often necessitates realigning multiple beams.

5.4.1 Coarse alignment

The goal of the coarse alignment is to align the optical axis of the objective to the axis defined by the vacuum viewport in the re-entrant bucket.

Guide beam

To identify the optical axis of the viewport, we first made a mask centered on the vacuum viewport assembly. Then, we launched a visible laser beam through the center of this mask. We adjusted the beam's propagation direction until its faint

retroreflection aligned with itself. At that point, the beam was both centered on the chamber and normal to the surface of the viewport. We refer to this as the guide beam.

Next, we placed a mask directly on top of the objective, indicating its center. The objective was then positioned on top of the viewport as designed, aligning the center of the mask with the guide beam.

A mirror was then placed in the beam path, causing the guide beam to back-propagate. The imaging optics, including the eyepiece and folding mirrors, were installed and aligned to the back-propagating guide beam.

Masks were also used to indicate the center of the chamber for side imaging. When determining the delivery position of the tODT beam, we used absorption imaging from the side to align the delivery position with the center of the mask. We specifically chose to use a vacuum bellow connecting the main chamber and the science chamber, as it provides great flexibility for coarse tuning the separation and the height between the two chambers.

5.4.2 Fine alignment

For coarse alignment, we determine the optical axis within a range of hundreds of micrometers using geometric masks. For fine alignment, we ultimately use the atoms to position the cloud precisely along the optical axis.

A trick of using the repump light

This method is inspired by the rubidium quantum gas microscope at the University of Strathclyde [25]. After using the guide beam to define the optical axis of the system, we align another beam path to it. This secondary beam path can serve as the fifth molasses beam or be used for fine alignment by introducing repump light, simply by swapping the light source at the fiber input without disturbing the alignment.

When sending the repump light through the objective along the optical axis, we perform an absorption image. Since the objective focuses the repump light to a small

spot (30–μm), only the region intersecting with the repump light will be illuminated and produce a signal in the absorption image. We use the atoms loaded in the tODT as the sample, as it forms an elongated target that spans a large search space and can be easily translated in the horizontal plane using the beam displacer.

After aligning the tODT to the optical axis defined by the repump light, we align all other laser beams to this position, including the anti-ODT, the light sheet, the horizontal molasses beams, and all the optical lattice beams.

Using spherical aberration as an indicator

The technique of using the repump light aids in aligning the atoms to the position where the optical axis intersects with the horizontal plane. However, it does not ensure that the cloud is at the correct vertical position, i.e., the optimal distance at which the atoms are focused with minimal aberration.

The objective is designed for a working distance of 6.5 mm in vacuum, meaning the atoms should be positioned 6.5 mm away from the vacuum-side surface of the viewport. However, due to the viewport thickness not being precisely 5 mm and the global defocus aberration induced by atmospheric pressure on the viewport, the optimal working distance deviates from the design value and must be experimentally determined through scanning.

In principle, at any working distance within a reasonable range, the fluorescence image of the atoms can be refocused by adjusting the distance between the eyepiece and the camera. However, in experiments, we observed that when the atom position deviates significantly from the optimal working distance, the resulting atom image exhibits pronounced spherical aberration when it is slightly defocused. This aberration manifests as a symmetrical concentric ring surrounding a central spot, a phenomenon confirmed by both the SNOM tip test and Zemax simulations.

When the atoms are at the correct focal plane, slight defocusing reveals other aberrations, such as residual astigmatism or coma, which often lack rotational symmetry. When the atoms are not at the correct focal plane, they can still be brought into focus on the camera. However, in this case, slight defocusing results in the ap-

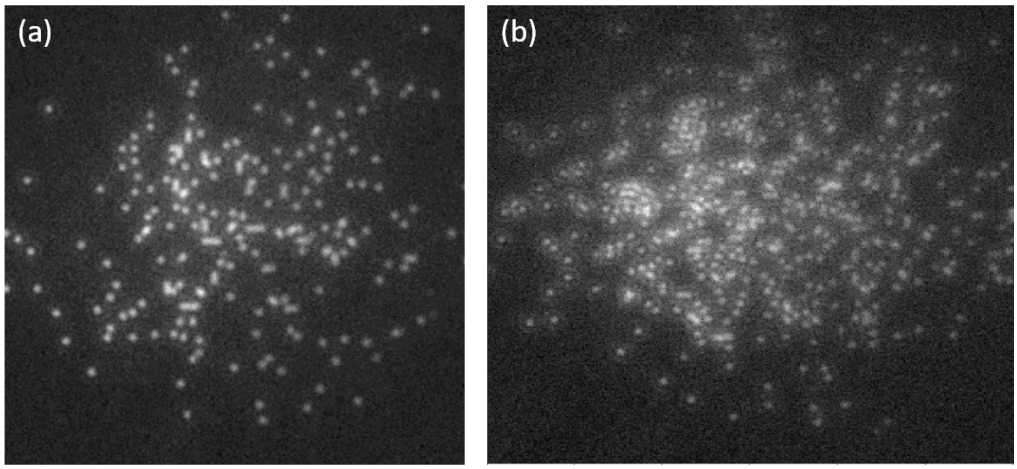

Figure 5-5: **Using the spherical aberration as an indicator to find the right focal plane.** When the atoms are not at the correct focal plane, they can still be brought into focus on the camera as shown in (a). However, in this case, slight defocusing results in the appearance of a symmetric ring, indicating that spherical aberration dominates all other aberrations as shown in (b).

pearance of a symmetric ring, indicating that spherical aberration dominates all other aberrations. This effect is demonstrated in Fig. 5-5.

It is useful to examine how spherical aberration is induced. While defocusing can be achieved by moving the camera closer or further, only one direction will lead to the ring-like aberration as shown in Fig 5-5(b), whereas the other direction will cause blurring without concentric rings. This asymmetry provides a diagnostic tool for determining the direction in which the atoms should be moved to reach the correct focal plane.

In our system, we found that if spherical aberration is induced by decreasing (increasing) the distance between the camera and the eyepiece, it indicates that the atoms are too far from (too close to) the objective. This sign relation has been verified through both the SNOM test and Zemax simulations and is used to align the atoms to the focal plane. When the atoms are correctly positioned at the focal plane, defocusing in either direction no longer produces concentric ring-like aberrations, as spherical aberration is no longer the dominant aberration.

5.5 Fluorescence imaging

5.5.1 Optical setup

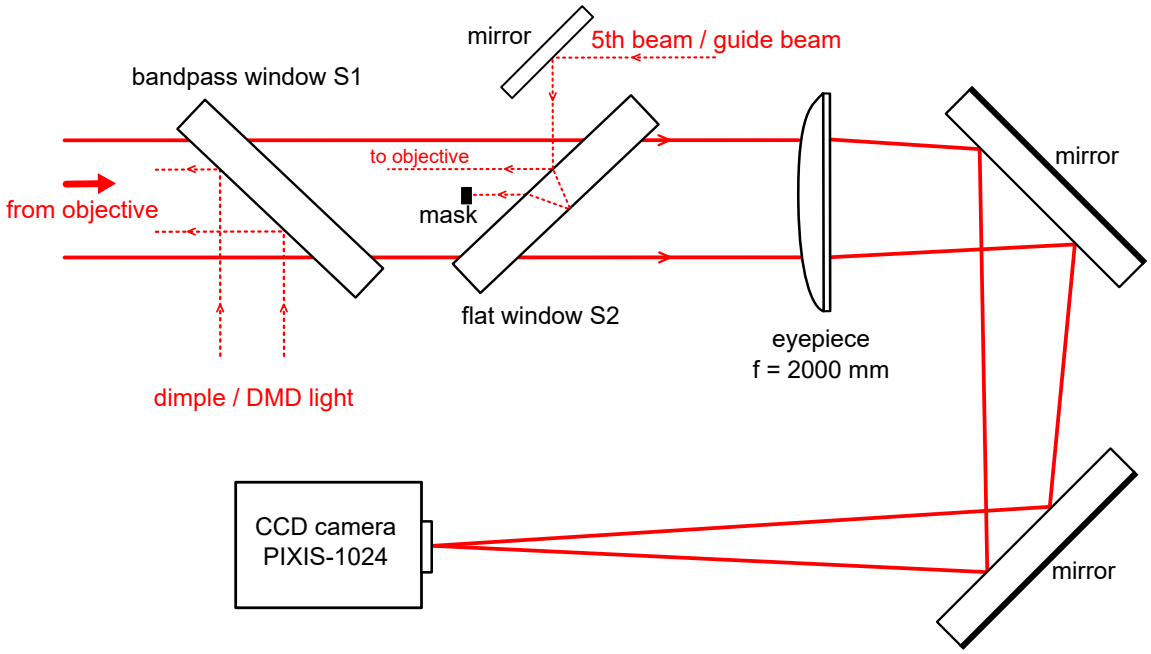

Figure 5-6: **Illustration of the imaging system layout of the microscope.** Window S1 is a specially coated optical flat with a surface flatness of $\lambda/10$. The side facing the objective is coated with an anti-reflection (AR) coating at 780 nm, while also reflecting 532 nm, 640 nm, 671 nm, 840 nm, and 1064 nm. The opposite side has a broadband AR coating optimized for 780 nm. As a result, this window selectively transmits only the imaging light at 780 nm while reflecting other wavelengths. This design enables potential future upgrades, such as introducing projection light through a digital micromirror device (DMD).

Figure 5-6 illustrates the complete optical layout of the imaging system. A key parameter in designing the imaging system is the focal length of the eyepiece, which determines the overall magnification. Since the camera sensor consists of discrete pixels, the magnification must be chosen carefully in relation to the pixel size. If the magnification is too small, the image of a single lattice site may be smaller than one pixel, making it impossible to resolve any spatial structure. This is acceptable in some optical tweezer experiments, where the goal is to concentrate all photons onto a single pixel and the shape of the point spread function is irrelevant. In our case, however, we require spatial information for image deconvolution and reconstruction,

and thus must resolve the point spread function. Conversely, if the magnification is too large, the point spread function extends over too many pixels, reducing the signal-to-noise ratio per pixel due to the fixed readout noise of the sensor.

We use the PIXIS-1024 CCD camera from Princeton Instruments, which has a pixel size of 13 μm. To balance spatial resolution with signal-to-noise performance, we choose a magnification of 62.6. Under this magnification, each pixel corresponds to approximately 200 nm $\times$ 200 nm in the object plane. Given that the objective has an effective focal length of 30 mm, achieving this magnification requires an eyepiece with a focal length of 2 m.

The exit pupil of the objective is approximately 40 mm in diameter. To avoid vignetting and ensure full light collection, we use 3-inch diameter optics throughout the imaging path, including the eyepiece. At an f-number greater than 20, a plano-convex lens used as the eyepiece is already diffraction-limited and sufficient for our imaging requirements.

Although the lens groups in the objective are coated to minimize reflection at 780 nm, a small amount of retro-reflected 780 nm light from the fifth beam can still reach the camera. This stray light is weak and remains stable from shot to shot. To account for it, we take an additional image without atoms in each experimental sequence and subtract it from the fluorescence image, effectively removing background contributions.

To further suppress stray light at other wavelengths during the long exposure, we place two interference filters (SEMROCK LL01-780-25) in front of the camera. These filters are designed to transmit only 780 nm light, thereby reducing noise from off-resonant illumination.

5.6 Reconstruction algorithm

The raw fluorescence images obtained by the quantum gas microscope needs to be converted to a two-dimension boolean matrix. Each matrix entry corresponds to an individual lattice site with 0 being empty and 1 being one. Due to the parity-

projection effect, the occupation number measured by the quantum gas microscope can only be either 0 or 1.

A reconstruction program is essential in running a quantum gas microscope. It takes in the raw fluorescence images, processes them, and outputs boolean matrices containing the lattice occupation information for each image. Depending on the β factor, different groups may adopt different types of reconstruction programs. For a typical β value between 1 and 1.5, deconvolution-based reconstruction algorithms are often used. However, for extreme β value exceeding 2, novel algorithms based on unsupervised learning have been demonstrated [33].

The reconstruction program used by the BEC4 quantum gas microscope is inspired by the architecture originated from Munich implemented through MATLAB [82,102]. We have developed our own version based on Python for versatility and to better integrate it into our existing workflow.

Simulation of the fluorescence images

One might think simulating the fluorescence images is not an essential part of the reconstruction algorithm. However, a good simulation can be used to benchmark the performance of the reconstruction algorithm. The robustness and the overhead of the program can be tested by introducing noises, inhomogeneities, and additional blurring [102]. It may become helpful if one is interested in implementing a machine-learning-based reconstruction algorithm [33] as the simulation can easily generate a lot of data for training. More importantly, when I was developing the reconstruction program for BEC4, we did not have good experimental fluorescence images so simulations were a must.

As shown in Fig. 5-7, we can simulate fluorescence images with various effective NAs. Due to the residue aberrations and imperfections, the final performance of the microscope may not reach the full specification of NA $= 0.8$. This simulation can be used to estimate the overhead we have before the imaging performance degrades too much. When the NA reduces below 0.5, it is hard to resolve the density distribution even for sparsely populated lattices.

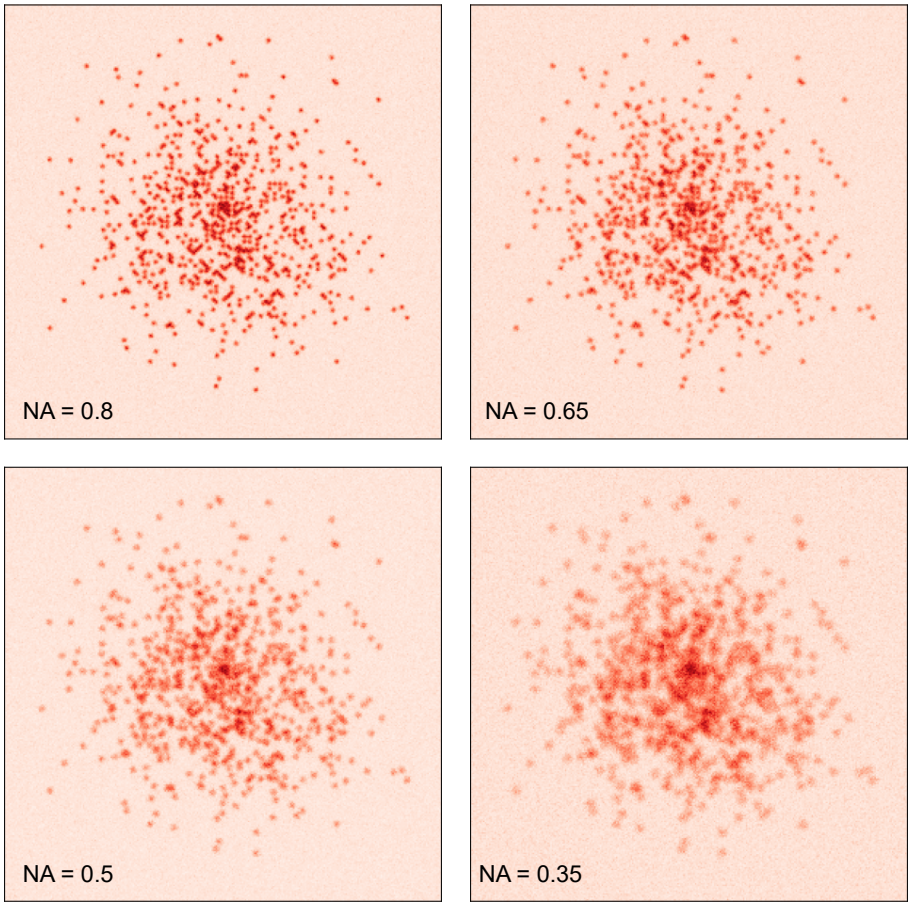

Figure 5-7: **Simulated fluorescence images with variable numerical apertures.** By convolving a point-spread function with the lattice occupation matrices, we can simulate fluorescence images. Here, we use a Gaussian distribution to model the cloud and Airy disk to model the point-spread function. To make the simulation more realistic, noise is added to the image, including readout noise and shot noise generated from the fluorescence signal and the background light. The atom distribution are kept to be the same across the four pictures, while Airy disks are changed via effective NAs. Even in the ideal case where the effective NA reaches 0.8, neighboring atoms cannot be directly resolved. As the effective NA decreases, the resulting images become increasingly blurred.

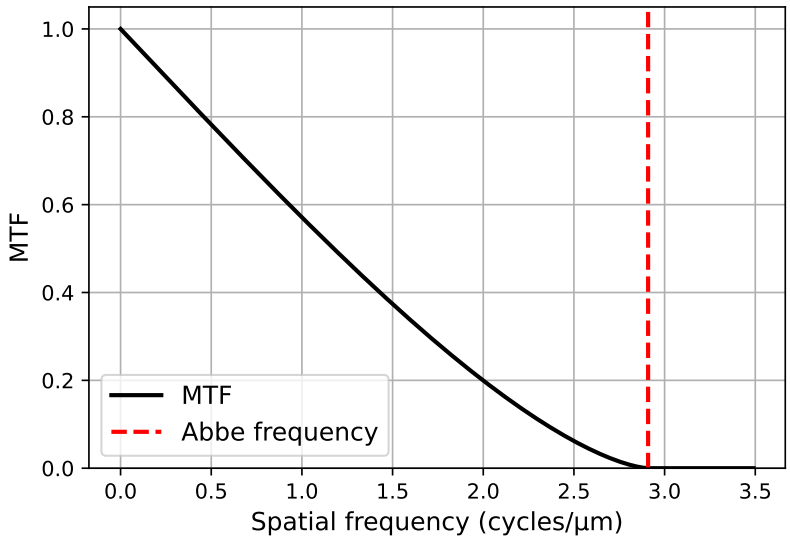

Figure 5-8: **Modulation transfer function of a diffraction-limited imaging system with a numerical aperture (NA) 0.8.** The black curve is the analytical solution of the modulation transfer function for a diffraction-limited circular aperture. The red dashed line indicates the location of the Abbe frequency $2\text{NA}/\lambda$.

Low-pass filter

In Chapter 3, we have discussed various criteria for determining the spatial resolution of a diffraction-limited imaging system. Although Rayleigh's criterion is more often used in the spatial domain, Abbe's expression is more relevant in the frequency domain.

As shown in Fig. 5-8, the modulation transfer function (MTF) of an imaging system acts like a low-pass filter. In the object space, any spatial frequency components higher than a cuf-off frequency have zero amplitude in the in the image space. The cut-off frequency, known as the Abbe frequency $f_{\text{Abbe}} = 2\text{NA}/\lambda$. The Abbe frequency has an intuitive interpretation: it corresponds to the highest spatial frequency that can be generated by two parallel beams striking the aperture edges of an ideal lens. At the focal plane, the Abbe frequency represents the spatial frequency of the resulting interference pattern.

Therefore, any frequency component higher than the Abbe frequency cannot originate from the atoms. Most high-frequency noise arises from the camera's readout noise. The first step is to apply a low-pass filter to clean the raw fluorescence images.

We perform a Fourier transform, set all amplitudes beyond a certain frequency to zero, and then transform the images back for further processing. To account for the finite signal-to-noise ratio, we set this cutoff frequency slightly below the theoretical limit defined by the Abbe frequency.

5.6.1 Deconvolution

As shown in Fig. 5-7, even in the ideal case where the effective NA reaches 0.8, neighboring atoms cannot be directly resolved. This is a common regime where a lot of the quantum gas microscopes operate at. Thus, a deconvolution algorithm is often required to reduce the blurring caused by the wave nature of light.

We consider an imaging system where the recorded image $I(x, y)$ is the convolution of the object $S(x, y)$ and the system's point-spread function (PSF) $p(x, y)$. Mathematically:

$$I(x,y) \;=\; (S * p)(x,y) \;=\; \int_{-\infty}^{\infty}\int_{-\infty}^{\infty} S(x',y')\, p\big(x-x',\, y-y'\big)\, dx'\, dy'. \tag{5.4}$$

Each point (x', y') of the object contributes to (x, y) in the image, weighted by the PSF.

We define the 2D Fourier transform of a function $f(x, y)$ by:

$$\mathcal{F}\{f(x,y)\} \;=\; \hat{f}(k_x,k_y) \;=\; \int_{-\infty}^{\infty}\int_{-\infty}^{\infty} f(x,y)\, e^{-i\,2\pi\left(k_x\,x+k_y\,y\right)}\, dx\, dy. \tag{5.5}$$

Then for our functions,

$$\hat{I}(k_x,k_y) = \mathcal{F}\{I(x,y)\}, \quad \hat{S}(k_x,k_y) = \mathcal{F}\{S(x,y)\}, \quad \hat{p}(k_x,k_y) = \mathcal{F}\{p(x,y)\}.$$

A key property of the Fourier transform is the convolution theorem, which states:

$$\mathcal{F}\{S * p\} \;=\; \hat{S}(k_x,k_y)\,\hat{p}(k_x,k_y). \tag{5.6}$$

Hence, taking the Fourier transform of both sides of Eqn. 5.4, we obtain

$$\hat{I}(k_x, k_y) \;=\; \hat{S}(k_x, k_y)\,\hat{p}(k_x, k_y). \tag{5.7}$$

In real space, convolution "mixes" values of S and p as we shift one function over the other. However, in the Fourier domain, these shifts and integrations correspond to simple products of the respective Fourier transforms.

At a glance, one may think it is possible to just inverse Eqn. 5.7 to obtain the Fourier transform of the object information $S(k_x, k_y)$ since $\hat{I}(k_x, k_y)$ and $\hat{p}(k_x, k_y)$ are both known. However, in practice, the observed image $I_{\text{obs}}(x, y)$ also contains noise $n(x, y)$ even after low-pass filtering:

$$I_{\text{obs}}(x, y) \;=\; (S * p)(x, y) + n(x, y), \tag{5.8}$$

and in Fourier space,

$$\hat{I}_{\text{obs}}(k_x, k_y) \;=\; \hat{S}(k_x, k_y)\,\hat{p}(k_x, k_y) + \hat{n}(k_x, k_y). \tag{5.9}$$

If we perform the inverse without suppressing the noise:

$$\frac{\hat{I}_{\text{obs}}(k_x, k_y)}{\hat{p}(k_x, k_y)} \;=\; \hat{S}(k_x, k_y) + \frac{\hat{n}(k_x, k_y)}{\hat{p}(k_x, k_y)}. \tag{5.10}$$

As shown in Fig. 5-8, the point-spread-function has zero amplitude beyond the Abbe frequency, which means singularity will occur in Eqn. 5.10 due to a division of zero.

To suppress the singularity that occurred in the inverse deconvolution, we add a regularizer to avoid the division by zero:

$$\hat{S}_{\text{reg}}(k_x, k_y) = \frac{\hat{I}_{\text{obs}}(k_x, k_y)}{\hat{p}(k_x, k_y) + \epsilon \times h(k_x, k_y)}, \tag{5.11}$$

where ϵ is the regularizer that controls the degrees of regularization and $h(k_x, k_y)$ is a filter function that is designed to have high-pass properties [80]. In practice, we

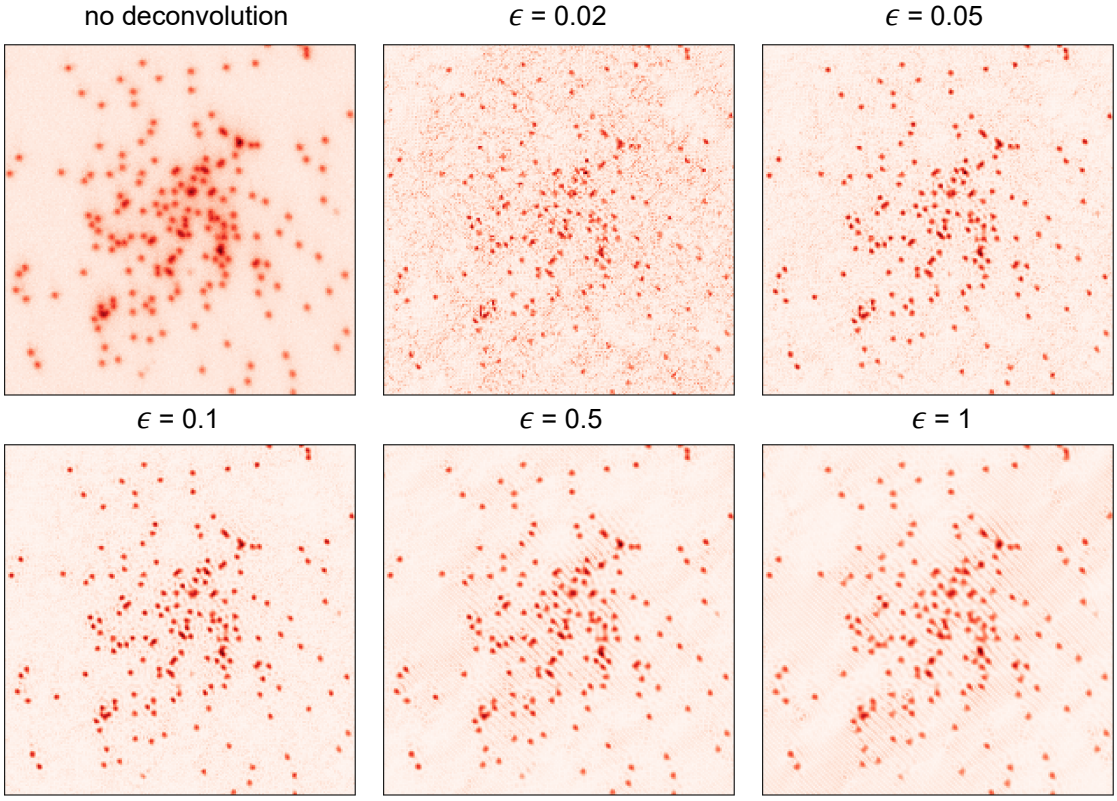

Figure 5-9: **Raw fluorescence image and its deconvolutions using various regularization filters.** The deconvolution process enhances the fluorescence image for further analysis. If the regularization parameter ϵ is too small, the deconvolution result becomes dominated by noise. Conversely, if ϵ is too large, high-frequency information of the point spread function is suppressed, leading to artifacts in the deconvolved image. An optimal range for the regularizer was determined to be between 0.05 and 0.1.

found that the exact detail of the function $h(k_x, k_y)$ does not play a significant role. The regularization is mainly adjusted by the magnitude of the regularizer ϵ.

As shown in Fig. 5-9, there exists an optimal value for the regularizer ϵ. When the regularization parameter ϵ is too small, the noise suppression is not enough and the resulting deconvolution image is completely dominated by noise. When the regularizer ϵ is too large, valuable high-frequency information of the point spread function is suppressed, leading to artifacts (fringes) in the deconvolved image. For our dataset, an optimal range for the regularizer was determined to be between 0.05 and 0.1.

5.6.2 Identify single isolated atoms

After deconvolution, the images are ready for the next stages of calibration to determine the underlying lattice structure. The core of this calibration process relies on the knowledge of the position of the single isolated atoms. Consequently, these calibrations are typically performed using images of sparsely populated lattices.

Binarization

To identify single isolated atoms, we first perform binarization of the image. Binarization is a process in which the pixel values are first normalized to the range [0,1], and then all pixels with values above a chosen threshold are set to 1, while the rest are set to 0.

As shown in Fig. 5-10, when the binarization threshold is low, the resulting image contains significant noise, as shot noise in the background can exceed the threshold and be misidentified as signal. This manifests as numerous small, disconnected white patches (objects). Conversely, when the threshold is too high, only the central regions containing strong fluorescence signals from multiple atoms exceed the threshold and are identified as 1. In this case, the resulting image contains fewer white patches.

This behavior can be quantitatively characterized by counting the number of small objects in the binarized image. An object is defined as a connected cluster of white pixels (1) that is enclosed by black pixels (0). Small objects are those with an area

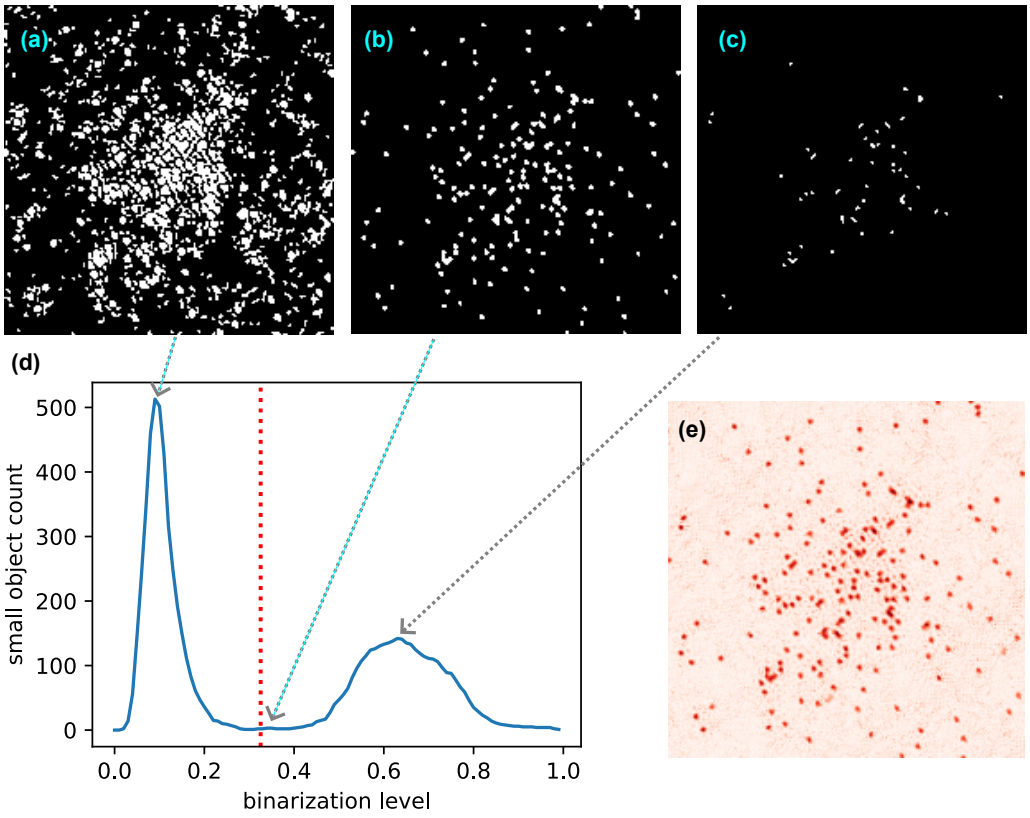

Figure 5-10: **Determining the optimal threshold for binarizing the image post-deconvolution.** (a)(b)(c) Binarized images with different threshold levels. (d) After binarization, we count the number of objects in the binarized image with an area smaller than 4 pixels, hence the label of the y-axis. As the binarization threshold varies, the number of small objects exhibits two peaks. The red dashed line indicates the optimal threshold, which is chosen as the midpoint between the two threshold values that produce local peaks. (e) Image before binarization but after proper deconvolution.

smaller than 4 pixels. As shown in Fig. 5-10, varying the threshold value results in a two-peak structure, which serves as a diagnostic tool for determining the optimal binarization threshold.

When choosing the threshold value in the middle of the two peaks, the binarized images shows a local minimum number of small objects. At this point, most of the objects are related to the atoms as their areas are larger than 4 pixels.

Identification of single isolated atoms

Binarization provides a coarse method for identifying signals that are highly likely associated with atoms. The next step is to select single, isolated atoms with high certainty while filtering out atom clusters and individual atoms that are too close to each other.

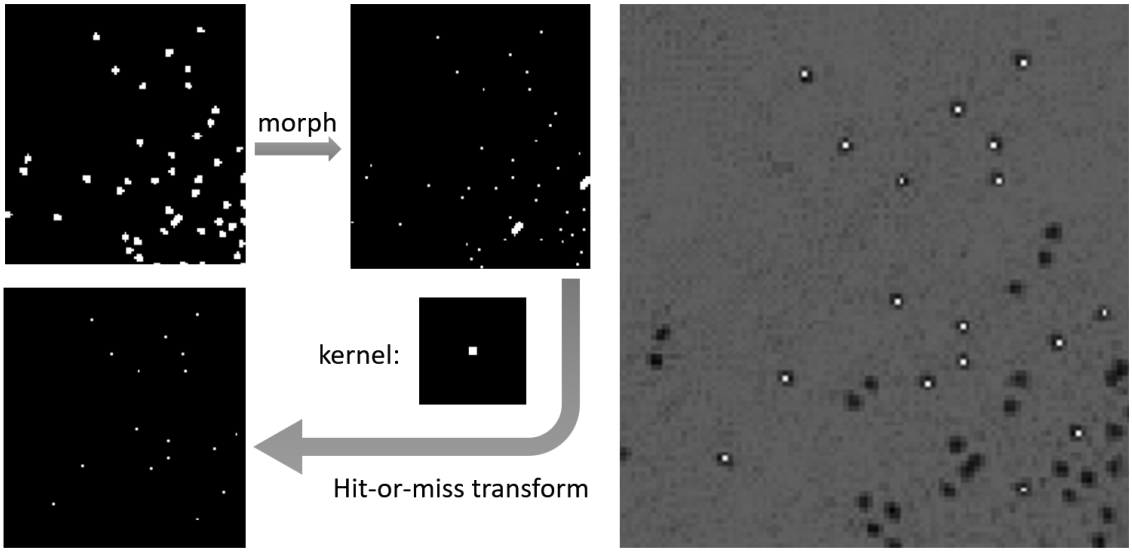

Figure 5-11: **Using hit-or-miss transform to identify single and isolated atoms.** The left panel illustrates the process of identifying the positions of single, isolated atoms. The right panel highlights these atoms using white pixels against the deconvoluted image (The single pixels in the subfigures are rendered and may show artificial blurring).

As shown in Fig. 5-11, we first filter out objects in the binarized image whose size exceeds 150% of the median size. These large objects typically correspond to clusters of multiple atoms. After this filtering step, we apply a morphological operation to reduce each remaining small object to a single pixel, whose location is determined by rounding the object's center of mass coordinates to the nearest integer.

Next, we apply a hit-or-miss transform using a kernel defined as a matrix of zeros with a single central element set to one. The matrix size corresponds to the effective radius used to define isolation — larger matrices improve atom isolation but reduce the number of available atoms.

After the hit-or-miss transform, we successfully identify a group of single, isolated

atoms. We then fit a two-dimensional Gaussian around each isolated atom and use the fitted Gaussian centers as more precise atomic coordinates, allowing for floating-point values.

5.6.3 Calibration

Lattice angle and constants

From the coordinates of the single, isolated atoms, we can compute their mutual distances. As shown in Fig. 5-12, the vector connecting two single, isolated atoms can be projected onto a given axis.

For example, consider a scenario in the camera frame where two single, isolated atoms have coordinates (x_1, y_1) and (x_2, y_2). We define the projection axis as one that is rotated by θ relative to the camera's x-axis. Then, the projected mutual distance d can be expressed as:

$$d = \left| \sqrt{(x_1 - x_2)^2 + (y_1 - y_2)^2} \cdot \cos\left(\arctan_{2Q} \frac{y_1 - y_2}{x_1 - x_2} - \theta \right) \right|, \tag{5.12}$$

where the $\arctan_{2Q}$ indicates the the 2-argument arctangent.

From a total of n identified single, isolated atoms, we can compute up to $n(n-1)/2$ mutual projected distances. When these distances are sorted into a histogram, a distinctive multi-peak structure emerges only when the projection axis aligns with the underlying lattice axis, as shown in Fig. 5-13. This occurs because the projected distances become integer multiples of the lattice constant.

To quantify the presence of a multi-peak structure in the histogram, we use the average height of the top 10 highest peaks as demonstrated in Fig. 5-13. This approach is intuitive since the total area of the histogram is conserved, so sharper peaks result in higher peak values.

One important consideration is that this calibration must be performed for both the x-axis and y-axis, as the underlying lattice may not be perfectly square but rather rhombic. This arises because when launching the x and y lattices, we did not ensure that the two beams were strictly perpendicular to each other. In our experiment, we

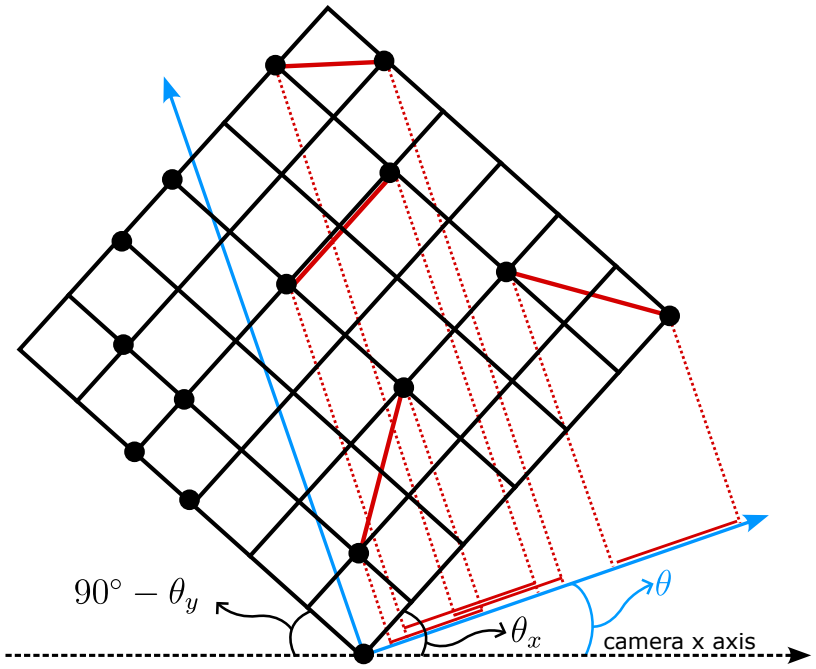

Figure 5-12: **Calibration for the pinning lattice angles and magnification.** In our case, the axes for the underlying square pinning lattice are rotated by roughly 45° with respect to the camera x-axis. The exact rotation angle θ_x and θ_y need to be calibrated independently. Note θ_x and θ_y are not necessarily identical, meaning the lattice geometry is parallelogram instead of square. To calibrate, we calculate the pair distances between the found single isolated atoms. Then the distances are projected onto another set of axes (blue) whose rotation angle θ is scanned. When $\theta = \theta_x$, the projected distances will show discrete distributions with sharp peaks located at multiples of the lattice period in the imaging plane. After fine tuning on the θ value, we determine the magnification from the period of discrete peaks in the projected distance distribution.

found $\theta_x \approx 42.6°$, $\theta_y \approx 44.2°$, where θ_x and θ_y are defined as shown in Fig. 5-12.

A more precise method for calibrating the lattice angles involves fitting an array of equally spaced, equal-height Gaussians to the histogram and minimizing the Gaussian width while scanning the angle [82, 85, 102]. We also implement this calibration, though it is more computationally intensive compared to the previously described scheme. The periodicity of this Gaussian array reveals the lattice constant in the image plane, from which we infer that our final magnification to be 62.6. Alternatively, the magnification can also be determined by Fourier transforming the histogram and identifying the most dominant frequency components [80].

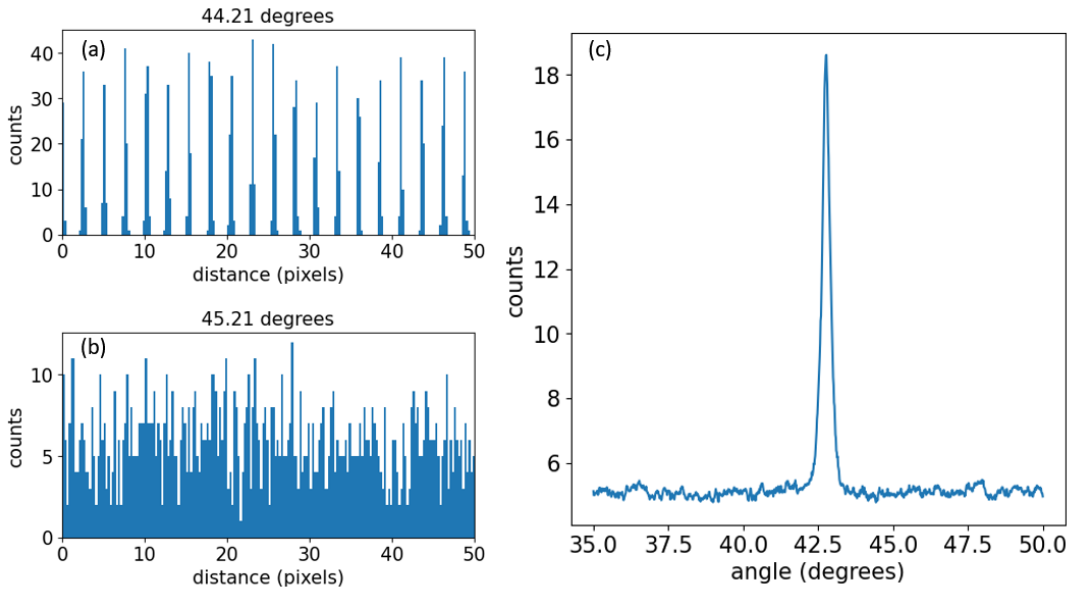

Figure 5-13: **Finding the angles of the underlying lattice.** When plotting the projected mutual distances into a histogram, a distinctive multi-peak structure appears if the projection axes align with the underlying lattice axis, as shown in (a). However, if the projection axes are misaligned, even a one-degree offset can wash out the multi-peak structure, as seen in (b). (c) When the histogram exhibits a multi-peak structure, the peak heights are higher compared to the misaligned case. The average height of the top 10 highest peaks serves as a reliable indicator for determining the underlying lattice angle.

Lattice phases

With the knowledge of the lattice angles and the lattice constant, we still need to determine the lattice origin (or phase) to fully define the underlying lattice structure.

The basis vectors spanning the lattice can be defined as:

$$\mathbf{v}_1 = a\,(\cos\theta_x\,\hat{\mathbf{e}}_x + \sin\theta_x\,\hat{\mathbf{e}}_y)$$
$$\mathbf{v}_2 = a\,(-\sin\theta_y\,\hat{\mathbf{e}}_x + \cos\theta_y\,\hat{\mathbf{e}}_y)$$

where a is the lattice constant in the image plane.

Given these basis vectors, we can generate a complete set of lattice grid points from each single isolated atom's coordinates. If everything were perfectly aligned, the generated lattice grids from each atom would overlap exactly. However, due to

imperfections in fitting atomic positions and residual field aberrations, these lattice grids exhibit small offsets relative to each other.

To define the lattice origin, we record the coordinates of the lattice site closest to the center of the camera as shown in Fig. 5-14. This choice is arbitrary, as the anchor point can be placed anywhere within the camera frame, but selecting the center is convenient. We repeat this process for each single isolated atom—generating a new lattice grid and recording the coordinates of the lattice site nearest to the camera center. Finally, we take the mean value of all recorded positions and define it as a representative lattice site, thereby determining the lattice origin (or phase).

Additionally, we compute the standard deviation of these coordinates for monitoring. If the standard deviation exceeds half a pixel, it suggests that the underlying lattice is not well-defined.

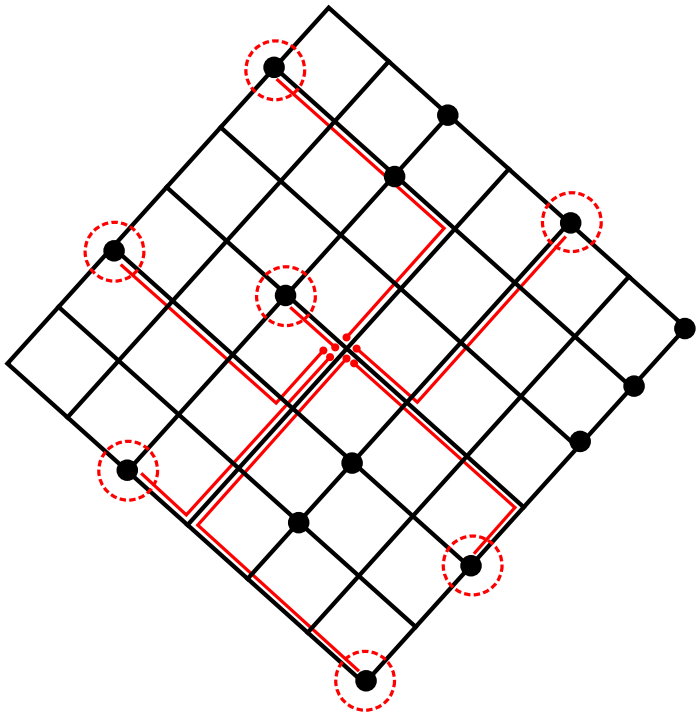

Figure 5-14: **Calibration for the underlying pinning lattice origin.** We start with the center coordinates of the found single, isolated atoms, indicated by the red dashed circle. With the calibrated lattice angle and constants, we span from each single, isolated atoms a set of underlying lattice and register the site coordinate that is closest to the camera center. This coordinate is the lattice origin linked to this specific isolated atom. The process is looped through all the found single, isolated atoms. The mean of each found lattice origin is used as the final lattice origin.

A side note related to the lattice phase: as mentioned in the previous chapter, floating the table is crucial for achieving a stable imaging condition. With the full capability of the reconstruction algorithm, we can take two consecutive images and track the absolute center positions of the same atom. For images taken 1.5 seconds apart, we confirm that the center of the same atom shifts by less than 100 nm in the atomic plane.

In this sense, the reconstruction algorithm ultimately makes the quantum gas microscope conceptually super-resolved, as the positions of atoms can be determined with a precision far exceeding the optical resolution limit.

5.6.4 Threshold

Ultimately, the reconstruction algorithm for the microscope images is a nonlinear process that reduces dense analog fluorescence information into binary (0 or 1) occupation values. This can be viewed as a classification problem: determining whether a given lattice site is occupied or empty.

With all lattice calibrations completed, we discretize the raw fluorescence images into individual lattice sites and sum the total signal at each site. We assign a 3×3 pixel matrix centered on the rounded coordinates of each lattice site. In an ideal case with infinite resolution and signal-to-noise ratio, one would count all photons within the Wigner–Seitz cell. However, in our setup, the 532 nm lattice constant maps to 2.56 pixels in the camera plane, based on the system's magnification and pixel size. As a result, a 3×3 matrix inevitably includes contributions from neighboring sites.

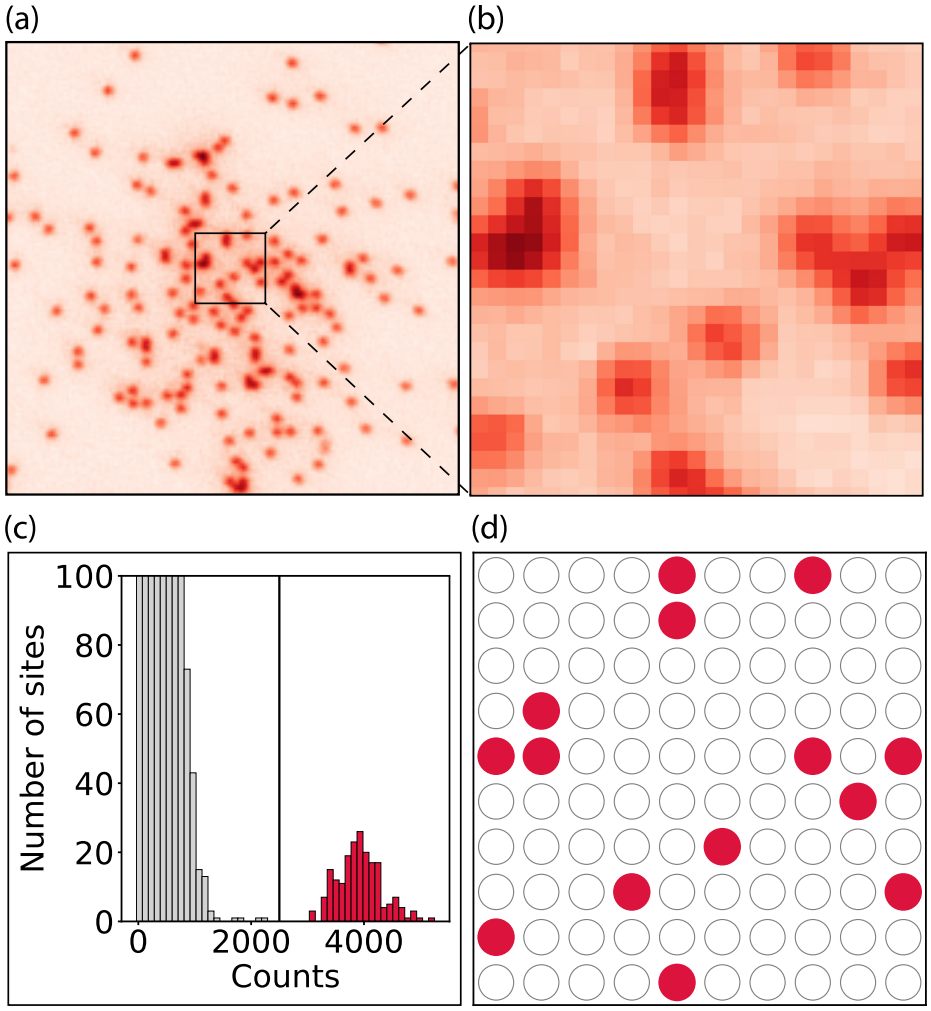

Figure 5-15: **From raw a fluorescence image to a reconstructed lattice site occupation.** (a) A typical raw, dilute fluorescence image with good signal-to-noise is shown. (b) We show a magnified view of a small region of the raw image, depicted for illustration purposes. (c) We bin pixel counts on a given lattice site and then generate a histogram showing the number of lattice sites with a given count value. The majority of lattice sites are unoccupied since the sample is dilute, as shown in the left peak of the histogram. The occupied lattice sites are shown in the right peak of the histogram in red. Based on this histogram, we determine a threshold (black vertical line), above which lattice sites are considered occupied. (d) We depict the digitized version of lattice site occupation, termed the "reconstructed" image. Lattice sites filled in red are occupied, while unshaded circles are unoccupied lattice sites.

To address the issue of signal crosstalk from neighboring sites, we apply a Gaussian-weighted sum centered at the precise (non-integer) lattice coordinates. This not only corrects for rounding errors when the lattice site center lies between pixels but also

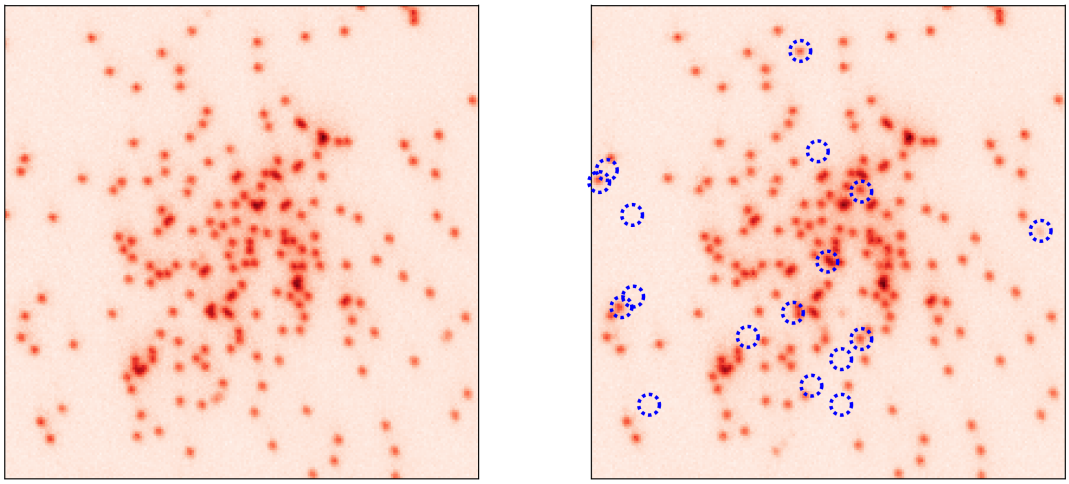

Figure 5-16: **Two consecutive exposures separated by 1.5 seconds.**The left image was taken first, followed by the right image 1.5 seconds later. The similarity between the two images demonstrates the long lifetime necessary for the long exposure time. A few loss and hopping events are visible in the second image, highlighted by dashed blue circles. Both images are raw fluorescence images without deconvolution.

assigns greater weight to the signal originating from the target site while suppressing contributions from neighboring sites. As a result, the histogram of photon counts per site exhibits a well-separated bimodal distribution: the lower peak corresponds to empty sites, and the higher peak to occupied ones. A threshold is then placed between the two peaks to distinguish occupation, as shown in Fig. 5-15(c).

Fidelity

As described in the previous sections, we have the ability to simulate fluorescence images to benchmark the accuracy of the reconstruction algorithm. By simulating images using the measured atomic point-spread function and a comparable noise level, and then feeding these simulated images into the reconstruction pipeline, we can compare the reconstructed lattice occupations with the known ground truth of the simulation. We find that, for sparsely populated samples as shown in Fig. 5-15, the reconstruction algorithm achieves an accuracy exceeding 99%.

In addition to potential inaccuracies from the reconstruction algorithm, a more

significant source of infidelity arises from the physical processes during imaging. During the one-second exposure, atoms may either hop to neighboring sites or be lost entirely. To monitor these effects, we take two consecutive fluorescence images in the sequence, separated by 1.5 seconds due to the CCD camera readout time. Two typical images are shown in Fig. 5-16. By comparing the differences in the reconstructed occupations between the two images, we find that approximately 5% of the atoms either hop or are lost in the second image, indicating an overall fidelity of 95%.

Chapter 6

Correlations in the Bosonic Fields

The following two chapters provide a detailed discussion of the scientific project enabled by the quantum gas microscope: the *in situ* measurement of bosonic bunching. We would like to place our experimental contribution into the broader reference frame of the long history of the Hanbury Brown and Twiss experiments. This chapter focuses on developing a conceptual understanding of bosonic correlations, while the next chapter presents the experimental methods and results.

6.1 Hanbury Brown and Twiss experiment

6.1.1 A tale of two interferometers

In modern astronomy, Michelson interferometry is the predominant technique for directly measuring stellar diameters. This method relies on coherently combining light collected from multiple apertures, and the visibility of the interference fringes contains information about the angular size of the star. Because Michelson interferometry involves the interference of the fields, it is sensitive to variations in optical path length or phase. Even small changes can wash out the interference fringes. In practice, Earth's atmosphere introduces rapid and random phase fluctuations, commonly known as "seeing", which pose a significant challenge to maintaining stable interference over long baselines or extended observing periods.

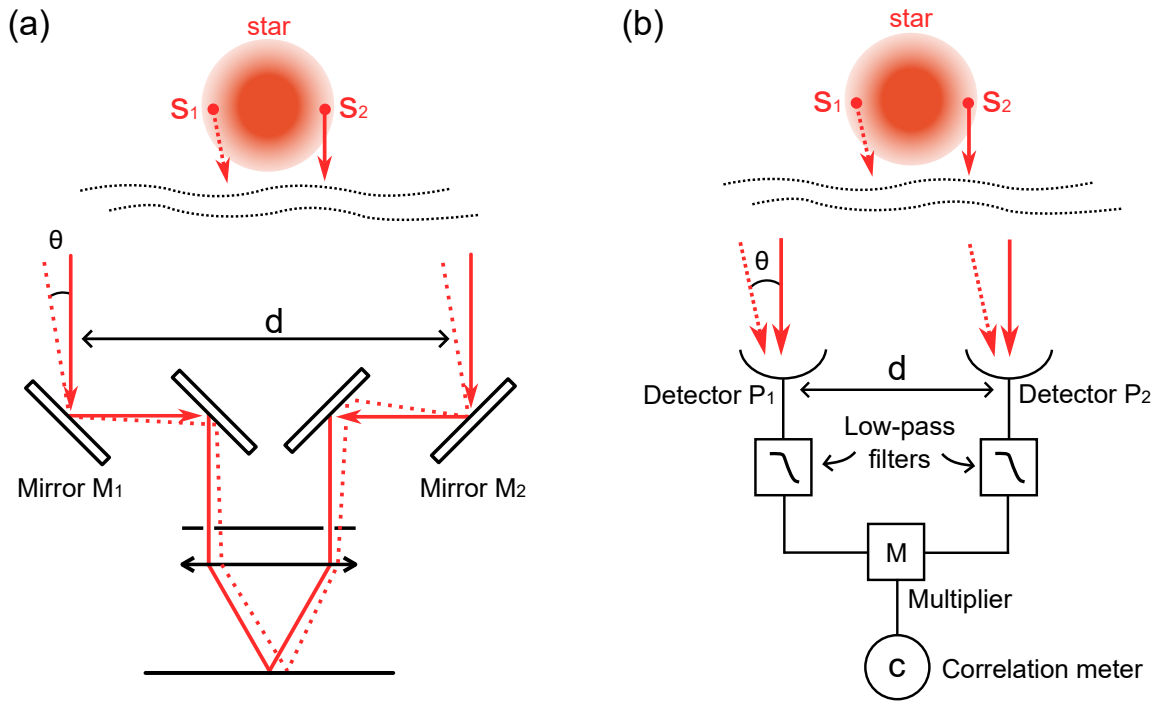

Figure 6-1: **Two types of stellar interferometers.** Both stellar interferometers measure the angular size of the distant star by probing the spatial coherence of the star. (a) Michelson stellar interferometer uses the amplitude of the incoming light and observes the decay of the contrast of the interference fringes as the mirror separation d increases. (b) Hanbury Brown and Twiss stellar interferometer measures the intensity of the two detectors and observes the decay of the correlation between the intensities as the detector separation d increases.

In the 1950s, Hanbury Brown and Twiss introduced a novel method for measuring the angular size of stars: intensity interferometry. Unlike Michelson interferometry, which relies on first-order amplitude or phase correlations, intensity interferometry measures second-order correlations in intensity. They observed a spatial correlation of the intensity fluctuations for light emitted from the distant star Sirius [107]. Since these correlations are much less sensitive to optical path-length differences, the technique does not require real-time phase stability between telescopes. As a result, Hanbury Brown–Twiss (HBT) interferometry enables much larger baseline separations (at that time) [108] and remains robust against atmospheric turbulence.

Since the pioneering work of Hanbury Brown and Twiss, Michelson-type stellar interferometry has seen significant technological advancements. One major breakthrough is *real-time fringe tracking*, where fast sensors monitor the fringe position

continuously. Another critical development is the implementation of *adaptive optics* (AO) systems, which use wavefront sensors and deformable mirrors to correct for atmospheric turbulence in real time [109]. The limitations that Hanbury Brown and Twiss originally identified in Michelson interferometry, namely, sensitivity to atmospheric turbulence and wavefront aberrations, have been largely mitigated through these innovations. As a result, amplitude interferometry has become the standard approach in contemporary interferometric observatories. In the optical domain, a notable example is the Very Large Telescope (VLT).

Although no longer a mainstream choice in the design of modern stellar interferometers, the original HBT experiment highlighted the importance of correlations in photon detection and played a foundational role in the emergence of quantum optics [107, 110–112].

6.1.2 A semi-classical explanation

There are various ways to interpret the original HBT experiment, which may explain the intense debate among physicists regarding its validity when it was first introduced in the 1950s. In the following, I will first present a semi-classical model, which already captures several key features of the HBT experiment.

According to the semi-classical theory of quantum optics, the photocurrent is proportional to the light intensity:

$$\begin{cases} E(\mathbf{r},t) = E^{(+)}(\mathbf{r},t) + E^{(-)}(\mathbf{r},t), \\ E^{(+)}(\mathbf{r},t) = \left[E^{(-)}(\mathbf{r},t)\right]^*. \end{cases}$$

The photodetector will measure the squared modulus of the classical complex electric field:

$$I(\mathbf{r},t) \propto \left|E^{(+)}(\mathbf{r},t)\right|^2 = E^{(-)}(\mathbf{r},t)E^{(+)}(\mathbf{r},t) \tag{6.1}$$

So the current correlation function can be expressed as:

$$g^{(2)}(\mathbf{r}_1, t_1; \mathbf{r}_2, t_2) = \frac{\langle i(\mathbf{r}_1, t_1)\, i(\mathbf{r}_2, t_2)\rangle}{\langle i(\mathbf{r}_1, t_1)\rangle \langle i(\mathbf{r}_2, t_2)\rangle}. \tag{6.2}$$

If the photocurrents $i(\mathbf{r}_1, t_1)$ and $i(\mathbf{r}_2, t_2)$ are uncorrelated, then the ensemble average of the product can be broken down into the product of the ensemble average, i.e., $\langle i(\mathbf{r}_1, t_1)\, i(\mathbf{r}_2, t_2)\rangle = \langle i(\mathbf{r}_1, t_1)\rangle \langle i(\mathbf{r}_2, t_2)\rangle$, which will result in a $g^{(2)}$ value of 1.

Combining Eqn. 6.1 and Eqn. 6.2, we have:

$$g^{(2)}(\mathbf{r}_1, t_1;\, \mathbf{r}_2, t_2) = \frac{\langle E^{(-)}(\mathbf{r}_1, t_1)\, E^{(+)}(\mathbf{r}_1, t_1)\, E^{(-)}(\mathbf{r}_2, t_2)\, E^{(+)}(\mathbf{r}_2, t_2)\rangle}{\langle E^{(-)}(\mathbf{r}_1, t_1)\, E^{(+)}(\mathbf{r}_1, t_1)\rangle \langle E^{(-)}(\mathbf{r}_2, t_2)\, E^{(+)}(\mathbf{r}_2, t_2)\rangle}. \tag{6.3}$$

Meanwhile, the Michelson stellar interferometer measures the visibility of the fringe. The interference is obtained from a coherent sum of the amplitudes of the electric field, not the intensity. Mathematically, the observable of the Michelson stellar interferometer is the first-order correlation function $g^{(1)}$ of the light:

$$g^{(1)}(\mathbf{r}_1, t_1; \mathbf{r}_2, t_2) = \frac{\langle E^{(-)}(\mathbf{r}_1, t_1)\, E^{(+)}(\mathbf{r}_2, t_2)\rangle}{\sqrt{\langle E^{(-)}(\mathbf{r}_1, t_1)\, E^{(+)}(\mathbf{r}_1, t_1)\rangle \langle E^{(-)}(\mathbf{r}_2, t_2)\, E^{(+)}(\mathbf{r}_2, t_2)\rangle}}. \tag{6.4}$$

Note that $g^{(1)}$ goes to 1 when $\mathbf{r}_1 = \mathbf{r}_2$ and $t_1 = t_2$ by definition, and goes to 0 when the field at $(\mathbf{r}_1, t_1)$ becomes completely uncorrelated with the field at $(\mathbf{r}_2, t_2)$.

Light emitted by a large number of uncorrelated emitters

Here I will explain how the two types of stellar interferometers are essentially connected as they are both probing the spatial coherence of the star. Mathematically, we will see how the second-order correlation function $g^{(2)}$ is related to the first-order correlation function $g^{(1)}$ through the Siegert relation [113, 114].

For simplicity, consider only the time-delay τ in evaluating the correlation functions, i.e., the source is assumed to have spatial coherence. Probing the spatial coherence while fixing the delay time τ to be 0 follows a similar derivation. The setup is illustrated in Fig. 6-2. For a large number of independent emitters, each emits a

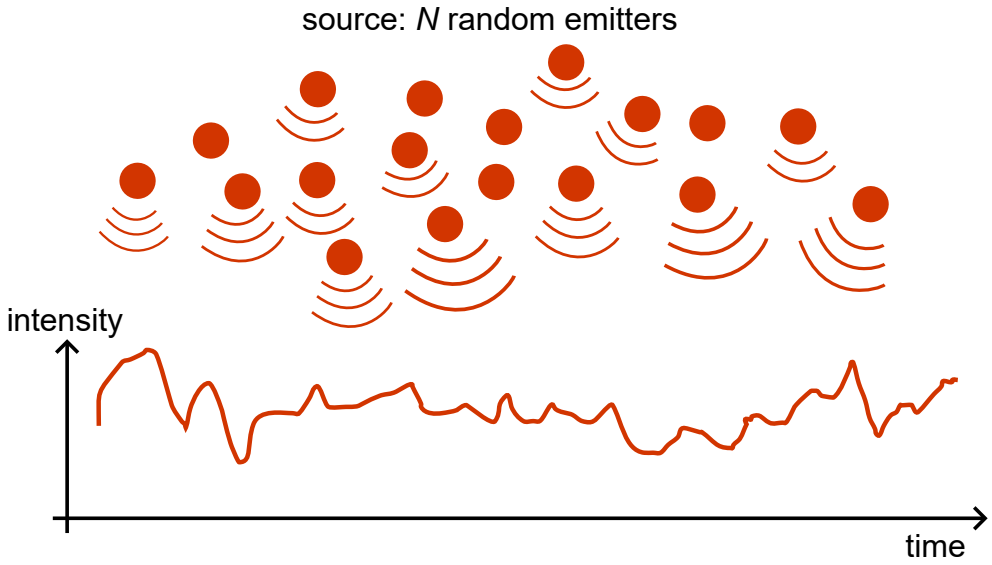

Figure 6-2: **Illustration of light emitted by a large number of uncorrelated emitters.** In the source, a collection of N random emitters is considered. Each emitter radiates a light field with a random phase relative to the others. The total field is the coherent sum of these individual fields, resulting in an intensity that exhibits temporal fluctuations.

field at the same angular frequency ω, but with a random phase $\phi_j(t)$. We write the jth-emitter field as

$$E_j(t) \;=\; A_j \,\exp\big[i(\omega t + \phi_j(t))\big], \tag{6.5}$$

where A_j is a (real) amplitude and $\phi_j(t)$ is distributed uniformly in $[0, 2\pi)$. The total electric field is then the sum:

$$E(t) \;=\; \sum_{j=1}^{N} E_j(t) \;=\; \sum_{j=1}^{N} A_j \,\exp\big[i(\omega t + \phi_j(t))\big]. \tag{6.6}$$

We define the unnormalized first-order correlation function in the stationary case by:

$$\begin{aligned} G^{(1)}(\tau) &= \big\langle E^*(t)\, E(t+\tau)\big\rangle \\ &= \Big\langle \Big(\sum_{j=1}^{N} A_j \,\exp\big[-i(\omega t + \phi_j(t))\big]\Big)\,\Big(\sum_{k=1}^{N} A_k \,\exp\big[i(\omega(t+\tau) + \phi_k(t+\tau))\big]\Big)\Big\rangle, \end{aligned} \tag{6.7}$$

where the angle brackets $\langle \dots \rangle$ denote an ensemble average over all random phases

$\{\phi_j\}$ (and possibly amplitudes if they vary).

Now we expand the product:

$$G^{(1)}(\tau) \;=\; \Big\langle \sum_{j=1}^{N}\sum_{k=1}^{N} A_j A_k \,\exp\big[-i(\omega t+\phi_j(t))\big]\,\exp\big[i(\omega(t+\tau)+\phi_k(t+\tau))\big]\Big\rangle. \quad (6.8)$$

Combine the exponentials:

$$G^{(1)}(\tau) \;=\; \sum_{j=1}^{N}\sum_{k=1}^{N} A_j A_k \,\exp(i\omega\tau)\,\big\langle \exp\big[i\,(\phi_k(t+\tau)-\phi_j(t))\big]\big\rangle. \quad (6.9)$$

Now we use the condition that the phase of each emitter ϕ_j is randomly sampled. Since ϕ_j are independent and uniformly distributed, we have the following relation:

$$\big\langle \exp\big[i\,(\phi_k(t+\tau)-\phi_j(t))\big]\big\rangle_{\{\phi\}} \;=\; \begin{cases} \big\langle \exp\big[i\,(\phi_j(t+\tau)-\phi_j(t))\big]\big\rangle, & j=k, \\ 0, & j\neq k. \end{cases} \quad (6.10)$$

Hence, all cross terms ($j \neq k$) vanish, leaving us with

$$G^{(1)}(\tau) \;=\; \sum_{j=1}^{N} A_j^2 \,\exp(i\omega\tau)\big\langle \exp\big[i\,(\phi_j(t+\tau)-\phi_j(t))\big]\big\rangle. \quad (6.11)$$

If each emitter has the same amplitude, i.e. $A_j = A$, then

$$G^{(1)}(\tau) \;=\; A^2 \,\exp(i\omega\tau)\sum_{j=1}^{N}\big\langle \exp\big[i\,(\phi_j(t+\tau)-\phi_j(t))\big]\big\rangle. \quad (6.12)$$

Now we need to properly normalize the first-order correlation function. By setting $\tau = 0$ in Eqn. 6.7, we have:

$$\langle I(t)\rangle = \langle I(t+\tau)\rangle = \big\langle E^*(t)\,E(t)\big\rangle = NA^2, \quad (6.13)$$

which simply means that the time-averaged intensity of the N random emitters are obtained by summing the intensity of each emitter incoherently.

Therefore, the normalized first-order correlation function $g^{(1)}(\tau)$ can be written as:

$$g^{(1)}(\tau) \;=\; \frac{G^{(1)}(\tau)}{\sqrt{\langle I(t)\rangle\,\langle I(t+\tau)\rangle}} = \frac{\exp(i\omega\tau)}{N}\sum_{j=1}^{N}\Big\langle \exp\big[i\,(\phi_j(t+\tau)-\phi_j(t))\big]\Big\rangle. \quad (6.14)$$

If we assume those N emitters only differ in a random phase but the time coherence properties are the same, i.e., the summands are identical to each other

$$\Big\langle \exp\big[i\,(\phi_j(t+\tau)-\phi_j(t))\big]\Big\rangle = \Big\langle \exp\big[i\,(\phi_0(t+\tau)-\phi_0(t))\big]\Big\rangle, \quad (6.15)$$

where $\phi_0(t)$ is the phase factor for a single random emitter. The expression of $g^{(1)}(\tau)$ can be further simplified to:

$$g^{(1)}(\tau) \;=\; e^{i\omega\tau}\Big\langle \exp\big[i\,(\phi_0(t+\tau)-\phi_0(t))\big]\Big\rangle. \quad (6.16)$$

Now we will derive the formula for the second-order correlation function $g^{(2)}(\tau)$. Starting with the unnormalized part $G^{(2)}(\tau)$:

$$G^{(2)}(\tau) = \big\langle I(t)\,I(t+\tau)\big\rangle = \big\langle E^*(t)E(t)E^*(t+\tau)E(t+\tau)\big\rangle. \quad (6.17)$$

Substitute the expressions in Eqn. 6.6 into Eqn. 6.17, we have:

$$\begin{aligned} E^*(t)E(t)E^*(t+\tau)E(t+\tau) = &\left(\sum_{j=1}^{N} A_j\, e^{\,i[\omega t+\phi_j]}\right)\left(\sum_{k=1}^{N} A_k\, e^{-\,i[\omega t+\phi_k]}\right) \\ &\times\left(\sum_{\ell=1}^{N} A_\ell\, e^{i[\omega(t+\tau)+\phi_\ell]}\right)\left(\sum_{m=1}^{N} A_m\, e^{-\,i[\omega(t+\tau)+\phi_m]}\right). \end{aligned} \quad (6.18)$$

Assume each emitter has the same amplitude $A_j = A$ for simplicity. Taking the ensemble average $\langle\cdots\rangle$ over the random phases:

$$G^{(2)}(\tau) = A^4 \sum_{j,k,\ell,m=1}^{N} \Big\langle e^{\,i[\phi_j(t)-\phi_k(t)+\phi_\ell(t+\tau)-\phi_m(t+\tau)]}\Big\rangle. \quad (6.19)$$

Using the same argument in Eqn. 6.10 to evaluate the statistical average of the four phase factors:

- If $j = k = l = m$:

$$\sum_{j,k,\ell,m=1}^{N} \langle e^{i[\phi_j(t)-\phi_k(t)+\phi_\ell(t+\tau)-\phi_m(t+\tau)]} \rangle_{\{\phi\}} = N$$

- If $j = k$ and $l = m$, but $j \neq l$:

$$\sum_{j,k,\ell,m=1}^{N} \langle e^{i[\phi_j(t)-\phi_k(t)+\phi_\ell(t+\tau)-\phi_m(t+\tau)]} \rangle_{\{\phi\}} = N(N-1),$$

- If $j = m$ and $k = l$, but $j \neq k$:

$$\begin{aligned}
&\sum_{j,k,\ell,m=1}^{N} \langle e^{i[\phi_j(t)-\phi_k(t)+\phi_\ell(t+\tau)-\phi_m(t+\tau)]} \rangle_{\{\phi\}} \\
&= \sum_{j,k=1,j\neq k}^{N} \langle e^{\left[i(\phi_j(t)-\phi_j(t+\tau))\right]} \rangle \langle e^{\left[-i(\phi_k(t)-\phi_k(t+\tau))\right]} \rangle \\
&= N(N-1) \left| \langle e^{\left[i\,(\phi_0(t+\tau)-\phi_0(t))\right]} \rangle \right|^2 \\
&= N(N-1) \left| g^{(1)}(\tau) \right|^2,
\end{aligned}$$

where in obtaining this formula, we assume N emitters only differ in a random phase but have the same temporal coherence properties just like we did in deriving Eqn. 6.15 and Eqn. 6.16.

All other terms in the summation that do not satisfy the abovementioned conditions will average to zero. Putting all the nonzeros summands together, we have:

$$G^{(2)}(\tau) = A^4 \left[N + N(N-1) + N(N-1) \left| g^{(1)}(\tau) \right|^2 \right] \tag{6.20}$$

Recall that the time-averaged (or ensemble-averaged) intensity is $\langle I(t) \rangle = NA^2$,

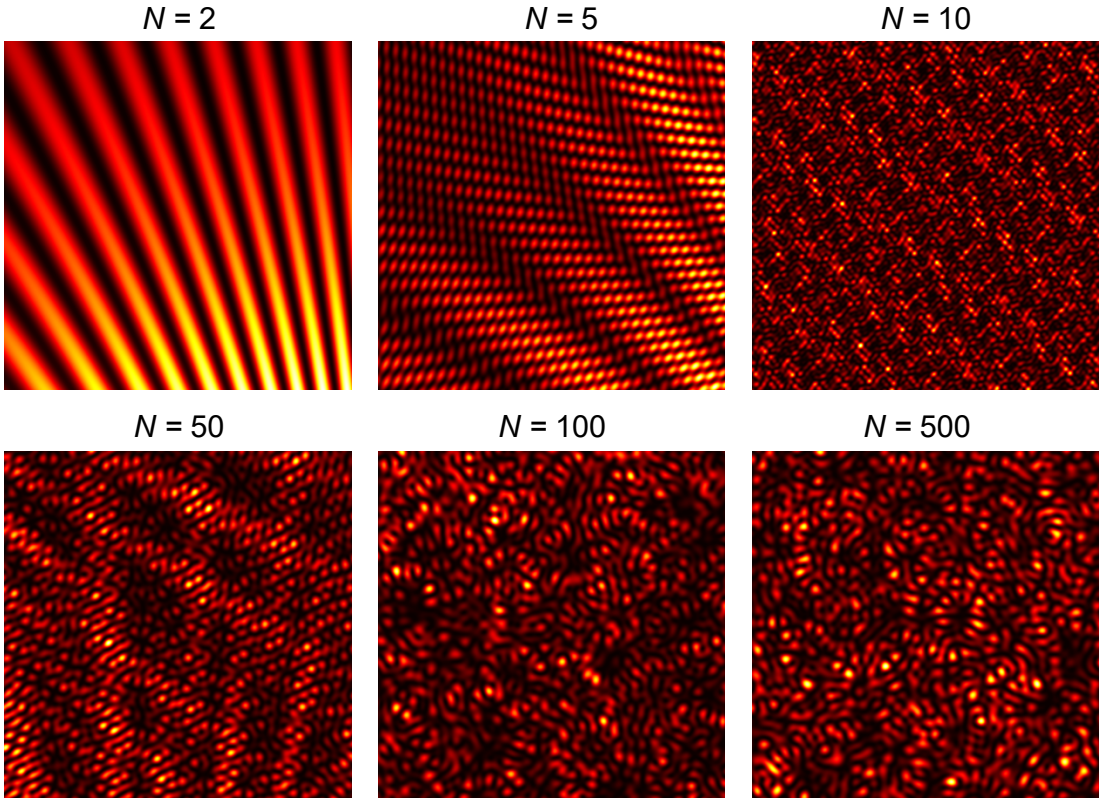

Figure 6-3: **Interference pattern generated by N random emitters.** A collection of N point emitters is arranged on a single source plane, with an observation plane parallel to the source plane. The interference pattern on the observation plane is determined by coherently summing the electric fields from N randomly positioned emitters. For $N = 2$, the pattern resembles that of a classic double-slit experiment. However, as N increases, the periodicity of the interference pattern gradually diminishes, giving rise to a complex speckle pattern.

the denominator in the Eqn. 6.2 is:

$$\langle I(t)\rangle\langle I(t+\tau)\rangle = N^2A^4. \tag{6.21}$$

Therefore by definition,

$$\begin{aligned} g^{(2)}(\tau) &= \frac{G^{(2)}(\tau)}{\langle I(t)\rangle\langle I(t+\tau)\rangle} \\ &= 1 + (1 - \frac{1}{N}) \left|g^{(1)}(\tau)\right|^2. \end{aligned} \tag{6.22}$$

When the total number of the random emitters is very large, i.e., $N \to \infty$, the $1/N$ in Eqn. 6.22 becomes negligible, we have the following equation that connects

the first-order (phase) and second-order (intensity) correlation:

$$g^{(2)}(\tau) = 1 + \left|g^{(1)}(\tau)\right|^2. \tag{6.23}$$

The Siegert relation in Eqn. 6.23 connects the Michelson interferometer and the HBT interferometer. Both types of stellar interferometers probe the spatial coherence of the source but differ in the order of coherence they use.

Speckle pattern

In addition to demonstrating the Siegert relation, the model of interference from many uncorrelated emitters also introduces the concept of the speckle pattern.

As demonstrated in Fig. 6-3, as the number of random emitters increases, the periodic interference pattern becomes increasingly washed out, giving rise to the emergence of a complex speckle pattern. Although the phase of the field is random, the intensity at different points within the speckle pattern exhibits spatial correlations. By measuring the intensity at two points within the same speckle field, one can observe correlations in the intensity fluctuations.

6.1.3 From photons to atoms

Since the original HBT experiments, the phenomena have been observed beyond photonic systems, extending to matter waves, including electrons [115–117], neutrons [118], cold atoms [50–52, 119–131], and cold molecules [38]. In our case with ^{87}Rb, both light and atoms can be described as bosonic fields, and many interference phenomena have close analogies between the two.

Near vs. far field

If we measure the speckle pattern in the near field for photons, the characteristic length scale is naturally set by the wavelength λ of the photon. Matter-wave fields exhibit an equivalent speckle pattern, with a characteristic grain size set by the thermal de Broglie wavelength, $\lambda_{\mathrm{dB}} = h/\sqrt{2\pi m k_B T}$. This atomic speckle is inherently

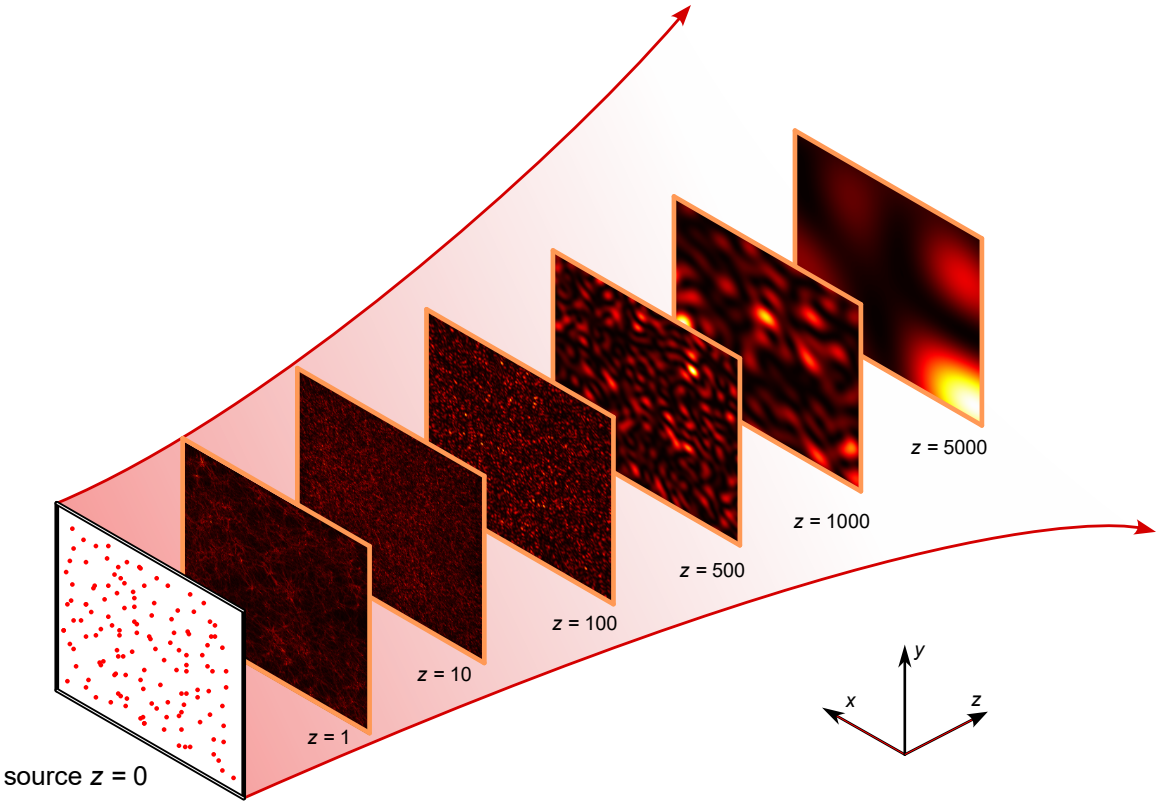

Figure 6-4: **Interference pattern from N random sources measured in the near and far fields.** A collection of N point emitters is arranged on a single source plane, with an observation plane parallel to it. The distance between the source and observation planes is varied from the near field to the far field, while keeping the size of the observation plane constant. The resulting interferogram forms a speckle pattern, with the characteristic length scale of the speckle increasing as the observation plane moves to the far field. For numerical calculations, choose the total emitter number to be $N = 500$ and set the wavelength to be 1.

quantum in nature, as its scale is determined by Planck's constant, h. In contrast, a classical gas exhibits purely Poissonian fluctuations, lacking any intrinsic length scale due to the absence of correlations.

However, in almost all HBT experiments, whether in photonic or matter-wave systems, a common denominator is that detection occurs in the far field. By definition, an HBT experiment measures the far-field intensity, as this is how the technique probes the size of a distant star. In nearly all matter-wave realizations, a time-of-flight stage is typically required before detection, during which the atomic wavefunctions freely propagate to the far field.

Here we would like to point out why all the HBT experiments are made possible by looking at the far field. Again, the model of many random emitters forming speckle patterns can be useful. As shown in Fig. 6-4, a series of interferograms generated by N random point emitters are displayed, from the near field to the far field. The multi-wave interferences result in complicated speckle patterns. But one can see in Fig. 6-4 that as the observation screen is moved further away from the source, the resulting speckle patterns show a larger and larger "grain size". The correlation length of this grain gets magnified from the near field to the far field.

HBT observed a spatial correlation of the intensity fluctuations for light emitted from the distant star Sirius. These fluctuations represent an optical speckle pattern with a characteristic length scale of the optical wavelength λ near the star's surface. As illustrated in Fig. 6-6, when light propagates from a distant star of radius R to the earth at distance D, the speckle size is magnified to $\lambda D/R$, which HBT determined to be around 5 m for Sirius.

Phase space cell

The magnification of the speckle pattern, as shown in Fig. 6-4, is suitable for understanding photonic HBT. For matter waves, one can use the concept of phase space cell.

According to Heisenberg's uncertainty principle, the position and momentum of a particle cannot be simultaneously determined with arbitrary precision:

$$\Delta x \Delta p \geq \frac{\hbar}{2}. \tag{6.24}$$

Now let's consider phase space, which includes both spatial and momentum dimensions. The uncertainty principle implies that the phase space needed to fully describe the information of particles is divided into finite "cells" with a volume on the order of $\hbar$. Here we consider a one-dimensional phase space for simplicity. Two particles residing within the same phase space cell are considered indistinguishable, as the quantum numbers used to label them are identical within the uncertainty limits.

Fig. 6-5(a) illustrates the phase space distribution in our system. By using a microscope with high spatial resolution, we can probe atoms localized within a small region. This imposes a spatial notch filter, limiting the uncertainty in initial position to a very narrow window. Atoms within this region are thus allowed to have a slightly broader momentum distribution while still being considered within a single phase space cell. Since the temperature T characterizes the momentum spread of the atoms, the uncertainty principle allows us to calculate the spatial uncertainty Δx for which atoms are still within one phase space cell. This Δx corresponds exactly to the thermal de Broglie wavelength λ_{dB}.

Fig. 6-5(b) shows the phase space distribution for an experiment where correlations are measured after a time-of-flight expansion, for example, the ultracold helium experiment [121]. In that case, bosonic bunching is probed in the temporal domain. Observation in the far field, with (nearly) simultaneous detection, acts as a momentum notch filter, ensuring that the particles originate from a narrow range of initial momenta. If we trace these two atoms back in phase space to the moment of release from the trap, their Δp is relatively small. As a result, they can have a larger spatial uncertainty, that is, a larger Δx, and still reside within a single phase space cell, showing bosonic bunching. The initial separation between them can be as large as the size of the atomic cloud.

Time-of-flight transforms the *in situ* measurement into a far-field one. It corresponds to free propagation of the matter waves. According to Liouville's theorem, the density of the phase space distribution remains unchanged during this evolution. Intuitively, time-of-flight stretches the phase space cells without compressing them. As a result, far-field detection connects to an initial distribution as illustrated in Fig. 6-5(b).

Quantitatively, the ballistic expansion of ultracold atoms magnifies the *in situ* correlation length in the far field by a factor of D/R, similar to the propagation of light [132]. We can derive this magnification factor from the dynamics of ballistic expansion as follows:

As illustrated in Fig. 6-6, consider a cloud of particles with an initial *in situ* size

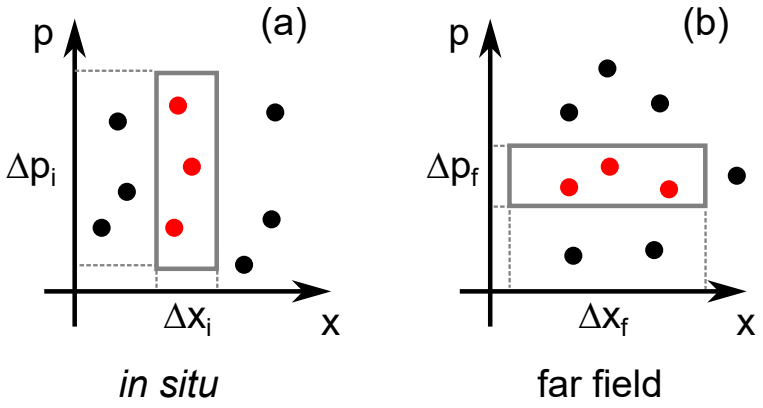

Figure 6-5: **Illustration of the phase space distribution for measuring bosonic bunching *in situ* vs far field**. The gray box indicates a phase space cell whose volume is given by the uncertainty principle. Particles that reside within a phase space cell (red disks) are indistinguishable. (a) Our experimental setup. The microscope enables high spatial resolution. Atoms localized within a thermal de Broglie wavelength are considered to occupy a single phase space cell, as their momentum distribution is characterized by the temperature T. (b) Previous matter-wave HBT experiments. Although most of them measure bosonic bunching in the far field, if we trace back to the moment when the particles are released, the particles contributing to the signal have a narrow momentum distribution but can be spatially separated by a large distance.

R. After a time-of-flight duration t_{TOF}, the cloud expands and the particles reach a detector located a distance D away, in the far field.

Since the particles arrive at the detector nearly simultaneously, their average velocity must be approximately D/t_{TOF}. However, for two particles located at opposite edges of the cloud to arrive at the detector at the same time, the one starting slightly farther from the detector must travel slightly faster. The difference in their travel distances is on the order of the initial cloud size R. This sets a rough estimate for the momentum uncertainty in the far field, Δp_f:

$$\Delta p_f \approx \frac{mR}{t_{\mathrm{TOF}}}. \tag{6.25}$$

On the other hand, since the propagation distance D corresponds to the radius of the expanding cloud, we can relate it to the initial momentum spread Δp_i via:

$$D \approx \frac{\Delta p_i t_{\mathrm{TOF}}}{m}, \tag{6.26}$$

which reflects the fact that the cloud expands due to its initial momentum distribution.

Combining the two expressions, we obtain:

$$\frac{\Delta p_i}{\Delta p_f} \approx \frac{D}{R}. \tag{6.27}$$

This shows that the momentum uncertainty in the far field is reduced by a factor of D/R. By the Heisenberg uncertainty principle, this implies that the spatial extent over which particles remain within the same phase space cell is correspondingly magnified:

$$\frac{\Delta x_f}{\Delta x_i} \approx \frac{D}{R}. \tag{6.28}$$

For the previous atomic HBT experiments, this magnification is crucial because the correlation length *in situ* (or in the near field) is too small to be detected. A time-of-flight expansion is needed to enlarge the correlation length to exceed the detector resolution.

As shown in Fig. 6-6, our experiment measures the atomic speckle pattern *in situ*, without requiring free propagation or magnification of the correlation length as in previous HBT experiments. This is made possible by the high spatial resolution of the microscope and careful state preparation, which ensures an ultracold thermal sample. The details of the state preparation will be discussed in the next chapter. To conclude this chapter, we show how our work connects to the broader context of HBT experiments and, hopefully, offers new perspectives on the fundamental requirements for observing bosonic enhancement.

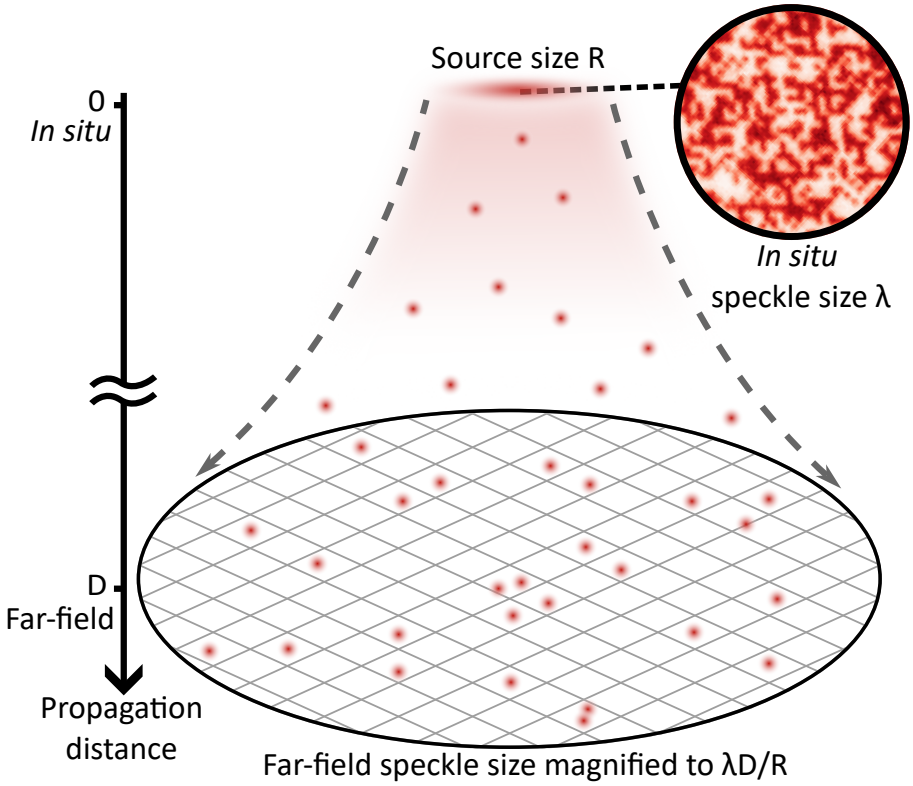

Figure 6-6: ***In situ* and far-field speckle patterns.** An ensemble of identical bosons exhibits a spatial length scale λ where density fluctuations are correlated. In photonic systems, the length scale of this speckle pattern is given by the optical coherence length, while for a gas of thermal atoms, it is the thermal de Broglie wavelength. In both the HBT experiment and previous cold atoms experiments, a free expansion over a distance D is employed to enlarge the far-field speckle size by D/R. In this work, we use a microscope with a spatial resolution smaller than the thermal de Broglie wavelength to directly image the atomic speckle *in situ*.

Chapter 7

Microscopic Study of the Correlation

As mentioned in the previous chapter, the magnification effect plays a crucial role in HBT-like experiments. With the aid of a quantum gas microscope, the resolving power of the imaging system can be made comparable to or even smaller than the correlation length, enabling direct access to spatial correlations at the relevant quantum scale.

Previously, the *in situ* study of the bosonic correlation was lacking. In this project, we report the first *in situ* observation of the atomic correlation length in a bulk, thermal Bose gas. The correlations and speckle pattern are quantitatively described by the second-order correlation function, $g^{(2)}$, which gives the joint probability of detecting two particles. The $g^{(2)}$ function is measured by cooling a small quasi two-dimensional ensemble of approximately 100 rubidium atoms to below 10 nK, with a corresponding thermal de Broglie wavelength $\lambda_{\mathrm{dB}} \approx 2.3$ μm, larger than the $a_{\mathrm{lat}} =$ 532 nm pinning lattice spacing used for imaging. Detection of such sparse samples is enabled by using a quantum gas microscope with single-atom resolution. Herein, we show a clear bunching signal and observe its spatial extent to be the thermal de Broglie wavelength.

7.1 Experimental setup

In this work, we extend quantum gas microscopy from discretized lattice systems to a harmonically trapped bulk gas. This allows high quantum efficiency readout of atomic

positions that far exceeds the signal-to-noise afforded by standard *in situ* absorption imaging. During detection, we quench on a two-dimensional pinning lattice to project the bulk atomic density distribution into a square grid with 532-nm spacing. The correlation function is correspondingly discretized. Subsequently, we ramp down the vertical lattice and ramp up a light sheet for tight vertical confinement during imaging. We employ polarization gradient cooling and collect the fluorescence photons. By reconstructing fluorescence images with high fidelity, we can determine the occupancy of individual lattice sites as depicted in Fig. 7-4.

7.1.1 Parameter regime

The second-order correlation function $g^{(2)}(\mathbf{r};\mathbf{r}')$ can be understood as the normalized probability of jointly detecting two particles at positions $\mathbf{r}$ and $\mathbf{r}'$. For identical bosons at temperatures $T > T_c$, where the ensemble is away from the quantum critical region, the second-order correlation function has a Gaussian form that depends on the separation distance $r = |\mathbf{r} - \mathbf{r}'|$ between two particles [133]:

$$g^{(2)}(r) = 1 + \exp\left(-2\pi r^2/\lambda_{\mathrm{dB}}^2\right). \tag{7.1}$$

When two particles occupy the same position, $g^{(2)}(0) = 2$, indicating a two-fold increase in the probability of double occupation. When pairs of atoms are sufficiently far apart that there is an absence of density-density correlation between them, $g^{(2)}(r)$ decays to 1. The spatial extent of the bosonic enhancement can be characterized by the root mean square (rms) width of the Gaussian profile, $l = \lambda_{\mathrm{dB}}/(2\sqrt{\pi})$, which increases as the temperature of the ensemble decreases.

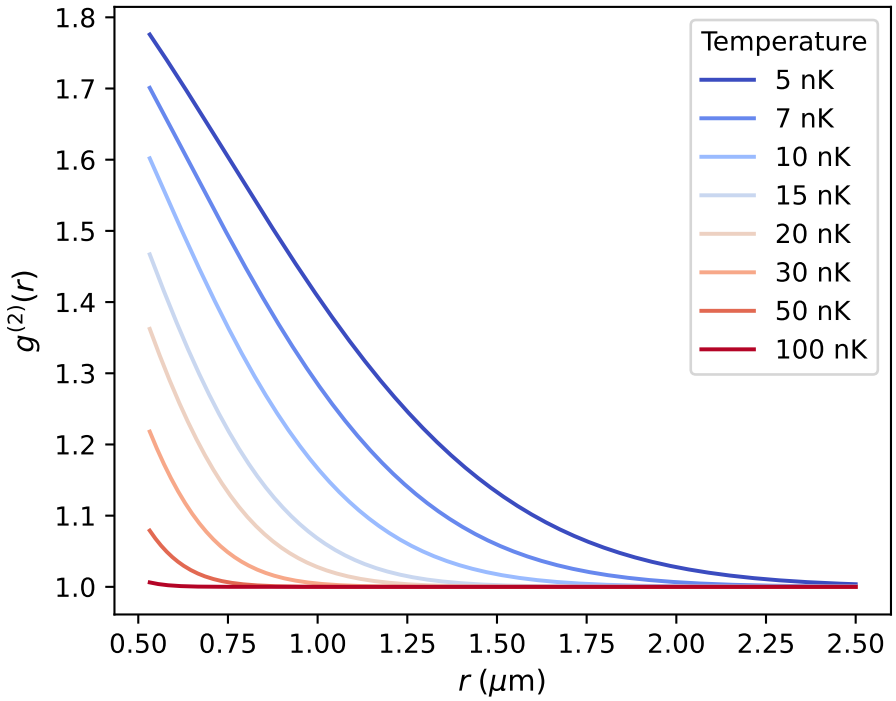

Figure 7-1: **Second-order correlation function for an ensemble of thermal ^{87}Rb atoms at various temperatures.** When the gas is sufficiently far from the BEC phase transition, the second-order correlation function exhibits a Gaussian profile. Its characteristic length scale is determined by the thermal de Broglie wavelength, which is inversely proportional to $\sqrt{T}$. Plotted here is a series of such Gaussian curves at various temperatures. Because of the relatively large mass of ^{87}Rb atoms, observing a clear signal requires cooling the sample to below 10 nK.

A central difficulty in this experiment is preparing a thermal cloud that is cold enough to exhibit strong *in situ* bunching, yet remains above the BEC transition. As shown in Fig. 7-1, significant second-order correlations only emerge when the thermal de Broglie wavelength becomes comparable to the imaging resolution, which requires temperatures well below 10 nK for ^{87}Rb. However, When bosons are cooled below the phase transition temperature T_c, they form a Bose-Einstein condensate (BEC). In analogy to single-mode lasers, a BEC has $g^{(2)}(r) = 1$, identical to that of uncorrelated classical particles. This complicates the measurement of the second-order correlation function of the Bose gas due to the spatial overlap of the BEC and thermal gas. To isolate correlations in the thermal gas, we carefully control $T > T_c$ by adjusting the total atom number N. Achieving this balance between maximizing bunching while

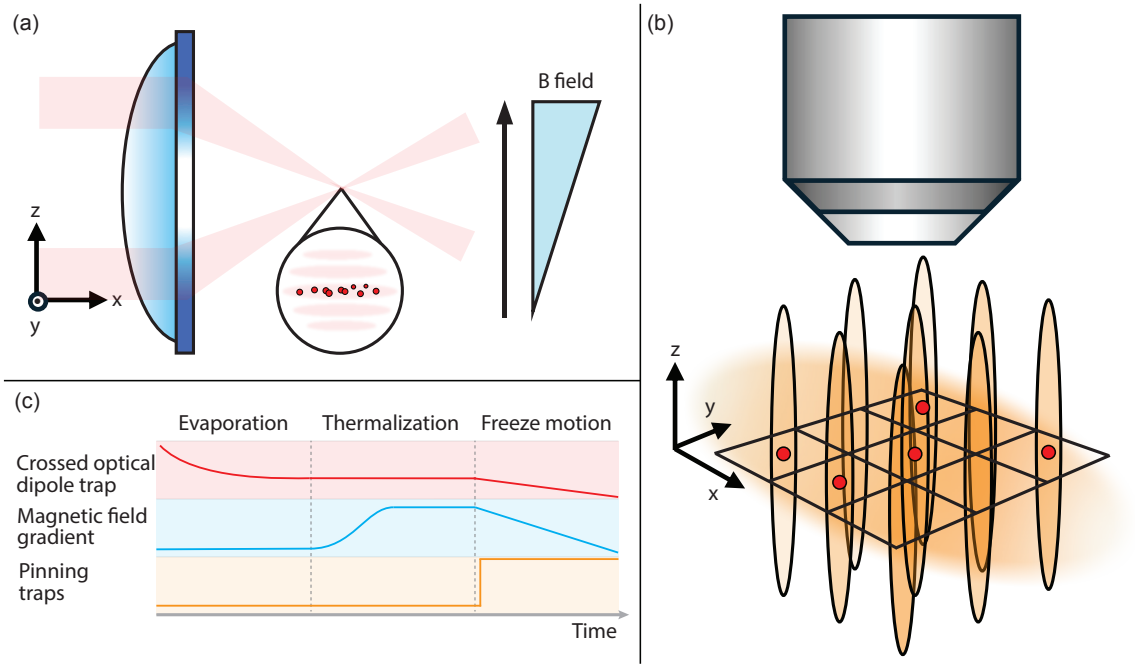

Figure 7-2: **Experimental setup.** (a) A 12-μm spacing vertical lattice is formed by intersecting two 1064-nm beams, which are focused onto the atoms at a 5° intersection angle by an aspheric lens. A magnetic field gradient is applied in the vertical direction to compensate for gravity. (b) To image the atom positions, the atoms are pinned down by two horizontal lattices intersected at approximately 90°. This forms a square grid of tubes elongated in the z-direction with 532-nm spacing. A light sheet, depicted as a diffuse oval along the x-axis, provides tight confinement in the z-direction. We employ polarization gradient cooling and collect the fluorescence photons with a microscope objective. (c) The experimental sequence is graphically depicted. The atoms are cooled in the crossed dipole trap by lowering the trap depths over 10 seconds. We subsequently ramp up a magnetic field gradient over 500 ms to compensate for gravity. To freeze the spatial distribution, we quench the pinning lattices in sub-microsecond time and ramp down the crossed dipole trap and magnetic field gradient. Fluorescence detection is performed in the deep pinning lattices.

staying in the thermal regime is one of the most technically demanding aspects of the entire experiment.

7.1.2 Sequence

Schematics and key steps of the experimental sequence to prepare and characterize a quasi two-dimensional thermal gas are shown in Fig. 7-2.

We start with approximately 10^4 ^{87}Rb atoms prepared in the spin-polarized $|F = 1, m_F = -1\rangle$ state loaded into a single node of a 12-μm spacing vertical lattice, as depicted in Fig. 7-2(a). The vertical lattice node has a cross-section with Gaussian widths of 5.4 μm and 96 μm in the vertical and horizontal directions, respectively. The atoms are loaded into the lattice from a co-propagating light sheet with Gaussian widths of 8 μm and 42 μm. An additional laser beam propagating in the y-direction, not depicted in Fig. 7-2(a), is used to provide confinement along the vertical lattice beam's propagation direction to form a crossed optical dipole trap. The atoms are then cooled through forced evaporation by lowering the trap depth of the crossed dipole trap over 10 seconds to allow for thermalization through collisions. A magnetic field gradient in the vertical direction is ramped up over 500 ms to compensate for gravity and ensure a favorable vertical trap frequency. The final trap frequencies for a sample with ≈ 100 atoms and $T \approx 6.5$ nK are $(\omega_x, \omega_y, \omega_z) = 2\pi \times (12, 15, 380)$ Hz. We measure the trap frequencies by parametric heating.

To observe correlations in the thermal gas, we carefully control the total atom number N to ensure that the BEC phase transition temperature T_c is lower than T.

For detection, we freeze the atomic motion by quenching on two horizontal pinning lattices intersected at 90° to 3000 E_r in sub-microsecond time before ramping down the cross dipole trap and magnetic field gradient (Fig. 7-2(b)). The light sheet is subsequently switched on to a few thousand E_r, where $E_r = h^2/(2m\lambda^2)$ is the recoil energy of a lattice photon with wavelength $\lambda = 1064$ nm for an atom of mass m. The atomic spatial distribution is projected onto a square grid with 532-nm spacing. The experimental sequence is summarized in Fig. 7-2(c). We then measure the lattice occupation by applying polarization gradient cooling and collecting the fluorescence photons with a microscope objective.

7.2 Thermometry

For our system size ($N \approx 100$), finite-N correction terms for the thermodynamic

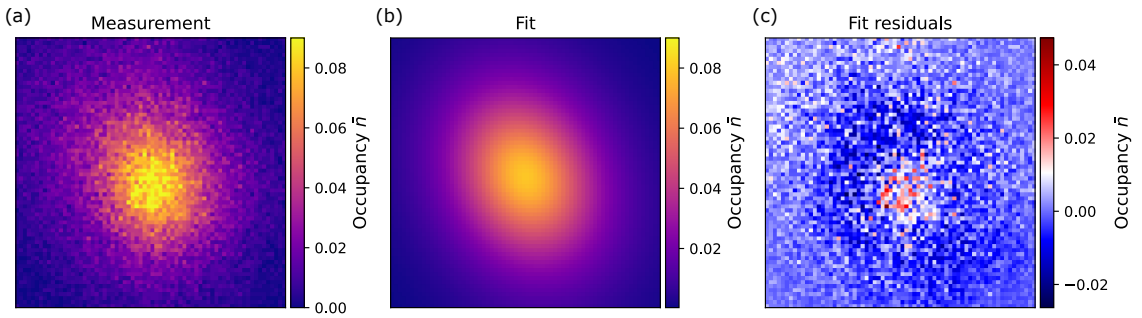

Figure 7-3: **Temperature determination.** (a) The mean occupancy $\bar{n}(x, y)$ on each lattice site averaged over all (≈ 650) experimental snapshots. (b) The fit to the data in panel (a) using Eq. (7.3). We extract $T = 6.5$ nK. (c) Residuals of fit.

equations of Bose gases (generally calculated for $N \to \infty$) are relevant. Following the treatment in Ref. [134], we properly estimate the populations in all oscillator states. We begin with the Bose-Einstein distribution formula:

$$n_k(E_i, T) = \frac{1}{e^{\beta(E_k - \mu)} - 1}. \tag{7.2}$$

For the three-dimensional harmonic trap, the energy for a given mode k is $E_k = \hbar(\omega_x n_x + \omega_y n_y + \omega_z n_z + 3/2)$. We count all states so no degeneracy factors are required. The chemical potential μ is treated as a normalization factor to ensure $N = \sum_k n_k(E_k)$.

First, we model the temperature of our ensemble including finite size effects. We average many experimental snapshots to determine the mean occupancy per lattice site $\bar{n}(x, y)$ as plotted in Fig. 7-3(a). Next, we fit the density distribution as a sum of Hermite polynomials denoted $\psi_{n_x,n_y}(x, y)$ (the solutions to the quantum harmonic oscillator):

$$n_{\text{fit}}(x, y) = \sum_{n_x} \sum_{n_y} n_k(n_x, n_y, T) |\psi_{n_x,n_y}(x, y)|^2. \tag{7.3}$$

$\psi_{n_x,n_y}(x, y)$ depends on the trap frequencies ω_x, ω_y which are independently calibrated via parametric heating. We fit $T = 6.5$ nK and plot the fitted density distribution in Fig. 7-3(b). Parameterized in terms of the two-dimensional condensate

temperature in the thermodynamic limit ($N \to \infty$),

$$k_B T_c^{2D} = \sqrt{N}\hbar\bar{\omega}_R\sqrt{6/\pi^2}, \tag{7.4}$$

we find $T/T_c^{2D} = 1.26$. The fit residuals are plotted in Fig. 7-3(c), showing good agreement between the experiment and data. Fitting instead to a two-dimensional Bose gas in the thermodynamic limit, we obtain $T = 5.6$ nK in reasonable agreement.

The effects of interactions are not included in this fit since they are weak. The first order correction would be adding a mean-field term to the Hamiltonian of $U_{\mathrm{MF}} = \tilde{g}\mathcal{D}(r)/\pi$ [135]. $\mathcal{D}(r)$ is the local phase space density. The dimensionless interaction strength is $\tilde{g} = \sqrt{8\pi}a/l_z$ with the tight-confinement harmonic oscillator length $l_z = \sqrt{\hbar/m\omega_z}$. For our trap parameters and s-wave scattering length $a \approx 100\ a_0$, $\tilde{g} = 0.04$, and thus interactions are a small correction to the extracted temperature T.

7.3 Data Analysis

To statistically evaluate the bosonic enhancement, we use a simple and robust analysis method: counting pairs of atoms separated by distance r. The measured separation between particles is discrete due to the underlying lattice structure. The three closest types of pairs are shown in Fig. 7-4b, with pair separations of 1, $\sqrt{2}$, and 2 a_{lat}, respectively. When the distance between atoms on two distinct lattice sites is within the thermal de Broglie wavelength, there will be an enhancement in the number of detected pairs compared to the classical expectation value.

For particles on a lattice site with indices (i, j), the nearest-neighbor (NN) pair corresponds to sites ($i \pm 1$, j) and (i, $j \pm 1$). In a homogeneous region of interest of $m \times m$ sites, assuming the probability of detecting one particle per site to be p, the expectation value for the number of classical (distinguishable) NN pairs is $2m(m-1)p^2$. The -1 accounts for the fact that the region of interest is finite and the correction varies as the pair separation increases. For indistinguishable particles, the expectation value for the number of NN pairs is $g^{(2)}(r = a_{\mathrm{lat}}) \times 2m(m-1)p^2$. In the

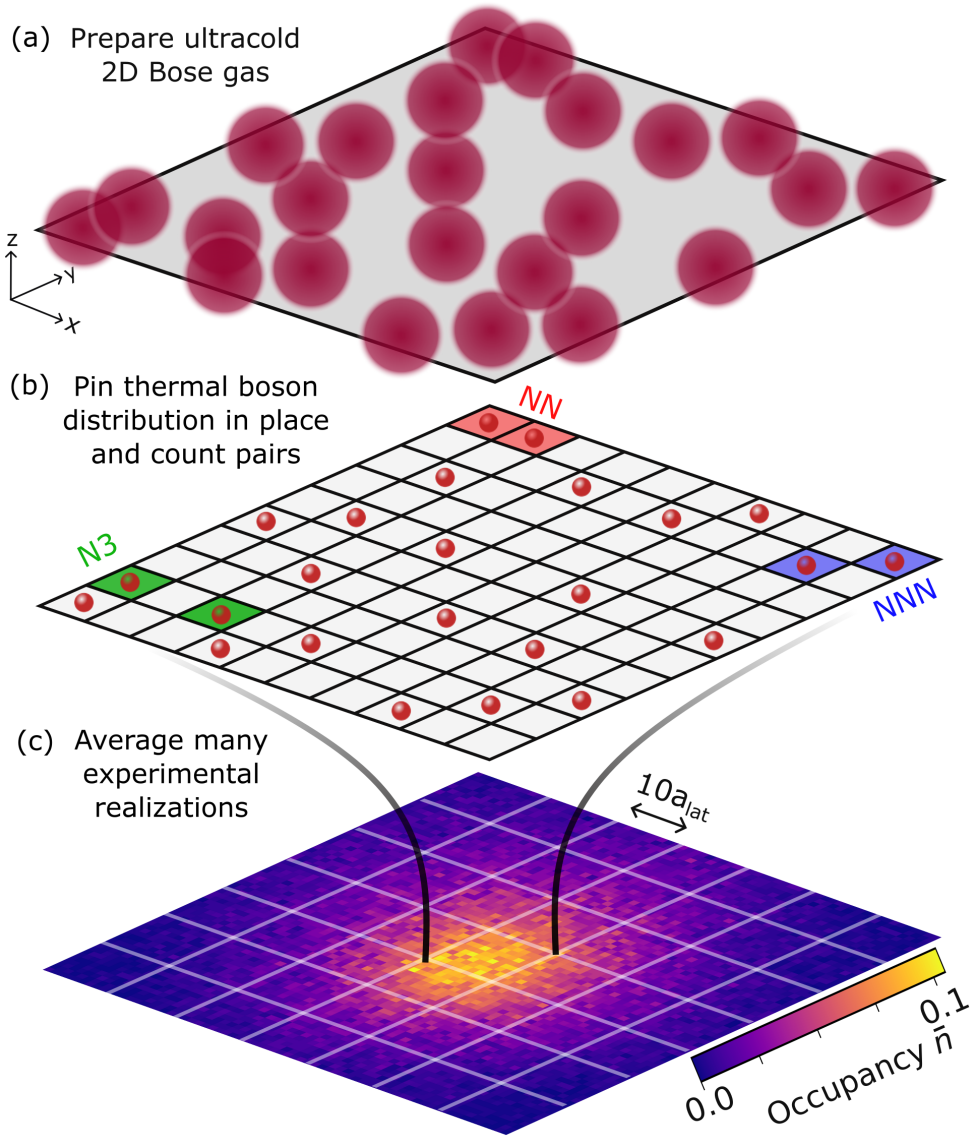

Figure 7-4: **Experimental overview.** (a) Using a ^{87}Rb quantum gas microscope, we probe *in situ* the density fluctuations in an ultracold, quasi two-dimensional thermal Bose gas. (b) We project the 2D Bose distribution onto a pinning lattice and reconstruct the site-by-site lattice occupation. To determine the bosonic enhancement, we count pairs of atoms separated by distance r and determine the enhancement factor $g^{(2)}(r)$ over the classical distribution corresponding to fully distinguishable particles. On the lattice grid, we show the distance between three types of pairs, corresponding to the nearest-neighbor (NN, red), next-nearest-neighbor (NNN, blue), and third-nearest-neighbor (N3, green). (c) To experimentally determine $g^{(2)}(r)$ with high signal-to-noise, we average over 650 experimental snapshots. The region of interest is sectioned into 10×10 boxes to address the spatial inhomogeneity of the harmonic trap. The mean occupancy $\bar{n}$ on each lattice site averaged over all snapshots is plotted. We remain dilute ($\bar{n} < 0.15$) to avoid double occupation and to ensure that we do not cross the BEC phase transition.

absence of technical corrections, the ratio of measured pairs to classically expected pairs gives the second-order correlation function $g^{(2)}(r)$.

Ideally, we would probe the $g^{(2)}$ function at $r = 0$, where the correlation signal is strongest. However, due to light-assisted collisions characteristic of quantum gas microscopes, double occupation on a single lattice site is parity projected to an empty site. Detecting pairs at $r = 0$ requires doublon detection schemes [136–139], which we do not implement in this work. The smallest separation we probe is $r = a_{\mathrm{lat}}$ and the largest is $r \approx 5$ μm.

Since the quasi two-dimensional cloud is prepared in a harmonic trap, the probability of detecting one particle per site has spatial dependence. We divide the total field of 70×70 sites into 49 smaller boxes of 10×10 sites, as illustrated in Fig. 7-4(c). This is directly analogous to applying the local-density approximation, where locally homogeneous regions are sampled. Within a 10×10 box, there is a residual spatial inhomogeneity that grows quadratically to $\approx 10\%$ for pairs separated by 5 μm. We determine the magnitude of this correction from a numerical simulation of our experimental density and experimentally confirm this correction with a high-temperature measurement where correlations are minimal.

Temporal atom number fluctuations between experimental snapshots are also a noise source that will enhance the number of observed pairs. This effect does not depend on the pair separation distance r and only adds an overall scaling factor to the absolute value of $g^{(2)}(r)$. While this effect can be mitigated by post-selecting data based on the total atom number [38], instead, we choose to include all data but normalize $g^{(2)}(r)$ by the pairs separated at a distance larger than 3 μm, where density fluctuations are uncorrelated. The details of the temporal atom number fluctuations will be explained later.

7.3.1 Spatial and thermal dependence

We implement our pair analysis technique to determine the spatial second-order correlation for our thermal Bose gas, presented in Fig. 7-5. At each discrete pair separation, we evaluate the pair enhancement. For a sample prepared at 6.5 nK, we observe a

31(2)% increase in the second-order correlation function for nearest-neighbor pairs separated by a_{lat}, as plotted in the Fig. 7-5 inset. The spatial dependence matches the theoretical prediction with the thermal de Broglie wavelength λ_{dB} being 2.3 μm.

We also observe the temperature dependence of the second-order correlation function. By raising the vertical lattice non-adiabatically to heat the cloud, we measure a higher temperature of 54 nK, corresponding to a thermal de Broglie wavelength λ_{dB} of 0.81 μm and an rms width l of 0.43 a_{lat}. As shown in Fig. 7-5, the enhancement of the second-order correlation is substantially reduced and no longer statistically significant. The fact that the function is flat at $g^{(2)}_{\mathrm{obs}}(r) = 1$ confirms our normalization procedure.

7.3.2 Thermal vs BEC

We also evaluated the $g^{(2)}(r)$ correlation function at the center of the BEC. By only evaluating the correlation function at the central dense part of the cloud, we measured the correlation function for the BEC. As shown in Fig. 7-6, the BEC data does not show a significant spatial dependence of the $g^{(2)}(r)$ function, which is consistent with the theoretical prediction that BEC has $g^{(2)}(r) = 1$. The slight uptick near $r = 0$ can be attributed to the region of interest being a mixture of both the BEC and the thermal cloud, and the thermal cloud part should produce an enhanced fluctuation.

We also have to mention that using our method to detect the $g^{(2)}(r)$ correlation function is not a sufficient but a necessary condition. The BEC part has a much higher density than the dilute thermal cloud. The density can be so high that parity projection is non-negligible; thus, the density profiles obtained from the fluorescence images are no longer a faithful representation of the original density distribution, but modulo two. This parity projection effect should also wash out any spatial feature of the correlation, namely the information on the thermal de Broglie wavelength.

Although the density profile is inevitably altered by the parity projection, we argue that the correlation function should remain unaffected for BECs. This is because the BEC's $g^{(2)}(r)$ correlation function does not exhibit any spatial features, similar to classical particles. As a result, the density-density fluctuations after parity projection

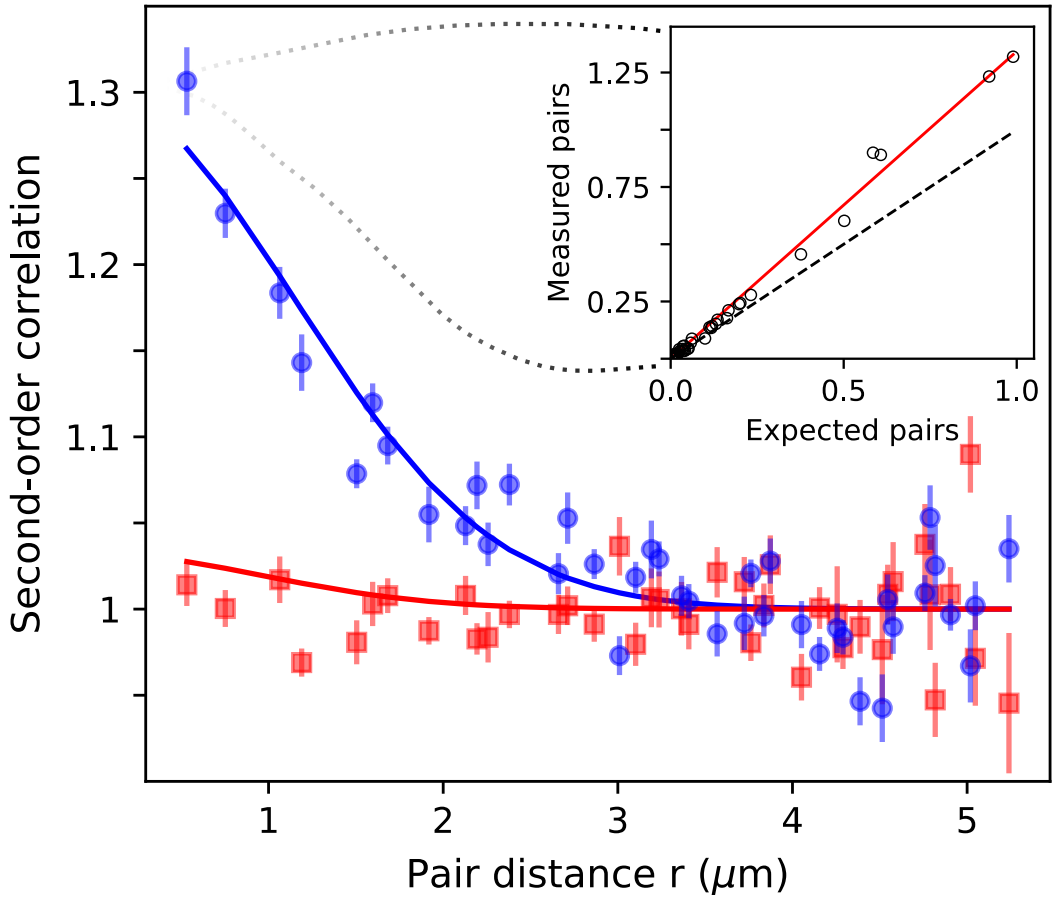

Figure 7-5: **Spatial and thermal dependence of the second-order correlation function.** $g^{(2)}(r)$ correlations determined from *in situ* microscope images are plotted for ensembles at temperatures $T = 6.5$ nK (blue circle) and 54 nK (red square), respectively. The solid lines are fits using Eq. (7.6), including corrections for higher motional n_z states and pinning lattice blurring. The thermal de Broglie wavelength is a fixed parameter. Both datasets are normalized by the mean of measurements at distance $r > 3$ μm, where no correlations are expected. Inset: For nearest-neighbor (NN) pairs, the number of measured pairs in 10×10 regions (see Fig. 7-4(c)) are plotted against the classical expectations. The red solid line is a linear fit to the data, while the black dashed line is the classical expectation. The fitted slope directly gives $g^{(2)}(r = a_{\mathrm{lat}})$, and the standard deviation of the fitted slope is used as the error bar in the main plot.

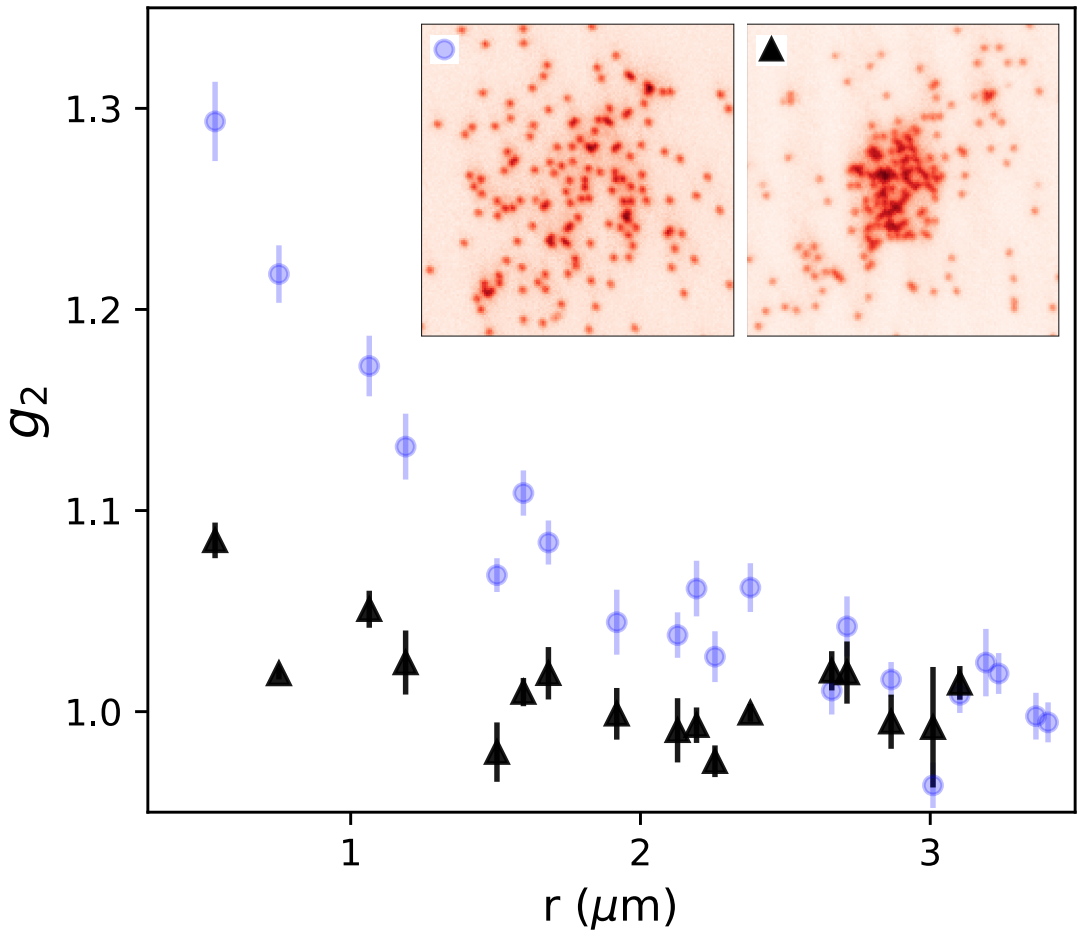

Figure 7-6: **Second-order correlation function evaluated in the thermal gas vs. in the BEC.** $g^{(2)}(r)$ correlations determined from *in situ* microscope images are plotted for thermal gas at temperatures $T = 6.5$ nK (blue circle) and BEC (black triangle), respectively. Insets: Typical fluorescence images of a thermal gas (blue circle) and a BEC (black triangle). Compared to the dilute thermal gas, the condensate clearly shows a dense core at the center in the spatial domain.

should also show no correlations, as confirmed by our data. In this sense, despite the effect of parity projection, our results remain consistent with the theoretical predictions for BECs.

To sufficiently probe the correlations of the BEC under the microscope, we need to prepare BEC samples at much lower temperatures and lower densities. However, at that low density, the requirements for repeated measurements are going to be much higher. More images are needed to obtain good statistics.

7.3.3 Systematic errors

Atom number fluctuation

For the cold ensemble, we average over approximately 650 images to determine the probability of detecting one particle per site, denoted by $\langle p \rangle$, where $\langle \cdot \rangle$ represents the ensemble average over experimental realizations. When p varies from shot to shot through total atom number fluctuations, the measured number of pairs will be enhanced due to the Cauchy-Schwarz inequality: $\langle p^2 \rangle \geq \langle p \rangle^2$. Therefore, in the first analysis, when we normalize the number of observed pairs by $\langle p \rangle^2$, we obtain an enhanced $g^{(2)}$ function. However, this effect does not depend on the pair separation distance r, it only contributes an overall scaling factor to the absolute value of $g^{(2)}(r)$ across all pairs. This was verified by numerical simulations of classical particles with added atom number fluctuations. We confirmed that such fluctuations indeed only contribute an overall scaling factor that is independent of pair separation.

Therefore, in the data analysis, we normalize $g^{(2)}(r)$ by the pairs separated at a distance larger than 3 μm where density fluctuations are uncorrelated. We also tried to post-select data based on total atom number and observed very similar results.

Spatial inhomogeneity

In the experiment, we determine the single particle filling probability for a region to be $\bar{p}$, where the average is taken over a spatial region. Within this region, consider a pair located at $(\mathbf{r}_1, \mathbf{r}_2)$ with corresponding local single-particle filling probabilities of p_1

and p_2 which are slightly different from $\bar{p}$ due to spatial inhomogeneity. The measured number of those pairs is proportional to $p_1 p_2$, whereas the number of uncorrelated pairs with short separation at positions r_1 and r_2 is proportional to $\bar{p^2} = \frac{p_1^2+p_2^2}{2}$. The inequality $(p_1 - p_2)^2 \geq 0$ implies $\frac{p_1^2+p_2^2}{2} \geq p_1 p_2$. This means that even for classical particles, the number of pairs will be smaller for larger pair separation.

This affects the data analysis because we use the pairs separated at a distance larger than 3 μm to normalize the absolute value of $g^{(2)}(r)$.

To address this issue, we segment the total field of 70×70 sites into 49 smaller 10×10 boxes, each with a different local density which is now almost homogeneous within the box. We then plot the measured number of pairs against the expected number of pairs in each box and fit a line $y = ax$ to the data. The slope of this line is the $g^{(2)}$ value for the specific pair separation r. Despite this approach, there remains approximately 10% residual spatial inhomogeneity for pairs separated by 5 μm within each 10×10 box. In the presence of a density gradient, the correction between $\bar{p^2}$ and $p_1 p_2$ simply varies quadratically as the pair separation r increases:

$$\frac{p_1 p_2}{(p_1^2 + p_2^2)/2} = \frac{1 - \Delta^2}{1 + \Delta^2} \approx 1 - 2\Delta^2 = 1 - cr^2 \tag{7.5}$$

where $p_1 = \bar{p}(1 + \Delta)$, $p_2 = \bar{p}(1 - \Delta)$ and $\Delta \propto r$.

To validate this correction, we conducted numerical simulations of classical particles drawn from the experimentally measured density distribution. Feeding the simulated data, which we expect to yield $g^{(2)}(r) = 1$, into our data analysis pipeline confirmed this quadratic correction, in agreement with the prediction above from the simple linear gradient model. The results are summarized in Fig. 7-7. We observed similar behavior in the initial data analysis of the hot sample where $g^{(2)}(r) \approx 1$, confirming the need for this classical systematic correction.

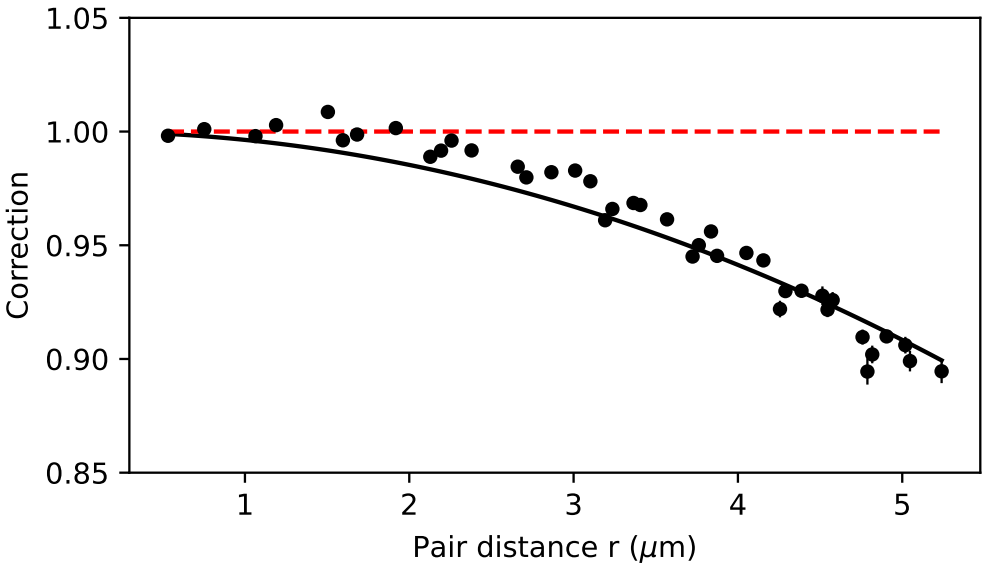

Figure 7-7: **Correction for spatial inhomogeneity.** For classical particles drawn from a uniform spatial density distribution, the $g^{(2)}$ function should measure 1 for all pair distances (red dashed line). Due to residual spatial inhomogeneity within each 10×10 box, the pair-counting method used to determine $g^{(2)}(r)$ will provide a systematically smaller number of pairs at large distances. This requires a correction of approximately 10% for pairs separated by 5 μm. The figure shows the number of pairs of numerically simulated classical particles drawn from the experimentally measured density distribution (black dots). The error bars represent the standard error of the mean across 100 independent numerical simulations. The number of pairs is normalized to one at zero distance. The behavior is well captured by a quadratic function, $y = 1 - cr^2$, where c is a fitting parameter (black solid line).

7.4 Quantum point spread fucntion

When extrapolated to $r = 0$, the observed correlation function $g^{(2)}_{\text{obs}}(r)$ for the cold sample approaches a value of 1.3, rather than the expected value of 2. This can be attributed to the finite spatial resolution of the pinning lattice and the fact that the system is not truly two-dimensional. Our systematic understanding of this reduction can be described by the following function:

$$g^{(2)}_{\text{obs}}(r) = 1 + \eta \frac{l^2}{\tilde{l}^2} \exp\left[-\frac{r^2}{2\tilde{l}^2}\right]. \tag{7.6}$$

In this expression, η accounts for effects that display a global reduction of $g^{(2)}_{\text{obs}}(r) - 1$ (independent of r). The finite spatial resolution σ of the underlying pinning lattice [132] broadens the correlation length l to $\tilde{l} = \sqrt{l^2 + (\sqrt{2}\sigma)^2}$.

When using a pinning lattice to probe free-space atoms, the spatial resolution is not limited by the optical resolution, as long as high-fidelity image reconstruction is achieved under the quantum gas microscope. However, due to the discretized nature of the pinning lattice, the atom's position cannot be resolved beyond the lattice spacing. Consequently, the observed density distribution is the convolution of the true continuous density distribution with the lattice-imposed spatial resolution [121, 132]. This effect broadens the profile of $g^{(2)}_{\text{obs}}(r)$ and lowers its value at $r = 0$.

7.4.1 Quench dynamics

The best scenario would be for the atom to fall into the nearest lattice well. Even in the best scenario, this protocol still acts like a low-pass filter that cannot process any spatial feature smaller than the Nyquist theorem would allow.

In addition to the fundamental limitation of the discretization, the effects of the pinning lattices can also depend on the dynamics of the lattice ramping.

If the lattice is ramped too fast, the atoms can be projected onto a high lattice band which has a non-negligible tunneling rate even in deep lattices. This effect may cause additional blurring in determining the position of the atoms. Thus, there exist

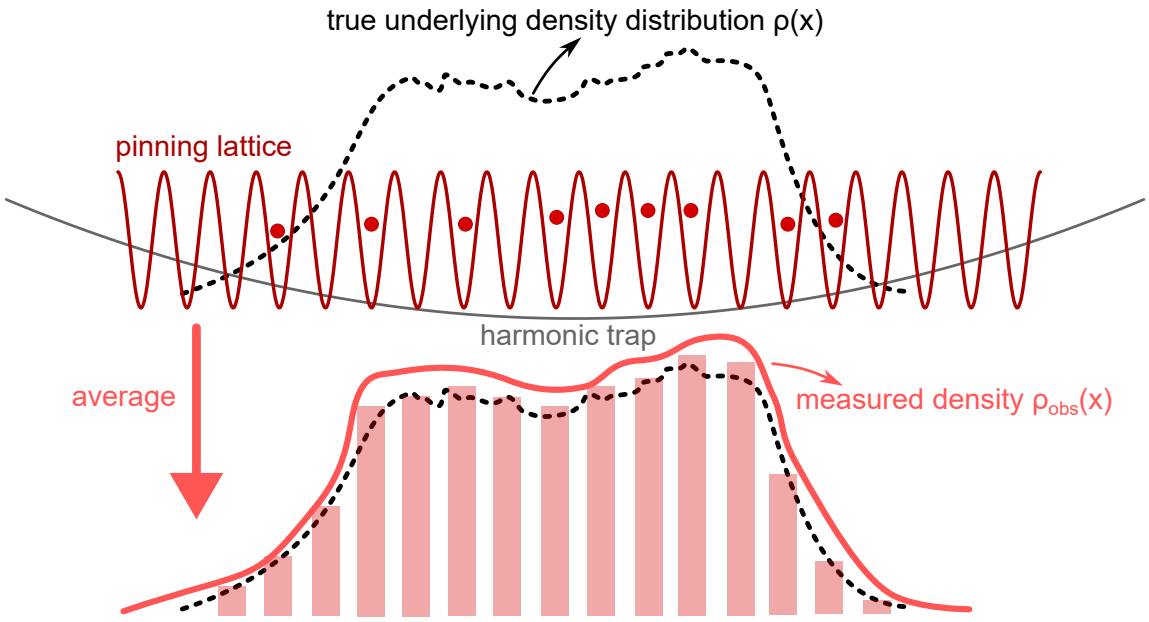

Figure 7-8: **Illustration of how pinning lattices are used to sample the density distribution of an ultracold gas in a continuum, along with their limitations.** The actual density distribution of cold atoms in a harmonic trap is a continuous function. In our measurement protocol, pinning lattices are quenched on to freeze the motion of the atoms. The same experimental sequence is repeated multiple times to obtain a statistical average of the measured density profile. As a result, the measured profile will deviate from the true underlying distribution.

an optimal region of the ramping speed where the measured density profile resembles most to the true underlying density distribution.

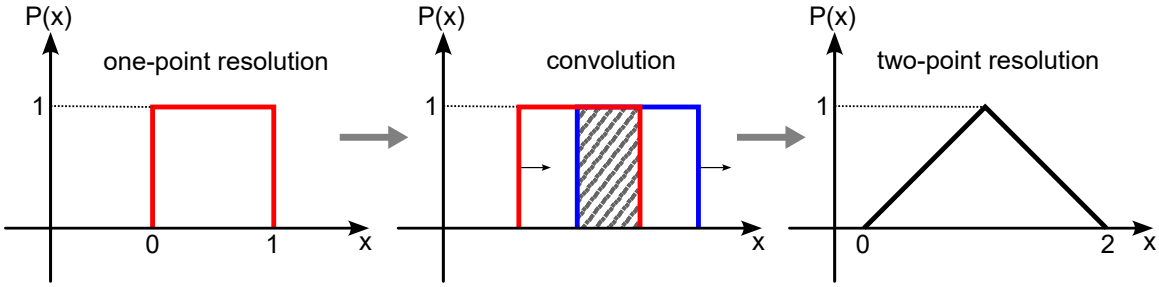

Figure 7-9: **Fundamental resolution limit for one-point and two-point detections.**Using a pinning lattice to sample the density from a continuum may encounter a fundamental resolution limit. According to the Nyquist theorem, discretized sampling cannot resolve spatial frequencies higher than the allowed limit. When an atom is pinned to its nearest lattice site, its original position is confined within a box of width 1 lattice site and height 1. Measuring the second-order correlation involves the two-particle nature of the system, convolving the single-particle resolution. This results in a triangular correlation function with a base of 2 lattice sites and a height of 1.

From a pure classical picture, consider billiard balls and a grid. Using the grid to discretize and determine the position of the ball has an ultimate resolution limit. The original position of the ball cannot be determined to be better than 1 grid size since the ball falling to its nearest grid well is the best situation without any additional blurring. In a one-dimensional case, this can be expressed as a boxcar function. When measuring the second-order correlation function $g^{(2)}$, the two boxcar functions will convolve with each other and produce a triangular blurring kernel, which has a base of 2 and a height of 1 [140]. Since the system is separable, when generalized to a two-dimensional sample, the two-point blurring kernel becomes the product of two triangular functions: one in the x direction and one in the y direction.

7.4.2 Model the blurring

The measured $g^{(2)}_{\text{obs}}$ correlation function is diminished by the finite resolution of the quantum gas microscope. As pointed out in Ref. [141], the microscope has a "quantum point spread function" limited by the fidelity of the pinning procedure. We

qualitatively model this effect as a Gaussian blurring process. Blurring effects on the $g^{(2)}$ function from finite detector resolution have already been modeled for previous experiments in Ref. [132]. In the absence of atoms in the BEC state, the $g^{(2)}$ function can be rewritten as the un-normalized $G^{(1)}$ function:

$$g^{(2)}(0,0) = 1 + \frac{|G^{(1)}(0,0)|^2}{\rho(0)^2}. \tag{7.7}$$

Next, we express the G_1 correlation function as a Gaussian

$$G^{(1)} = \exp\left(-\pi \frac{r^2}{\lambda_{\mathrm{dB}}^2}\right) = \exp\left(-\frac{r^2}{4l^2}\right), \tag{7.8}$$

parameterized by a correlation length $l = \lambda_{\mathrm{dB}}/(2\sqrt{\pi})$, which is the Gaussian standard deviation for the $G^{(2)}$ function. The correlation length is substantially shorter than λ_{dB}.

Next closely following the derivation from Ref. [132], we determine how finite spatial resolution affects the experimentally observed correlation function $G^{(1)}_{\mathrm{obs}}$. The effective imaging resolution is modeled by convoluting $G^{(1)}$ with a Gaussian of standard deviation σ:

$$|G^{(1)}_{\mathrm{obs}}(x,x')|^2 = \int dx_0 dx_0' |G^{(1)}(x_0,x_0')|^2 \times \frac{e^{-(1/2)[(x-x_0)/2\sigma]^2}}{\sqrt{2\pi}\sigma} \frac{e^{-(1/2)[(x'-x_0')/2\sigma]^2}}{\sqrt{2\pi}\sigma} \tag{7.9}$$

$$= \frac{|A|^2}{\sqrt{1+2\sigma^2/l^2}} e^{-(x-x')^2/[2(l^2+2\sigma^2)]}. \tag{7.10}$$

Evaluated at $(x = 0, x' = 0)$ we have:

$$g^{(2)}_{\mathrm{obs}}(0,0) - 1 = \frac{|G^{(1)}_{\mathrm{obs}}(0,0)|^2}{\rho_{\mathrm{obs}}(0)^2} = \prod_{\alpha=x,y} \frac{1}{\sqrt{1+2\sigma_\alpha^2/l_\alpha^2}} = \frac{l^2}{2\sigma^2+l^2}. \tag{7.11}$$

Using our experimental parameters $\lambda_{\mathrm{dB}} = 2.32\ \mu$m, $l_\alpha = 1.23 \times 532$ nm, and fitted $\sigma = 1.25 \times 532$ nm we find $\frac{l^2}{l^2+2\sigma^2} = 0.33$ when performing a 2D convolution.

When atoms are projected onto a lattice with period a_{lat}, the point spread function of a simple classical model is a boxcar function with a full width at half maximum (FWHM) of a_{lat}, which corresponds to a rms width of $\sigma_{\mathrm{classical}} = a_{\mathrm{lat}}/\sqrt{12}$. For the

distance between two atoms, the instrumental function is the convolution of this box with itself, producing a triangular function of FWHM a_{lat} (rms width $a_{\mathrm{lat}}/\sqrt{6}$). We model our resolution as a Gaussian with an effective rms width σ. The rms length of the measured second-order correlation function is broadened to $\tilde{l} = \sqrt{l^2 + (\sqrt{2}\sigma)^2}$, where the $\sqrt{2}$ factor reflects the spatial resolution for detecting two-particle correlations. We fit our data using Eq. (7.6), where we fix η from independent measurements and use only σ as an adjustable parameter. We obtain $\sigma = 1.25\ a_{\mathrm{lat}}$. The additional broadening compared to the classical limit is likely caused by the dynamics during the fast lattice ramp, as this can cause atoms to be excited to higher bands and have significant tunneling rates [48,141]. It is an interesting question for future research to determine the ultimate quantum point spread function for a quantum gas microscope.

7.5 Other corrections

7.5.1 Quasi two-dimensionality

Even with perfect spatial resolution, the amplitude of $g^{(2)}_{\mathrm{obs}}(r)$ can be reduced by line-of-sight integration, as we are probing a quasi two-dimensional sample. This effect does not broaden the profile of $g^{(2)}_{\mathrm{obs}}(r)$ and is represented by the η factor in Eq. (7.6). In a purely two-dimensional gas, where only the ground state of the vertical trapping potential is populated, this effect would be eliminated.

Atoms in different n_z states of the vertical harmonic oscillator potential are "distinguishable" and therefore uncorrelated, reducing the $g^{(2)}$ contrast. We know the state populations based on the thermometry. The fraction of atoms in a n_z level is denoted P_{n_z}. We calculate $P_0 = 0.95$ using Eq. (7.2) with the fitted experimental temperature. We note that our system is thermodynamically well approximated by a Maxwell-Boltzmann distribution ($P_0^{\mathrm{MB}} = 0.94$).

We evaluate the first three z levels and calculate the correction:

$$\eta = P_0^2 + P_1^2 + P_2^2 = 0.91 \tag{7.12}$$

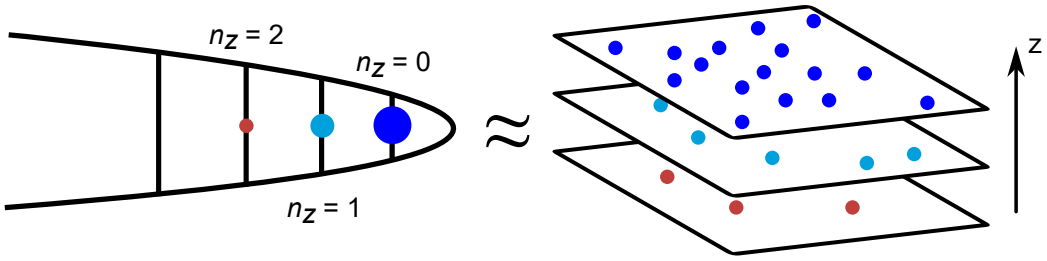

Figure 7-10: **Illustration demonstrating how the finite trap frequency along the z-direction reduces the contrast of the second-order correlation function.** Because the gas is at a finite temperature and subject to a finite trapping frequency along the z-direction, the atoms also occupy excited states in that axis. When the z coordinate is integrated out to reduce the three-dimensional correlation function $g^{(2)}(x, y, z)$ to its two-dimensional counterpart $g^{(2)}(x, y)$, atoms with different n_z quantum numbers remain orthogonal. This can be understood by viewing the system as multiple layers along the z-axis, each separated by a distance much greater than the correlation length. As a result, atoms in different layers do not interfere with each other.

7.5.2 Finite system size corrections

Another fundamental reduction of the contrast is due to the effect of finite particle numbers [142]. As the enhanced correlations are due to exchange terms, they are reduced by $(N-1)/N$, as there is no exchange of a boson with itself. This effect can already be seen from the semi-classical model indicated by Eqn. 6.22. More importantly, near the phase transition, the lowest states are already populated with multiple atoms, and this reduces the exchange terms further.

Canonical vs. grand canonical ensemble

While equivalent in the thermal dynamic limit, the choice of canonical vs. grand canonical ensemble can lead to different predictions when the particle number is finite. This is close to the regime where our experiment works. Here I will first show that a grand canonical ensemble will predict a $g^{(2)}(0) = 2$, no matter how many particles N are in the system. However, the $g^{(2)}(0)$ will be modified if we assume to use the canonical approach, which is more realistic to the real experiment.

The derivation starts by looking at the case of N particles in a box, which has simple solutions [143]:

$$G^{(2)}(r=0) = \Big\langle \frac{1}{V^2} \sum_{k \neq l} 2 n_k n_l + \frac{1}{V^2} \sum_k n_k (n_k - 1) \Big\rangle. \tag{7.13}$$

There are three terms in the summation:

$$2 \sum_{k \neq l} \big\langle n_k n_l \big\rangle + \sum_k \big\langle n_k^2 \big\rangle - \sum_k \big\langle n_k \big\rangle. \tag{7.14}$$

The first term is separable under grand canonical ensemble: $\big\langle n_k n_l \big\rangle = \langle n_k \rangle \langle n_l \rangle$. The second term can be related to the variance of the particle number in a quantum state. In grand canonical formalism, it can be written as $\langle n_k^2 \rangle = 2 \langle n_k \rangle^2 + \langle n_k \rangle$. Then the three terms summation can be expressed as:

$$2 \sum_{k \neq l} \langle n_k \rangle \langle n_l \rangle + 2 \sum_k \langle n_k \rangle^2 = 2 \left[\sum_k \langle n_k \rangle \right]^2 = 2 \langle \hat{N} \rangle^2. \tag{7.15}$$

Thus the numerator $G^{(2)}(r=0) = \frac{2}{V^2} \langle \hat{N} \rangle^2$. Note that the denominator is $\frac{1}{V^2} \langle \hat{N} \rangle^2$. So the normalized $g^{(2)}(0) = 2$ in the grand canonical ensemble regardless of the total atom number.

There is another way to simplify the summation which is more suitable in the canonical ensemble. Instead of breaking the term $\big\langle n_k n_l \big\rangle$, it can be written as:

$$\Big\langle \sum_{k \neq l} n_k n_l \Big\rangle = \Big\langle \left(\sum_k n_k \right)^2 - \sum_k n_k^2 \Big\rangle = \langle \hat{N}^2 \rangle - \sum_k \langle n_k^2 \rangle. \tag{7.16}$$

Then the numerator becomes:

$$G^{(2)}(r=0) = \frac{1}{V^2} \left(2 \langle \hat{N}^2 \rangle - \sum_k \langle n_k^2 \rangle - \sum_k \langle n_k \rangle \right). \tag{7.17}$$

The denominator is still $\frac{1}{V^2} \langle \hat{N} \rangle^2$. However, in the canonical ensemble, there is no fluctuation in the total particle number N, which means $\langle \hat{N}^2 \rangle = \langle \hat{N} \rangle^2 = N^2$. As a result, the second-order correlation function at zero distance $g^2(0)$ will be smaller than 2:

$$g^{(2)}_{\mathrm{c.e.}}(0) = 2 - \frac{1}{N^2}\left(\sum_k \langle n_k^2\rangle + \sum_k \langle n_k\rangle\right). \tag{7.18}$$

As a conclusion, the grand canonical ensemble gives the unphysical result $g^2(0) = 2$, even below the transition temperature and also for a pure condensate. It is well-known that variance in the total atom number N becomes unphysical for ideal Bose gases in the grand canonical ensemble [144,145]. This is the term that exactly cancels the finite-N corrections predicted by the canonical ensemble. We will model this finite-N correction more quantitatively in the following.

Analytical modeling

To simplify the analytical calculation, we model the trap potential for the atoms to be homogeneous instead of harmonic. In a homogeneous two-dimensional box potential, the $g^{(2)}$ function can be expressed at $r = 0$ as [143]:

$$G^{(2)}(r=0) = \frac{1}{V^2}\sum_{k\neq l} 2n_k n_l + \frac{1}{V^2}\sum_k n_k(n_k - 1). \tag{7.19}$$

Given $N^2 = (\sum_k n_k)(\sum_l n_l) = \sum_k n_k^2 + \sum_{k\neq l} n_k n_l$, rearranging terms we arrive at:

$$g^{(2)}(r=0) = 2 - \frac{1}{N} - \sum_k \langle n_k^2\rangle/N^2. \tag{7.20}$$

Eq. (7.20) is exact for the canonical ensemble as demonstrated by Eqn. 7.18. We use $\langle n_k^2\rangle = \langle n_k\rangle^2 + \mathrm{Var}(n_k)$. There is no explicit expression for $\mathrm{Var}(n_k)$ in the canonical ensemble. However, for sufficiently small population numbers, one can regard each state in a bath of the atoms in other states, and use the grand-canonical expression $\mathrm{Var}(n_k) = \langle n_k\rangle + \langle n_k\rangle^2$.

$$g^{(2)}(r=0) = 2 - \frac{2}{N} - 2\sum_k \langle n_k\rangle^2/N^2. \tag{7.21}$$

We numerically solve for $\langle n_k\rangle$ for a range of different N values at $T = T_c$. For a

three-dimensional homogeneous potential, the critical temperature is:

$$k_B T_c^{3D} = \frac{4\epsilon_1}{\pi}\left(\frac{N}{\zeta(3/2)}\right)^{2/3}. \tag{7.22}$$

This is calculated in the thermodynamic limit using an integral with the density of states $N_c = \int_0^\infty d\epsilon\, g(\epsilon)\langle n_k\rangle$, where $g(\epsilon) \propto \sqrt{\epsilon}$ for a 3D box. Here ζ is the Riemann Zeta function and $\epsilon_1 = \pi^2\hbar^2/2mL^2$ is the first excited state energy. At criticality ($T = T_c$) in two and three dimensions, we systematically vary the total atom number N and numerically calculate $g^{(2)}$ from Eq. (7.21). The numerically calculated $g^{(2)}$ function at $r = 0$ is plotted in Fig. 7-11.

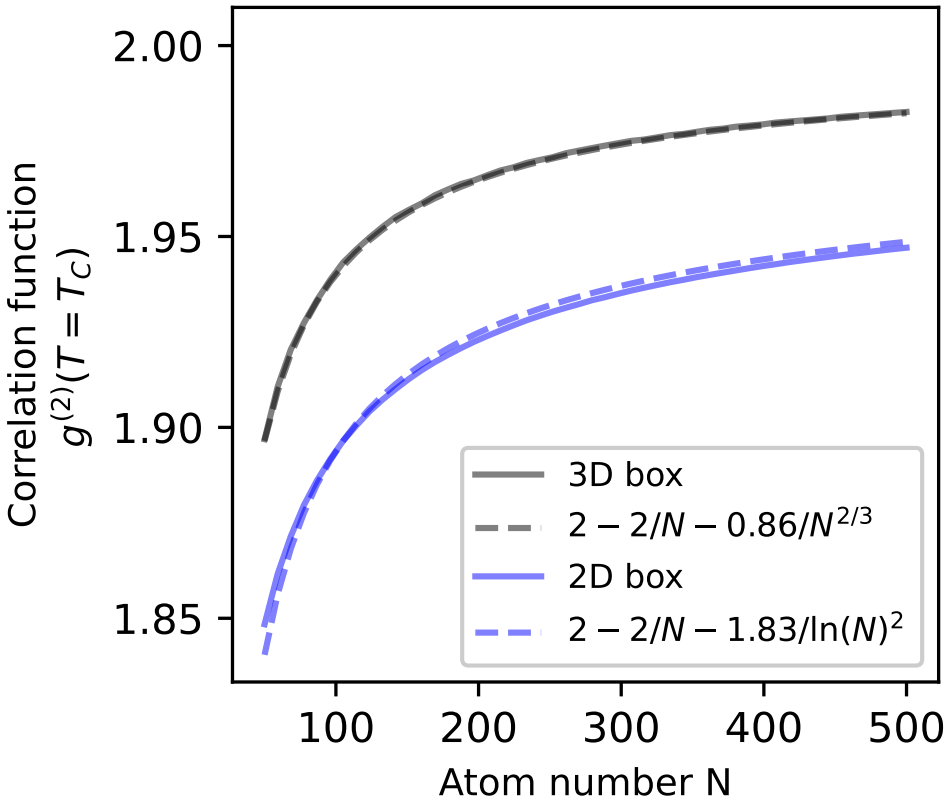

Figure 7-11: $g^{(2)}$ **corrections with finite atom number.** For a 2D and 3D homogeneous potential at $T = T_c$, we vary the total atom number N and numerically determine the state populations $\langle n_k\rangle$ from a Bose-Einstein distribution. From Eq. (7.21), we calculate $g^{(2)}$.

To gain further intuition and to confirm our numerics, we derive an approximate

analytical expression for the $g^{(2)}$ function. This requires obtaining an analytical expression for $2\sum_k \langle n_k\rangle^2/N^2$. These sums can first be written as integrals evaluated in a 3D homogeneous potential:

$$\sum_k \langle n_k\rangle^2/N = \int_0^\infty d\epsilon\ g(\epsilon)\langle n_k\rangle^2 / \int_0^\infty d\epsilon\ g(\epsilon)\langle n_k\rangle. \tag{7.23}$$

The integral $\int_0^\infty d\epsilon\ g(\epsilon)\langle n_k\rangle$ is analytically solvable (as in Eq. (7.22)) and equals $\zeta(3/2)\Gamma(3/2) = 2.61\sqrt{\pi}/2$. The integral $\int_0^\infty d\epsilon\ g(\epsilon)\langle n_k\rangle^2$ diverges as $\epsilon \to 0$. To address this we set the lower bound of the integrand at the energy of the first excited state $\beta\epsilon_1$.

$$\frac{1}{\beta^{3/2}} \int_{\beta\epsilon_1}^\infty d\beta\epsilon\ \frac{\sqrt{\beta\epsilon}}{[e^{\beta\epsilon}-1]^2}. \tag{7.24}$$

Applying a Taylor expansion $e^x \approx 1+x$ to isolate the singular behavior, we arrive at $\epsilon^{-1/2}|_{\beta\epsilon_1}^\infty$. Re-writing $\beta\epsilon_1 = \pi/4[\zeta(3/2)/N]^{2/3} = 1.49N^{-2/3}$ and plugging in values, we obtain the key result:

$$\sum_k \langle n_k\rangle^2/N \approx 0.71N^{1/3}. \tag{7.25}$$

Plugging Eq. (7.25) into Eq. (7.21), we obtain an analytical expression for the $g^{(2)}$ correlation function for a 3D homogeneous system.

$$g^{(2)}(r=0) \approx 2 - \frac{2}{N} - 1.4N^{-2/3}. \tag{7.26}$$

The prefactor for the $N^{-2/3}$ term is only an approximation, since we replaced the discrete summation by an integral with a cutoff at ϵ_1. Any other choice of cutoff will yield the same $N^{-2/3}$ term, albeit with a different prefactor.

Another derivation focuses on the lowest energy states. For the lowest energy state, the occupation number $n_0 = -1/\beta\mu$, where μ is the chemical potential. For the first excited state it is $n_1 = 1/\beta(\epsilon_1 - \mu)$. To estimate the scaling of μ at finite particle number, we express the total atom number splitting off the ground state

$$N = \frac{L^3}{\lambda_{\mathrm{dB}}^3} g_{3/2}(z) + \frac{z}{1-z}, \tag{7.27}$$

in terms of the fugacity $z = e^{\beta\mu} = e^{-\alpha}$. Expanding z around $z = 1$ for small α, $g_{3/2}(\alpha) \approx \zeta(3/2) - 2\sqrt{\pi\alpha}$. Plugging into Eq. 7.27, $N = \frac{L^3}{\lambda_{\mathrm{dB}}^3}[\zeta(3/2) - 2\sqrt{\pi\alpha}] + \frac{1}{\alpha}$. Using $N_{\mathrm{c}} = \frac{L^3}{\lambda_{\mathrm{dB}}}\zeta(3/2)$, we obtain $\alpha = [\frac{\zeta(3/2)}{2\sqrt{\pi}}]^{2/3} N_{\mathrm{c}}^{-2/3} = 0.82 N_{\mathrm{c}}^{-2/3} = 0.55\beta\epsilon_1$. Since $1/\beta \propto N^{2/3}$, one finds again an $N^{-2/3}$ correction term for $g^{(2)}$. Our numerical calculations confirm the $N^{-2/3}$ scaling with a fitted prefactor of 0.86.

For a two-dimensional homogeneous system, the density of states is constant. Thus $N_{\mathrm{c}} = \int_0^\infty d\epsilon \langle n_k \rangle$ diverges. To address this, the first excited state ϵ_1 may be used as described in Ref. [134]. Doing this, one arrives at an expression for the effective critical temperature $\tilde{T}_{\mathrm{c}}^{2D}$:

$$N = \frac{k_B \tilde{T}_{\mathrm{c}}^{2D} \pi}{4\epsilon_1} \ln\left(\frac{k_B \tilde{T}_{\mathrm{c}}^{2D} \pi}{4\epsilon_1}\right), \tag{7.28}$$

or in leading order

$$\frac{k_B \tilde{T}_{\mathrm{c}}^{2D} \pi}{4\epsilon_1} = N / \ln N. \tag{7.29}$$

Using the same approximations as in 3D, one finds the population of the low-lying states to be proportional to $\frac{1}{\beta\epsilon_1}$. But now $1/\beta \propto N/\ln N$, and therefore the correction term for $g^{(2)}$ scales with $1/(\ln N)^2$. Numerical calculations (see Fig. 7-11) are in agreement with this predicted scaling. For a 2D homogeneous box at our operating temperature $T/T_{\mathrm{c}}^{2D} = 1.26$ and atom number $N \approx 100$, we obtain a $g^{(2)}$ value of 1.93.

The effect of finite particle number on the correlation function can be further explored experimentally in our system. For a harmonically trapped ideal Bose gas, researchers have predicted intriguing phenomena such as two-body anticorrelation in the density fluctuations when the particle number is finite [142]. With the future addition of a DMD, we will be able to project a box potential to confine atoms in a homogeneous two-dimensional trap. This clean setup will provide a textbook testbed for systematically studying effects that arise from the canonical ensemble formalism.

Chapter 8

Conclusion and Outlook

8.1 Conclusion

8.1.1 Building

This thesis reviews the design, calibration, and implementation of the rubidium quantum gas microscope at BEC4. The microscope can detect individual atoms on single sites, providing high resolution and insights into the many-body system.

A central design feature of the microscope is the customized objective, which is designed to be diffraction-limited with an NA of 0.8. Such a large NA—combined with the fact that the objective is mounted directly on the vacuum viewport—presents several engineering challenges. The optical performance of the system is sensitive to the flatness of the vacuum viewport. This thesis explains how the viewport's surface profile was measured using a white-light interferometer, and how its deformation leads to astigmatism aberration, along with the steps taken to correct it. During alignment and optimization, additional aberrations such as coma and spherical aberration were discovered, analyzed, and ultimately corrected. These efforts in understanding and correcting aberrations are documented in detail.

Alongside the optical engineering work, this thesis also covers the broader requirements for achieving quantum gas microscopy. On the hardware side, the existing apparatus underwent significant upgrades, including a new vacuum system, a new

beam delivery system, and a new magnetic field control setup. On the software side, the thesis includes a detailed discussion of the deconvolution and reconstruction algorithm, which is crucial for obtaining binary lattice occupation information. As a result, the rubidium quantum gas microscope is now capable of imaging single atoms on a lattice grid of 532 nm lattice spacing with high fidelity.

8.1.2 Scientific project

With the help of the quantum gas microscope, the first scientific project we carried out was to use it to measure the spatial density-density correlation in a cold Bose gas. In this project, instead of using the optical lattice to generate a fundamental discretized Hamiltonian for quantum simulation of many-body physics, we simply use it as a pinning lattice to freeze the motion of atoms from the continuum in order to probe their spatial information. This technique has not been established before, and we are among the pioneering works to employ this idea [46–48, 146].

Due to quantum statistics, bosons show bunching at a length scale of the thermal de Broglie wavelength. Previous experiments are almost all Hanbury Brown and Twiss variants for matter waves, in which they probe the correlation in the far field when the correlation length is magnified beyond the detector resolution. The thesis offers a semi-classical picture for understanding bosonic bunching and its magnification in the far field through the speckle pattern generated by the interference of many randomly positioned emitters.

With the high resolution enabled by the quantum gas microscope, we report the first direct *in situ* experimental observation of density fluctuations on the scale of the thermal de Broglie wavelength in an ultracold gas of bosons. Bunching of ^{87}Rb atoms in a quasi-two-dimensional system is observed by single-atom imaging using a quantum gas microscope. Compared to a classical ensemble, we observe a 30 percent enhancement of the second-order correlation function. We show the spatial and thermal dependence of these correlations and systematically examine the factors that may lead to a reduction of the second-order correlation.

8.2 Outlook

8.2.1 Hardware

One immediate hardware upgrade to the machine would be to add optics capable of projecting potentials through the objective—for example, using a digital micromirror device (DMD) [147]. This would allow us to project arbitrary potentials to realize novel quantum systems.

Other hardware upgrades include the ability to detect double occupancy on a single lattice site [136–139], as well as spin-resolved readout of atoms in different hyperfine states [40, 137, 139].

8.2.2 More on *in situ* correlation

A natural direction to pursue is to build upon the capability of *in situ* correlation detection and apply this technique to other quantum systems.

With a homogeneous potential—potentially enabled by a DMD—one could observe modifications to the correlation function near the BEC phase transition, where the correlation length diverges and a power-law decay is expected [148]. Implementing doublon detection would enable the study of correlations at $r = 0$, where the strongest signal is expected, and could also allow probing of interaction effects that are negligible at the length scales explored in this study. Such interaction effects become dominant in a Tonks gas [149], where strong interactions, enhanced by low dimensionality, lead to the fermionization of bosons, resulting in anti-correlations in the *in situ* density profile.

8.2.3 Matter-wave emission

The simplest light-matter system is that of a single atom coupled to a single photon (excitation), which already exhibits rich physical phenomena ranging from spontaneous emission to coherent vacuum Rabi oscillations. Spontaneous emission arises from the irreversible coupling of the excited atom to the continuum of the vacuum

electromagnetic field [150]. In contrast, if the atom couples to discrete modes of the electromagnetic field within a cavity, the system can undergo coherent Rabi oscillations [151].

Cold atoms in optical lattices can be a platform to simulate and study light-matter interactions where the light is replaced by a matter wave, i.e. an atom, in the form of a system of "emitter + matter-wave (excitation)" [152, 153]. In addition to displaying the behaviors described above, a matter-wave analogue with optical lattices provides tunability to enter a non-Markovian regime in which the timescale of the decay of the emitter can be comparable to the analogue to the optical period. As a result, spontaneous emission can be partly reversible in this analogue system.

Our proposed future work will explore matter-wave emission under the microscope. This builds on research at Stony Brook, which has investigated the physics of spontaneous emission and beyond in a cold atom platform with the aid of optical lattices [154, 155].

Specifically, we can engineer a spin-dependent lattice that is experienced by only one hyperfine state $|a\rangle$ and not the other $|b\rangle$. The mapping goes as the following: an unoccupied lattice site corresponds to a ground-state atom, whereas an occupied lattice site (with an atom in the state $|a\rangle$) corresponds to an excited atom. The "atom" can now emit its excitation when state $|a\rangle$ is coupled (via a microwave or Raman transition) to state $|b\rangle$. Using spin-dependent lattices, the atom in the state $|b\rangle$ does not feel the optical lattice and moves away from its origin—it has been emitted into free space and propagates away from the emitter. A non-Markovian regime can be accessed by tuning the strength and frequency detuning of the coupling between atomic states $|a\rangle$ and $|b\rangle$. Thus far, previous studies have relied only on bulk measurements [154, 155]. We aim to leverage the resolving power of the microscope to probe these processes *in situ*.

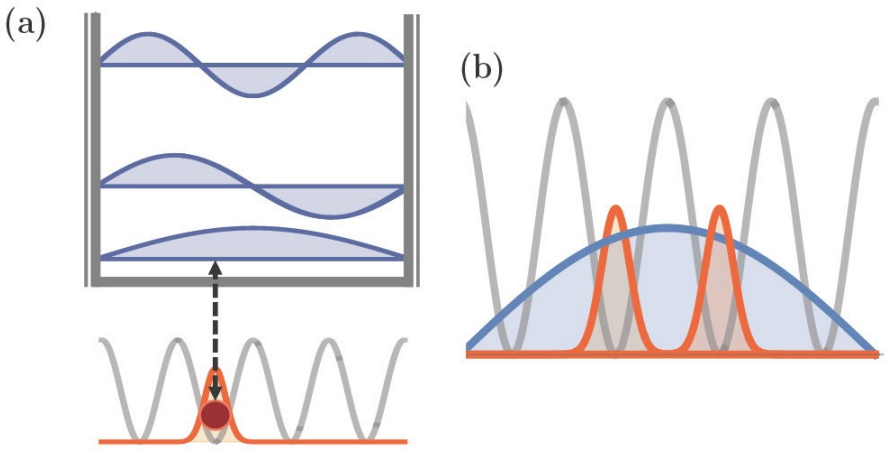

Figure 8-1: **Simulation of matter-wave emission under the microscope.** (a) Bottom: An atom in state $|a\rangle$ is localized in an optical lattice site. A projected repulsive potential creates a box with a length of a few lattice sites. Top: An atom in state $|b\rangle$, which does not feel the lattice, has the discrete energy spectrum of a particle in a box. A microwave drive can couple the $|a\rangle$ atom to a single mode of the matter-wave field. (b) The ground state of the matter-wave overlaps spatially with multiple lattice sites (emitters), which can now constructively interfere in their coupling to the (blue) matter-wave and display the analogue of superradiance.

As illustrated in Fig. 8-1, we propose to study this process with a microscope for a single or controlled number of emitters, and also add (via the projection system) a box around the emitter, analogous to an optical cavity. This will extend the simulation of light-matter phenomena from the spontaneous emission regime to the regime of cavity physics. We will use two hyperfine states of rubidium as $|a\rangle = |F = 1, m_F = -1\rangle$ and $|b\rangle = |F = 2, m_F = 0\rangle$. The microscope, with its ability to address single atoms, makes it possible to prepare a state with a controlled number of lattice occupations instead of an averaged number of occupations. By projecting a repulsive potential, we can create boundaries to prepare bounded chains with any desired number of lattice sites [156], which modifies the energy spectrum for the $|b\rangle$ state from a continuum to discrete energy levels. We can now turn on a microwave coupling from an occupied lattice site to a single mode of the matter wave, as sketched in Figure 8-1(a), and possibly observe Rabi oscillations between the ground and excited states when the

atom is emitted from a lattice site and periodically returns to its initial state. If we program in multiple emitters, as illustrated in Figure. 8-17(b), they could emit into the same mode of the matter-wave field and therefore show collective behavior analogous to optical superradiance.

Appendix A

Preparation of the Spin-Mott State: A Spinful Mott Insulator of Repulsively Bound Pairs

This appendix contains a reprint of Ref. [54]: Julius de Hond, Jinggang Xiang, Woo Chang Chung, Enid Cruz-Colón, Wenlan Chen, William Cody Burton, Colin J. Kennedy, and Wolfgang Ketterle, *Preparation of the Spin-Mott State: A Spinful Mott Insulator of Repulsively Bound Pairs*, Physical Review Letters **128**, 093401 (2022).

Preparation of the Spin-Mott State: A Spinful Mott Insulator of Repulsively Bound Pairs

Julius de Hond, Jinggang Xiang (项晶罡), Woo Chang Chung,* Enid Cruz-Colón, Wenlan Chen,† William Cody Burton,‡ Colin J. Kennedy,‡ and Wolfgang Ketterle

Research Laboratory of Electronics, MIT-Harvard Center for Ultracold Atoms, Department of Physics, Massachusetts Institute of Technology, Cambridge, Massachusetts 02139, USA

(Received 30 September 2021; accepted 28 January 2022; published 28 February 2022)

We observe and study a special ground state of bosons with two spin states in an optical lattice: the spin-Mott insulator, a state that consists of repulsively bound pairs that is insulating for both spin and charge transport. Because of the pairing gap created by the interaction anisotropy, it can be prepared with low entropy and can serve as a starting point for adiabatic state preparation. We find that the stability of the spin-Mott state depends on the pairing energy, and observe two qualitatively different decay regimes, one of which exhibits protection by the gap.

DOI: 10.1103/PhysRevLett.128.093401

Mott insulator states of ultracold atoms in optical lattices have played a central role in ultracold atoms research [1,2]. Because they are a well-isolated low-entropy state protected by an energy gap, such states have been considered as qubits [3], as a starting point for adiabatic state preparation [4,5], and for studies of many-body physics [6], in particular quantum magnetism [7]. They were used in seminal work on Heisenberg spin Hamiltonians [8–10] and as a platform to study Rydberg crystals [11] and magnetic polarons [12].

When the spin degree of freedom is added to a Mott insulator, it opens up low-lying excitations, and much lower temperatures are needed to reach the ground state. For occupations of $N = 1$, the energy scale is set by superexchange, the process by which two spins can be swapped via a virtual intermediate state. This energy scale is often smaller than 1 nK (e.g., for rubidium). As a result, magnetically ordered ground states were only observed using fermionic lithium (which, due to its low mass, has comparatively large tunneling and exchange energies) [13] or using special ramping schemes [14,15].

Because preparing spinful ground states is challenging, many experiments probed spin dynamics through quenches, where an initial spin-polarized state is suddenly rotated into a spin superposition. This has enabled study of transport of bound states [16] and spin waves in isotropic [17] and anisotropic [18,19] $S = 1/2$ Heisenberg models. Recently, we have also studied the relaxation of rotated spin states in $S = 1$ Heisenberg models [20]. Parallel efforts have succeeded in preparing bipartite product states through carefully shaped ramps [21,22].

Here, we show that the situation is drastically different for a spinful Mott insulator with two particles per site. If the on-site interaction energy U_{AB} between opposite spins is considerably lower than that between identical spins (U), there is an effective pairing energy $D = U - U_{AB}$ favoring the formation of repulsively bound pairs of opposing spins. The ground state of the $N = 2$ Mott insulator, then, is a Mott insulator of spin-paired doublons with an excitation gap D. This implies that a spinful $N = 2$ Mott insulator has a region in its phase diagram where the excitation gap is of scale D or U, which typically corresponds to 50 nK for rubidium, and is thus much larger than the superexchange scale (see Fig. 1). As a function of D, there is a phase transition in the spin domain between a spin superfluid (also known as a counterflow superfluid) and a spin insulator. This is in full analogy with the superfluid-to-Mott insulator transition in the charge domain [23]. The spin-Mott state can serve as an ideal starting point for adiabatic preparation of states with different spin ordering [4]. It is also analogous to the band insulator of fermions for $N = 2$ occupation [5], since this state is (in the limit of large pairing energy) a product state of spin-paired doublons on each site.

In this Letter, we demonstrate techniques to prepare and probe the spin-Mott state and study its stability. Our system comprises two different hyperfine states of ^{87}Rb in a (spin-dependent) optical lattice, which are described by the two-component Bose-Hubbard Hamiltonian [24]. In one dimension, and assuming equal tunneling for both components, this is given by

$$H = -t\sum_i (a_i^\dagger a_{i+1} + b_i^\dagger b_{i+1} + \text{H.c.}) + \frac{U}{2}\sum_i \sum_{k\in\{a,b\}} n_i^k(n_i^k - 1) + U_{AB}\sum_i n_i^a n_i^b. \quad (1)$$

Here, n_i^k is the number operator acting on component k on site i, t is the nearest-neighbor tunneling parameter; U and U_{AB} are the intra- and interspecies on-site interactions, respectively, where we have assumed $U = U_{AA,BB}$.

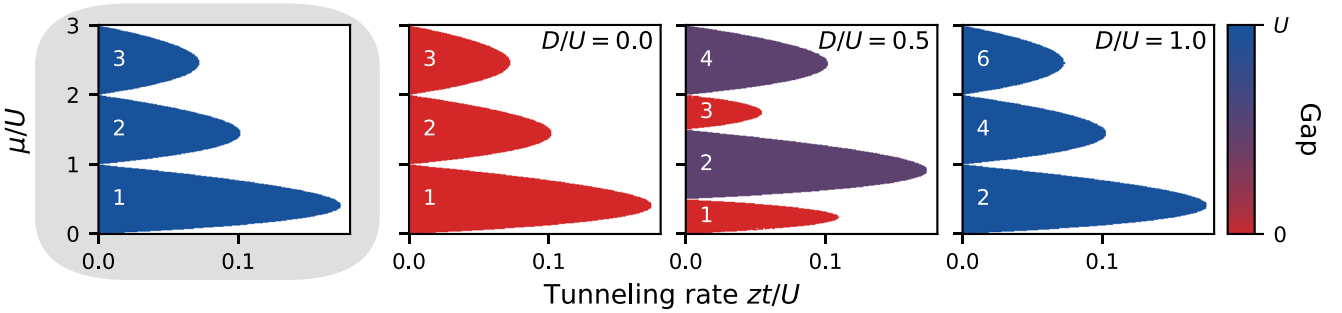

FIG. 1. Mean-field phase diagram of the (two-component) Mott insulator showing the number of atoms per site for a chemical potential μ and tunneling rate t (which, in the mean-field model, is enhanced by the coordination number z). The leftmost panel contains the phase diagram of the single-component system [23]. The other panels, from left to right, show the two-component phase diagram for $D/U = 0$, 0.5, and 1.0. As D increases, the lobes with an uneven number of particles shrink until they vanish because the absence of interactions leads to the formation of two independent Mott insulators. The lobe color indicates the excitation gap. In the single-component system, the first-excited state is a particle-hole pair, which costs an energy U to create. In the two-component system it is a spin excitation with an energy on the order of D. The numbers in the lobes indicate $\langle n\rangle = \langle n^a\rangle + \langle n^b\rangle$.

Restricting ourselves to a deep lattice with two particles per site, this model maps onto an $S = 1$ Hamiltonian [4,24], with the spin-Mott insulator as the ground state for $U_{AB} \ll U$. This is a product state with a single A and B atom per site, which in the spin mapping corresponds to $|S_z = 0\rangle$.

Correlations become important when the pairing and superexchange energy become comparable: $D \approx J \equiv -4t^2/U_{AB}$ [20,25,26]; in this regime second-order tunneling induces quantum fluctuations of the spin around the spin-Mott insulator. Here, the ground state is an xy ferromagnet that contains correlations between sites [4]; this bears resemblance to the superfluid phase of the single-component system, where the excitation gap vanishes, and where number fluctuations drive correlations between sites [23].

Experimental setup.—Our experiment starts with a Bose-Einstein condensate (BEC) of approximately 10^4 atoms. A mixture of the hyperfine states $A = |F = 1, m_F = -1\rangle$ and $B = |F = 1, m_F = 1\rangle$ is created using microwave sweeps, after which the cloud is loaded into a three-dimensional lattice with depths of at least 25 E_R to be deep in the Mott-insulating regime. Here $E_R = h^2/2m\lambda^2$ is the recoil energy of a lattice photon with wavelength λ for an atom of mass m. The interaction between different hyperfine states of rubidium is nearly isotropic [27,28], and hence for any pair $D \approx 0$. The interaction scale U_{AB} can be adjusted, however, by separating the Wannier functions of A and B atoms in the lattice. This can be done using spin-dependent potentials based on the vector AC Stark shift, which separates spin states with different magnetic moments. We create such a lattice using a 810-nm wavelength laser and a tunable polarization gradient [29]. The two transverse lattices are created using 1064-nm light.

Preparing the spin-Mott insulator.—For $D \approx U$, the absence of interspecies interactions leads to the formation of two independent Mott insulators (see Fig. 1). Here, the system exhibits a large excitation gap that we have measured through lattice modulation [29]. This is similar to the single-component case that has a gap of U; hence, it is straightforward to prepare the ground state of Eq. (1). We do so by creating an equal mixture of the two components, followed by a ramp of the lattice while maintaining $D \approx U$. If the atom number is adjusted to fall within the $N = 2$ Mott insulator plateau (but such that it avoids the $N = 3$ sector), we prepare a highly ordered spin state with the same wave function on every site.

The pairing fraction is measured using the detection protocol as described in Ref. [20]; in short, we quench to $D = 0$ (see insets in Fig. 3), and take three measurements using absorption imaging: one of the total atom number, one of the atom number after removing all pairs using a Feshbach resonance, and one after selectively removing just the AB pairs using a Feshbach resonance [36]. The removal procedure has been measured to saturate the losses over the time during which it is applied, from which we conclude it to be efficient. The pairing fraction is given by the ratio of differences of these measurements, which makes it susceptible to shot-to-shot number fluctuations. To mitigate this, all data presented throughout is obtained as the average of three measurements in each of the three channels, with the error bar reflecting the standard error of the mean. Our measurement protocol directly determines the spin temperature of the system. It is not affected by holes and singly occupied sites (it is affected by triplons, which we minimize by our state preparation protocol).

To highlight the correspondence between the spin-Mott insulator and its single-component cousin, we have measured the characteristic superfluid-to-Mott insulator phase transition [37]. Both components were imaged individually using Stern-Gerlach separation during time of flight; see Fig. 2. From these images, we can determine the condensate fractions in each state. Using our pair measurement

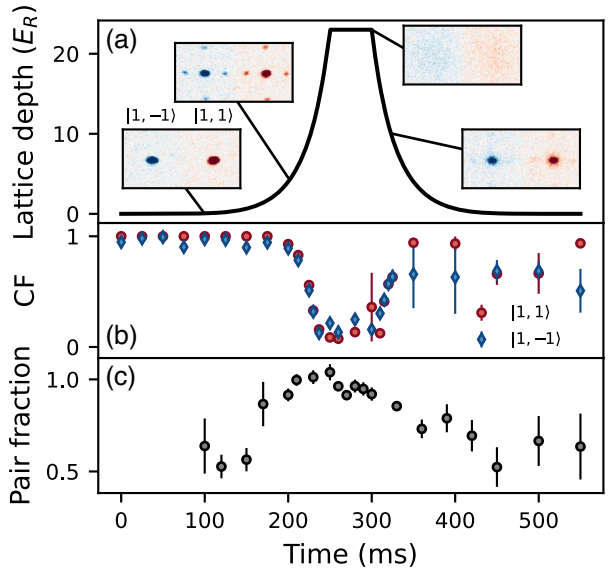

FIG. 2. The superfluid-to-Mott insulator phase transition for a system with two spin states. (a) Starting with a spinor BEC in an equal superposition state of $|1,-1\rangle$ and $|1,1\rangle$, we ramp up the lattice into the Mott-insulating regime while $D = U$. (b) In the Mott plateau, we observe a dip in condensate fraction (CF), while (c) the pairing fraction approaches unity.

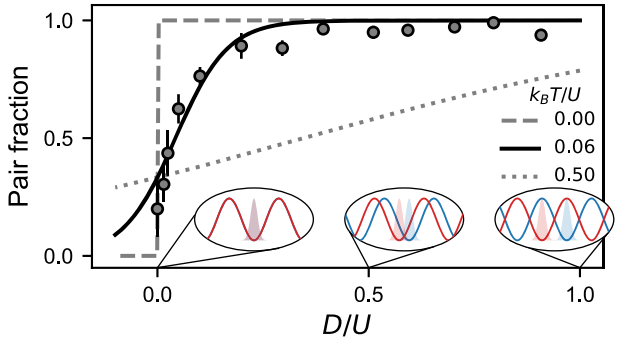

FIG. 3. Preparation of the spin-Mott state for various pairing energies D. The decrease of the spin pairing fraction for small D is explained by a finite temperature. Lines are based on the model of Eq. (2) at various temperatures. Insets: lattice configuration at various values of D/U.

protocol, we verify that the spin-Mott insulator (realized for deep lattices) has a pairing fraction close to unity.

The gap of the spin-Mott state shrinks as D is decreased. We have explored how small D can become before we observe a degradation of the spin-Mott state due to finite temperature or nonadiabatic loading. Figure 3 shows the initial pairing fraction as a function of D, after ramping into a deep lattice (23 E_R). We find that it is possible to attain high pairing fractions of over 0.9 for a wide range of initial values of D.

According to matrix product–state calculations, the spin-Mott state is the ground state for $D > 0.05U$ at a lattice depth of 8 E_R [4]. The imperfect pairing fraction observed for $D < 0.2U$ in a 23 E_R lattice can be explained by finite spin temperature. We can deduce the temperature from a model where tunneling is assumed to be negligible, and hence the Hamiltonian is diagonal on each site in the basis $\{|AA\rangle, |AB\rangle, |BB\rangle\}$. Generalizing the treatment of a single-component Mott insulator [38], we obtain the pairing fraction (i.e., the population in $|AB\rangle$), for a thermal state $|\psi_T\rangle$ at temperature T as

$$|\langle AB|\psi_T\rangle|^2 = [1 + 2\exp(-D/k_BT)]^{-1}. \quad (2)$$

Fitting this expression to our data, we obtain $k_BT/U \approx 0.06 \pm 0.01$, which corresponds to 4 ± 1 nK for $U/2\pi \approx 1300$ Hz. This is comparable to temperatures reported for single-component Mott insulators [39,40]. We expect that the charge temperature (set by defects) and the spin temperature are in equilibrium during the lattice ramp while tunneling is fast. After loading, the charge temperature increases by diffusion of defects from outer parts of the cloud, while the spin temperature is protected as long as $D \gg t$ (see Fig. 4). The latter is lower than the temperature of the initial BEC due to adiabatic cooling during the lattice ramp [4]. Figures 2 and 3 represent the main result of this Letter: the successful preparation of the ground state of a spinful $N = 2$ bosonic Mott insulator, which has not been accomplished before.

Relaxation behavior.—The decay of the spin-Mott state determines how it can be used as a low-entropy starting point for further experiments. To investigate this, we measure the lifetime as a function of lattice parameters. After the preparation, we ramp D during 100 ms while staying in a deep (25 E_R) lattice—this can be considered a quench since the tunneling rate is on the order of 1 Hz. We then lower the lattice to 16 E_R and measure how the pairing fraction decays.

We can distinguish two qualitatively different relaxation regimes as a function of D; see Fig. 4(a). When quenching D close to 0, the system quickly approaches the thermal state: an incoherent equal mixture of $|AA\rangle$, $|AB\rangle$, and $|BB\rangle$ on every lattice site, which leads to a pairing fraction of $1/3$. For larger values of D the behavior is qualitatively different: not only does the relaxation take longer, the pairing fraction also does not decay to $1/3$ over experimentally accessible timescales; rather it goes to $\sim 1/2$. This is what one would expect if thermalization were constrained to the symmetric subspace; i.e., the states $|AB\rangle$ and $(|AA\rangle + |BB\rangle)/\sqrt{2}$ with each receiving half the population. If all couplings preserve the initial symmetry, the system is constrained to this subspace.

The two different regimes also show up in the relaxation behavior as a function of lattice depth. In Fig. 4(b) we compare the system when held in the spin-Mott phase and after quenching to $D = 0$. For small values of D, the decay rate scales linearly with the tunneling rate, while in the spin-Mott state the decay rate is lattice-depth independent.

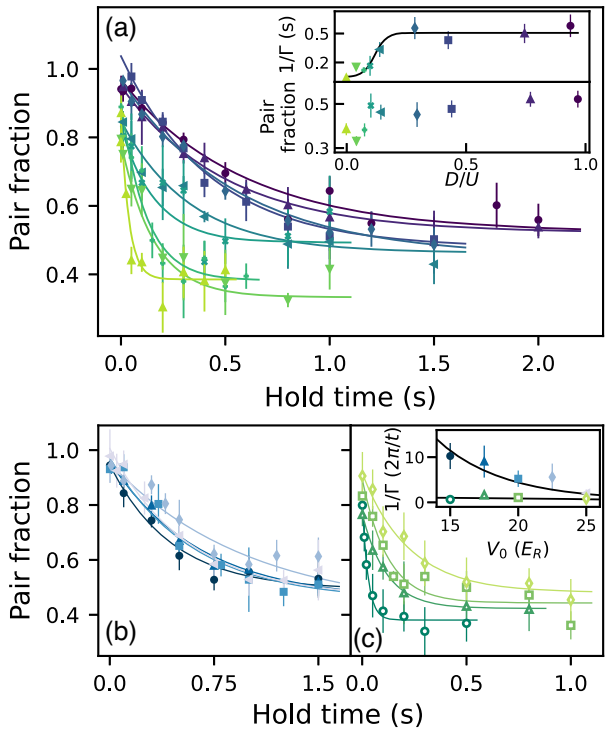

FIG. 4. Lifetime of the spin-Mott insulator. (a) The relaxation shows qualitatively different behavior as a function of D: the pair fraction either approaches the infinite temperature limit ($1/3$, if D is small) or not ($1/2$, if D is large). Different colors represent different values of D/U. Inset: fitted lifetimes $1/\Gamma$ and the equilibrium values of the pair fraction. (b),(c) Lifetime at various lattice depths, represented by different colors, where D is fixed to be either within the spin-Mott insulator [$D = 0.3U$, (b)] or at the isotropic point where $D = 0$ (c). Inset: fitted lifetime for both datasets scaled by the tunneling time $2\pi/t$. For $D = 0$ we observe that the decay scales with tunneling, whereas for $D = 0.3U$ it is independent of t. A single fit of all the lifetimes was done using Eq. (3), which is shown by the black lines.

This behavior is captured by modeling the total decay rate as the sum of a background contribution and a term that depends linearly on tunneling but which is suppressed by D:

$$\Gamma(t, D) = \Gamma_0 + (t/2\pi)/[1 + c_1 \exp(D/c_2)]. \quad (3)$$

Here, c_1 and c_2 are fit parameters, and the form is such that $\Gamma(t, D) \to \Gamma_0$ if D is large, as it is in the spin-Mott insulator. This expression gives us a quantitative description of the lifetimes measured in Fig. 4 (see Ref. [29]).

We conjecture that a combination of factors causes this. For $D \approx 0$ we enter the regime where the temperature of the $N = 2$ plateau is sufficiently large to drive deviations from perfect pairing already observed during loading (see Fig. 3). First-order tunneling with imperfections in the Mott insulator will allow entropy transport from the outer regions of the system inward, which will rapidly increase the spin temperature. This is a plausible explanation for the scaling with tunneling rate.

At higher values of D the excitation gap protects against relaxation. It is seen through longer lifetimes that are lattice-depth independent. This makes it unlikely that the decay is caused solely by either tunneling or light scattering–related mechanisms. This is confirmed by a measurement of a spin-polarized Mott insulator that *does* show a scaling of lifetime with lattice intensity. Nevertheless, the interplay between different effects in our experiment is complicated; increasing the lattice depth increases both light scattering and confinement. With our current setup it is hard to disentangle such mechanisms. The cause of the slow spin relaxation could be mobile atoms in excited bands created by technical noise of the lattice beams, or grazing collisions with background gas atoms.

Discussion and conclusions.—While the spin-Mott insulator is a product state, it can be used as a starting point for adiabatically preparing correlated spin states such as the xy ferromagnet [4,24]. Similar schemes have been proposed for fermions, where the (gapped) band insulator can be used to adiabatically prepare an antiferromagnet [5]. In that case the initial product state is stabilized by the band gap, whereas in our case it is stabilized by the pairing energy D. This difference in energy scales also makes our system suitable for studying spin-charge separation [41].

Adiabatic state preparation requires that the gaps between many-body states are traversed sufficiently slowly; in a Landau-Zener model of avoided crossings, the maximum rate is set by the coupling between states [42–44]. In a deep lattice this scales with second-order tunneling as $\propto 4t^2/U$ [4,20,25]. Furthermore, coupling between different many-body states scales inversely with the number of sites in a chain. For our present system the superexchange scale is maximally 10 Hz at a longitudinal lattice depth of 12 E_R. This is comparable to some of the decay rates reported in Fig. 4. Therefore, attempts to adiabatically sweep the spin-Mott state into correlated spin states were not successful.

Other atomic species are favorable; cesium, e.g., has a larger fine-structure splitting that makes it possible to create a spin-dependent potential at larger detunings with less light scattering. The lanthanides are also attractive because they feature spin-orbit coupling in the ground state, and hence have a vector AC Stark shift for any lattice detuning.

The future addition of a quantum-gas microscope to our setup [45] will mitigate some of these issues. With single-site resolution, experiments can be performed on short chains with definite length that are fully decoupled from surrounding thermal reservoirs.

In conclusion, we have prepared and characterized the spin-Mott state that is the ground state of the two-component Bose-Hubbard model in deep lattices, which can be mapped onto an $S = 1$ Heisenberg Hamiltonian. This state features a large pairing gap, and is a promising platform for adiabatic preparation of magnetic phases and

the study of other many-body phenomena. Additionally, since the spin-Mott state is a product state of repulsively bound pairs it offers a way to study pair superfluidity [46,47] and quantum droplets [48]. Analogous to Ref. [49], one could do this by creating a dilute gas of repulsively bound dimers after reducing the harmonic confinement and emptying out the singly occupied sites.

We thank Yoo Kyung Lee for a critical reading of our manuscript. We acknowledge support from the NSF through the Center for Ultracold Atoms and Grant No. 1506369, ARO-MURI Non-equilibrium Many-Body Dynamics (Grant No. W911NF14-1-0003), AFOSR-MURI Quantum Phases of Matter (Grant No. FA9550-14-1-0035), ONR (Grant No. N00014-17-1-2253), and a Vannevar-Bush Faculty Fellowship. W. C. C. acknowledges additional support from the Samsung Scholarship.

*Present address: ColdQuanta Inc., Boulder, Colorado, USA.
†Present address: Department of Physics and State Key Laboratory of Low Dimensional Quantum Physics, Tsinghua University, and Frontier Science Center for Quantum Information, Beijing 100084, China.
‡Present address: Honeywell Quantum Solutions, Broomfield, Colorado, USA.

[1] I. M. Georgescu, S. Ashhab, and F. Nori, Rev. Mod. Phys. **86**, 153 (2014).
[2] D. Jaksch and P. Zoller, Ann. Phys. (Amsterdam) **315**, 52 (2005), special issue.
[3] C. Weitenberg, M. Endres, J. F. Sherson, M. Cheneau, P. Schauß, T. Fukuhara, I. Bloch, and S. Kuhr, Nature (London) **471**, 319 (2011).
[4] J. Schachenmayer, D. M. Weld, H. Miyake, G. A. Siviloglou, W. Ketterle, and A. J. Daley, Phys. Rev. A **92**, 041602(R) (2015).
[5] M. Lubasch, V. Murg, U. Schneider, J. I. Cirac, and M.-C. Bañuls, Phys. Rev. Lett. **107**, 165301 (2011).
[6] I. Bloch, J. Dalibard, and W. Zwerger, Rev. Mod. Phys. **80**, 885 (2008).
[7] J. J. García-Ripoll, M. A. Martin-Delgado, and J. I. Cirac, Phys. Rev. Lett. **93**, 250405 (2004).
[8] J. Struck, C. Ölschläger, R. Le Targat, P. Soltan-Panahi, A. Eckardt, M. Lewenstein, P. Windpassinger, and K. Sengstock, Science **333**, 996 (2011).
[9] A. de Paz, A. Sharma, A. Chotia, E. Maréchal, J. H. Huckans, P. Pedri, L. Santos, O. Gorceix, L. Vernac, and B. Laburthe-Tolra, Phys. Rev. Lett. **111**, 185305 (2013).
[10] J. Simon, W. S. Bakr, R. Ma, M. E. Tai, P. M. Preiss, and M. Greiner, Nature (London) **472**, 307 (2011).
[11] P. Schauß, J. Zeiher, T. Fukuhara, S. Hild, M. Cheneau, T. Macrı, T. Pohl, I. Bloch, and C. Gross, Science **347**, 1455 (2015).
[12] J. Koepsell, J. Vijayan, P. Sompet, F. Grusdt, T. A. Hilker, E. Demler, G. Salomon, I. Bloch, and C. Gross, Nature (London) **572**, 358 (2019).
[13] A. Mazurenko, C. S. Chiu, G. Li, M. F. Parsons, M. Kanász-Nagy, R. Schmidt, F. Grusdt, E. Demler, D. Greif, and M. Greiner, Nature (London) **545**, 462 (2017).
[14] H. Sun, B. Yang, H.-Y. Wang, Z.-Y. Zhou, G.-X. Su, H.-N. Dai, Z.-S. Yuan, and J.-W. Pan, Nat. Phys. **17**, 990 (2021).
[15] D. Greif, G. Jotzu, M. Messer, R. Desbuquois, and T. Esslinger, Phys. Rev. Lett. **115**, 260401 (2015).
[16] T. Fukuhara, P. Schauß, M. Endres, S. Hild, M. Cheneau, I. Bloch, and C. Gross, Nature (London) **502**, 76 (2013).
[17] S. Hild, T. Fukuhara, P. Schauß, J. Zeiher, M. Knap, E. Demler, I. Bloch, and C. Gross, Phys. Rev. Lett. **113**, 147205 (2014).
[18] P. N. Jepsen, J. Amato-Grill, I. Dimitrova, W. W. Ho, E. Demler, and W. Ketterle, Nature (London) **588**, 403 (2020).
[19] P. N. Jepsen, W. W. Ho, Amato-Grill, I. Dimitrova, E. Demler, and W. Ketterle, Phys. Rev. X **11**, 041054 (2021).
[20] W. C. Chung, J. de Hond, J. Xiang, E. Cruz-Colón, and W. Ketterle, Phys. Rev. Lett. **126**, 163203 (2021).
[21] H. Bernien, S. Schwartz, A. Keesling, H. Levine, A. Omran, H. Pichler, S. Choi, A. S. Zibrov, M. Endres, M. Greiner *et al.*, Nature (London) **551**, 579 (2017).
[22] S. Trotzky, P. Cheinet, S. Fölling, M. Feld, U. Schnorrberger, A. M. Rey, A. Polkovnikov, E. A. Demler, M. D. Lukin, and I. Bloch, Science **319**, 295 (2008).
[23] J. K. Freericks and H. Monien, Europhys. Lett. **26**, 545 (1994).
[24] E. Altman, W. Hofstetter, E. Demler, and M. D. Lukin, New J. Phys. **5**, 113 (2003).
[25] A. B. Kuklov and B. V. Svistunov, Phys. Rev. Lett. **90**, 100401 (2003).
[26] L.-M. Duan, E. Demler, and M. D. Lukin, Phys. Rev. Lett. **91**, 090402 (2003).
[27] D. M. Stamper-Kurn and M. Ueda, Rev. Mod. Phys. **85**, 1191 (2013).
[28] A. Widera, F. Gerbier, S. Fölling, T. Gericke, O. Mandel, and I. Bloch, New J. Phys. **8**, 152 (2006).
[29] See the Supplemental Material at http://link.aps.org/supplemental/10.1103/PhysRevLett.128.093401 for details on the experimental setup, our fitting procedure, and the mean-field model, which includes Refs. [30–35].
[30] R. Grimm, M. Weidemüller, and Y. B. Ovchinnikov, Adv. At. Mol. Opt. Phys. **42**, 95 (2000).
[31] F. Le Kien, P. Schneeweiss, and A. Rauschenbeutel, Eur. Phys. J. D **67**, 92 (2013).
[32] P. L. Gould, G. A. Ruff, and D. E. Pritchard, Phys. Rev. Lett. **56**, 827 (1986).
[33] C. Sias, H. Lignier, Y. P. Singh, A. Zenesini, D. Ciampini, O. Morsch, and E. Arimondo, Phys. Rev. Lett. **100**, 040404 (2008).
[34] R. Ma, M. E. Tai, P. M. Preiss, W. S. Bakr, J. Simon, and M. Greiner, Phys. Rev. Lett. **107**, 095301 (2011).
[35] M. P. A. Fisher, P. B. Weichman, G. Grinstein, and D. S. Fisher, Phys. Rev. B **40**, 546 (1989).
[36] A. M. Kaufman, R. P. Anderson, T. M. Hanna, E. Tiesinga, P. S. Julienne, and D. S. Hall, Phys. Rev. A **80**, 050701(R) (2009).
[37] M. Greiner, O. Mandel, T. Esslinger, T. W. Hänsch, and I. Bloch, Nature (London) **415**, 39 (2002).
[38] F. Gerbier, Phys. Rev. Lett. **99**, 120405 (2007).
[39] J. F. Sherson, C. Weitenberg, M. Endres, M. Cheneau, I. Bloch, and S. Kuhr, Nature (London) **467**, 68 (2010).

[40] W. S. Bakr, A. Peng, M. E. Tai, R. Ma, J. Simon, J. I. Gillen, S. Foelling, L. Pollet, and M. Greiner, Science **329**, 547 (2010).
[41] A. Kleine, C. Kollath, I. P. McCulloch, T. Giamarchi, and U. Schollwöck, Phys. Rev. A **77**, 013607 (2008).
[42] C. Zener and R. H. Fowler, Proc. R. Soc. A **137**, 696 (1932).
[43] L. Landau, Phys. Z. Sowjetunion **2**, 46 (1932); Reprinted as L. Landau, in Collected Papers of L.D. Landau (Pergamon Press, 1965), pp. 63–66, https://www.sciencedirect.com/science/article/pii/B9780080105864500146.
[44] J. R. Rubbmark, M. M. Kash, M. G. Littman, and D. Kleppner, Phys. Rev. A **23**, 3107 (1981).
[45] W. S. Bakr, J. I. Gillen, A. Peng, S. Fölling, and M. Greiner, Nature (London) **462**, 74 (2009).
[46] C. Menotti and S. Stringari, Phys. Rev. A **81**, 045604 (2010).
[47] A. J. Daley, J. M. Taylor, S. Diehl, M. Baranov, and P. Zoller, Phys. Rev. Lett. **102**, 040402 (2009).
[48] I. Morera, G. E. Astrakharchik, A. Polls, and B. Juliá-Díaz, Phys. Rev. Lett. **126**, 023001 (2021).
[49] T. Volz, N. Syassen, D. Bauer, E. Hansis, S. Dürr, and G. Rempe, Nat. Phys. **2**, 692 (2006).

Supplemental Material for
Preparation of the spin-Mott state: a spinful Mott insulator of repulsively bound pairs

Julius de Hond, Jinggang Xiang (项晶罡), Woo Chang Chung,* Enid Cruz-Colón,
Wenlan Chen,† William Cody Burton,‡ Colin Kennedy,‡ and Wolfgang Ketterle
Research Laboratory of Electronics, MIT-Harvard Center for Ultracold Atoms, Department of Physics, Massachusetts Institute of Technology, Cambridge, Massachusetts 02139, USA

SUPPLEMENTAL MATERIALS

Experimental considerations

The experimental setup and sample preparation sequence are similar to what is described in Ref. [S1], except that here we create a spin-dependent lattice using an 810-nm wavelength laser. The laser has a detuning from the D_1 and D_2 lines of ^{87}Rb that is comparable to the fine-structure splitting, and hence there is an appreciable vector AC Stark shift [S2, S3]. The lattice is generated using a polarization gradient, which is created by rotating the linearly polarized input beam using a liquid-crystal rotator before it is reflected back onto the atoms (see Fig. S1). An advantage of the liquid crystal is its large aperture, but it has a finite response time, which puts the lower bound on the sweep rates that can be achieved at approximately 50 ms. The lattice is only spin dependent if the light can have a well-defined circularity; for that it is important that the quantization axis is oriented along the lattice, otherwise each hyperfine state will just see the same potential. This means that this scheme can only generate a spin-dependent lattice along one axis.

The 1D lattice is in a lin-ϑ-lin configuration, where both beams are linearly polarized, and there is an angle ϑ between them. In general, both the intensity and the polarization gradient contribute to the lattice potential via the scalar and vector AC Stark shift, respectively. At the chosen wavelength of 810 nm, the scalar polarizability is larger than the vector polarizability, and therefore $U_{AB} \approx U$ for small polarization angles. U_{AB} tends to zero only for near orthogonal polarizations.

The separation between the two sublattices can be derived by decomposing the the total lattice into a linearly polarized part that affects both components equally (through the scalar AC Stark shift), and two circular parts that are displaced by $\pm\lambda/8$ and that lead to a spin-dependent force (through the vector AC Stark shift), which depends on the polarization angle ϑ. One can show that, as a function of ϑ, the separation between the two sublattices is

$$\Delta x/\lambda = \frac{1}{4\pi} \arccos\left(\frac{\cos^2\vartheta - R^2\sin^2\vartheta}{\cos^2\vartheta + R^2\sin^2\vartheta}\right), \tag{S1}$$

where $R \approx 1/8$ is the vector-to-scalar AC polarizability ratio for ^{87}Rb at our wavelength [S2, S3], which depends on the detuning compared to the fine-structure splitting. For constant input intensity the lattice depth experienced by $F = 1, |m_F| = 1$ atoms scales with ϑ as

$$V_0 \propto \sqrt{\cos^2\vartheta + R^2\sin^2\vartheta}. \tag{S2}$$

Using this, U_{AB} can be calculated through the overlap integral of two Wannier functions which have a relative displacement of Δx, which is the value used to obtain D in the main text (see Fig. S2 for the numerical result). The scaling of Eq. (S2) was confirmed by measuring the lattice depth at various angles through Kapitza–Dirac diffraction [S4], see the right panel in Fig. S2.

To confirm the calibration of U_{AB}, we loaded a small number of atoms into a lattice without any polarization gradient ($\vartheta = 0°$) avoiding any major population of doubly occupied sites. We then rotated the lattice angle away from zero and lowered the longitudinal lattice depth to 14 E_R while the transverse lattices were held at 35 E_R. Formation of doublons by tunneling was induced by applying a sinusoidal modulation to the lattice depth of $\pm 10\%$. Modulating at a frequency of $U_{AB}/\hbar$ ($U/\hbar$) induces doublon formation between different (the same) spin states [S5, S6].

The formed pairs are detected by selectively inducing

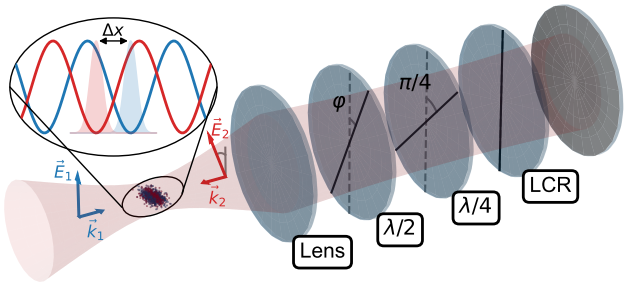

FIG. S1. Experimental setup for creating the the spin-dependent lattice. The input beam is reflected through standard wave plates ($\lambda/2$ and $\lambda/4$ signify a half- and quarter-wave plate, respectively) and a liquid-crystal rotator (LCR), which has a tunable retardance. The solid lines denote the slow axes of the polarization components. They rotate the polarization by $\vartheta = 4\varphi + \eta$ in total, where η is the retardance of the LCR.

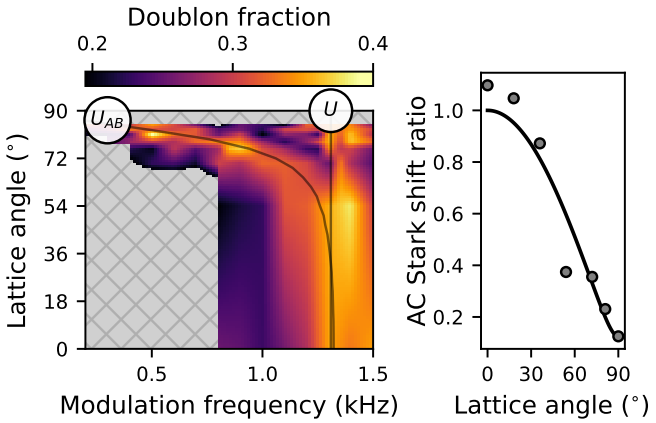

FIG. S2. Characterization of the lattice and interaction energies. Left: U and U_{AB} are observed as two separate energy scales through lattice modulation spectroscopy. The measurements were done at different lattice angles, and we interpolated the data in between. The solid lines are calculations based on the overlap of Wannier functions using the lattice separation Δx of Eq. (S1). Right: Measurement of lattice depth for $m_F = 1$ atoms using Kapitza–Dirac scattering. The ratio of lattice depths at $\vartheta = 0°$ and $90°$ is roughly 1/8, as predicted using the lattice wavelength and the fine structure of rubidium.

losses on doubly-occupied sites. Our method is described in detail in Ref. [S1]; briefly, we rotate the lattice back to $\vartheta = 0°$ and transfer the atoms to a pair of states that has a narrow Feshbach resonance at a magnetic field close to 9 G [S7]. By modulating the field around this value, atoms in doubly-occupied sites undergo a loss process. The doublon fraction is obtained by taking the ratio between shots with and without induced losses; Fig. S2 shows the spectroscopic measurement of pairing energies.

Fitting the relaxation behavior

The phenomenological decay rate function of Eq. (3) is inspired by the measurement presented in Fig. 3, where we observe a high-quality spin-Mott state as long as D is above some threshold. Below that threshold thermal effects start to play a role, and we assume that a similar mechanism affects the lifetime: As the gap shrinks, the system is no longer protected from tunneling from the outer shells of the Mott insulator, and we expect the lifetime to scale with the tunneling rate.

The solid lines shown in Fig. 4 are based on an overall fit to the lifetime data to Eq. (3) using $c_1 = 0.086$, $c_2 = 0.025U$, and $\Gamma_0 = 2.0\ \mathrm{s}^{-1}$.

Mean-field phase diagram

We have extended the mean-field treatment of the single-component Bose–Hubbard Hamiltonian (see e.g. Refs. [S8, S9]) to the two-component case of Eq. (1). There are two types of particles annihilated (created) by the operators acting on site i: a_i ($a_i^\dagger$) and b_i ($b_i^\dagger$). Under the assumption that the correlations between sites are small, we can replace the operators by their deviation from the mean field (e.g. by setting $a_i = \langle a\rangle + \delta a_i$ and neglecting cross terms such as $\delta a_i \delta a_j$). This results in the mean-field Hamiltonian:

$$H_{\mathrm{MF}} = \sum_i \Big[-zt\Big(\alpha a_i^\dagger + \alpha^* a_i + \beta b_i^\dagger + \beta^* b_i - |\alpha|^2 - |\beta|^2\Big) + \frac{U}{2}\left[n_i^a(n_i^a-1) + n_i^b(n_i^b-1)\right] + U_{AB} n_i^a n_i^b - \mu(n_i^a + n_i^b)\Big] \tag{S3}$$

Here we have defined $\alpha \equiv \langle a\rangle$ and $\beta \equiv \langle b\rangle$, and use z to denote the number of nearest neighbors. The averages α and β take on the role of variational parameters. In principle, they are independent, but in our experiment we strive to achieve similar populations in both components, so by symmetry we can assume they are equal. The mean-field Hamiltonian is defined on the single-site Fock basis $|n^a\rangle \otimes |n^b\rangle$, where $|n^p\rangle \in \{|0\rangle, |1\rangle \cdots |n_{\max}\rangle\}$, and we can obtain the overall ground state by minimizing the lowest-energy eigenstate as a function of α.

To obtain the phase diagram, we carry out this procedure for a range of parameters $(t/U, \mu/U, U_{AB}/U)$. The Mott insulating phase is characterized the absence of number fluctuations, and hence $\langle a\rangle = 0$. There are two limiting cases; if $U_{AB}/U = 1$ there is effectively no difference between the two components, and everything maps onto the single-component system. If $U_{AB}/U = 0$, on the other hand, the two components do not interact at all, and they form two separable Mott insulators. This is the spin-Mott phase. See Fig. 1 for the phase diagram evaluated at different values of U_{AB}/U. As this parameter is tuned away from zero, shells with an uneven integer number of particles develop between the spin-Mott shells that have an even number of particles.

* Present address: ColdQuanta Inc., Boulder, CO, United States of America
† Present address: Department of Physics and State Key Laboratory of Low Dimensional Quantum Physics, Tsinghua University, and Frontier Science Center for Quantum Information, Beijing, 100084, China
‡ Present address: Honeywell Quantum Solutions, Broomfield, CO, United States of America

[S1] W. C. Chung, J. de Hond, J. Xiang, E. Cruz-Colón, and W. Ketterle, Phys. Rev. Lett. **126**, 163203 (2021).

[S2] R. Grimm, M. Weidemüller, and Y. B. Ovchinnikov, Advances In Atomic, Molecular, and Optical Physics **42**, 95 (2000).

[S3] F. Le Kien, P. Schneeweiss, and A. Rauschenbeutel, The European Physical Journal D **67**, 92 (2013).

[S4] P. L. Gould, G. A. Ruff, and D. E. Pritchard, Phys. Rev. Lett. **56**, 827 (1986).

[S5] C. Sias, H. Lignier, Y. P. Singh, A. Zenesini, D. Ciampini, O. Morsch, and E. Arimondo, Phys. Rev. Lett. **100**, 040404 (2008).

[S6] R. Ma, M. E. Tai, P. M. Preiss, W. S. Bakr, J. Simon, and M. Greiner, Phys. Rev. Lett. **107**, 095301 (2011).

[S7] A. M. Kaufman, R. P. Anderson, T. M. Hanna, E. Tiesinga, P. S. Julienne, and D. S. Hall, Phys. Rev. A **80**, 050701(R) (2009).

[S8] J. K. Freericks and H. Monien, Europhysics Letters (EPL) **26**, 545 (1994).

[S9] M. P. A. Fisher, P. B. Weichman, G. Grinstein, and D. S. Fisher, Phys. Rev. B **40**, 546 (1989).

Bibliography

[1] R. P. Feynman, "Simulating physics with computers," *International Journal of Theoretical Physics*, vol. 21, no. 6–7, pp. 467–488, 1982.

[2] I. M. Georgescu, S. Ashhab, and F. Nori, "Quantum simulation," *Rev. Mod. Phys.*, vol. 86, pp. 153–185, Mar 2014.

[3] M. H. Anderson, J. R. Ensher, M. R. Matthews, C. E. Wieman, and E. A. Cornell, "Observation of Bose-Einstein condensation in a dilute atomic vapor," *science*, vol. 269, no. 5221, pp. 198–201, 1995.

[4] C. C. Bradley, C. Sackett, J. Tollett, and R. G. Hulet, "Evidence of Bose-Einstein condensation in an atomic gas with attractive interactions," *Physical review letters*, vol. 75, no. 9, p. 1687, 1995.

[5] K. B. Davis, M.-O. Mewes, M. R. Andrews, N. J. van Druten, D. S. Durfee, D. Kurn, and W. Ketterle, "Bose-Einstein condensation in a gas of sodium atoms," *Physical review letters*, vol. 75, no. 22, p. 3969, 1995.

[6] B. DeMarco and D. S. Jin, "Onset of Fermi degeneracy in a trapped atomic gas," *science*, vol. 285, no. 5434, pp. 1703–1706, 1999.

[7] F. Schreck, L. Khaykovich, K. Corwin, G. Ferrari, T. Bourdel, J. Cubizolles, and C. Salomon, "Quasipure Bose-Einstein condensate immersed in a Fermi sea," *Physical Review Letters*, vol. 87, no. 8, p. 080403, 2001.

[8] A. G. Truscott, K. E. Strecker, W. I. McAlexander, G. B. Partridge, and R. G. Hulet, "Observation of Fermi pressure in a gas of trapped atoms," *Science*, vol. 291, no. 5513, pp. 2570–2572, 2001.

[9] I. Bloch, J. Dalibard, and W. Zwerger, "Many-body physics with ultracold gases," *Rev. Mod. Phys.*, vol. 80, pp. 885–964, Jul 2008.

[10] M. Greiner, O. Mandel, T. Esslinger, T. W. Hänsch, and I. Bloch, "Quantum phase transition from a superfluid to a Mott insulator in a gas of ultracold atoms," *Nature*, vol. 415, pp. 39–44, 2002.

[11] M. Köhl, H. Moritz, T. Stöferle, K. Günter, and T. Esslinger, "Fermionic atoms in a three dimensional optical lattice: observing Fermi surfaces, dynamics, and interactions," *Physical review letters*, vol. 94, no. 8, p. 080403, 2005.

[12] J. Simon, W. S. Bakr, R. Ma, M. E. Tai, P. M. Preiss, and M. Greiner, "Quantum simulation of antiferromagnetic spin chains in an optical lattice," *Nature*, vol. 472, pp. 307–312, 2011.

[13] J. Struck, C. Ölschläger, R. Le Targat, P. Soltan-Panahi, A. Eckardt, M. Lewenstein, P. Windpassinger, and K. Sengstock, "Quantum simulation of frustrated classical magnetism in triangular optical lattices," *Science*, vol. 333, pp. 996–999, 2011.

[14] N. Fläschner, B. Rem, M. Tarnowski, D. Vogel, D.-S. Lühmann, K. Sengstock, and C. Weitenberg, "Experimental reconstruction of the Berry curvature in a Floquet Bloch band," *Science*, vol. 352, no. 6289, pp. 1091–1094, 2016.

[15] G. Jotzu, M. Messer, R. Desbuquois, M. Lebrat, T. Uehlinger, D. Greif, and T. Esslinger, "Experimental realization of the topological Haldane model with ultracold fermions," *Nature*, vol. 515, no. 7526, pp. 237–240, 2014.

[16] A. J. Daley, H. Pichler, J. Schachenmayer, and P. Zoller, "Measuring entanglement growth in quench dynamics of bosons in an optical lattice," *Physical review letters*, vol. 109, no. 2, p. 020505, 2012.

[17] P. N. Jepsen, Y. K. E. Lee, H. Lin, I. Dimitrova, Y. Margalit, W. W. Ho, and W. Ketterle, "Long-lived phantom helix states in Heisenberg quantum magnets," *Nature Physics*, vol. 18, no. 8, pp. 899–904, 2022.

[18] R. Grimm, M. Weidemüller, and Y. B. Ovchinnikov, "Optical dipole traps for neutral atoms," in *Advances in atomic, molecular, and optical physics*, vol. 42, pp. 95–170, Elsevier, 2000.

[19] W. S. Bakr, J. I. Gillen, A. Peng, S. Fölling, and M. Greiner, "A quantum gas microscope for detecting single atoms in a Hubbard-regime optical lattice," *Nature (London)*, vol. 462, no. 7269, pp. 74–77, 2009.

[20] J. F. Sherson, C. Weitenberg, M. Endres, M. Cheneau, I. Bloch, and S. Kuhr, "Single-atom-resolved fluorescence imaging of an atomic Mott insulator," *Nature (London)*, vol. 467, no. 7311, pp. 68–72, 2010.

[21] M. Endres, H. Bernien, A. Keesling, H. Levine, E. R. Anschuetz, A. Krajenbrink, C. Senko, V. Vuletic, M. Greiner, and M. D. Lukin, "Atom-by-atom assembly of defect-free one-dimensional cold atom arrays," *Science*, vol. 354, no. 6315, pp. 1024–1027, 2016.

[22] J. Wilson, S. Saskin, Y. Meng, S. Ma, R. Dilip, A. Burgers, and J. Thompson, "Trapping alkaline earth Rydberg atoms optical tweezer arrays," *Physical review letters*, vol. 128, no. 3, p. 033201, 2022.

[23] A. Cooper, J. P. Covey, I. S. Madjarov, S. G. Porsev, M. S. Safronova, and M. Endres, "Alkaline-earth atoms in optical tweezers," *Physical Review X*, vol. 8, no. 4, p. 041055, 2018.

[24] B. Xiao, X.-K. Wang, Y.-G. Zheng, Y.-M. Yang, W.-Y. Zhang, G.-X. Su, M.-D. Li, X. Jiang, and Z.-S. Yuan, "Generating two-dimensional quantum gases with high stability," *Chinese Physics B*, vol. 29, no. 7, p. 076701, 2020.

[25] I. Despard, *The construction of a bosonic quantum-gas microscope*. PhD thesis, University of Strathclyde,, 2022.

[26] D. Mitra, *Exploring attractively interacting fermions in 2D using a quantum gas microscope*. PhD thesis, Princeton University, 2018.

[27] J. Yang, L. Liu, J. Mongkolkiattichai, and P. Schauss, "Site-resolved imaging of ultracold fermions in a triangular-lattice quantum gas microscope," *PRX Quantum*, vol. 2, no. 2, p. 020344, 2021.

[28] K. Kwon, K. Kim, J. Hur, S. Huh, and J.-y. Choi, "Site-resolved imaging of a bosonic Mott insulator of ^{7}Li atoms," *Physical Review A*, vol. 105, no. 3, p. 033323, 2022.

[29] D. Greif, M. F. Parsons, A. Mazurenko, C. S. Chiu, S. Blatt, F. Huber, G. Ji, and M. Greiner, "Site-resolved imaging of a fermionic Mott insulator," *Science*, vol. 351, no. 6276, pp. 953–957, 2016.

[30] A. Omran, M. Boll, T. A. Hilker, K. Kleinlein, G. Salomon, I. Bloch, and C. Gross, "Microscopic observation of Pauli blocking in degenerate fermionic lattice gases," *Phys. Rev. Lett.*, vol. 115, no. 26, p. 263001, 2015.

[31] L. W. Cheuk, M. A. Nichols, M. Okan, T. Gersdorf, V. V. Ramasesh, W. S. Bakr, T. Lompe, and M. W. Zwierlein, "Quantum-gas microscope for fermionic atoms," *Phys. Rev. Lett.*, vol. 114, no. 19, p. 193001, 2015.

[32] E. Haller, J. Hudson, A. Kelly, D. A. Cotta, B. Peaudecerf, G. D. Bruce, and S. Kuhr, "Single-atom imaging of fermions in a quantum-gas microscope," *Nature Physics*, vol. 11, no. 9, pp. 738–742, 2015.

[33] A. Impertro, J. F. Wienand, S. Häfele, H. von Raven, S. Hubele, T. Klostermann, C. R. Cabrera, I. Bloch, and M. Aidelsburger, "An unsupervised deep learning algorithm for single-site reconstruction in quantum gas microscopes," *Communications Physics*, vol. 6, no. 1, p. 166, 2023.

[34] J. Trisnadi, M. Zhang, L. Weiss, and C. Chin, "Design and construction of a quantum matter synthesizer," *Review of Scientific Instruments*, vol. 93, no. 8, 2022.

[35] S. Buob, J. Höschele, V. Makhalov, A. Rubio-Abadal, and L. Tarruell, "A strontium quantum-gas microscope," *PRX Quantum*, vol. 5, no. 2, p. 020316, 2024.

[36] R. Yamamoto, J. Kobayashi, T. Kuno, K. Kato, and Y. Takahashi, "An ytterbium quantum gas microscope with narrow-line laser cooling," *New Journal of Physics*, vol. 18, no. 2, p. 023016, 2016.

[37] L. Su, A. Douglas, M. Szurek, R. Groth, S. F. Ozturk, A. Krahn, A. H. Hébert, G. A. Phelps, S. Ebadi, S. Dickerson, *et al.*, "Dipolar quantum solids emerging in a Hubbard quantum simulator," *Nature*, vol. 622, no. 7984, pp. 724–729, 2023.

[38] J. S. Rosenberg, L. Christakis, E. Guardado-Sanchez, Z. Z. Yan, and W. S. Bakr, "Observation of the Hanbury Brown–Twiss effect with ultracold molecules," *Nat. Phys.*, vol. 18, no. 9, pp. 1062–1066, 2022.

[39] L. W. Cheuk, M. A. Nichols, K. R. Lawrence, M. Okan, H. Zhang, E. Khatami, N. Trivedi, T. Paiva, M. Rigol, and M. W. Zwierlein, "Observation of spatial charge and spin correlations in the 2D Fermi-Hubbard model," *Science*, vol. 353, no. 6305, pp. 1260–1264, 2016.

[40] M. Boll, T. A. Hilker, G. Salomon, A. Omran, J. Nespolo, L. Pollet, I. Bloch, and C. Gross, "Spin and charge resolved quantum gas microscopy of antiferromagnetic order in Hubbard chains," *arXiv preprint arXiv:1605.05661*, 2016.

[41] A. Mazurenko, C. S. Chiu, G. Li, M. F. Parsons, M. Kanász-Nagy, R. Schmidt, F. Grusdt, E. Demler, D. Greif, and M. Greiner, "A cold-atom Fermi–Hubbard antiferromagnet," *Nature*, vol. 545, pp. 462–466, 2017.

[42] M. A. Nichols, L. W. Cheuk, M. Okan, T. R. Hartke, E. Mendez, T. Senthil, E. Khatami, H. Zhang, and M. W. Zwierlein, "Spin transport in a Mott insulator of ultracold fermions," *Science*, vol. 363, no. 6425, pp. 383–387, 2019.

[43] P. T. Brown, D. Mitra, E. Guardado-Sanchez, R. Nourafkan, A. Reymbaut, C.-D. Hébert, S. Bergeron, A.-M. Tremblay, J. Kokalj, D. A. Huse, *et al.*, "Bad metallic transport in a cold atom Fermi-Hubbard system," *Science*, vol. 363, no. 6425, pp. 379–382, 2019.

[44] M. Xu, L. H. Kendrick, A. Kale, Y. Gang, G. Ji, R. T. Scalettar, M. Lebrat, and M. Greiner, "Frustration-and doping-induced magnetism in a Fermi-Hubbard simulator," *Nature*, vol. 620, no. 7976, pp. 971–976, 2023.

[45] M. L. Prichard, B. M. Spar, I. Morera, E. Demler, Z. Z. Yan, and W. S. Bakr, "Directly imaging spin polarons in a kinetically frustrated Hubbard system," *Nature*, vol. 629, no. 8011, pp. 323–328, 2024.

[46] R. Yao, S. Chi, M. Wang, R. J. Fletcher, and M. Zwierlein, "Measuring pair correlations in bose and fermi gases via atom-resolved microscopy," *Physical Review Letters*, vol. 134, no. 18, p. 183402, 2025.

[47] T. de Jongh, J. Verstraten, M. Dixmerias, C. Daix, B. Peaudecerf, and T. Yefsah, "Quantum gas microscopy of fermions in the continuum," *Physical Review Letters*, vol. 134, no. 18, p. 183403, 2025.

[48] J. Verstraten, K. Dai, M. Dixmerias, B. Peaudecerf, T. de Jongh, and T. Yefsah, "*In situ* imaging of a single-atom wave packet in continuous space," *Physical Review Letters*, vol. 134, no. 8, p. 083403, 2025.

[49] J. Xiang, E. Cruz-Colón, C. C. Chua, W. R. Milner, J. de Hond, J. F. Fricke, and W. Ketterle, "In situ imaging of the thermal de broglie wavelength in an ultracold bose gas," *Physical Review Letters*, vol. 134, no. 18, p. 183401, 2025.

[50] J. Esteve, J.-B. Trebbia, T. Schumm, A. Aspect, C. I. Westbrook, and I. Bouchoule, "Observations of density fluctuations in an elongated Bose gas: Ideal gas and quasicondensate regimes," *Phys. Rev. Lett.*, vol. 96, no. 13, p. 130403, 2006.

[51] V. Guarrera, P. Würtz, A. Ewerbeck, A. Vogler, G. Barontini, and H. Ott, "Observation of local temporal correlations in trapped quantum gases," *Phys. Rev. Lett.*, vol. 107, no. 16, p. 160403, 2011.

[52] A. Blumkin, S. Rinott, R. Schley, A. Berkovitz, I. Shammass, and J. Steinhauer, "Observing atom bunching by the Fourier slice theorem," *Phys. Rev. Lett.*, vol. 110, no. 26, p. 265301, 2013.

[53] W. C. Chung, J. de Hond, J. Xiang, E. Cruz-Colón, and W. Ketterle, "Tunable single-ion anisotropy in spin-1 models realized with ultracold atoms," *Physical Review Letters*, vol. 126, no. 16, p. 163203, 2021.

[54] J. de Hond, J. Xiang, W. C. Chung, E. Cruz-Colón, W. Chen, W. C. Burton, C. J. Kennedy, and W. Ketterle, "Preparation of the spin-Mott state: a spinful Mott insulator of repulsively bound pairs," *Physical Review Letters*, vol. 128, no. 9, p. 093401, 2022.

[55] W. C. Chung, *Quantum simulation of spin-1 physics with bosons in optical lattice*. PhD thesis, Massachusetts Institute of Technology, 2021.

[56] D. Jaksch and P. Zoller, "The cold atom Hubbard toolbox," *Annals of Physics*, vol. 315, no. 1, pp. 52–79, 2005. Special Issue.

[57] C. Weitenberg, M. Endres, J. F. Sherson, M. Cheneau, P. Schauß, T. Fukuhara, I. Bloch, and S. Kuhr, "Single-spin addressing in an atomic Mott insulator," *Nature*, vol. 471, pp. 319–324, 2011.

[58] J. Schachenmayer, D. M. Weld, H. Miyake, G. A. Siviloglou, W. Ketterle, and A. J. Daley, "Adiabatic cooling of bosons in lattices to magnetically ordered quantum states," *Phys. Rev. A*, vol. 92, p. 041602, Oct 2015.

[59] M. Lubasch, V. Murg, U. Schneider, J. I. Cirac, and M.-C. Bañuls, "Adiabatic preparation of a Heisenberg antiferromagnet using an optical superlattice," *Phys. Rev. Lett.*, vol. 107, p. 165301, Oct 2011.

[60] J. J. García-Ripoll, M. A. Martin-Delgado, and J. I. Cirac, "Implementation of spin hamiltonians in optical lattices," *Phys. Rev. Lett.*, vol. 93, p. 250405, Dec 2004.

[61] A. de Paz, A. Sharma, A. Chotia, E. Maréchal, J. H. Huckans, P. Pedri, L. Santos, O. Gorceix, L. Vernac, and B. Laburthe-Tolra, "Nonequilibrium quantum magnetism in a dipolar lattice gas," *Phys. Rev. Lett.*, vol. 111, p. 185305, Oct 2013.

[62] P. Schauß, J. Zeiher, T. Fukuhara, S. Hild, M. Cheneau, T. Macrì, T. Pohl, I. Bloch, and C. Gross, "Crystallization in Ising quantum magnets," *Science*, vol. 347, no. 6229, pp. 1455–1458, 2015.

[63] J. Koepsell, J. Vijayan, P. Sompet, F. Grusdt, T. A. Hilker, E. Demler, G. Salomon, I. Bloch, and C. Gross, "Imaging magnetic polarons in the doped Fermi–Hubbard model," *Nature*, vol. 572, pp. 358–362, 2019.

[64] E. Altman, W. Hofstetter, E. Demler, and M. D. Lukin, "Phase diagram of two-component bosons on an optical lattice," *New Journal of Physics*, vol. 5, pp. 113–113, sep 2003.

[65] T. Fukuhara, P. Schauß, M. Endres, S. Hild, M. Cheneau, I. Bloch, and C. Gross, "Microscopic observation of magnon bound states and their dynamics," *Nature*, vol. 502, pp. 76–79, 2013.

[66] S. Hild, T. Fukuhara, P. Schauß, J. Zeiher, M. Knap, E. Demler, I. Bloch, and C. Gross, "Far-from-equilibrium spin transport in Heisenberg quantum magnets," *Phys. Rev. Lett.*, vol. 113, p. 147205, Oct 2014.

[67] P. N. Jepsen, J. Amato-Grill, I. Dimitrova, W. W. Ho, E. Demler, and W. Ketterle, "Spin transport in a tunable Heisenberg model realized with ultracold atoms," *Nature*, vol. 588, pp. 403–407, 2020.

[68] P. N. Jepsen, W. W. Ho, Amato-Grill, I. Dimitrova, E. Demler, and W. Ketterle, "Transverse spin dynamics in the anisotropic Heisenberg model realized with ultracold atoms," *arXiv:2103.07866*, 2021.

[69] A. Kleine, C. Kollath, I. P. McCulloch, T. Giamarchi, and U. Schollwöck, "Spin-charge separation in two-component Bose gases," *Phys. Rev. A*, vol. 77, p. 013607, Jan 2008.

[70] C. Zener and R. H. Fowler, "Non-adiabatic crossing of energy levels," *Proceedings of the Royal Society of London. Series A*, vol. 137, no. 833, pp. 696–702, 1932.

[71] L. Landau, "Zur Theorie der Energieubertragung. II," *Physikalische Zeitschrift der Sowjetunion*, vol. 2, pp. 46–51, 1932.

[72] J. R. Rubbmark, M. M. Kash, M. G. Littman, and D. Kleppner, "Dynamical effects at avoided level crossings: A study of the Landau-Zener effect using rydberg atoms," *Phys. Rev. A*, vol. 23, pp. 3107–3117, Jun 1981.

[73] A. B. Kuklov and B. V. Svistunov, "Counterflow superfluidity of two-species ultracold atoms in a commensurate optical lattice," *Phys. Rev. Lett.*, vol. 90, p. 100401, Mar 2003.

[74] B. Yang, H. Sun, C.-J. Huang, H.-Y. Wang, Y. Deng, H.-N. Dai, Z.-S. Yuan, and J.-W. Pan, "Cooling and entangling ultracold atoms in optical lattices," *Science*, vol. 369, no. 6503, pp. 550–553, 2020.

[75] Y.-G. Zheng, A. Luo, Y.-C. Shen, M.-G. He, Z.-H. Zhu, Y. Liu, W.-Y. Zhang, H. Sun, Y. Deng, Z.-S. Yuan, *et al.*, "Counterflow superfluidity in a two-component Mott insulator," *Nature Physics*, pp. 1–6, 2025.

[76] J. B. Pendry, "Negative refraction makes a perfect lens," *Physical review letters*, vol. 85, no. 18, p. 3966, 2000.

[77] E. P. Goodwin and J. C. Wyant, *Field Guide to Interferometric Optical Testing*, vol. FG06 of *Field Guides*. Bellingham, WA: SPIE Press, 2006.

[78] C. Kennedy, *Creating novel quantum states of ultracold bosons in optical lattices*. PhD thesis, Massachusetts Institute of Technology, 2017.

[79] K. Niu and C. Tian, "Zernike polynomials and their applications," *Journal of Optics*, vol. 24, no. 12, p. 123001, 2022.

[80] L. W. Cheuk, *Quantum gas microscopy of strongly correlated fermions*. PhD thesis, Massachusetts Institute of Technology, Department of Physics, 2017.

[81] J. I. Gillen, *The quantum gas microscope*. PhD thesis, Harvard University, 2009.

[82] C. Weitenberg, *Single-atom resolved imaging and manipulation in an atomic Mott insulator*. PhD thesis, LMU München, 2011.

[83] Y. Tian, Z. Zhang, J. Ye, Y. Zhao, J. Hu, and W. Chen, "Quantum gas microscope assisted with T-shape vacuum viewports," *Optics Express*, vol. 30, no. 20, pp. 36912–36920, 2022.

[84] C. T. Gersdorf, "A quantum gas microscope for fermionic atoms," Master's thesis, EHT-Zürich, 2012.

[85] Q. Xie, *Development and application of a quantum gas microscope*. PhD thesis, University of Science and Technology of China, 6 2018.

[86] S. Brakhane, W. Alt, D. Meschede, C. Robens, G. Moon, and A. Alberti, "Note: Ultra-low birefringence dodecagonal vacuum glass cell," *Review of Scientific Instruments*, vol. 86, no. 12, 2015.

[87] M. Holynski, *Creating a two dimensional cold mixture experiment.* PhD thesis, University of Birmingham, 2012.

[88] X. Zhong, T. Wang, J. Yan, and G. Jin, "Aberrations correction of tilted plane-parallel plate in convergent rays," *Applied Optics*, vol. 54, no. 7, pp. 1758–1764, 2015.

[89] A. Hebert, *A dipolar erbium quantum gas microscope.* PhD thesis, Harvard University, 2021.

[90] C. Robens, S. Brakhane, W. Alt, F. Kleißler, D. Meschede, G. Moon, G. Ramola, and A. Alberti, "High numerical aperture (NA= 0.92) objective lens for imaging and addressing of cold atoms," *Optics letters*, vol. 42, no. 6, pp. 1043–1046, 2017.

[91] EdmundOptics, "Beam quality and Strehl ratio."

[92] V. N. Mahajan, "Strehl ratio for primary aberrations in terms of their aberration variance," *JOSA*, vol. 73, no. 6, pp. 860–861, 1983.

[93] E. W. Streed, ^{87}*Rubidium Bose-Einstein condensates: machine construction and quantum Zeno experiments.* PhD thesis, Massachusetts Institute of Technology, 2006.

[94] J. F. Fricke, "Towards a rubidium quantum gas microscope," Master's thesis, ETH Zurich, 2023.

[95] J. H. Moore, C. C. Davis, and M. A. Coplan, *Building scientific apparatus.* Cambridge university press, 2009.

[96] A. Rudelis, B. Hu, J. Sinclair, E. Bytyqi, A. Schwartzman, R. Brenes, T. Kadosh Zhitomirsky, M. Schleier-Smith, and V. Vuletić, "Degradation of Ta2O5/SiO2 dielectric cavity mirrors in ultra-high vacuum," *Optics Express*, vol. 31, no. 24, pp. 39670–39680, 2023.

[97] TheEyeNews, "What is the cause of the crazing on my eyeglass lenses?."

[98] D. J. Smith, M. McCullough, C. Smith, T. Mikami, and T. Jitsuno, "Low stress ion-assisted coatings on fused silica substrates for large aperture laser pulse compression gratings," in *Laser-Induced Damage in Optical Materials: 2008*, vol. 7132, pp. 123–129, SPIE, 2008.

[99] M. Harris, C. Adams, S. Cornish, I. McLeod, E. Tarleton, and I. Hughes, "Polarization spectroscopy in rubidium and cesium," *Physical Review A—Atomic, Molecular, and Optical Physics*, vol. 73, no. 6, p. 062509, 2006.

[100] M. S. Miranda, *Quantum gas microscope for ytterbium atoms.* PhD thesis, Tokyo Institute of Technology, 2016.

[101] R. E. Thompson, D. R. Larson, and W. W. Webb, "Precise nanometer localization analysis for individual fluorescent probes," *Biophysical journal*, vol. 82, no. 5, pp. 2775–2783, 2002.

[102] J. M. Jacobsen, "A reconstruction algorithm for fluorescence images of lithium atoms in a triangular optical lattice," Master's thesis, University of Hamburg, 2017.

[103] D. J. Wineland, J. Dalibard, and C. Cohen-Tannoudji, "Sisyphus cooling of a bound atom," *JOSA B*, vol. 9, no. 1, pp. 32–42, 1992.

[104] C. J. Foot, *Atomic physics*, vol. 7. Oxford university press, 2005.

[105] P. D. Lett, W. D. Phillips, S. Rolston, C. E. Tanner, R. Watts, and C. Westbrook, "Optical molasses," *Journal of the Optical Society of America B*, vol. 6, no. 11, pp. 2084–2107, 1989.

[106] L. Christakis, *Microscopy of quantum correlations in an ultracold molecular gas*. PhD thesis, Princeton University, 2023.

[107] R. Hanbury Brown and R. Q. Twiss, "A test of a new type of stellar interferometer on Sirius," *Nature (London)*, vol. 178, no. 7120, pp. 1046–1048, 1956.

[108] A. Aspect, "Hanbury Brown and Twiss, Hong Ou and Mandel effects and other landmarks in quantum optics: From photons to atoms," *arXiv preprint arXiv:2005.08239*, 2020.

[109] A. Eddington, "Stellar interference," *Interference: The History of Optical Interferometry and the Scientists Who Tamed Light*, p. 151, 2023.

[110] R. Hanbury Brown and R. Q. Twiss, "Correlation between photons in two coherent beams of light," *Nature (London)*, vol. 177, no. 7120, pp. 27–29, 1956.

[111] R. J. Glauber, "Coherent and incoherent states of the radiation field," *Phys. Rev.*, vol. 131, no. 6, p. 2766, 1963.

[112] R. J. Glauber, "The quantum theory of optical coherence," *Phys. Rev.*, vol. 130, no. 6, p. 2529, 1963.

[113] D. Ferreira, R. Bachelard, W. Guerin, R. Kaiser, and M. Fouché, "Connecting field and intensity correlations: the Siegert relation and how to test it," *American Journal of Physics*, vol. 88, no. 10, pp. 831–837, 2020.

[114] A. Siegert, *On the fluctuations in signals returned by many independently moving scatterers*. Radiation Laboratory, Massachusetts Institute of Technology, 1943.

[115] W. D. Oliver, J. Kim, R. C. Liu, and Y. Yamamoto, "Hanbury Brown and Twiss-type experiment with electrons," *Science*, vol. 284, no. 5412, pp. 299–301, 1999.

[116] M. Henny, S. Oberholzer, C. Strunk, T. Heinzel, K. Ensslin, M. Holland, and C. Schönenberger, "The fermionic Hanbury Brown and Twiss experiment," *Science*, vol. 284, no. 5412, pp. 296–298, 1999.

[117] H. Kiesel, A. Renz, and F. Hasselbach, "Observation of Hanbury Brown–Twiss anticorrelations for free electrons," *Nature (London)*, vol. 418, no. 6896, pp. 392–394, 2002.

[118] M. Iannuzzi, A. Orecchini, F. Sacchetti, P. Facchi, and S. Pascazio, "Direct experimental evidence of free-fermion antibunching," *Phys. Rev. Lett.*, vol. 96, no. 8, p. 080402, 2006.

[119] M. Yasuda and F. Shimizu, "Observation of two-atom correlation of an ultracold neon atomic beam," *Phys. Rev. Lett.*, vol. 77, no. 15, p. 3090, 1996.

[120] R. G. Dall, S. S. Hodgman, A. G. Manning, M. T. Johnsson, K. G. H. Baldwin, and A. G. Truscott, "Observation of atomic speckle and Hanbury Brown–Twiss correlations in guided matter waves," *Nat. Comm.*, vol. 2, no. 1, p. 291, 2011.

[121] M. Schellekens, R. Hoppeler, A. Perrin, J. V. Gomes, D. Boiron, A. Aspect, and C. I. Westbrook, "Hanbury Brown Twiss effect for ultracold quantum gases," *Science*, vol. 310, no. 5748, pp. 648–651, 2005.

[122] T. Jeltes, J. M. McNamara, W. Hogervorst, W. Vassen, V. Krachmalnicoff, M. Schellekens, A. Perrin, H. Chang, D. Boiron, A. Aspect, and C. I. Westbrook, "Comparison of the Hanbury Brown-Twiss effect for bosons and fermions," *Nature (London)*, vol. 445, pp. 402–405, 2007.

[123] A. G. Manning, S. S. Hodgman, R. G. Dall, M. T. Johnsoon, and A. G. Truscott, "The Hanbury Brown-Twiss effect in a pulsed atom laser," *Optics Express*, vol. 18, no. 18, pp. 18712–18719, 2010.

[124] A. G. Manning, W. RuGway, S. S. Hodgman, R. G. Dall, K. G. H. Baldwin, and A. G. Truscott, "Third-order spatial correlations for ultracold atoms," *New Journal of Physics*, vol. 15, p. 013042, 2013.

[125] K. F. Thomas, S. Li, A. H. Abbas, A. G. Truscott, and S. S. Hodgman, "N-body antibunching in a degenerate fermi gas of ^{3}He* atoms," *Phys Rev Research*, vol. 6, p. L022003, 2024.

[126] A. Perrin, R. Bücker, S. Manz, T. Betz, C. Koller, T. Plisson, T. Schumm, and J. Schmiedmayer, "Hanbury Brown and Twiss correlations across the Bose-Einstein condensation threshold," *Nat. Phys.*, vol. 8, no. 3, pp. 195–198, 2012.

[127] S. Sunami, V. P. Singh, E. Rydow, A. Beregi, E. Chang, L. Mathey, and C. J. Foot, "Detecting phase coherence of 2D Bose gases via noise correlations," *arXiv preprint arXiv:2406.03491*, 2024.

[128] S. Fölling, F. Gerbier, A. Widera, O. Mandel, T. Gericke, and I. Bloch, "Spatial quantum noise interferometry in expanding ultracold atom clouds," *Nature (London)*, vol. 434, no. 7032, pp. 481–484, 2005.

[129] T. Rom, T. Best, D. Van Oosten, U. Schneider, S. Fölling, B. Paredes, and I. Bloch, "Free fermion antibunching in a degenerate atomic Fermi gas released from an optical lattice," *Nature (London)*, vol. 444, no. 7120, pp. 733–736, 2006.

[130] C. Sanner, E. J. Su, A. Keshet, R. Gommers, Y.-i. Shin, W. Huang, and W. Ketterle, "Suppression of density fluctuations in a quantum degenerate Fermi gas," *Phys. Rev. Lett.*, vol. 105, no. 4, p. 040402, 2010.

[131] T. Müller, B. Zimmermann, J. Meineke, J.-P. Brantut, T. Esslinger, and H. Moritz, "Local observation of antibunching in a trapped Fermi gas," *Phys. Rev. Lett.*, vol. 105, no. 4, p. 040401, 2010.

[132] J. V. Gomes, A. Perrin, M. Schellekens, D. Boiron, C. I. Westbrook, and M. Belsley, "Theory for a Hanbury Brown Twiss experiment with a ballistically expanding cloud of cold atoms," *Phys. Rev. A*, vol. 74, no. 5, p. 053607, 2006.

[133] M. Naraschewski and R. J. Glauber, "Spatial coherence and density correlations of trapped Bose gases," *Phys. Rev. A*, vol. 59, no. 6, p. 4595, 1999.

[134] W. Ketterle and N. J. van Druten, "Bose-Einstein condensation of a finite number of particles trapped in one or three dimensions," *Phys. Rev. A*, vol. 54, no. 1, p. 656, 1996.

[135] Z. Hadzibabic and J. Dalibard, "Two-dimensional Bose fluids: An atomic physics perspective," *La Rivista del Nuovo Cimento*, vol. 34, no. 6, pp. 389–434, 2011.

[136] C. Gross and W. S. Bakr, "Quantum gas microscopy for single atom and spin detection," *Nat. Phys.*, vol. 17, no. 12, pp. 1316–1323, 2021.

[137] P. M. Preiss, R. Ma, M. E. Tai, J. Simon, and M. Greiner, "Quantum gas microscopy with spin, atom-number, and multilayer readout," *Phys. Rev. A*, vol. 91, no. 4, p. 041602, 2015.

[138] T. Hartke, B. Oreg, N. Jia, and M. Zwierlein, "Doublon-hole correlations and fluctuation thermometry in a Fermi-Hubbard gas," *Phys. Rev. Lett.*, vol. 125, no. 11, p. 113601, 2020.

[139] J. Koepsell, S. Hirthe, D. Bourgund, P. Sompet, J. Vijayan, G. Salomon, C. Gross, and I. Bloch, "Robust bilayer charge pumping for spin-and density-resolved quantum gas microscopy," *Phys. Rev. Lett.*, vol. 125, no. 1, p. 010403, 2020.

[140] M. Schellekens, *The Hanbury Brown and Twiss effet for cold atoms*. PhD thesis, Université Paris Sud-Paris XI, 2007.

[141] M. Pyzh, S. Krönke, C. Weitenberg, and P. Schmelcher, "Quantum point spread function for imaging trapped few-body systems with a quantum gas microscope," *New Journal of Physics*, vol. 21, no. 5, p. 053013, 2019.

[142] T. M. Wright, A. Perrin, A. Bray, J. Schmiedmayer, and K. V. Kheruntsyan, "Two-body anticorrelation in a harmonically trapped ideal Bose gas," *Phys. Rev. A*, vol. 86, no. 2, p. 023618, 2012.

[143] J. T. M. Walraven *Atomic Hydrogen in Magnetostatic Traps, pg. 16, eq. 2.32*, 1996.

[144] M. Wilkens and C. Weiss, "Particle number fluctuations in an ideal Bose gas," *Journal of Modern Optics*, vol. 44, no. 10, pp. 1801–1814, 1997.

[145] V. V. Kocharovsky, V. V. Kocharovsky, M. Holthaus, C. R. Ooi, A. Svidzinsky, W. Ketterle, and M. O. Scully, "Fluctuations in ideal and interacting Bose–Einstein condensates: From the laser phase transition analogy to squeezed states and Bogoliubov quasiparticles," *Advances in Atomic, Molecular, and Optical Physics*, vol. 53, pp. 291–411, 2006.

[146] S. Brandstetter, C. Heintze, K. Subramanian, P. Hill, P. M. Preiss, M. Gałka, and S. Jochim, "Magnifying the wave function of interacting fermionic atoms," *arXiv preprint arXiv:2409.18954*, 2024.

[147] P. P. Zupancic, "Dynamic holography and beamshaping using digital micromirror devices," *LMU Münich, Grainer Lab Harvard*, vol. 242, 2013.

[148] Y.-K. Lu, Y. Margalit, and W. Ketterle, "Bosonic stimulation of atom–light scattering in an ultracold gas," *Nat. Phys.*, vol. 19, no. 2, pp. 210–214, 2023.

[149] Y. Hao, Y. Zhang, Y. Liu, and L. Wang, "N-body correlation of Tonks–Girardeau gas," *The European Physical Journal D*, vol. 76, no. 12, p. 237, 2022.

[150] V. Weisskopf and E. Wigner, "Berechnung der natürlichen linienbreite auf grund der diracschen lichttheorie," *Part I: Particles and Fields. Part II: Foundations of Quantum Mechanics*, pp. 30–49, 1997.

[151] R. Miller, T. Northup, K. Birnbaum, A. Boca, A. Boozer, and H. Kimble, "Trapped atoms in cavity QED: coupling quantized light and matter," *Journal of Physics B: Atomic, Molecular and Optical Physics*, vol. 38, no. 9, p. S551, 2005.

[152] C. Navarrete-Benlloch, I. de Vega, D. Porras, and J. I. Cirac, "Simulating quantum-optical phenomena with cold atoms in optical lattices," *New Journal of Physics*, vol. 13, no. 2, p. 023024, 2011.

[153] I. de Vega, D. Porras, and J. Ignacio Cirac, "Matter-wave emission in optical lattices: Single particle and collective effects," *Physical review letters*, vol. 101, no. 26, p. 260404, 2008.

[154] L. Krinner, M. Stewart, A. Pazmiño, J. Kwon, and D. Schneble, "Spontaneous emission of matter waves from a tunable open quantum system," *Nature*, vol. 559, no. 7715, pp. 589–592, 2018.

[155] M. Stewart, J. Kwon, A. Lanuza, and D. Schneble, "Dynamics of matter-wave quantum emitters in a structured vacuum," *Physical Review Research*, vol. 2, no. 4, p. 043307, 2020.

[156] A. Di Carli, C. Parsonage, A. La Rooij, L. Koehn, C. Ulm, C. W. Duncan, A. J. Daley, E. Haller, and S. Kuhr, "Commensurate and incommensurate 1d interacting quantum systems," *Nature Communications*, vol. 15, no. 1, p. 474, 2024.